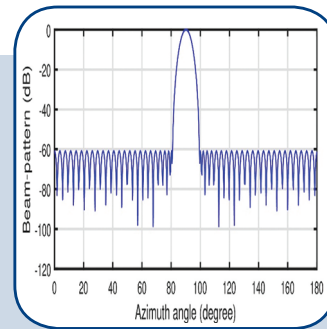
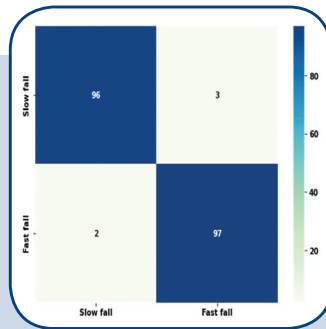
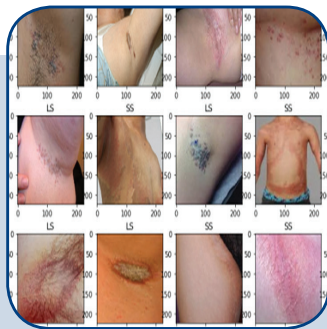
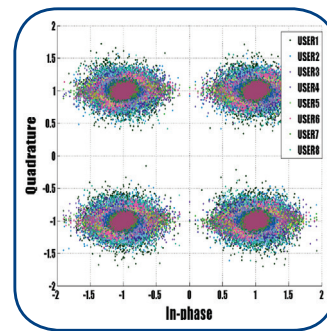
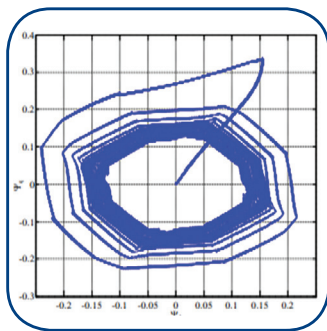


International Journal of Electrical and Computer Engineering Systems



INTERNATIONAL JOURNAL OF ELECTRICAL AND COMPUTER ENGINEERING SYSTEMS

Published by Faculty of Electrical Engineering, Computer Science and Information Technology Osijek,
Josip Juraj Strossmayer University of Osijek, Croatia

Osijek, Croatia | Volume 13, Number 8, 2022 | Pages 611 - 728

The International Journal of Electrical and Computer Engineering Systems is published with the financial support
of the Ministry of Science and Education of the Republic of Croatia

CONTACT

**International Journal of Electrical
and Computer Engineering Systems
(IJECES)**

Faculty of Electrical Engineering, Computer
Science and Information Technology Osijek,
Josip Juraj Strossmayer University of Osijek, Croatia
Kneza Trpimira 2b, 31000 Osijek, Croatia
Phone: +38531224600, Fax: +38531224605
e-mail: ijeces@ferit.hr

Subscription Information

The annual subscription rate is 50€ for individuals,
25€ for students and 150€ for libraries.
Giro account: 2390001 - 1100016777,
Croatian Postal Bank

EDITOR-IN-CHIEF

Tomislav Matić
J.J. Strossmayer University of Osijek,
Croatia

MANAGING EDITOR

Goran Martinović
J.J. Strossmayer University of Osijek,
Croatia

EXECUTIVE EDITOR

Mario Vranješ
J.J. Strossmayer University of Osijek, Croatia

ASSOCIATE EDITORS

Krešimir Fekete
J.J. Strossmayer University of Osijek, Croatia

Damir Filko
J.J. Strossmayer University of Osijek, Croatia

Davor Vinko
J.J. Strossmayer University of Osijek, Croatia

EDITORIAL BOARD

Marinko Barukčić
J.J. Strossmayer University of Osijek, Croatia

Leo Budin
University of Zagreb, Croatia

Matjaz Colnarič
University of Maribor, Slovenia

Aura Conci
Fluminense Federal University, Brazil

Bojan Čukić
West Virginia University, USA

Radu Dobrin
Malardalen University, Sweden

Irena Galić
J.J. Strossmayer University of Osijek, Croatia

Radoslav Galić
J.J. Strossmayer University of Osijek, Croatia

Ratko Grbić
J.J. Strossmayer University of Osijek, Croatia

Marijan Herceg
J.J. Strossmayer University of Osijek, Croatia

Darko Huljenić
Ericsson Nikola Tesla, Croatia

Željko Hocenski
J.J. Strossmayer University of Osijek, Croatia

Gordan Ježić
University of Zagreb, Croatia

Dražan Kozak
J.J. Strossmayer University of Osijek, Croatia

Sven Lončarić
University of Zagreb, Croatia

Tomislav Kilić
University of Split, Croatia

Ivan Maršić
Rutgers, The State University of New Jersey, USA

Kruno Miličević
J.J. Strossmayer University of Osijek, Croatia

Tomislav Mrčela
J.J. Strossmayer University of Osijek, Croatia

Srete Nikolovski
J.J. Strossmayer University of Osijek, Croatia

Davor Pavuna

Ecole Polytechnique Fédérale de
Lausanne, Switzerland

Nedjeljko Perić
University of Zagreb, Croatia

Marjan Popov
Delft University, The Netherlands

Sasikumar Punnekkat
Mälardalen University, Sweden

Chiara Ravasio
University of Bergamo, Italy

Snježana Rimac-Drlje
J.J. Strossmayer University of Osijek, Croatia

Gregor Rozinaj
Slovak University of Technology, Slovakia

Imre Rudas
Budapest Tech, Hungary

Ivan Samardžić
J.J. Strossmayer University of Osijek, Croatia

Dražen Šlišković
J.J. Strossmayer University of Osijek, Croatia

Marinko Stojkov
J.J. Strossmayer University of Osijek, Croatia

Cristina Secleanu
Mälardalen University, Sweden

Siniša Srblić
University of Zagreb, Croatia

Zdenko Šimić
University of Zagreb, Croatia

Damir Šljivac
J.J. Strossmayer University of Osijek, Croatia

Domen Verber
University of Maribor, Slovenia

Dean Vučinić
Vrije Universiteit Brussel, Belgium
J.J. Strossmayer University of Osijek, Croatia

Joachim Weickert
Saarland University, Germany

Drago Žagar
J.J. Strossmayer University of Osijek, Croatia

Proofreader

Ivanka Ferčec
J.J. Strossmayer University of Osijek, Croatia

Editing and technical assistance

Davor Vrandečić
J.J. Strossmayer University of Osijek, Croatia

Stephen Ward
J.J. Strossmayer University of Osijek, Croatia

Dražan Bajer
J.J. Strossmayer University of Osijek, Croatia

Journal is referred in:

- Scopus
- Web of Science Core Collection
(Emerging Sources Citation Index - ESCI)
- Google Scholar
- CiteFactor
- Genamics
- Hrčak
- Ulrichweb
- Reaxys
- Embase
- Engineering Village

Bibliographic Information

Commenced in 2010.
ISSN: 1847-6996
e-ISSN: 1847-7003
Published: quarterly
Circulation: 300

IJECES online
<https://ijeces.ferit.hr>

Copyright

Authors of the International Journal of Electrical
and Computer Engineering Systems must transfer
copyright to the publisher in written form.

TABLE OF CONTENTS

An automatic feature extraction technique from the images of granular parakeratosis disease611

Original Scientific Paper

Sheetal Janthakal | Girisha Hosalli

A Smart Content-Based Image Retrieval Approach Based on Texture Feature and Slantlet Transform ...621

Original Scientific Paper

Hakeem Imad Mhaibes | Qahtan Makki Shallal | May Hattim Abood

Transfer Learning Based Deep Neural Network for Detecting Artefacts in Endoscopic Images633

Original Scientific Paper

Kirthika Natarajan | B. Sargunam

Efficient segmentation and classification of the tumor using improved encoder-decoder architecture in brain MRI images643

Original Scientific Paper

Archana Ingle | Mani Roja | Dr. Manoj Sankhe | Dr. Deepak Patkar

An improved Gaussian Mixture Model with post-processing for multiple object detection in surveillance video analytics653

Original Scientific Paper

Fancy Joy | V. Vijayakumar

Real-time object detection and selection with the LabVIEW program661

Original Scientific Paper

Nihat Pamuk

Spatio-Temporal Information for Action Recognition in Thermal Video Using Deep Learning Model669

Original Scientific Paper

P. Srihari | J. Harikiran

The effect of quantized ETF, grouping, and power allocation on non-orthogonal multiple accesses for wireless communication networks681

Original Scientific Paper

Amir F. Banob | Fayez W. Zaki | Mohammed M. Ashour

Design of Sparse Uniform Linear Array Beamformer using Modified FRM Structure for Varied Applications695

Original Scientific Paper

Parvathi Ammothum Kandy | Sakthivel Vellaisamy

Fuzzy Controller Based DTC of SRM Drive Fed by Common High Side Asymmetric Switch Converter701

Original Scientific Paper

Ashok Kumar Kolluru | Kiran Kumar Malligunta

Scheduling Algorithms: Challenges Towards Smart Manufacturing587

Original Scientific Paper

Abebaw Degu Workneh | Maha Gmira

A quadratic boost converter derived multi output converter for electric vehicles application709

Original Scientific Paper

I. S. Sree Devi | D. M. Mary Synthia Regis Prabha

An observer design for the flux of line start permanent magnet synchronous motors721

Case Study

Hoang-Giang Vu

About this Journal

IJECES Copyright Transfer Form

An automatic feature extraction technique from the images of granular parakeratosis disease

Original Scientific Paper

Sheetal Janthakal

Department of Computer Science and Engineering,
Ballari Institute of Technology and Management,
Ballari, Karnataka, India
Department of Computer Science and Engineering,
Rao Bahadur Y. Mahabaleswarappa Engineering College,
Ballari, Karnataka, India
sjanthakal@yahoo.co.in

Girisha Hosalli

Rao Bahadur Y. Mahabaleswarappa Engineering College,
Department of Computer Science and Engineering,
Ballari, Karnataka, India
hosalligiri@gmail.com

Abstract – The largest and most vital part of the human body is skin and any change in the features of skin is termed as a skin lesion. The paper considers granular parakeratosis lesion that is an epidermal reaction occurring due to the disorder of keratinization, and mainly seen in intertriginous areas. The manual inspection of the lesion features is a bit cumbersome due to which an automated system is proposed in this paper. The main goal is to determine the size and depth of granular parakeratosis lesions using the proposed ensemble algorithm, partition clustering and region properties method. As a flow of the proposed model, segmentation is done using U-net with binary cross entropy, features are extracted using partition clustering and region properties method, and classification is done using SVM 10-fold model. The proposed feature extraction method estimates the depth and absolute size of K lesions in each image by predicting the absolute height and width of the lesion in terms of pixel square. After extracting the features, classification is done, thereby obtaining an accuracy of 95%, sensitivity and specificity of 100%. The proposed model provides better performance compared to state-of-the-art models. The main application of this automated system is in dermatology field where some skin lesions have same features which makes the experts to diagnose the disease incorrectly. If the proposed system is incorporated, diagnosis can be done in an effective manner considering all the relevant features.

Keywords: U-net with Binary Cross Entropy, Partition Clustering, Region Properties, Depth and Absolute Size, SVM 10-fold

1. INTRODUCTION

Granular parakeratosis appears as red or brown hyperkeratotic papules or plaques in intertriginous areas. Patients of various ages have been diagnosed with the illness, and is more common in women than in men [1]. Granular parakeratosis was once assumed to be a contact dermatitis caused by hygiene products like deodorants and antiperspirants; however, cases have been documented even without the application of any personal hygiene products in the affected areas, ruling out contact dermatitis as the cause [2]. Other intertriginous and non-intertriginous body parts, such as the face, have also been reported to develop granular parakeratosis.

As described above, Granular parakeratosis is a type of skin disease. For the diagnosis of such type of diseases, most of the dermatologists rely on traditional methods. Though these methods have shown improved performance, they are still not feasible for a variety of factors such as a large number of patients, infrastructure, technical equipment, etc. Further, granular parakeratosis shares many of the characteristics of benign lesions in its early stages, making it difficult to distinguish. Experts find it difficult to detect the disease with the naked eye. Also, the diagnosis process is quite challenging as the analysis depends on the clinical expertise of the experts.

To overcome this problem, there is a requirement of an automated system that can adapt to technological advancements in the discipline of dermoscopy and assist specialists in detecting lesions accurately and giving a better path to diagnosis. Computer-aided diagnosis (CAD) systems use a variety of machine learning techniques for extracting the features from a given lesion dataset. Several texture analysis techniques like Principal Component Analysis (PCA) and Gray-Level Co-Occurrence Matrix (GLCM) have recently been presented in this arena, and their models have gained widespread acceptance for feature extraction, resulting in enhanced classification [3]. These techniques adopt dermoscopic images and are able to detect the most required features of the affected area.

“The malignant and benign lesions are classified using several feature extraction algorithms such as the ABCD rule, the seven-point checklist method, three-point checklist, and CASH algorithm. The ABCDE rule (Asymmetry, Border, Color, Diameter, Evolve), the 7-point checklist, and the Menzies technique are three clinical diagnosis methods used by dermatologists to distinguish melanoma from nevus [4]. These feature extraction techniques are dependent on lesion color, shape, geometry, texture, and structure [5]. An important screening tool for the detection of melanoma with accurate sensitivity and specificity is ABCD [6]”.

Feature extraction is regarded as a necessary tool for properly analysing an image. Many authors explored a variety of features for classification as explained above; however none of them properly distinguish benign and malignant lesions. Several lesion extraction techniques have been developed in the past to aid specialists in finding the lesions automatically. However, due to variations in shapes and sizes, extracting the features from dermoscopic lesions is a hard task since it results in inaccurate extraction and increases the computational time. To tackle the aforementioned hurdles for more accurate lesion extraction, a new technique for extracting the features from lesion is created.

The novelty of the proposed work lies in feature extraction that is described as follows:

- In this paper, different digital images of parakeratosis have been analyzed.
- Initially, U-net with binary cross entropy technique is applied to segment the dataset, followed by which features (size and depth) of the segmented lesion are extracted using the region properties method, and finally classification of the lesion into starting or later stage is done using the SVM 10-fold validation model.
- Following that, a thorough discussion based on the findings is presented.

The paper comprises four sections, starting with the literature review, where a brief overview of the existing literature is presented. Next, the proposed methodol-

ogy section describes the system architecture and the method implemented. The results and discussion section gives the results obtained from the experiments and discussions on them, and eventually, the final section concludes the paper.

2. LITERATURE REVIEW

Feature selection is a technique used in both machine learning and statistical pattern recognition. This is crucial in a variety of applications, including classification. Many methods for detecting melanoma have been reported in the last decade [7], [8]. Some of these attempts were to imitate dermatologists' performance by extracting and detecting most dermoscopic structures, such as pigment networks, irregular streaks, granularities, blotches, etc. Many studies utilised global approaches to classify skin lesions, whereas others employed local ones [9]. Several feature extraction techniques for various types of skin lesions investigated so far are described.

Features, which are retrieved using local, global, or local-global scenarios, play an important part in classification. For melanoma detection using dermoscopic pictures, Barata et al. [10] used a local-global technique. Local methods were employed to extract features using bag-of-words, whereas global methods were studied for skin lesions categorization in terms of higher sensitivity and specificity, with encouraging results.

The author of [11] suggested an entropy-controlled neighbourhood component analysis paradigm for most discriminant feature selection and dimensionality reduction (ECNCA). A model for lesion classification is also proposed that leverages deep feature information to build the best discriminant feature vector. The ECNCA framework improves fused characteristics by removing the duplicate and superfluous data and selecting the most important components. After the application of the proposed feature framework, the classification is done by testing on four datasets: PH2, ISIC MSK, ISIC UDA, and ISBI-2017, leading to an accuracy of 98.8%, 99.2%, 97.1%, and 95.9%, respectively. The drawback of the method is that it is applicable only to a limited dataset.

The article [12] proposed a diagnosis guided feature fusion (DGFF) that uses lesion information from the melanoma to improve skin lesion segmentation pixel-wise classification performance. It creates feature representations that distinguish between melanoma and non-melanoma lesions and also improves the network's ability to recognise various sorts of skin lesions using dermoscopic images. The extracted features are fed into the pixel-wise classification task, leading to an accuracy of 88.2%, a sensitivity of 63.3%, and a specificity of 94.2%. This method has the limitation of not considering some of the dermoscopic images that contain redness around the lesion area and black spots in an image.

The framework of [13] proposes the Self-supervised Topology Clustering Network (STCN) to segment the skin images automatically. The STCN consists of a transformation-invariant network that comprises a feature extraction function, a self-expression function, and a self-supervision deep topology clustering algorithm. The main goal is to determine the appearance characteristics and keep them consistent across multiple variations. These features will further be automatically partitioned into groups using the Deep Topology Clustering (DTC) algorithm, which will be used to construct pseudo labels for skin images. Finally, the DTC module is used as the self-supervision component to train a classification network using the estimated annotations. But the model is unable to use hand-craft features due to which the required information will be ignored.

To investigate the textural complexity of a skin lesion, a fractal-based regional texture analysis (FRTA) technique was created. FRTA separated the lesion area into smaller subregions based on textural complexity. Successful feature extraction from dermoscopic images has been achieved using a fractal-based border irregularity measurement and regional texture analysis technique. The performance of classification is increased when the Support Vector Machine (SVM) recursive feature elimination (RFE) technique is applied before each stage of the layered structured model [14], but the difficult cases present in an image cannot be classified correctly.

The labels are defined as a method of grouping items into clusters in which objects in one cluster are almost identical and objects in other clusters are significantly different. Clustering's main purpose is to extract sets of patterns, points, or objects from natural groupings [15]. Clusters of various forms and densities are determined using the MDCUT algorithm (Multi-Density Clustering) [16]. It is a density based clustering algorithm that can handle noisy data and discover neighbouring and imbricated clusters. The drawback is that only a few pre-processing methods are applied to the dataset.

Trabelsi et al. [17] used a variety of clustering techniques, including fuzzy c-means, modified fuzzy c-means, and K-means, to segment a skin disease with an 83% true positive rate. The clustering algorithms depend on the identification of a centroid that can generalise a cluster of data. However, the performance of these algorithms degrades with the presence of noisy data and outliers.

Table 1.: Overview of the literature

Method	Major contributions	Limitations
ECNCA	Improves fused characteristics	Works only for Small dataset
DGFF	Improves pixel-wise classification performance	Doesn't consider black spots in an image
STCN	Determines the appearance characteristics	Ignores the required information
FRTA	Improves the performance	Difficult cases are ignored

According to literature, there are various problems with successful feature extraction. The proposed integrated system plays a significant role in overcoming the obstacles of accurate disease diagnosis based on visual and simulated evaluation by measuring the effective features and diagnosing the disease with a higher degree of accuracy. The proposed method employs the conjunction of clustering and region properties methods to overcome these. The suggested approach extracts the size and depth of lesions in an image by applying several morphological functions to the given dataset.

3. PROPOSED METHODOLOGY

3.1. FEATURE EXTRACTION

"Relevant information for accomplishing the computing tasks associated with a certain application" is defined as a feature. There are two types of features: local ones and global ones [18]. In order to build a classification rule, a collection of numerical criteria that describe the object or phenomena seen (supervised or not) is described. Several feature extraction algorithms have been developed, each with their own set of principles [19]. Here, a feed-form method of partition clustering and the region properties method are proposed.

3.2 SYSTEM ARCHITECTURE

The architecture of the proposed system is shown in figure 1. To begin, 224x224 lesion images are acquired, segmentation is performed using the U-net method, followed by watershed-based separation of lesions (formation of clusters), then, extracting the features using regionprop and finally, classification is done using SVM 10-fold model.

If features extracted from the lesion are efficient, it can lead to a better classification of granular parakeratosis. Here, the parakeratosis image consists of several lesions that can be easily identified by labeling the lesions and then determine the width, height, and depth of a lesion. The detailed steps of pre-processing and feature extraction using clustering and region properties are shown in figure 2. Some transformations like thresholding and morphology are applied to the clustered lesion to extract the most descriptive set of features. Using the regionprops approach, the size and depth of the clustered lesions obtained in figure 1 are extracted.

The proposed feature extraction method, being an unsupervised one, extracts the size and depth of a lesion in the following manner:

- Morphology pre-processing techniques remove any small objects and holes in the image.
- The touching cells in an image can be effectively separated using distance transform and thresholding. Thus, leading to the separation of lesions and non-lesions, followed by which a number of clusters of lesions are created.

- Different lesions in the clusters are labeled, after which watershed filling is applied. For each label, the size and depth of the lesion is extracted using the regionprops method of skimage.

3.3 CLUSTERING

One of the most prominent approaches for skin disease segmentation and classification is the clustering algorithm. Clustering, often known as cluster analysis, is a machine learning technique for organizing unlabeled data. It is defined as "**grouping similar data points into different clusters**". Clustering is a form of unsupervised learning that works with unlabeled data. The advantage of clustering algorithms is that they are flexible, easy to implement, and can generalize features having a similar statistical variance. *Here, lesions in a group have possible similarities and have fewer or no similarities with another group.*

Partition Clustering

It's a type of clustering in which data is split into non-hierarchical groups. This strategy is also known as the centroid-based method [20]. In this type, the dataset is divided into K groups, with K denoting the number

of pre-defined groups. The cluster centre is designed in such a way that the distance between one cluster data point is the smallest when compared to the cluster centroid of the other cluster.

The type of clustering used in the implementation is partitioning clustering. The patterns like size and depth of lesions are considered, and the data points having the same size and depth are formed into a cluster (group). After the application of the clustering technique, each cluster is provided with a cluster ID (or label id) and the area and depth of each cluster (lesion) are found.

Mathematical analysis involved in the partition clustering

An image can be partitioned into K clusters such that the total of Manhattan distances (L1) between locations and the cluster's centre is kept to a minimum. Then, the sum of L1 absolute errors (SAE) can be minimised by using the following equation 1.

$$SAE = \sum_{i=1}^K \sum_{x \in C_i} dist_{L_1}(c_i, x) \quad (1)$$

where $dist_{L_1}$ is L_1 distance, C_i is the i^{th} cluster, x is a point in C_i , and c_i is the i^{th} cluster average.

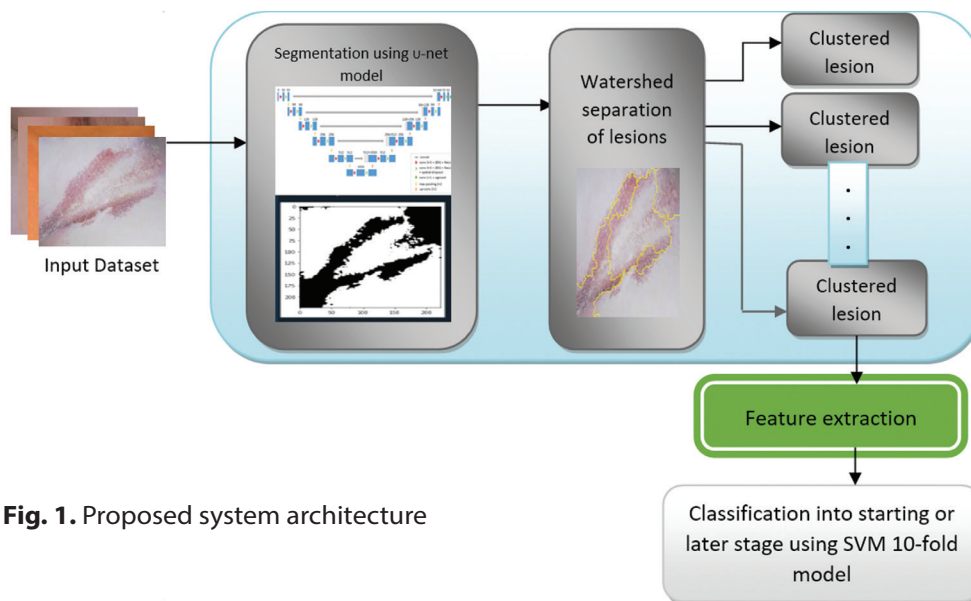


Fig. 1. Proposed system architecture

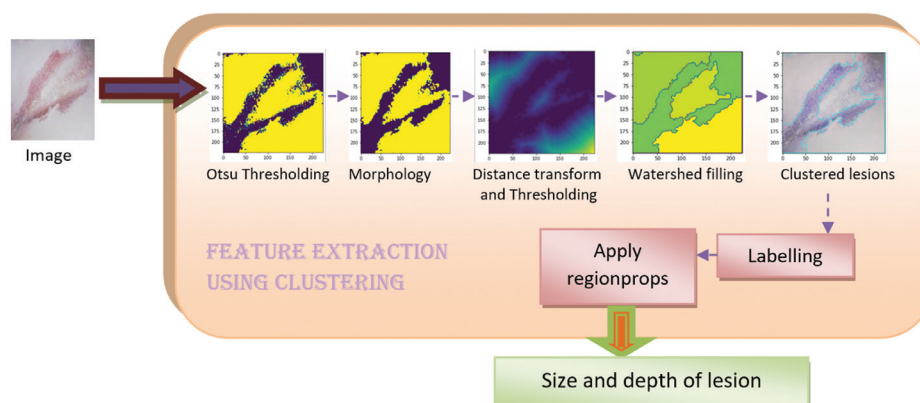


Fig. 2. Feature extraction using clustering

3.4 Dataset

To test the proposed methodology, publicly available DermnetNZ and DermIS datasets are chosen [21], [22]. These datasets consist of several RGB images of granular parakeratosis and is partitioned into two classes, starting stage and later stage wherein 79 samples are considered for each class. For the implementation of size and depth features, the OpenCV library and the python machine learning package, Scikit-learn library, are adapted. All the experiments are run on a Windows 10 system with an i5 processor. Figure 3 shows some of the sample images of granular parakeratosis.



Fig. 3. Samples of granular parakeratosis

3.5 Implementation

The given skin image undergoes several steps like normalization, clustering (form the clusters of skin lesion), extract the size and depth features, and pass them to the classification model.

In this section, the implementation of the distance transform, watershed, and clustering algorithms for extracting the features from the granular parakeratosis dataset is described. The model is trained on 79 dermoscopy images.

The below mentioned algorithm describes the generalised steps incorporated by the proposed model:

- Step 1:** Initially, import the libraries required for feature extraction
- Step 2:** Then, read an image by defining pixel size
- Step 3:** Perform segmentation using the U-net model. The result of the U-net model is transformed to binary image (threshold image to separate lesion boundaries) using Otsu thresholding
- Step 4:** Watershed based separation of lesions: Apply morphological functions to enhance the boundaries and create a mask
- Step 5:** Label the lesions in an image
- Step 6:** Extract the size and depth of each lesion using regionprops method
- Step 7:** Output results into a csv file

A detailed description of the flow of the implementation is as follows:

1. Initially, segmentation is done using the encoder-decoder process of the U-net model with binary cross entropy as a loss function. The main aim of choosing binary cross entropy is to minimise the loss so as to improve performance of the model. A 224x224 image is passed into the

network for which 32 filters are applied. Then, it gets converted into 112x112x64, 56x56x128, 28x28x256, 14x14x512, and 7x7x1024 as it passes through different levels of the network. In the decoder path, each level concatenates with the corresponding level in the encoder path, leading to a 7x7x1024, 14x14x512, 28x28x256, 56x56x128, 112x112x64, and 224x224x32 image. To this image, the last layer with a filter of size 1x1 and a sigmoid activation function is applied, generating 224x224x1 segmented-image.

2. Otsu thresholding: It is an auto-thresholding technique that automatically calculates a threshold value for a binary image. The flags cv2.THRESH_BINARY & cv2.THRESH_OTSU are passed as parameters to the cv2.threshold() function with the threshold value set as zero. The main goal of Otsu's approach is to minimise the variance by choosing the correct value for the threshold. If it is chosen wrong, the variance of one or more classes will be significant. Thus, to get the total variance, add all the within-class and between-class variances together as shown in equation

$$\sigma_T^2 = \sigma_w^2(t) + \sigma_b^2(t) \quad (2)$$

where $\sigma_w^2(t) = w_1(t)\sigma_1^2(t) + w_2(t)\sigma_2^2(t)$ and

$$\sigma_b^2(t) = w_1(t)w_2(t)[\mu_1(t) - \mu_2(t)]^2$$

$w_1(t)$ and $w_2(t) \rightarrow$ probabilities of the classes divided by threshold t (0-255)

$\mu_i \rightarrow$ class i^{th} mean

3. Morphological transformations are straightforward operations that are usually applied to binary images. OpenCV's morphologyEx() function is as follows:
 - Morphological transformations are simple procedures done on images depending on their shape to remove noise, small holes in foreground objects, and so on. Erosion, dilation, opening, and closing are some of the morphological operations. In implementation part, after otsu thresholding, opening morphology is done. To execute opening morphological procedures on a given image, the MORPH_OPEN operation in the morphologyEx() method is used.
4. To extract the exact lesion in an image, a distance transform followed by a threshold is applied [23]. The distance transform function calculates the approximate distance from every pixel in the image to the zero pixel. For zero pixels, it will be zero. Out of several distance types available, DIST_L2 is chosen which runs the linear-time algorithm. This algorithm makes use of squared Euclidean (or quadratic) distance described as follows. Let G stand for regular grid and $f:G \rightarrow R$ be

a grid function where R is the range of distance function d . The distance transform of f is defined by equation 3.

$$D_f(p) = \min_{q \in G} (d(p, q) + f(q)) \quad (3)$$

where $d(p, q)$ is a distance measure between p and q . A point q that is close to p and with a small $f(q)$ is discovered for each point p .

Let $G = \{0, \dots, n - 1\}$ be a one dimensional grid, and $f : G \rightarrow R$ an arbitrary grid function. The squared Euclidean (or quadratic) distance transform of f is described by equation 4.

$$D_f(p) = \min_{q \in G} ((p - q)^2 + f(q)) \quad (4)$$

5. The non-lesion area can be found by applying dilation to the result obtained in the previous step. To determine the area which is not sure of a lesion or non-lesion (also called boundaries or border of lesion, where lesion and non-lesion touch each other), watershed algorithm is applied.
6. A *watershed* is a transition defined on a grayscale image. This technique aids in the detection of touching and overlapping lesions in an image. The watershed algorithm extracts the completely lesion area and the completely non-lesion area, leading to the creation of clusters. Several clusters of lesions are identified and then markers are applied to detect the exact boundaries (labeling). These markers assign positive numbers to completely lesion and non-lesion areas and zero to the area that is not sure to be lesion or non-lesion **using cv2.connectedComponents()**. Finally, after labelling the regions, apply the watershed algorithm for filling.
7. After identifying labelled lesions in an image, the features of these lesions can be determined using the `regionprops()` module of the `skimage` library. The size and depth of lesions in an image are calculated by measuring the cluster's height and width in pixel square.
8. The features obtained are then given as an input to the SVM 10 fold cross validation model. The reason for choosing SVM is that it finds the best separator to differentiate the classes. Thus, SVM serves as a binary classifier. Here, it classifies the lesions into starting stage or later stage. In SVM 10 fold model, 224x224 images from which the features extracted using the region properties technique are input into the SVM classifier with hinge loss and linear activation function. Hinge loss is a function that is mainly used to train the SVM classifier. The linear activation function decides the output of the model and when associated with neurons, it decides whether a neuron should be activated or not depending on the input provided. The output of this SVM

classifier is then fed into the 10 fold validation model wherein the model is trained on one partition and evaluated on other nine partitions, thereby increasing an accuracy to 95%, sensitivity to 100% and specificity to 100%. The output of classification is shown in figure 4.

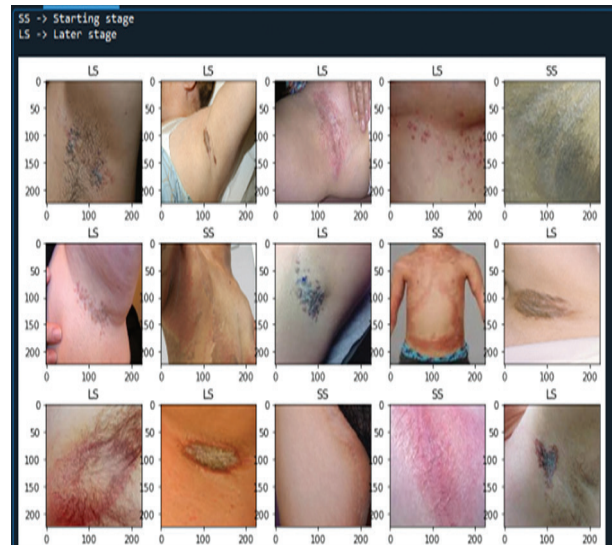


Fig. 4. Classification of granular parakeratosis into starting or later stage

4. RESULTS AND DISCUSSION

4.1 QUANTITATIVE EVALUATION

The model is evaluated quantitatively using accuracy, sensitivity, and specificity metrics. This is computed as

$$\begin{aligned} \text{Accuracy} &= \frac{TP+TN}{TP+FN+TN+FP} \\ \text{Sensitivity} &= \frac{TP}{TP+FN} \\ \text{Specificity} &= \frac{TN}{TN+FP} \end{aligned}$$

Abbreviations: TP - True Positive, TN - True Negative, FP - False Positive and FN - False Negative

4.2 ANALYSIS

The size and depth of the lesion (segmented object) are determined in the model. Figure 5 shows the samples of original image, an overlay on the original image, a segmented image, and the size and depth extracted from the lesions of sample images. The results obtained for other images are shown in Table 2. The table shows that for each image, different lesions are identified and labeled with a unique number. For each label, the area and depth of the lesion are found. For example, the first four rows (excluding the heading) of the table correspond to an image, images.bmp. This image consists of four lesions identified by lesion numbers 1, 2, 3, and 4 (second column). For each of these lesions, an area and depth are computed. The same thing is repeated for the other images in the dataset (from the fifth row).

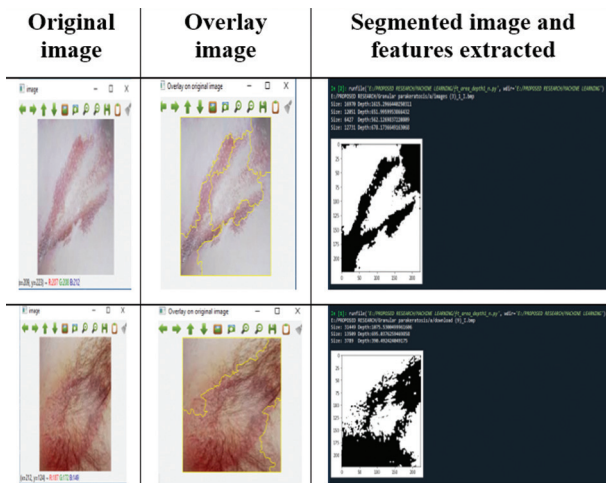


Fig. 5. Original image, overlay image, segmented image and features extracted

Table 2. Simulation results of the model

Image Name	Lesion#	Area	Depth
images.bmp	1	4242.5	1615.297
images.bmp	2	3012.75	651.996
images.bmp	3	1606.75	562.127
images.bmp	4	3182.75	678.1737
download.bmp	1	7862.25	1075.53
download.bmp	2	3377.25	695.0376
download.bmp	3	947.25	390.4924
Axillary Granular Parakeratosis.bmp	1	2846.5465	1207.022
Axillary Granular Parakeratosis.bmp	2	8344	1199.578
Axillary Granular Parakeratosis.bmp	3	934.5	313.2203
Axillary-Granular-Parakeratosis-1.bmp	1	6636.25	1308.71
Axillary-Granular-Parakeratosis-1.bmp	2	1522.75	479.2031
Axillary-Granular-Parakeratosis-1.bmp	3	1146	419.2386
Axillary-Granular-Parakeratosis-1.bmp	4	111.25	89.25483
Axillary-Granular-Parakeratosis-1.bmp	5	101.25	114.1604
Axillary-Granular-Parakeratosis-1.bmp	6	91	104.332
Axillary-Granular-Parakeratosis-1.bmp	7	140.75	119.1665
Axillary-Granular-Parakeratosis-1.bmp	8	41.25	59.35534
Axillary-Granular-Parakeratosis-1.bmp	9	280.5	171.3797
Axillary-Granular-Parakeratosis-1.bmp	10	26	47.83452
Axillary-Granular-Parakeratosis-1.bmp	11	172.25	137.3026
Axillary-Granular-Parakeratosis-1.bmp	12	136.5	121.3026
Axillary-Granular-Parakeratosis-1.bmp	13	53.75	95.01219
Axillary-Granular-Parakeratosis-1.bmp	14	67.25	73.39697
Axillary-Granular-Parakeratosis-1.bmp	15	207.25	144.6518
Axillary-Granular-Parakeratosis-1.bmp	16	16.5	33.14214
Axillary-Granular-Parakeratosis-1.bmp	17	270.5	196.5097

Experiment shows that the proposed strategy produces good results. The performance of the proposed model provides a better result compared to the state-of-art methods. After the application of the partition clustering and region properties method to the given

dataset, the output is fed to SVM 10-fold model that achieved an accuracy of 95%, a sensitivity of 100% and a specificity of 100%. The performance of each fold in 10-fold model is presented in table 3.

Table 3. Fold-wise performance of 10-fold

Fold	Accuracy	Sensitivity	Specificity
1	95	99.99	99.99
2	94.99	99.99	100
3	94.99	99.98	99.98
4	95	100	99.99
5	94.99	100	100
6	95	99.99	100
7	94.99	100	99.99
8	95	100	100
9	95	100	100
10	95	100	100
Average	94.99	99.99	99.99

Table 4 shows the performance of the existing models and compares them with the proposed model after feature extraction.

Table 4. Comparison of the proposed method to state-of-the-art techniques in terms of classification performance

Model	Feature extracted	Accuracy	Sensitivity	Specificity
Morphological geodesic active contour [24]	Color	94.59	91.72	97.99
Fuzzy clustering [25]	Area, perimeter, and centroid	97.6	96.82	96.94
Scattered Wavelet Transform[26]	Hand-crafted features	93.14	-	-
Stationary Wavelet Transform[27]	Entropy	91.5	90	93
RESNET-50 [28]	Contrast	89.8	-	-
Proposed model	Size and depth	95	100	100

The model proposed by salih et al. achieved an accuracy of 97.6 which is bit higher than the proposed model. Though this model achieved higher accuracy, it didn't work well with few of the skin lesions and couldn't achieve higher sensitivity and specificity. Thus, the proposed hybrid model can be used for parakeratosis feature extraction that not only works well with all of the training samples but also achieved better performance metrics, including accuracy, sensitivity, and specificity.

Figure 6 shows the graphical representation of the performance comparison of proposed and existing models.

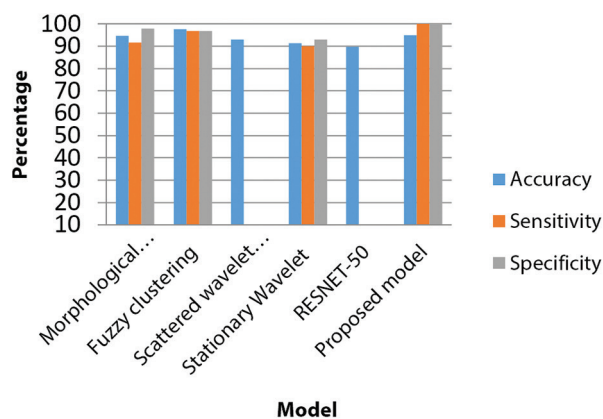


Fig. 6. Performance comparison

5. CONCLUSION

An estimation of the features of lesions in an image is an important application of medical image processing. The paper proposes an automatic method for size and depth extraction using partition clustering and the region properties method. The model performs the segmentation of the given dataset using U-net with binary cross entropy technique, extracts the features using partition clustering and region properties methods, and finally classify into starting or later using SVM cross validation model. The proposed method estimates the depth and absolute size of K lesions in each image by predicting the absolute height and width of the lesion in terms of pixel square. After extracting the size and depth, classification is performed using SVM 10-fold model. The experiment results demonstrate that the proposed model provides a better performance compared to the other models.

The model has the limitation that it works well only for the limited number of samples. As a future work, the model can be improved in such a way that it works well even for a large dataset.

6. REFERENCES:

- [1] J. Mcgrath, "Dermatology, Venereology & Leprology", Vol. 74, No. 1, 2008, pp. 53-55.
- [2] P. Chirasuthat, S. Chirasuthat, P. Suchonwanit, "Follicular Granular Parakeratosis: A Case Report, Literature Review, Proposed Classification", Skin Appendage Disorder, Vol. 7, No. 2, 2021, pp. 144-148.
- [3] G. Pavithra, C. Palanisamy, S. S. Rajasekar, R. S. Soundariya, "Skin Lesion Analysis - Feature Extraction Methods Using Dermoscopy Image", International Journal of Aquatic Science, Vol. 12, No. 3, 2021, pp. 1821-1829.
- [4] Q. Abbas, F. Ramzan, M. U. Ghani, "Acral melanoma detection using dermoscopic images and convolutional neural networks", Visual Computing for Industry, Biomedicine, Art, 2021.
- [5] S. Sengupta and N. Mittal, "Analysis of Various Techniques of Feature Extraction on Skin Lesion Images", Proceedings of the 6th International Conference on Reliability, Infocom Technologies and Optimization, Noida, India, 20-22 September 2017.
- [6] S. Majumder and M. A. Ullah, "A Computational Approach to Pertinent Feature Extraction for Diagnosis of Melanoma Skin Lesion", Pattern Recognition and Image Analysis, Vol. 29, No. 3, 2019, pp. 503-514.
- [7] K. Chinpong et al., "ABCD Feature Extraction for Melanoma Screening Using Image Processing: A review", The Journal of Chulabhorn Royal Academy, Vol. 5203, No. 4, 2021, pp. 230-245.
- [8] L. Hoang, S. H. Lee, E. J. Lee, K. R. Kwon, "Multi-class Skin Lesion Classification Using a Novel Lightweight Deep Learning Framework for Smart Healthcare", Applied Sciences, Vol. 12, No. 5, 2022.
- [9] H. A. Mahmood, "Appending Global to Local features for Skin Lesion Classification on Dermoscopic Images", Journal of Engineering Research, Vol. 10, 2022, pp. 1-19.
- [10] M. Francisco, "Two Systems for the Detection of Melanomas in Dermoscopy Images using Texture and Color Features", IEEE Systems Journal, Vol. 8, No. 3, 2013, pp. 965-979.
- [11] T. Akram et al. "A multilevel features selection framework for skin lesion classification", Human-centric Computing and Information Sciences, Vol. 10, No. 1, 2020.
- [12] X. Wang, X. Jiang, H. Ding, Y. Zhao, J. Liu, "Knowledge-aware deep framework for collaborative skin lesion segmentation and melanoma recognition", Pattern Recognition, Vol. 120, 2021, p. 108075.
- [13] D. Wang, N. Pang, Y. Wang, H. Zhao, "Biomedical Signal Processing and Control Unlabeled skin lesion classification by self-supervised topology clustering network", Biomedical Signal Processing and Control, Vol. 66, 2021, p. 102428.
- [14] S. Chatterjee, D. Dey, S. Munshi, "Integration of morphological preprocessing and fractal based

feature extraction with recursive feature elimination for skin lesion types classification", *Computer Methods and Programs in Biomedicine*, Vol. 178, 2019, pp. 201-218.

- [15] J. Oyelade, I. Isewon, O. Oladipupo, O. Emebo, Z. Omogbadegun, "Data Clustering : Algorithms and Its Applications", *Proceedings of the 9th International Conference on Computational Science and Its Applications*, St. Petersburg, Russia, 1-4 July 2019, pp. 71-81.
- [16] S. Louhichi and B. Abdallah, "Skin Lesion Segmentation Using Multiple Density Clustering Algorithm MDCUT And Region Growing", *Proceedings of the IEEE/ACIS 17th International Conference on Computer and Information Science*, 6-8 June 2018, pp. 74-79.
- [17] O. Trabelsi, "Skin Disease Analysis and Tracking based on Image Segmentation.", *2013 International Conference on Electrical Engineering and Software Applications*, 2013.
- [18] E. Salahat, M. Qasaimeh, "Recent advances in features extraction and description algorithms: A comprehensive survey", *Proceedings of the IEEE International Conference on Industrial Technology*, Toronto, ON, Canada, 22-25 March 2017, pp. 1059-1063.
- [19] S. Benyahia et al. "Multi-Features Extraction Based on Deep Learning for Skin Lesion Classification", *Tissue and Cell*, Vol. 74, 2021.
- [20] S. Ayram and T. Kainen, "Introduction to partitioning-based clustering methods with a robust example", *Reports of the Department of Mathematical Information Technology Series C. Software and Computational Engineering*, Vol. 35, No. C, 2006.
- [21] "Granular parakeratosis images | DermNet NZ." <https://dermnetnz.org/topics/granular-parakeratosis-images?stage=Live> (accessed: 2021).
- [22] DermIS, <https://www.dermis.net/dermisroot/en/32551/diagnose.htm>.
- [23] P. F. Felzenszwalb, D. P. Huttenlocher, "Distance transforms of sampled functions", *Technical Report, TR20041963*, Vol. 4, 2004, pp. 1-15.
- [24] F. F. Ximenes Vasconcelos, A. G. Medeiros, S. A. Peixoto, P. P. Rebouças Filho, "Automatic skin lesions segmentation based on a new morphological approach via geodesic active contour", *Cognitive Systems Research*, Vol. 55, 2019, pp. 44-59.
- [25] S. H. Salih and S. Al-Raheym, "Comparison of skin lesion image between segmentation algorithms", *Journal of Theoretical and Applied Information Technology*, Vol. 96, No. 18, 2018, pp. 6085-6094.
- [26] S. Raja, S. Kotra, R. Babu, P. Goriparthi, V. Kotra, L. Chiau, "Journal of King Saud University - Science Dermoscopic image classification using CNN with Handcrafted features", *Journal of King Saud University - Science*, Vol. 33, No. 6, 2021, p. 101550.
- [27] S. M. Kumar, J. R. Kumar, K. Gopalakrishnan, "Skin Cancer Diagnostic using Machine Learning Techniques - Stationary Wavelet Transform and Random Forest Classifier", *International Journal of Innovative Technology and Exploring Engineering*, Vol. 3075, No. 2, 2019, pp. 4705-4708.
- [28] M. A. Khan, T. Saba, M. Sharif, "Multi-Model Deep Neural Network based Features Extraction and Optimal Selection Approach for Skin Lesion Classification", *Proceedings of the International Conference on Computer and Information Sciences*, Sakaka, Saudi Arabia, 3-4 April 2019, pp. 1-7.

A Smart Content-Based Image Retrieval Approach Based on Texture Feature and Slantlet Transform

Original Scientific Paper

Hakeem Imad Mhaibes

Middle Technical University,
Kut Technical Institute
Baghdad, Iraq
hakeem.emade@mtu.edu.iq

Qahtan Makki Shallal

Management Technical College of Basra
Basrah, Iraq
qahtan.makii@stu.edu.iq

May Hattim Abood

Al Iraqia University,
Computer Engineering Department, College of Engineering,
Baghdad, Iraq
may.hattim@gmail.com

Abstract – With the advancement of digital storing and capturing technologies in recent years, an image retrieval system has been widely known for Internet usage. Several image retrieval methods have been proposed to find similar images from a collection of digital images to a specified query image. Content-based image retrieval (CBIR) is a subfield of image retrieval techniques that extracts features and descriptions content such as color, texture, and shapes from a huge database of images. This paper proposes a two-tier image retrieval approach, a coarse matching phase, and a fine-matching phase. The first phase is used to extract spatial features, and the second phase extracts texture features based on the Slantlet transform. The findings of this study revealed that texture features are reliable and capable of producing excellent results and unsusceptible to low resolution and proved that the SLT-based texture feature is the perfect mate. The proposed method's experimental results have outperformed the benchmark results with precision gaps of 28.0 % for the Caltech 101 dataset. The results demonstrate that the two-tier strategy performed well with the successive phase (fine-matching) and the preceding phase (coarse matching) working hand in hand harmoniously.

Keywords: Image Processing, Information retrieval, CBIR, Slantlet Transform, Features extraction, Similarity measure

1. INTRODUCTION

Today Due to the information explosion on the Internet, an image retrieved system has become a well-known method used to seek the most similar images for a given specified query image from a large database of images [1]. As a result, one of the most difficult problems in computer vision is retrieving and managing desired images from large image databases [2, 3]. Researchers have recently focused on difficult problems in CBIR in various domains such as machine learning, pattern recognition, and computer vision, among others. Generally, there are two classes of image retrieved methods. Text-based image retrieval (TBIR) and CBIR [3, 4].

In TBIR, images are denoted by headings and keywords in the database, and the manual text is used to search and retrieve images depending on users labeling ways [5]. The limitations of TBIR are (1) inaccurate results because users wrongly annotate images, (2) the overall image information cannot be described by a single keyword, and (3) it is a time-consuming process since it requires manual annotation of the images [6-8]. To overcome the limitations of TBIR, a new CBIR method of image retrieval was invented by a researcher. CBIR extracts image features and descriptions content such as color, texture, and shapes from images to find similarities from a huge database [1, 9]. The general structure of CBIR is illustrated in Fig1.



Fig. 1. The general structure of CBIR

CBIR consists of two key steps: feature extraction and matching [10]. At first, features for both the query image and database images are extracted and stored in features vectors format and then matched to find similar images using a predefined distance measurement formula. According to the least similarity index, the matched images are ranked [11]. The main objective of the present work is to develop a new method for image retrieval with higher accuracy compared to the state of art technique by introducing a new technique consisting of two phases, coarse matching, and good matching, to extract useful texture features from both spatial and frequency domains to represent image characteristics and find the closest matching image. In the first phase, a shortlist of thirty images closely resembling the query image is produced. The matching process is further refined at the fine-matching phase, where the shortlist will be used as the feeder or input. In the end, the closest matching image will prevail.

2. RELATED WORKS

Several CBIR algorithms using various feature extraction methods have been presented for image retrieval applications. Each technique competes to locate the best similar photos to the query image with the highest precision rate [1]. This section examines state-of-the-art CBIR techniques currently in use.

In 2016, S. Somnugpong et al. proposed a new CBIR that prioritizes spatial information in images by combining color correlograms and the Edge direction histogram. In the case of the same image but different colors, a color correlogram will treat information about spatial color correlation, whereas EDH will provide geometry information. Simple calculations, such as the Euclidean Distance between the query image and the image in the database, are used to evaluate performance. This work proves that containing the combination of image texture and spatial correlation of pairs of color in feature provides more robustness to a high changing image. Although using color correlation remains some limitation in the color term, EDH will fulfill the image semantic in terms of texture and geometry. Accuracy achieved in this method reached 73 % [12].

In 2018, Nazir et al. proposed a novel colour and texture-based CBIR technique. Local features such as the discrete wavelet transform and colour histogram features are extracted locally, whilst global features such as the edge histogram descriptor are extracted globally. As a result, Manhattan distance measurement was used to compare the feature vectors of the query image and the feature vectors of the images in the da-

taset. According to the study's findings, it has a 73.5 percent accuracy rate [13].

In 2019, S. P. Rana et al. presented the CBIR method, which combines three invariant features and is implemented across five different picture databases, achieving substantial precision values compared to previous techniques. It employs a feature vector of 247, which is relatively long compared to other algorithms and may result in increased time complexity. As a result, reducing the length of feature vectors will be a future issue because time is also a critical attribute of CBIR systems. Another consideration would be the purification of obtained results through relevant feedback (RF). The query results would be filtered through human intervention, and the feedback would be fed back to the system for better outcomes in the next iteration. Due to the large feature vector dimension, the suggested approach has a high computational cost. According to the outcomes of the study, the recommended approach had a 65 percent accuracy rate [14].

In 2019 Q. Zheng and colleagues developed a new end-to-end CBIR based on a deep convolutional neural network (CNN) and a differential learning algorithm. Compared to the standard method of matching the image by employing deep convolutional activation features as the feature vector. They make the method's retrieval process easier and reduce the problem of semantic gaps. In the dataset manufacturing stage, the approach creates an image matching dataset based on the gravitational field model, which includes adding the similarity score label for each image. As the number of returned images increases, the retrieval accuracy of the system decreases slightly and eventually becomes stable at a high value. The limitation of their work is that more enhancement is required in terms of the speed of the training and testing stages and more time to construct the gravitational field database. The retrieval accuracy for this strategy is 88.5 percent on average [15].

In 2020, Mohammed Q et al. proposed a new method for CBIR. Three descriptors developed in this approach to increase matching image accuracy for medical images retrieval. In this approach, student or a medical specialist is assumed to be a user and the query is a medical image. The average matching accuracy was 70 % [16].

In 2020, Akshara et al. developed a novel CBIR approach that based on coarse-to-fine progressive RS image descriptor and decoded in partial compressed JPEG 2000 domain. At first, decodes the code-blocks that associated only to the coarse wavelet resolution, to discards the most dissimilar images to the query based on the similarity measurement. Following that,

the code-blocks connected with the remaining images' sub-sequent resolution are decoded, and the most irrelevant images are removed using computing similarities based on image attributes associated with both resolutions. This is accomplished by the use of the pyramid match kernel similarity measure, which gives higher weights to traits associated with finer wavelet resolution than to those associated with coarse wavelet resolution [17].

In 2021, Mounika proposed a new CBIR based on integrated machine learning and convolution neural network and incorporate with principal component analysis (PCA) for extracting salient features from the images. The proposed method focused on artificial intelligent based deep learning approach to estimate semantic features. It uses Euclidean distance as a similarity measurement [18].

In 2021, Ali Ahmed and Sara Muhamed suggested a new method for CBIR. In this research, a set of color and texture attributes is proposed to be employed in both fusion procedures. The early fusion stage uses an early combination of eighteen color characteristics and twelve texture features to create a single vector representation, while the late fusion stage uses three of the most popular distance measures. Our results on two typical picture datasets show that our suggested method has good retrieval results when compared to the traditional method of employing single features descriptors, as well as acceptable retrieval results when compared to various state-of-the-art methods. For the Corel-1K and GHIM-10K datasets, our suggested technique has an overall accuracy of 60.6 percent and 39.07 percent, respectively [19].

3. THE AIM AND OBJECTIVE OF THE STUDY

The goal of this work is to offer a novel CBIR approach that is more accurate than the current state of the art. As a result, two key objectives must be satisfied.

1. Represent picture properties that involves extracting effective texture features from both the spatial and frequency domains.
2. Create a two-tier picture retrieval approach that incorporates both spatial and frequency-based data.

4. RESEARCH METHODOLOGY

CBIR is influenced by various factors, including feature extraction strategy, utilization of appropriate features, similarity measurement approach, mathematical conversion, and reaction mechanisms. In CBIR, all of these elements are crucial. Improving some of the prompting components can result in a more effective retrieval process [20].

4.1. FEATURE EXTRACTION

Feature extraction is a fundamental step in a CBIR system. Based on low- and high-level features, images repre-

sent their features. Color, shape, and texture are low-level features, while high-level features are based on machine learning techniques [21]. One of the most important advantages of color-space conversion is that it allows choosing the most appropriate among the various color-spaces (RGB). The majority of color spaces are three-dimensional. HSV and YCbCr have a higher inherent value than RGB and are more similar to human perception. This study uses the Y and H channels from YCbCr and HSV, respectively. Features extraction perceives the luminance component in a better way than the chrominance component [22]. The formula for calculating the Y, Cb, and Cr channels from R, G, and B channels is defined by (1).

$$\begin{pmatrix} Y \\ Cb \\ Cr \end{pmatrix} = \begin{pmatrix} 0.299 & 0.587 & 0.177 \\ -0.299 & -0.587 & 0.886 \\ 0.701 & -0.587 & -0.114 \end{pmatrix} \begin{pmatrix} R \\ G \\ B \end{pmatrix} + \begin{pmatrix} 16 \\ 128 \\ 128 \end{pmatrix} \quad (1)$$

For HSV color conversion, the dominant spectral component, red, blue, or yellow, is represented by the hue (H). When white is added to a pure color, the color changes; the less white, the more saturated the color becomes. This is the saturation level (S). The brightness of color is represented by the value (V). The following formulas can be used to convert a pixel's HSV values from its RGB representation:

$$H = \arctan \frac{\sqrt{3}(G - B)}{(R - G) + (R - B)} \quad (2)$$

$$S = 1 - \frac{\min\{R, G, B\}}{V} \quad (3)$$

$$V = \left(\frac{R + G + B}{3} \right) \quad (4)$$

The texture is easy to recognize but more difficult to define. It is orthogonal to color because it is normally defined solely by grey levels. Smoothness, coarseness, and regularity are all texture characteristics [23]. As a result, four texture features are computed and extracted from each block of the Y and H images in this study: variance, coefficient of variation, energy, and entropy. The variance represents the deviation of each pixel in the block from the mean and is calculated using Eq. 5;

$$\sigma^2 = \frac{1}{W \times W} \sum_{i=1}^W \sum_{j=1}^W (I(i, j) - m)^2 \quad (5)$$

Where W represents the size of the block, $I(i, j)$ is image intensity value at the pixels i and j , and m is the mean intensity level calculated by the equation;

$$m = \frac{1}{W \times W} \sum_{i=1}^W \sum_{j=1}^W I(i, j) \quad (6)$$

The coefficient of variation is used to compare the degree of variation from one pixel to the next. It is defined as the standard deviation divided by the mean. Coefficient of variation measures the relative dispersion defined such as:

$$\eta = \frac{\sigma}{m} \quad (7)$$

Energy calculates the brightness value. A brighter pattern will have greater energy than a darker one. It is given as;

$$E = -\frac{1}{W \times W} \sum_{i=1}^W \sum_{j=1}^W (I(i,j))^2 \quad (8)$$

Shannon entropy is used in this proposed algorithm to estimate the average amount of data contained in each block, given as;

$$E_s = \frac{1}{W \times W} \sum_{i=1}^W \sum_{j=1}^W (I(i,j))^2 \log(I(i,j))^2 \quad (9)$$

4.2. SLANTLET TRANSFORM (SLT)

The execution of the discrete wavelet transform (DWT) is based on filter bank iteration, although the processing time is greater because DWT is not well adapted to capture all of the information in a signal when the optimal time localization is unclear. Selesnick [24] proposed a new technique for this purpose, a Slantlet Transform (SLT), which gives a new parameter that is orthogonal to DWT [25].

A 2D SLT decomposition separates an image into four components, as shown in Fig. 2, High-High (HH), Low-Low (LL), High-Low (HL), and Low-High (LH), where H and L represent the high and low-frequency bands, respectively.

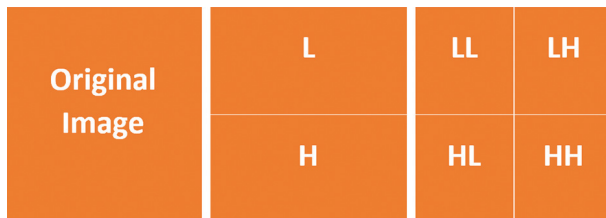


Fig. 2. 2D SLT scheme for splitting an image

The innovative image information is stored in the image's low-frequency band, denoted as LL. The HH, LH, and HL high- and medium-frequency bands, on the other hand, communicate information about the image's contour, edge, and other features. High coefficients characterize the image's important information. Meanwhile, the insignificant coefficients are brushed aside as meaningless information or background noise. In order to acquire the best outcomes in subsequent procedures, these small coefficients should be neglected.

The SLT method is commonly applied to the gray-scale channel; however, in this work, the SLT is applied to each RGB channel independently. An image is separated into three independent channels, R, G, and B, before being decomposed and partitioned into 32x32 pixel blocks for each channel - the block size was chosen empirically through a series of trials ranging from 8x8 to 64x64 pixels. Then, the SLT is used to bring out the texture features in each block [26].

4.3. QUALITY MEASUREMENT

The quantitative assessment is performed based on of three parameters, accuracy, precision, and recall, see following equations;

$$accuracy = \frac{TN + TP}{TN + TP + FN + FP} \quad (10)$$

$$precision = \frac{TP}{TP + FP} \quad (11)$$

$$recall = \frac{TP}{TP + FN} \quad (12)$$

The precision metric indicates the number of recovered images relevant to the query in the initial evaluation of an image retrieval system. The recall is the number of successfully retrieved images related to the query [27]. The suggested retrieval method's correctness is specified as the accuracy metric. Concerning that, a confusion matrix and its measuring parameters' definition are given in Table 1.

Table 1. Definition of the measuring parameters

Parameter	Definition
TP (True Positive)	Related images correctly retrieved by the query.
FN (False Negative)	Related images were wrongly rejected by the query.
FP (False Positive)	Not related images were wrongly retrieved by the query.
TN (True Negative)	Not related images were correctly rejected by the query.

4.4. DATASET

The standard datasets used to validate the proposed image retrieval technique are WANG V1.0, WANG V2.0 and Caltech 101. About 40 to 800 images per category and each picture is approximately 300 × 200 pixels in size. Description of the used datasets as shown in Table 2.

4.5. FEATURE MATCHING

There are several numbers of similarity measurements methods that can be used to compute the similarity between a query image and images in the database. In this work, Euclidean Distance is used to compute color, shapes, and texture features. The following is how the Euclidean Distance is calculated [28].

$$d(x_1, x_2) = \sqrt{\sum_{i=1}^{i=n} (x_1(i) - x_2(i))^2} \quad (13)$$

Where x_1 is the feature vector of query image, and x_2 is the feature vector of images in database.

5. PROPOSED METHOD

This section provides detailed discussions on the proposed CBIR method, as shown in Figure 3. It involves two main phases:

(1). Coarse Matching Phase: where a shortlist of images will be selected from the dataset that have been considered to match with the query image, and choose 30 the closest-match images

(2). Fine Matching Phase: In this stage, the query image will be matched with the shortlist's images to find the closest match images.

5.1. COARSE-MATCHING PHASE

This phase determines a shortlist from which the closest-match image is drawn. It is the same as removing all dissimilar photos from the collection and leaving just those similar resembling the query image. Algorithm 1 and Fig. 4 (a) illustrated the main steps of this phase.

Algorithm 1: Coarse-Matching Phase

1. Let q_i be an image.
2. Convert colour image RGB of q into YCbCr using Eq. (1), and into HSV using Eq. (2), Eq. (3), and Eq. (4).
3. Select Y and H from YCbCr and HSV, respectively.
4. Split the Y and H into n blocks of 128×128 pixels, respectively. Where n depends on image size.

5. For each block of Y, calculate Variance f_1 , Coefficient of variance f_2 , Entropy f_3 and Energy f_4 .
6. For each block of H, calculate Variance f_5 , Coefficient of variance f_6 , Entropy f_7 and Energy f_8 .
7. Concatenate all the features to form a block-based feature vector $F_i = \{f_{-1}, f_{-2}, \dots, f_{-8}\}$.
8. Repeat Step 5 to Step 7 until all blocks are exhausted.
9. Upon completion, concatenate all block-based feature vectors to form an image-based feature vector of the query image $F_{total} = \{F_1, F_2, \dots, F_m\}$.
10. Repeat 1 to 9 for query image to build its feature vector.
11. Use Eq. (13) to calculate the similarity between the feature vector of query image and database images to produce distances $d_{coarse} = \{d_1, d_2, \dots, d_n\}$.
12. Arrange the distances in ascending order (i.e. the smallest distance at the top and the biggest one at the bottom) and pick the top 30 images to form a shortlist.

Table 2. The Datasets Used

Datasets	No. of Images	No. of Categories	No. of images per category	Image size	No. of blocks	No. of features
WANG V1.0	1000	10	100	256x384 or 384*256	6	48
WANG V2.0	10000	100	1000	128*256 or 256*128	2	16
Caltech 101	9146	101	40-800	300*200 or 200*300	4	32

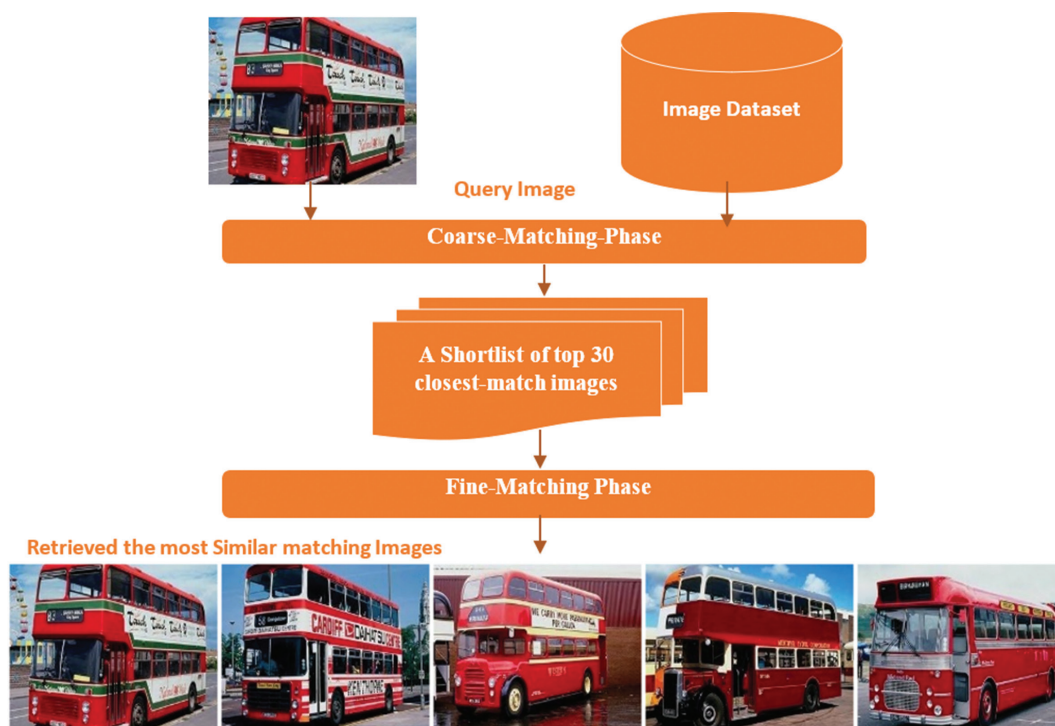


Fig. 3. Proposed diagram of Coarse-to-Fine matching image retrieval based on Slantlet transform.

5.2. FINE-MATCHING PHASE

In this phase, a shortlist of images is used instead of the entire image collection. This speeds up the CBIR. Algorithm 2 and Figure 4 (b) illustrated this phase.

This study uses the Slantlet transform. Afterwards, three features, mean, standard deviation and maximum value, are calculated. Algorithm 2 illustrates steps of the fine-matching;

Algorithm 2: Fine-matching phase

1. Let q_i be an image (RGB).
2. Partition each R, G and B channel into n blocks of 8×8 pixels.
3. For each block of R, decompose the block using SLT and calculate mean f_1 , standard deviation f_2 and maximum f_3 .
4. For each block of G, decompose the block using SLT and calculate mean f_4 , standard deviation f_5 and maximum f_6 .
5. For each block of B, decompose the block using SLT and calculate mean f_7 , standard deviation f_8 and maximum f_9 .
6. Concatenate all the features to form a block-based feature vector $F_i = \{F_1, F_2, \dots, F_n\}$.
7. Repeat Step 3 to Step 9 until stop condition.
8. Upon completion, concatenate all block-based feature vectors to form an image-based feature vector of the query image $F_{total} = \{F_1, F_2, \dots, F_m\}$.
9. Repeat 1 to 8 for query image to build its feature vector.
10. Use Eq. (13) to calculate the similarity between the feature vector of query image and shortlist images obtained from first phase to produce 30 distances $d_{fine} = \{d_1, d_2, \dots, d_{30}\}$.
11. Choose the image with the least distance as the closest match.

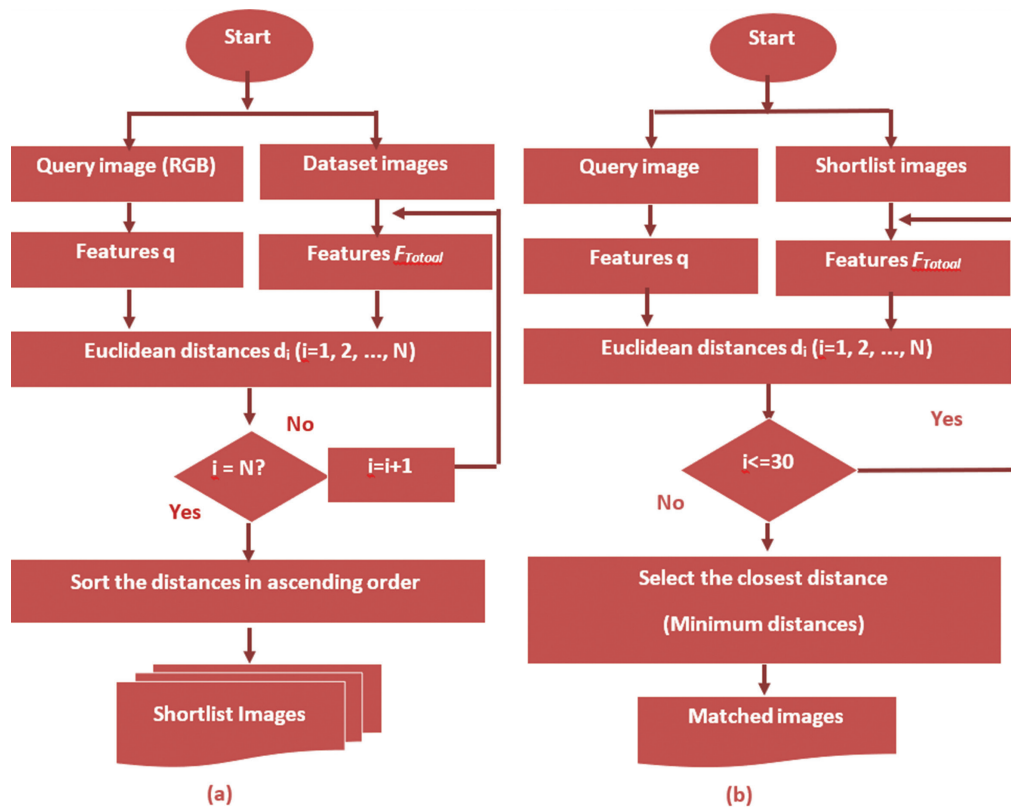


Fig.4. (a) The Coarse-Matching Phase, (b) Fine-Matching Phase

6. EXPERIMENTAL RESULTS AND DISCUSSION

MATLAB (R2020a) was employed as a software platform programming on Windows 10 in this study. The tests are performed on an Acer Intel(R) Core (TM) i3-2310M CPU (2.10 GHz) with 4 GB RAM and a 1 TB hard drive. Several studies were carried out in this regard, utilizing three well-known datasets (WANG V1.0, WANG

V2.0 and Caltech 101). Furthermore, the proposed approach focuses on precision and accuracy to assess the value of the recommended technique's high accuracy and consistency under standard image retrieval processes. The findings of the performance evaluation are presented in the form of tables.

6. 1. RESULT OF COARSE-MATCHING PHASE

This study arbitrarily chose one query image from each class found in the datasets. The results are arranged and presented class by class. Due to limited spaces, only ten classes from each dataset are carried out.

For WANG V1.0, classes are (Africa, Beach, Monuments, Buses, Dinosaur, Elephant, Roses, Horse, Mountain and Food). For WANG V2.0, classes are carried out (Shuttle, Building, Sky, Nightfall, Cowboys,

Flag, Mountains, desert, boat and Forest). Moreover, for Caltech 101, 101 queries have been made, and the ten classes are (Accordion, Cellphone, Chair, Chandelier, Cougar_face, Crab, Crocodile_head, Cup, Dalmatian, Dollar_bill and Airplanes).

Table 3, 4, and 5 provides the accuracy and precision measures for the first phase using WANG V1.0, WANG V2.0 and Caltech 101 datasets respectively.

Table 3. Accuracy and precision using Coarse-Matching For WANG V1.0.

Classes	Accuracy	Precision
Africa	0.8794	0.3828
Beach	0.8739	0.3504
Monuments	0.8829	0.4029
Buses	0.8905	0.4469
Dinosaur	0.9897	0.9532
Elephant's	0.8748	0.3561
Roses	0.9098	0.5540
Horse	0.9275	0.6482
Mountains	0.8801	0.3870
Food	0.8642	0.2927
Average	0.8973	0.4774

Based on Table 3, it can be seen that the suggested approach achieved high accuracy and an acceptable level of precision, with averages of around 0.90 and 0.48. In comparison to the other classes, the Dinosaur class achieved the greatest precision (0.95). This is not surprising since the photographs in this category have a smooth background that contrasts with the item or foreground. In contrast, the Food class scored the lowest accuracy, below 0.30, because to the structure of the query picture, which comprises several little things of varied shapes and hues that form an uneven-textured surface. Ironically, one notable aspect of the data is that the accuracy is always more than 0.86 despite the precision being much lower (except for the Dinosaur class). This is because the coarse matching approach created a large number of false positives (FP), the irrelevant photos incorrectly obtained by the query.

Overall, the suggested technique obtained greater accuracy and precision, which averaged around 0.95 and 0.45 for the one hundred classes in the total dataset, respectively. In connection to this, the Flag class

achieved the greatest levels of accuracy (0.98 and precision (0.84)) in comparison to the other classes. Contrarily, the Cowboys class obtained the lowest accuracy, less than 0.30. This is because of the structure of the query picture, which comprises several items of varied forms and hues, resulting in a patchy texture surface. Consistent with the results of the Wang V1.0, the accuracy has never been greater than the precision. This demonstrated that the coarse matching method created a substantial number of false positives (FP).

Table 4. Accuracy and precision using Coarse-Matching for WANG V2.0.

Classes	Accuracy	Precision
Shuttle	0.9317	0.3764
Building	0.9322	0.3819
Sky	0.9384	0.4425
Nightfall	0.9328	0.3874
Cowboys	0.9231	0.2915
Flag	0.9815	0.8396
Mountains	0.9277	0.3378
Desert	0.9536	0.5863
Boat	0.9335	0.3942
Forest	0.9443	0.4982
Average	0.9510	0.4480

Table 5. Accuracy and precision using Coarse-Matching For Caltech 101.

Classes	Accuracy	Precision
Accordion	0.9753	0.5265
Cellphone	0.9803	0.6497
Chair	0.9714	0.5132
Chandelier	0.9581	0.5906
Cougar_Face	0.9661	0.4800
Crab	0.9676	0.5326
Crocodile	0.9757	0.4868
Cup	0.9770	0.5751
Dalmatian	0.9663	0.4681
Dollar_Bill	0.9776	0.5458
Average	0.9670	0.5368

Based on Table 5, the coarse matching achieved better accuracy and precision results, averaging around 0.967 and 0.537 respectively, for the entire dataset. In the same context, based on the results of Precision eleven queries, which represent 10% of total queries, three classes, the Cougar face, Crocodile head and Dalmatian, have attained lower precision, which is below 0.50, compared to the rest. Because of the features shows that these images share a common trait (i.e. complex background), which naturally leads to uneven-texture surfaces. Conversely, the Cellphone class, which has clear contrast that separates the cellphone from its background, has outper-

formed the rest in terms of accuracy and precision. Again, the accuracy is always higher than the precision in all cases. This undoubtedly reaffirmed the findings that the coarse matching technique generated a lot of FP.

6.2. RESULT OF FINE-MATCHING PHASE

This section provides results of the fine-matching phase to evaluate the performance. The findings are then compared to the coarse matching results to see how effectively it reduces FP concerns and improves precision. Again, the experimental findings are provided in the following order: Wang V1.0, then Wang V2.0, and finally Caltech 101 datasets. At the conclusion of the fine matching, the query should return just the image with the nearest proximity among all of the images in the shortlist generated by the coarse matching.

The aforementioned 10 classes of the WANG V1.0 dataset are compared in terms of average precision in Table 6.

Table 6. Performance study of recovered images acquired by coarse matching and fine matching techniques for WANG V1.0.

Classes	Accuracy	Precision
Africa	0.3828	0.672
Beach	0.3504	0.6113
Monuments	0.4029	0.7607
Buses	0.4469	0.873
Dinosaur	0.9532	1
Elephant's	0.3561	0.7643
Roses	0.554	0.9667
Horse	0.6482	0.9333
Mountains	0.387	0.6817
Food	0.2927	0.6243
Average	0.4774	0.7887

Table 6 demonstrates unmistakably that the precision produced by fine matching is far superior than the precision obtained by coarse matching, with an average of 0.79, while retaining a high level of accuracy. The dinosaur received flawless scores for both accuracy and precision. The accuracy of the remaining classes ranged between 26.0 and 42.0 percent. Fine texture details uncovered by the Slantlet transform are principally responsible for the substantial gain in accuracy.

Similar to the preceding Wang V1.0, a total of one hundred inquiries were conducted for Wang V2.0, consistent with earlier efforts. Performance metrics are provided in Table 7.

The results clearly show that the precision attained by fine matching is significantly better than that of the coarse matching with an average of around 0.79.

Similarly, for Caltech 101. The results of precision, which measure the performance of the fine matching relative to the coarse matching, are given in Table 8.

Table 7. Performance study of recovered images acquired by coarse matching and fine matching techniques for WANG V2.0.

Classes	Accuracy	Precision
Shuttle	0.3764	0.588
Building	0.3819	0.773
Sky	0.4425	0.8083
Nightfall	0.3874	0.895
Cowboys	0.2915	0.6383
Flag	0.8396	1
Mountains	0.3378	0.7927
Desert	0.5863	0.9543
Boat	0.3942	0.6473
Forest	0.4982	0.7807
Average	0.4536	0.7878

Table 8. Performance study of recovered images acquired by coarse and fine matching phases for Caltech

Classes	Accuracy	Precision
Accordion	0.5265	1
Airplanes	0.6009	1
Beaver	0.4898	0.8817
Binocular	0.7324	0.8903
Bonsai	0.417	0.915
Brontosaurus	0.5349	0.8667
Buddha	0.4961	0.892
Camera	0.583	0.9383
Cannon	0.5047	0.8233
Cellphone	0.6497	0.9493
Chair	0.5132	0.856
Chandelier	0.5906	0.8957
Cougar_Body	0.5998	0.8135
Cougar_Face	0.48	0.922
Crab	0.5326	0.921
Crayfish	0.5961	0.761
Crocodile	0.4868	0.8113
Crocodile_Head	0.5722	0.7943
Cup	0.5751	0.9577
Dalmatian	0.4681	0.8877
Dollar_Bill	0.5458	0.9057
Dolphin	0.531	0.8587
Average	0.5494	0.8882

As anticipated, Caltech 101 frequently beat Wang V1.0 and Wang V2.0, as seen in Tables 8, where precision was around 0.89 and accuracy was practically flawless. Accordion and Airplanes were awarded perfect scores. The Crayfish has the lowest accuracy and precision of all the models, both of which are consistent with the earlier results. The findings shown that the precision gained by Fine-matching is 33,00 percent greater than

that of coarse matching, with an average of around 0.88, while achieving almost flawless accuracy. However, the fine-matching has effectively addressed the shortcomings of the coarse-phase. It has been noticed that the decrease of FP has not only influenced precision favorably, but also accuracy positively. It is mostly attributable to the Slantlet transform displaying minute texture details.

Concerning the preceding study, numerous writers developed a system based on special domain feature extraction and combined it with frequency domain approaches to improve image retrieval and achieve a high precision average. However, the precision of our suggested approach, which uses Slantlet transfer to extract features from colour channels, was the highest. Table 9 clearly shows that the proposed technique outperformed the others..

The drawbacks and limitations of the previous methods are mostly resolved. These achievements were mainly attributed to the following contribution; (1) It incorporated two types of texture features, spatial and SLT-based. The former was extracted from HSV and YCbCr colour spaces, while the latter was drawn from the SLT-decomposed image. Here, two original ideas were brought forth. The way spatial-based texture features are drawn via HSV and YCbCr. Moreover, another idea is the way the SLT-based texture feature is computed via RGB instead of greyscale. Consequently, only the first two rows of the SLT matrix are used for each channel to extract texture features. (2) A novel Coarse-to-Fine approach is introduced instead of the threshold-based approach, which was previously adopted by the majority. Like a coarse-grained sugar filter, which

separates granulated sugar from caster sugar. In this study, the query image is first coarsely matched against the entire dataset to form a shortlist. Afterwards, the fine matching is applied using the shortlist as the input, from which the most likely candidate that resembles the query image is chosen.

7. CONCLUSIONS AND FUTURE WORK

Despite encouraging milestones, many challenging issues remain unresolved, such as FP and low precision. Hence, against the backdrop, this study has proposed a two-tier approach that worked for hand in hand in achieving both high precision and high accuracy, in which the coarse matching became the feeder to the fine matching. Texture characteristics, according to the Caltech 101 dataset, are reliable and capable of producing excellent results while also being resistant to low resolution. It also demonstrated that spatial-based texturing alone cannot achieve the desired precision and that the SLT-based texture feature is the ideal partner. Despite the promising results of the proposed strategy, there are still many areas for development.

For the issue of an FP, the best precision reached to date is [0.885 – 0.888], indicating that the problem is still there. Furthermore, it is not easy to achieve complete precision due to inadequacies in the ground truth. Some photographs were incorrectly sorted manually, resulting in different images being placed into the same class while nearly identical images were grouped into multiple classes. Interclass similarity and intra-class dissimilarity are terms used to describe this situation. As a result, a more accurate ground truth has been long required.

Table. 9. Precision comparison between the proposed method and state-of-the-art

Dataset	Proposed CBIR	S. Somnugong et al. 2016 [12]	Nazir et al. 2018 [13]	S. P. Rana et al. 2019 [14]	Q. Zheng et al. 2019 [15]
WANG V1.0	0.788	0.723	0.693	0.753	0.735
WANG V2.0	0.787	0.756	0.703	0.642	0.761
Caltech 101	0.888	0.725	0.735	0.645	0.885

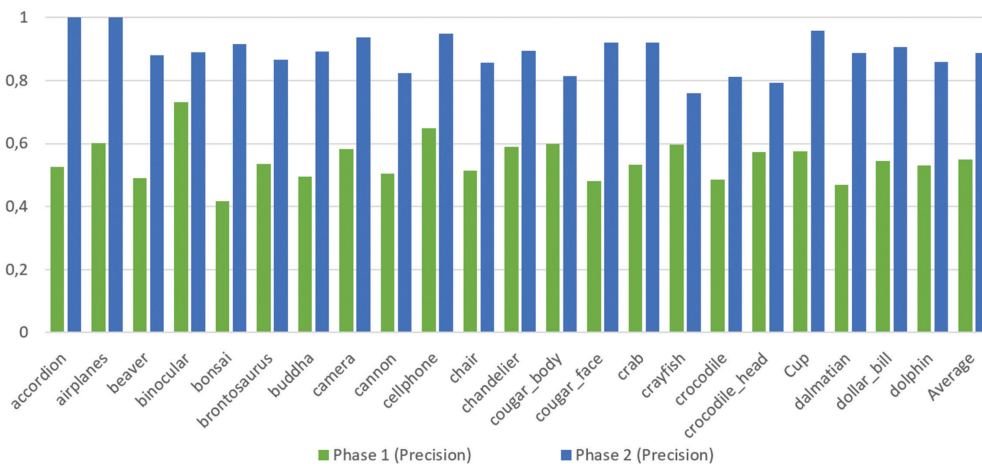


Fig. 5. Comparison of performance evaluation using proposed two phases in terms of Precision.

8. REFERENCES:

- [1] I. M. Hameed, S. H. Abdulhussain, B. M. Mahmood, "Content-Based Image Retrieval: A Review of Recent Trends", *Cogent Engineering*, Vol. 8, No. 1, 2021, pp. 1-37.
- [2] M. K. Alsmadi, "Content-Based Image Retrieval Using Color, Shape and Texture Descriptors and Features", *Arabian Journal for Science and Engineering*, Vol. 45, No. 4, 2020, pp. 3317-3330.
- [3] S. Hossain, R. Islam, "A New Approach of Content Based Image Retrieval Using Color and Texture Features", *Current Journal of Applied Science and Technology*, Vol. 51, No. 3, 2017, pp. 1-16.
- [4] M. Danish, R. Rawat, R. Sharma, "A Survey: Content Based Image Retrieval Based on Color, Texture, Shape & Neuro Fuzzy", *Image*, Vol. 3, No. 5, 2013, pp. 839-844.
- [5] M. Sharma, A. Batra, "Analysis of Distance Measures in Content Based Image Retrieval", *Global Journal of Computer Science and Technology*, Vol.14, No. 2, 2014, pp. 11-16.
- [6] M. F. Sadique, B. K. Biswas, S. R. Haque. "Unsupervised Content-Based Image Retrieval Technique Using Global and Local Features". *Proceedings of the 1st International Conference on Advances in Science, Engineering and Robotics Technology*, Dhaka, Bangladesh, 3-5 May 2019, pp. 1-6.
- [7] O. Beijbom et al. "Towards Automated Annotation of Benthic Survey Images: Variability of Human Experts and Operational Modes of Automation", *PloS one*, Vol. 10, No. 7, 2015, pp. e0130312.
- [8] Z. Hu et al. "A Novel Method Based on a Mask R-Cnn Model for Processing Dpcr Images", *Analytical Methods*, Vol. 11, No. 27, 2019, pp. 3410-3418.
- [9] X. Li, J. Yang, J. Ma, "Recent Developments of Content-Based Image Retrieval (CBIR)", *Neurocomputing*, Vol. 452, 2021, pp. 675-689.
- [10] A. Latif et al. "Content-Based Image Retrieval and Feature Extraction: A Comprehensive Review", *Mathematical Problems in Engineering*, Vol. 2019, 2019, pp. 1-21.
- [11] X. Jiang, J. Jiang, A. Fan, Z. Wang, J. Ma, "Multiscale Locality and Rank Preservation for Robust Feature Matching of Remote Sensing Images", *IEEE Transactions on Geoscience and Remote Sensing*, Vol. 57, No. 9, 2019, pp. 6462-6472.
- [12] S. Somnugpong, K. Khiewwan, "Content-Based Image Retrieval Using a Combination of Color Correlograms and Edge Direction Histogram", *Proceedings of the 13th International Joint Conference on Computer Science and Software Engineering*, Khon Kaen, Thailand, 13-15 July 2016, pp.1-5.
- [13] A. Nazir, R. Ashraf, T. Hamdani, N. Ali, "Content Based Image Retrieval System by Using Hsv Color Histogram, Discrete Wavelet Transform and Edge Histogram Descriptor", *Proceedings of the International Conference on Computing, Mathematics and Engineering Technologies*, Sukkur, Pakistan, 3-4 March 2018, pp. 1-6
- [14] S. P. Rana, M. Dey, P. Siarry, "Boosting Content Based Image Retrieval Performance through Integration of Parametric & Nonparametric Approaches", *Journal of Visual Communication and Image Representation*, Vol. 58, 2019, pp. 205-219.
- [15] Q. Zheng, X. Tian, M. Yang, H. Wang, "Differential Learning: A Powerful Tool for Interactive Content-Based Image Retrieval", *Engineering Letters*, Vol. 27, No. 1, 2019, pp. 202-215.
- [16] M. Q. Shatnawi, M. Alrousan, S. Amareen, "A new approach for content-based image retrieval for medical applications using low-level image descriptors", *International Journal of Electrical and Computer Engineering*, Vol. 10, No. 4, 2020, pp. 4363-4371.
- [17] A. P. Byju, B. Demir, L. Bruzzone, "A Progressive Content Based Image Retrieval in JPEG 2000 Compressed Remote Sensing Archives", *IEEE Transactions on Geoscience and Remote Sensing*, Vol. 8, No. 85, 2020, pp. 5739-5751.
- [18] M. Jammula, "Content Based Image Retrieval System Using Integrated ML and DL-CNN", *Annals of R.S.C.B*, Vol. 25, No. 4, 2021, pp. 9656-9666.
- [19] A. Ahmed, S. Mohamed, "Implementation of early and late fusion methods for content-based image retrieval", *International Journal of Advanced and Applied Sciences*, Vol. 8, No. 7, 2021, pp. 97-105.

- [20] A. Alzu'bi, A. Amira, N. Ramzan, "Semantic Content-Based Image Retrieval: A Comprehensive Study", *Journal of Visual Communication and Image Representation*, Vol. 32, 2015, pp. 20-54.
- [21] S. Zakariya, I. A. Khan, "Analysis of Combined Approaches of Cbir Systems by Clustering at Varying Precision Levels", *International Journal of Electrical & Computer Engineering*, Vol. 11, No. 6, 2021, pp. 5009-5015.
- [22] J. Chaki, N. Dey, "Image Color Feature Extraction Techniques: Fundamentals and Applications", 1st Edition, Springer Nature, 2021.
- [23] C. Singh, K. P. Kaur, "A Fast and Efficient Image Retrieval System Based on Color and Texture Features", *Journal of Visual Communication and Image Representation*, Vol. 41, 2016, pp. 225-238.
- [24] I. W. Selesnick, "The Slantlet Transform", *IEEE Transactions on Signal Processing*, Vol. 47, No. 5, 1999, pp. 1304-1313.
- [25] V. SS, B. Vasista, V. N Sansthanik, "Slantlet Transform: An Efficient Approach for Compression and De-Noising of Power Quality Events", *International Journal of Computer Applications*, Vol. 91, No. 4, 2014, pp. 27-31.
- [26] M. S. H. Al-Tamimi, "Combining Convolutional Neural Networks and Slantlet Transform for an Effective Image Retrieval Scheme", *International Journal of Electrical & Computer Engineering*, Vol. 9, No. 5, 2019, pp. 4382-4395.
- [27] S. F. Da Silva, M. X. Ribeiro, J. d. E. B. Neto, C. Traina-Jr, A. J. Traina, "Improving the Ranking Quality of Medical Image Retrieval Using a Genetic Feature Selection Method", *Decision Support Systems*, Vol. 51, No. 4, 2011, pp. 810-820.
- [28] H. Wu, Y. Cao, H. Wei, Z. Tian, "Face Recognition Based on Haar Like and Euclidean Distance", *Journal of Physics: Conference Series*, 2021, pp. 1-6.

Transfer Learning Based Deep Neural Network for Detecting Artefacts in Endoscopic Images

Original Scientific Paper

Kirthika Natarajan

School of Engineering, Avinashilingam Institute for Home Science and Higher Education for Women, Varapalayam, Coimbatore, Tamilnadu 641 108, India.
prof.kirthika@gmail.com

Sargunam Balusamy

School of Engineering, Avinashilingam Institute for Home Science and Higher Education for Women, Varapalayam, Coimbatore, Tamilnadu 641 108, India.
sargunamb@gmail.com

Abstract – Endoscopy is typically used to visualize various parts of the digestive tract. The technique is well suited to detect abnormalities like cancer/polyp, taking sample tissue called a biopsy, or cauterizing a bleeding vessel. During the procedure, video/images are generated. It is affected by eight different artefacts: saturation, specularly, blood, blur, bubbles, contrast, instrument and miscellaneous artefacts like floating debris, chromatic aberration etc. The frames affected by artefacts are mostly discarded as the clinician could extract no valuable information from them. It affects post-processing steps. Based on the transfer learning approach, three state-of-the-art deep learning models, namely YOLOv3, YOLOv4 and Faster R-CNN, were trained with images from EAD public datasets and a custom dataset of endoscopic images of Indian patients annotated for artefacts mentioned above. The training set of images are data augmented and used to train all the three-artefact detectors. The predictions of the artefact detectors are combined to form an ensemble model whose results outperformed well compared to existing literature works by obtaining a mAP score of 0.561 and an IoU score of 0.682. The inference time of 80.4ms was recorded, which stands out best in the literature.

Keywords: Deep learning, Artefacts, Endoscopy, Transfer learning

1. INTRODUCTION

Endoscopy is a non-surgical technique that encompasses inserting a thin and long flexible tube called an endoscope down through the throat to inspect a person's gastrointestinal tract. The flexible tube is attached with a light and a camera. A gastroenterologist uses an endoscope to diagnose and treat common ailments in the digestive tract, collect tissue samples called a biopsy, pass special tools through the endoscope to treat bleeding vessels, remove a foreign body or a polyp etc.

Recent technologies allow doctors to switch between imaging modalities like narrow-band imaging (NBI), fluorescence light and white light to detect abnormalities better. These technologies improve the visualization of the mucosal surface and microvascular pattern. The internal organ is viewed on a television monitor connected outside during the procedure. Also, the complete process is recorded. The clinician can review the recorded video for planning further treatment, re-

port preparation, discussion with a senior clinician and follow-up etc.

Artefacts [1] are the artificial effect found in most endoscopy images but are not present in the imaged organ. The presence may be due to mishandling miniaturized components, hand movements, natural causes etc. These artefacts affect the video quality and increase procedure time. In the recorded video, most of the frames are affected by artefacts. Hence, the most affected frames are discarded, which reduces the quality of the video during post-processing, thus directly affecting the quality of treatment and diagnosis. Also, these artefacts may obscure features/ characteristics relevant to an abnormality like cancer. They also increase false detection rates in Computer-Aided Diagnostic (CAD) systems. Thus, an efficient method to detect these artefacts prior may help the doctors to speed up the procedure with improved accuracy. It can be accomplished by deploying artificial intelligence. Figure 1 displays endoscopic images affected by artefacts.

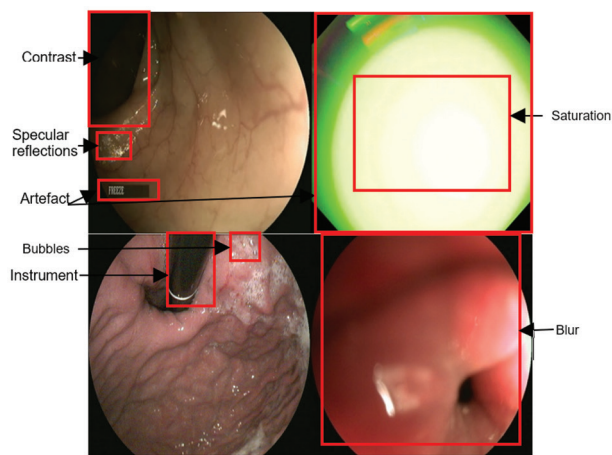


Fig. 1. Endoscopic images affected by artefacts

Figure 1. highlights only a few artefacts to maintain clarity. Encouragingly, Deep Learning (DL) algorithms, a subset of AI, have the power to extract features from annotated images without human intervention. Congregating the study toward endoscopy, we deploy pre-trained DL-based object detection models for detecting endoscopic artefacts in this research.

The motivation behind the research is as follows. Firstly, the clinician cannot adequately examine the underlying tissue due to the presence of various artefacts, which increases procedure time. Secondly, the procedure is recorded, and specific regions are imaged for further examination and report preparation. Most of the frames are affected by endoscopic imaging artefacts, due to which the affected frames are discarded as no helpful information can be extracted from them.

Third, the artefact varies in size and location in an endoscopic image. The size of artefact-like specular reflection is tiny, occurring in groups. On the other hand, other artefacts like saturation and contrast cover a large area. This challenges the object detection algorithm to detect objects of various scales. Interestingly more than one artefact occurs in most of the frames. Thus, locating tiny to significant artefacts in a single frame adds complexity to the existing problem.

Fourth, deep learning models need many labelled data to train themselves. Especially in the medical imaging sector, the amount of labelled data for every abnormality is significantly less. In such a scenario, Transfer Learning (TL) lends its helping hand. It is important to note that choosing the suitable model for every application is a tedious and trial and error process. It is an unsolved research issue to date. This research considers the unique property of every algorithm in the literature and selects the one that meets the accuracy and inference time balance. For this research purpose, several algorithms are trained; namely, You Only Look Once (YOLO)v3 [2], YOLOv4[3] and RetinaNet [4], Faster Region-based -Convolutional Neural Network (R-CNN) [5] with various backbones. The final model is chosen after estimating the performance of all trained models.

To train any DL-based object detection algorithm massive dataset is essential. A few datasets are available for research / academic purposes to study artefacts in endoscopic images. They are the Kvasir-Instrument dataset [6], Computer Vision Centre (CVC)-ClinicSpec [7], Cholec80 dataset [8] etc. Most of these datasets hold annotations for a single artefact only. But in real-time endoscopic images are severely affected by various other artefacts also. To serve the purpose of multiple artefact detection: The endoscopic Artefact Detection (EAD) dataset [9][10] is available. The datasets hold annotations for common artefacts like saturation, specular reflections, blur, blood, bubbles, instrument, contrast and miscellaneous imaging artefacts.

Authors reported that the EAD datasets suffer from a class imbalance problem [11][12]. A standard solution accepted across the globe is to use the data augmentation technique [13]. It is also vital that all the data augmentation techniques cannot be adopted to all medical images. Carefully choosing the method is essential. After trivial analysis considering the availability of data, pre-trained models, hardware requirements etc., This research paper seeks to analyze the performance of three different object detection models using a custom dataset.

The specific contribution of this research article is as follows:

- A new dataset has been curated with clinician assistance to add more images to the dataset with patients of Indian origin to combat data requisite for DL algorithms.
- We have trained 3 DL-based object detection models, namely YOLOv3, YOLOv4 and Faster R-CNN, for multi-class artefact detection.
- All the three trained artefact detectors are combined to form an ensemble model for improved performance.
- The research results prove superior performance over literature outcomes, and the results are compared with recently reported literature works.

The outline of the research article is as follows. Section 2 explores literature works related to multiple endoscopic artefact detection. Section 3 addresses the details of curation of the new dataset, annotation protocols and the details of the public dataset. Section 4 gives a comprehensive report on methodology, transfer learning approach, training of various models and design of proposed ensemble model architecture, followed by a detailed description of the results obtained. The last section reports the conclusion and presents the future scope of this research findings.

2. RELATED LITERATURE WORKS

Deep learning algorithms have shown exceptional performance in every branch of the health care industry in the past decade. In recent years, deploying DL algorithms in detecting multiple artefacts gained im-

portance after the release of EAD datasets. This section concisely presents the literature works relevant to the field of multiclass endoscopic artefact detection.

Pengyi Zhang et al. (2019) [14] proposed a modified version of Mask R-CNN called Mask Aided R-CNN. Initially, a basic Mask R-CNN is trained for the segmentation task. The trained Mask R-CNN is used to predict instant masks for training samples from the detection set. The masks are predicted only for ground truth bounding boxes. The predicted masks are termed soft-pixel level labels which are added to the segmentation set to retrain the network. This strategy proves to be the best in the detection task.

Yan-Yi Zhang and Di Xie (2019) [15] proposed a cascaded R-CNN-based model and trained the model by gradually increasing the Intersection over Union (IoU) threshold. The model was initially pre-trained using Microsoft Common Objects in Context (MSCOCO) dataset [16] and later retrained with EAD datasets.

Hoang Manh Hung et al. (2020) [17] presented a DL-based cascaded R-CNN with ResNeXt-101 backbone followed by Feature Pyramid Network (FPN). This combination improved the feature extraction capability of the network and recall rate. To differentiate the object from the background, the authors added Deformable Convolution (DCN) to the network, improving the performance.

Hongyu Hu and Yuanfan Guo (2020) [18] designed a cascaded R-CNN-based architecture with ResNeXt as backbone and FPN to extract features. The author adopted multi-scale detection techniques to scale images from 512x512 to 1024x1024 randomly. Flipping images horizontally was employed to expand the dataset size. Soft-Non-Max Suppression (NMS) was adopted, which avoids unnecessary ignoring of objects.

Zhimiao Yu and Yuanfan Guo (2020) [19] used a cascaded R-CNN-based model with ResNet101 as the backbone with FPN. The network used an ImageNet pre-trained backbone. The author adopted data augmentation, soft-NMS, cosine decay strategy for learning rate schedule, cross-entropy loss and smoothL1 loss for classification and regression.

Xiaohong Gao and Barbara Braden (2020) [20] presented a DL network based on RetinaNet. The author incorporated a real-time instance segmentation task into RetinaNet to cater for the need for object detection and instance segmentation.

Anand Subramanian and Koushik Srivatsan (2020) [21] experimented RetinaNet with ResNet101 feature extractor for artefact detection. The authors used image correlation-based trackers to reduce inference time, improving the network performance.

This section summarized recent works of literature in the domain of endoscopic artefact detection. All the researchers used EAD datasets to train the algorithms. The authors selected a state-of-the-art object detec-

tion model and trained the model with various backbone and learning strategies, deployed augmentation techniques, and cascaded the structures to produce efficient results.

3. DATASETS

EAD2019 is a dataset that covers seven major artefacts like specularity, saturation, contrast, blur, bubbles, instruments and miscellaneous imaging artefacts. The dataset contains 2147 images. Figure 2 shows sample images from the EAD2019 dataset. EAD2020 comprises 2531 images and covers eight imaging artefacts, including blood and all seven artefacts covered by the EAD2019 dataset. Figure 3 illustrates some images from the EAD2020 dataset. Expert clinicians suggested all the artefacts mentioned above.

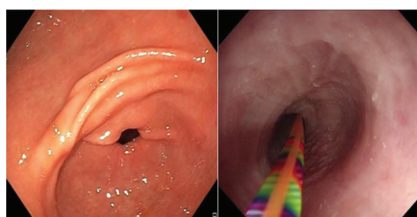


Fig. 2. Sample images from EAD2019 dataset

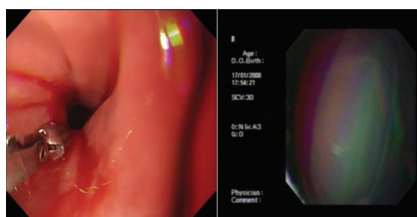


Fig. 3. Sample images from EAD2020 dataset

Both the datasets are multi-patient, i.e., the images are from 6 distinctive centres globally. It is a multi-organ dataset covering the oesophagus, stomach, liver, colon and bladder. Also, it is a multi-tissue and multi-modality dataset (white light, fluorescence light, and Narrow band imaging). Videos collected from these centres were imaged using standard endoscopes manufactured by Karl Storz, Olympus and Bio spec. The images hosted in the dataset do not contain any patient information.

Initially, senior clinicians annotated the images and later, the experienced post-doctoral fellows. Finally, the senior clinicians validated the images. All the images were annotated (bounding box) for artefact detection using python, Qt, and an Open-CV-based in-house tool. The dataset contains images and a binary mask for semantic segmentation.

3.1 CUSTOM DATASET

The public dataset contains images of patients from western countries. The images with artefacts like blur, instrument and saturation were not much found. There-

fore 2400 endoscopic images of Indian patients were collected, which includes more images on saturation, blur and instrument to combat class imbalance problems in the public dataset. Initially, images were annotated in the presence of a senior clinician to gain expertise. Later annotations were done individually and finally validated by the clinician in the ratio of 1:10(no. of images). Figure 4 shows random sample images from the custom dataset.

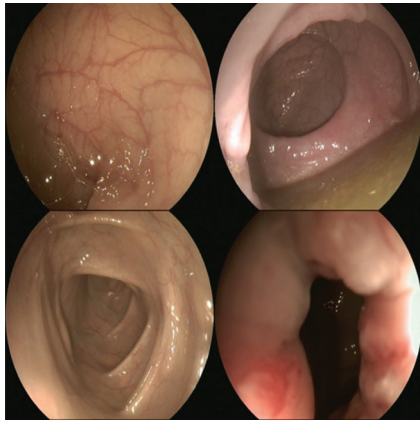


Fig. 4. Images from custom dataset

3.2 ANNOTATION PROTOCOLS

Annotation protocols from the EAD dataset [22] were followed for annotating the custom dataset. Images from EAD and custom dataset were used to train the endoscopic artefact detector. Thus, uniform annotation protocols were used to maintain homogeneity across all three datasets. Figure 5 portrays images of a custom dataset labelled for eight commonly occurring artefacts. Artefacts like instruments, saturation, blur and contrast cover a larger area when compared to the artefact called specularity. Specular reflections cover a small region; for precise delineation, most specular reflections are marked with a separate bounding box.

One single bounding box was used in some cases where the reflections are found in a series fashion. In the curated custom dataset, care was taken that no patient information was visible. It is apparent from the images exhibited that more than one artefact is said to be present in almost all the frames.

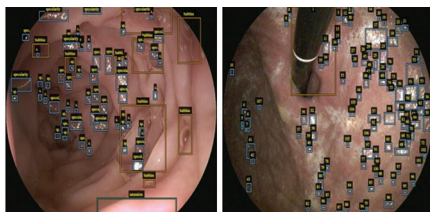


Fig. 5. Annotated images from custom dataset

3.3 ANNOTATION SOFTWARE

All annotations were done using VGG (Visual Geometry Group) Image Annotator (VIA) [23], an open-source annotation tool offered by Oxford University, United Kingdom.

4. METHODOLOGY

Deep learning models like YOLOv3, YOLOv4 and Faster R-CNN were chosen. The former two were selected based on their faster inference and faster R-CNN for its accuracy. All the models were trained and tested with images from EAD and custom datasets. This training was thoroughly carried out with Google Co-laboratory [24] single Graphics Processing Unit (GPU) environment. After training, all three models were evaluated, tuned, retrained and combined for an ensemble model. The ensemble model is tested with images from the test set. To attain the best performance transfer learning approach was chosen.

4.1 TRANSFER LEARNING

Transfer learning is a technique to train DL models on massive datasets like MSCOCO, ImageNet [25] etc. Later, for specific applications, these models can be re-trained. During retraining, the model with already stored knowledge learns the features of new applications at a faster rate with reasonable accuracy. TL helps reduce the training time, hardware cost and the required high-dimensional dataset. In the present decade, many pre-trained models are available in the model zoo [26][27] for research purposes. Figure 6 shows a simple TL model. The following sub-sections discuss the three deep learning models used in this study.

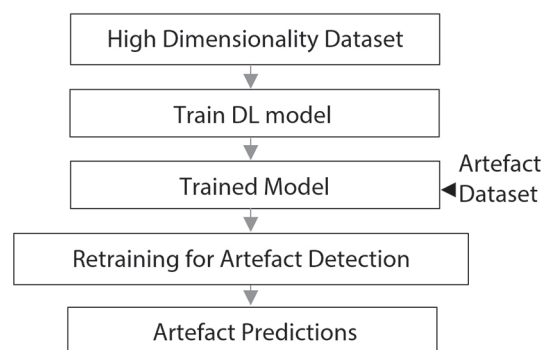


Fig. 6. Outline of transfer learning-based detection model

4.2 YOLOV3

YOLO first came into existence in the year 2016. Out of all updated versions of YOLO, YOLOv3 was tagged for its best performance in terms of speed. YOLOv3 looks at the complete image once and divides it into small grids. In each grid, bounding boxes will be drawn if there is a meaningful object. The predictions and their similarity with the predefined classes are calculated. When the score is high, it is considered a positive detection. YOLOv3 uses Darknet53 as the backbone to extract features. YOLOv3 also finds a good balance between detecting various sizes of objects, from tiny to large. This characteristic is beneficial in the case of detecting artefacts like specular reflections, which are small and artefacts like contrast and instrument, which are prominent.

4.3 YOLOV4

YOLOv4 is the fourth principal member added to the YOLO family in 2020 by Alexey Bochkovskiy. It has many special features. One or more of the features can be combined and utilized for applications to obtain state-of-the-art results. They are grouped under two heads: Bag of Specials (BoS) and Bag of Freebies (BoF). BoF helps to improve model accuracy without compromising the model inference time. On the other hand, BoS aid in improving accuracy at the cost of inference time. Thus, the researcher must select the best strategies for the best results.

4.4 FASTER R-CNN

Faster R-CNN is a two-stage object detector from the R-CNN family. It uses the Region proposal Network (RPN) to improve its performance.

In Faster R-CNN, the input image is passed into the ConvNet, which returns the feature maps, and RPN is applied to the feature maps to get object proposals. Using the Region of Interest (ROI) pooling layer, all the proposals are brought down to the same size. Finally, they are sent to a fully connected layer to classify and predict the classes of the objects in the bounding boxes.

5. EXPERIMENTAL ANALYSIS

This section presents details of datasets, training and testing of models, evaluation criteria and results obtained.

5.1 DATASET

EAD datasets embrace endoscopic images annotated for various artefacts like saturation, specularity, blood, bubbles, contrast, blur, instruments and miscellaneous artefacts. In total, 2147 images from the EAD2019 dataset and 2531 images from the EAD2020 dataset were used in this research. Apart from the existing public dataset, the newly curated dataset with 2400 annotated images was used. Thus approximately 7000 images were pooled to form the training and test set.

5.2 TRAINING AND TESTING

The proposed research work is written using python. The training of the artefact detection model was done on a google co-laboratory single GPU environment. Initially, all the images were pooled and manually split into train and test with 80% and 20% split-up. Later train set was divided into train and validation sets. Finally, 70% of the images were allocated for training, 10% of total images for validation and 20% of total images for testing. Three models, namely YOLOv3, YOLOv4 and Faster R-CNN, were trained using the train set's augmented images. The training strategy followed for each model is discussed in the sections below.

It is well known that more images are required to train deep learning-based algorithms. Images avail-

able may not be sufficient to make the detector robust; hence data augmentation was adopted.

5.3 DATA AUGMENTATION

Augmentation is a technology that magnifies the dataset by slightly modifying the existing images [28]. The augmentation technique must be carefully chosen. It may affect the performance of the detector if not appropriately selected. For our study, we have adopted rotation at various angles, namely $0^\circ, 90^\circ, 180^\circ, 270^\circ$ and flipping. Hence the existing data expanded eight times. Then augmented dataset was used to train all three algorithms. Along with manual augmentation techniques, this research adopts run time augmentation techniques like a mosaic, varying hue, saturation, brightness and other augmentation techniques offered by the network to make the detector more robust.

5.4 TRAINING OF YOLOV3

YOLOv3 was cloned from Darknet [29]. The augmented dataset was used to train YOLOv3 for artefact detection. The algorithm has various runtime augmentation techniques like varying hue, saturation and exposure; it was also considered during training. Various parameters set during training are as follows, learning rate = 0.001, batch size=64, maximum batches = 16,000, image size=416x416. By setting all the initializations, the training started with pre-trained weights. The training lasted until the network reached a minimum average loss. Approximately after 55,000 iterations, the average loss curve was found to be smoothed. Once the average loss no longer reduces, the iterations can stop. On the other hand, the iterations can be stopped when the loss reaches 0.05, provided the dataset is small, and 3.0 if the dataset is bigger [29]. The average loss did not improve after 55,000 iterations. The training was stopped at 70,000 iterations. Various weight files extracted during training are tested for their performance in terms of mAP and IoU. Weights file extracted at 65,000th iteration gave its best results.

5.5 TRAINING OF YOLOV4

The basic network architecture was cloned from [30]. YOLOv4 was customized with the following features: CSPdarknet53 as the backbone, PanNet for aggregating the features and YOLOv3 head for final predictions. Special features from BoF and BoS like mosaic augmentation, Mish Activation function, NMS, optimized anchors etc., were handpicked. Pre-trained weights were opted to reduce training time.

The other important initial hyper-parameters set for training are as follows, image size= 512x512, batch size=64, momentum=0.949, decay=0.0005 and learning rate=0.013. Few run-time data augmentation techniques like varying hue, saturation, exposure, cut-mix and mosaic were deployed. With the above set parameters, training lasted till 85,000 iterations. Until 35,000

iterations, handpicked features like cut-mix and mosaic augmentation were employed. The loss did not converge as expected. Hence on trial-and-error bases, cut-mix augmentation was removed, which yielded results as expected. The training was stopped at 95,000 iterations. Weights files extracted during the training process were examined for best results, and it was decided to use the 76,000th weight file, which gave a good balance between mAP, IoU and inference time as well.

5.6 TRAINING OF FASTER R-CNN

Faster R-CNN was adopted from detectron2 [31], built by Facebook AI Research (FAIR). It holds a model zoo consisting of trained model files for faster implementations and several baselines for research. The training parameters set to train Faster R-CNN is as follows: Image size=512x512, backbone = Resnet50, learning rate =0.1, ROI head size= 256 x 256 and batch size = 4. Faster R-CNN training started with the initialized training parameters. Model checkpoints were set to every 1000th iteration. The training lasted for 80,000 iterations. The trained weight file extracted at the 74,000th iteration gave good accuracy and reasonable inference time.

All three models are trained with pre-trained weight. The need to choose the TL approach in this research is to reduce the training time. The images available for training is also limited; hence it was preferred to use TL rather than training from scratch. The impact of TL has been proven by exhibiting accurate results in lesser iterations and with a limited size of the training dataset.

5.7 PROPOSED ENSEMBLE MODEL

The term 'ensemble' means collective or collaborative. Ensemble learning model combines the predictions of multiple object detection models to improve the overall performance.

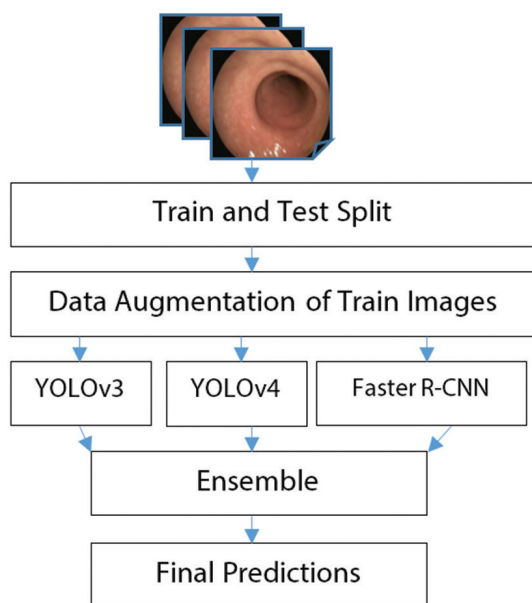


Fig. 7. Ensemble endoscopic artefact detection model

Ensemble models are classified into three types: affirmative, unanimous, and consensus. The proposed ensemble model combines the benefits of both single-stage and two-stage object detectors. The trained and tested model files of YOLOv3, YOLOv4 and Faster R-CNN are blended together for predictions. A test image is passed into the model. All three trained models predict every artefact present in the image. Based on the ensemble method chosen, final predictions will be generated. Out of all three methods result of the consensus, the model proved exemplary. Figure 7 depicts the proposed ensemble model.

5.8 RESULTS

This section discusses the performance of the proposed ensemble model against different literature results compared based on standard performance parameters like IoU, mAP and Inference time.

5.8.1 Mean average precision (mAP)

Average Precision (AP) can be calculated by intersecting the precision-recall (PR) curve and coordinate axis at recall values, say r_1, r_2, \dots, r_n . Equation (1) is used to calculate the AP score.

$$AP = \sum_n (r_{n+1} - r_n) P_{interp}(r_{n+1}) \quad (1)$$

where $p_{interp} = \max p(r)$ and mAP can be calculated by taking the mean of every AP using Equation (2) over all artefacts i . $N=8$, is the total number of classes.

$$mAP = \frac{1}{N} \sum_i AP_i \quad (2)$$

5.8.2 Intersection over union (IoU)

IoU must be calculated using the formula in (3). IoU is a ratio between the intersection of ground truth(A) and predicted bounding boxes(B) and the union of ground truth(A) and predicted bounding boxes(B).

$$IoU = \frac{A \cap B}{A \cup B} \quad (3)$$

5.8.3 Score_d

Score_d is a weighted score of IoU and mAP as given in Eq. (4).

$$Score_d = 0.6 * mAP + 0.4 * IoU \quad (4)$$

The ensemble artefact detection model combines predictions of all three base learners and produces a final prediction based on the ensemble methods chosen. In the affirmative method, all the models can predict objects in the image. Even if one model proposes a bounding box for an object, it will be considered for the final predictions of the ensemble model. In a unanimous approach, all the models can predict bounding boxes around the objects in the image. If all the three models predict the same instance, then that instance is considered for final predictions provided if the IoU

is greater than 0.5. Finally, in the consensus approach, a bounding box around an instance will be considered if most models generate the same box. Fig. 8 illustrates the results of the ensemble model with a consensus approach.

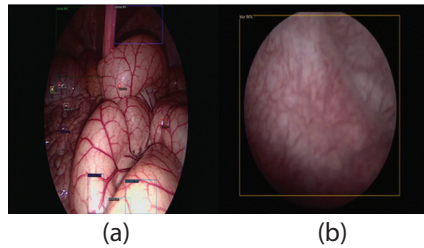


Fig. 8(a) &(b): Artefact detection by ensemble model

In Fig. 8(a), three different locations are affected by an artefact called saturation. Each of them was detected with 86%,99% and 98% accuracy. Similarly, artefact contrast was detected with 86% and 96% accuracy. Specular reflections are scattered around the image; each of them was predicted with 70%-98% of accuracy. In Fig. 8(b), the artefact blur was detected with 86% accuracy. Hence the prediction accuracy proves the robustness of the detector.

5.9 COMPARATIVE ANALYSIS

This section presents the comparative analysis of the multi-class endoscopic artefact detection model with literature results. This study compares research outcomes based on performance evaluators of the detectors in terms of mAP, IoU, Score_d and inference time. The average precision obtained by the model in detecting every artefact is tabulated in Table 1.

Table 1. Class-wise average precision scores

Class	YOLOv3-Spatial Pyramid Pooling[32]	Proposed model
Specular reflections	34.7	48.12
Saturation	55.7	56.46
Miscellaneous Artefact	48.0	44.91
Blur	7.5	51.31
Contrast	72.1	36.74
Bubbles	55.9	51.61
Blood	-	58.39
Instrument	-	100.00

From the table, it is evident that the model has a balanced performance over predicting all artefacts. The combination of EAD and custom datasets to counterbalance the class imbalance problem has turned prolific. Specular reflections and a few miscellaneous artefacts are tiny, but saturation covers comparatively a bigger area. But all three artefacts have a common attribute of having bright pixel areas. Yet the trained model is capable of differentiating them well. Contrast has different characteristics of having dark pixel areas.

Blur has an attribute of un-sharpness or having a poor spatial resolution. Artefacts like bubbles, blood and instrument have different attributes like well-defined boundaries for instruments and colour features for blood and bubbles. Often artefacts like bubbles, miscellaneous artefacts and specular reflections overlap, yet in most cases, the model predicts the artefacts well.

The common metric used to evaluate the performance of every detection model is the mAP and IoU. The model is evaluated by having a threshold value of 0.5. The results are deliberated in Table 2. Score_d is a metric exerted from the EAD challenge [22]. The metric is used to compare the performance of the proposed model with literature results.

Table 2. Comparative analysis

Author	mAP	IoU	Score_d
Yan-Yi Zhang and Di Xie [15]	-	-	0.3429
Xiaohong Gao and Barbara Braden [20]	-	-	0.2205
Pengyi Zhang et al. [14]	0.3117	0.4051	0.361
Anand Subramanian and Koushik Srivatsan [21]	0.2151	-	-
Proposed method	0.561	0.682	0.6094

Almost all researchers concentrated on accuracy, but inference time is equally essential when it comes to real-time implementation of the modules in CAD and semi-automated/ fully automated robotic systems. Thus, this ensemble model with trained base learners produced an impactful research output in detecting multiple endoscopic artefacts. Often authors try to balance inference time and accuracy. An inference time of 80.4ms was observed during the testing of the proposed ensemble model. Most of the authors concentrate on prediction accuracy. Thus, there are not plenty of results to analyze the work based on inference time. This result can be a benchmark for researchers in this area.

6. CONCLUSION AND FUTURE SCOPE

For this study, three different state-of-the-art object detection models: YOLOv3, YOLOv4, and Faster R-CNN, were trained using an augmented train set comprising 56,000 images. The test set contains 1400 images. With all the three base learners trained on EAD and custom datasets, a new ensemble model has been designed, which combines the predictions of all the models. The final proposed model is evaluated against performance criteria like mAP, IoU and inference time. It was observed that the ensemble model under the consensus method with three base learners mentioned above was said to perform well against literature results proposed in [14][15][17–21] with mAP=0.561 and IoU score of 0.62 and inference time of 80.4ms.

This work can be expanded by incorporating a restoration algorithm for every possible artefact. The endoscopic artefact detector could be re-trained to detect

all possible clinical abnormalities in the GI tract. Thus, it could become an all-in-one detection and restoration system, which could aid clinician with better viewability of internal organs, reduces procedure time, improve the prediction accuracy of the CAD system and aid associated post-processing steps. The custom dataset curated can be expanded by adding more images to create a large benchmark dataset.

7. STATEMENT OF ETHICS

This research involves collecting endoscopic images to prepare a custom dataset for which ethical clearance was obtained from the institution's human ethics committee.

8. ACKNOWLEDGEMENTS

This research work is supported by DST-CURIE-AI Facility, Avinashilingam Institute for Home Science and Higher Education for Women, Coimbatore.

9. REFERENCES:

- [1]. Wikipedia, Artifact (Error), [https://en.wikipedia.org/wiki/Artifact_\(error\)](https://en.wikipedia.org/wiki/Artifact_(error)) (accessed: 2022)
- [2]. J. Redmon, A. Farhadi, "YOLOv3: An Incremental Improvement", arXiv:1804.02767, 2018.
- [3]. A. Bochkovskiy, C. Y. Wang, H. Y. M. Liao, "YOLOv4: Optimal Speed and Accuracy of Object Detection", arXiv:2004.10934, 2020, pp.1-17.
- [4]. T. Y. Lin, P. Goyal, R. Girshick, K. He, P. Dollár, "Focal Loss for Dense Object Detection", *IEEE Transactions on Pattern Analysis and Machine Intelligence*, Vol. 42, No. 2, 2020, pp. 318-327.
- [5]. S. Ren, K. He, R. Girshick, J. Sun, "Faster R-CNN: Towards Real-Time Object Detection with Region Proposal Networks", *Proceedings of the 28th International Conference on Neural Information Processing Systems*, Montreal, Canada, Vol. 1, 7-12 December 2015, pp. 91-99.
- [6]. Simula Research Laboratory, Kvasir-Instrument dataset, <https://datasets.simula.no/kvasir-instrument/> (accessed: 2022)
- [7]. CVC-ClinicSpec dataset: <http://www.cvc.uab.es/CVC-Colon/index.php/cvc-clinicspec/> (accessed: 2022)
- [8]. Research Group CAMMA, Cholec80 datasets, <http://camma.u-strasbg.fr/datasets> (accessed: 2022)
- [9]. S. Ali et al. "Endoscopy Artefact Detection (EAD) Dataset", Mendeley Data, 2019, V2.
- [10]. S. Ali et al. "Endoscopy Artefact Detection (EAD) Dataset (includes updated 2020 version)", Mendeley Data, V4, 2021.
- [11]. I. Oksuz, J. R. Clough, A. P. King, J. A. Schnabel, "Artefact Detection in Video endoscopy Using RetinaNet Architecture and Focal Loss Function", *Proceedings of the Challenge on Endoscopy Artefacts Detection: Multi-class Artefact Detection in Video Endoscopy*, Venice, Italy, 8 April 2019.
- [12]. X. Wang, C. Wang, "Detect Artefacts of various Sizes on the Right Scale for each Class in Video Endoscopy", *Proceedings of the Challenge on Endoscopy Artefacts Detection: Multi-class Artefact Detection in Video Endoscopy*, Venice, Italy, 8 April 2019.
- [13]. F. López, "Class Imbalance: Random Sampling and Data Augmentation with Imbalanced-Learn", <https://towardsdatascience.com/class-imbalance-random-sampling-and-data-augmentation-with-imbanced-learn-63f3a92ef04a> (accessed: 2022)
- [14]. P. Zhang, X. Li, Y. Zhong, "Ensemble Mask Aided R-CNN", *Proceedings of the Challenge on Endoscopy Artefacts Detection: Multi-class Artefact Detection in Video Endoscopy*, Venice, Italy, 8 April 2019.
- [15]. Y. Y. Zhang, D. Xie, "Detection and Segmentation of Multi-class Artefacts in Endoscopy", *Journal of Zhejiang University, Science-B*, Vol. 20, No. 12, 2019, pp. 1014-1020.
- [16]. Microsoft Common Object in Context dataset (MSCOCO) dataset, <https://cocodataset.org> (accessed: 2022)
- [17]. H. M. Hung, P. T. D. Thinh, H. J. Yang, S. H. Kim, G. S. Lee, "Artefact Detection and Segmentation using Cascaded R-CNN & U-Net", *Proceedings of the 2nd International Workshop and Challenge on Computer Vision in Endoscopy*, Iowa City, USA, 3 April 2020, pp. 47-50.
- [18]. H. Hu, Y. Guo, "Endoscopic Artefact Detection in MM Detection", *Proceedings of the 2nd International Workshop and Challenge on Computer Vi-*

- sion in Endoscopy, Iowa City, IA, USA, 3 April 2020, pp. 78-79.
- [19]. Z. Yu, Y. Guo, "Endoscopic Artefact Detection using Cascaded R-CNN Based Model", Proceedings of the 2nd International Workshop and Challenge on Computer Vision in Endoscopy, Iowa City, IA, USA, 3 April 2020, pp. 42-46.
- [20]. X. Gao, B. Braden, "Artefact Detection and Segmentation Based on Deep Learning System", Proceedings of the 2nd International Workshop and Challenge on Computer Vision in Endoscopy, Iowa City, IA, USA, 3 April 2020, pp. 80-81.
- [21]. A. Subramanian, K. Srinivasan, "Exploring Deep Learning-based Approaches for Endoscopic Artefact Detection and Segmentation", Proceedings of the 2nd International Workshop and Challenge on Computer Vision in Endoscopy, Iowa City, IA, USA, 3 April 2020, pp.51-56.
- [22]. S. Ali et al. "Endoscopy Artifact Detection (EAD 2019) Challenge Dataset", 2019.
- [23]. VGG Image Annotator (VIA), <https://www.robots.ox.ac.uk/~vgg/software/via/via.html> (accessed: 2022)
- [24]. Google Co-laboratory, <https://colab.research.google.com> (accessed: 2022)
- [25]. ImageNet Dataset, <https://www.image-net.org/> (accessed: 2022)
- [26]. Facebook AI research, Detectron2 model zoo: https://github.com/facebookresearch/detectron2/blob/main/MODEL_ZOO.md (accessed: 2022)
- [27]. Darknet, YOLOv4 model zoo: <https://github.com/AlexeyAB/darknet/wiki/YOLOv4-model-zoo> (accessed: 2022)
- [28]. C. Shorten, T. M. Khoshgoftaar, "A Survey on Image Augmentation for Deep Learning," Journal of Big Data, Vol. 6, 2019. pp. 1-48.
- [29]. Darknet, YOLOv3, <https://pjreddie.com/darknet/yolo> (accessed: 2022)
- [30]. Darknet, YOLOv4, <https://github.com/AlexeyAB/darknet> (accessed: 2022)
- [31]. Facebook AI research, Detectron2, <https://github.com/facebookresearch/detectron2> (accessed: 2022)
- [32]. S. Ali, F. Zhou, A. Bailey, B. Braden, J.E. East, X. Lu, J. Rittscher, "A Deep Learning Framework for Quality Assessment and Restoration in Video Endoscopy", Medical Image Analysis, Vol. 68, 2021, pp.1-25.

Efficient segmentation and classification of the tumor using improved encoder-decoder architecture in brain MRI images

Original Scientific Paper

Archana Ingle

TSEC, University of Mumbai,
EXTC Department,
Mumbai, India
archana.ingle@thadomal.org

Mani Roja

TSEC, University of Mumbai,
EXTC Department,
Mumbai, India
maniroja@thadomal.org

Manoj Sankhe

MPSTME, NMIMS University,
EXTC Department,
Mumbai, India
Manoj.Sankhe@nmims.edu

Deepak Patkar

Nanavati Max Super Speciality Hospital,
Medical Services and Imaging Department,
Mumbai, India
drdppatkar@gmail.com

Abstract – Primary diagnosis of brain tumors is crucial to improve treatment outcomes for patient survival. T1-weighted contrast-enhanced images of Magnetic Resonance Imaging (MRI) provide the most anatomically relevant images. But even with many advancements, day by day in the medical field, assessing tumor shape, size, segmentation, and classification is very difficult as manual segmentation of MRI images with high precision and accuracy is indeed a time-consuming and very challenging task. So newer digital methods like deep learning algorithms are used for tumor diagnosis which may lead to far better results. Deep learning algorithms have significantly upgraded the research in the artificial intelligence field and help in better understanding medical images and their further analysis. The work carried out in this paper presents a fully automatic brain tumor segmentation and classification model with encoder-decoder architecture that is an improvisation of traditional UNet architecture achieved by embedding three variants of ResNet like ResNet 50, ResNet 101, and ResNext 50 with proper hyperparameter tuning. Various data augmentation techniques were used to improve the model performance. The overall performance of the model was tested on a publicly available MRI image dataset containing three common types of tumors. The proposed model performed better in comparison to several other deep learning architectures regarding quality parameters including Dice Similarity Coefficient (DSC) and Mean Intersection over Union (Mean IoU) thereby enhancing the tumor analysis.

Keywords: UNet, ResNet, ResNext, Deep Learning, Transfer Learning, CNN, Brain tumor Segmentation

1. INTRODUCTION

According to the published statistics from the American Society of Clinical Oncology Foundation, brain and other nervous system cancer is the 10th major reason for loss of life across the world. An estimated 308,102 individuals were detected with brain and nervous system cancer worldwide in 2020. Out of which, brain tumors alone account for 85% to 90% of all brain and nervous system cancer [1]. The brain is the complex and essential organ where all main functions of the human body like thought, speech, vision, and body activities are controlled. So as the tumor grows in the brain can affect these necessary activities. Specialists are taking efforts to learn about brain tumors and find the best treatment. To achieve the same, precise classification and tumor segmentation are necessary. Achieving

high-level accuracy for the exact determination of tumors for saving lives requires a great amount of research. Generally, the diagnosis begins with Magnetic Resonance Imaging (MRI), which is a non-invasive process. MRI is a preferred way over other scanning techniques as it provides detailed images of soft tissues, but the manual segmentation of its images is quite a time-consuming and very challenging task. With recent advancements in technologies to enhance tumor detection deep learning methods can be integrated with different imaging modalities. The result of these methods extremely relies upon the quality of the image [2]. Using the deep learning algorithms on MRI images, the analysis and accuracy can be enhanced to far better levels in very less time. So, there is a very wide scope and need for research in this area.

Generally, deep learning techniques are categorized into supervised and non-supervised techniques. Supervised learning requires a massive amount of dataset which helps in better generalization. It is challenging in the medical field to gather huge datasets with labels as annotation requires extensive time from medical experts with multiple expert judgments to overcome human error. Along with this, privacy and legal issues, data interoperability, and data standards are the major challenges in the healthcare system [3]. Overfitting is another major challenge wherein the model performs well on the training dataset as compared to the test dataset. To resolve this training should be done on a larger dataset. To address the scarcity of data the data augmentation technique is used to raise the dataset artificially from the existing training dataset by applying random transformations which provide a diversity of data available for the training model [4, 5]. A pretrained model on the large standard dataset can be utilized for the different tasks as a feature extractor with a comparatively lesser available dataset is known as transfer learning, which removes the need of having a large dataset for model training and also reduces long learning time [6]. Contributions to this work are:

Traditional UNet architecture is improved by embedding three architectures ResNet 50, ResNet 101, and ResNext 50. To the best of our knowledge, such a combination of architecture has never been used before for brain tumor segmentation which inherently has the advantage of UNet and ResNet architecture.

Exhaustive experimentation on different hyperparameters like gamma, learning rate, type of optimizer, batch size, and step size is done to tune them to the best value which ultimately results in enhancing the performance of the proposed architecture. Also, comparative analysis between three models is done for several epoch values.

The given model is also tested in real-time for segmenting brain tumor MRI images obtained especially from renowned Nanavati Max Super Speciality Hospital, located in Mumbai, India, which is best known for providing medical service for 70 years to people across India. The results obtained are also verified by the radiological experts of the hospital.

2. RELATED WORKS

Various authors proposed several architectures for the segmentation and classification of brain tumors listed and compared their performance on the Dice Similarity Coefficient (DSC) or Accuracy measure in Table 1. Since we require a labeled dataset, supervised techniques are used.

Sérgio Pereira et al. [7] implemented the hierarchical system for whole tumor segmentation and intratumoral tissue segmentation. Histogram standardization is used as preprocessing method and implemented fully CNN-based UNet. Leaky Rectifier Linear Unit is used as nonlinear activation.

Saddam Hussain et al. [8] proposed an input concatenated CNN architecture using two types of patch-based training. To avoid overfitting max-out and dropout layers are used. Image normalization and bias field correction is used for preprocessing and morphological operators are used for post-processing to remove small false positives.

Mohammad Havaei et al. [9] implemented various two-path cascaded architectures with concatenations at different stages by exploiting simultaneous extraction of local as well as global features. To tackle tumor label imbalance two-phase training process is used. The final fully connected layer is replaced by a convolutional layer that speeds up the segmentation procedure. The segmentation time of the brain varies between 25 seconds to 3 minutes.

Francisco Javier et al. [10] Proposed pixel-based classification with three different paths which are concatenated to give output out of four different classes through the fully connected layer. Overfitting is avoided by using elastic transformation as a data augmentation procedure.

Benjamin Maas et al. [11] proposed Two dimensional fully convolutional neural networks consisting of four encoders and decoders each. Skip connections like UNet architecture are employed at the encoder and decoder having similar spatial resolution. In the decoding stages, unpooling layers are used. To create a precise, consistent, and quicker network architecture for brain tumor segmentation it uses a modified cross-entropy loss function with an ADAM optimizer.

Mohamed Naser et al. [12] implemented a combined model for tumor segmentation, detection, and grading simultaneously of low-grade gliomas with Deep CNN using UNet with transfer learning from VGG-16. Rotation, zoom, shift, and horizontal flip are used as data augmentation techniques.

Mostefa et al. [13] Ensemble learning is used to develop a fully automatic deep learning model using incremental deep CNN with the advantage of GPU implementation. An efficient training method is implemented by considering the most important hyperparameters for best results.

Yongchao Jiang et al. [14] proposed an AIU-Net model. To improve network performance without adding extra parameters, receptive field expansion is done by adding Atrous convolution in the Inception module. It increases the depth and width of the architecture but has longer training and testing time. Residual connection is added for faster convergence between input and output.

Muhammad Sajjad et al. [15] implemented a computer-aided diagnosis system for tumor segmentation and classification using Deep CNN with extensive data augmentation techniques. Using a transfer learning approach pre-trained VGG-19 network is fine-tuned for

tumor classification. Two different datasets are used, and the accuracy achieved is compared which proves that the performance of the system is improved using data augmentation.

Amjad Rehman Khan et al. [16] used K means clustering to segment the region of interest and classification into benign or malignant by fine-tuning fully connected weights of VGG-19 with synthetic data augmentation.

Kang, J et. al [17] proposed a hybrid model for classification using pre-trained CNN and ML classifiers for deep feature extraction and tumor classification respectively. From exhaustive experimentation on several pre-trained CNN models, and ML classifiers on three datasets concluded with different combinations of these are better in the case of a smaller dataset with two classes, a large dataset with two classes, and a large dataset with four classes.

Zahid Ullah et al. [2] used a median filter, histogram equalization, and image conversion as preprocessing techniques for image enhancement. Discrete wavelet transform is used to extract features from enhanced images. From the proposed advanced deep neural network, human brain MRI images are classified as normal or pathological.

Table 1. Summarizes related work to brain tumor segmentation and classification

Author	CNN Architecture	Dataset	Performance Metric
S'ergio Pereira et al. 2016	Fully CNN-based UNet	BraTS 2013	DSC: 85%
Saddam Hussain et.al 2017	Input Concatenated CNN	BraTS 2013	DSC: 80%
Mohammad Havaei et.al 2017	two-path cascaded CNN	BraTS 2013	DSC: 88%
Francisco Javier et al. 2021	Three path output concatenation CNN	Nanfang Hospital	DSC: 82.8%
Benjamin Maas et al. 2021	Two dimensional CNN	Nanfang Hospital	DSC: 74.4%
Mohamed Naser et al. 2020	UNet	Private Data	DSC: 84%
Mostefa et al. 2018	Deep CNN	BraTS 2017	DSC: 88%
Yongchao Jiang et al. 2021	A-Inception based UNet	BraTS 2019	(Whole Tumor) DSC: 86.96% MIoU: 84.25%
Muhammad Sajjad et al. 2019	Deep CNN using extensive data augmentation	Radiopaedia Nanfang Hospital	Accuracy: 90.67% Accuracy: 94.58%
Amjad Khan et al. 2021	VGG-19	BraTS 2015	Accuracy: 94.06%

3. METHODOLOGY

3.1 DATASET

The dataset used is publicly available at figshare.com and Kaggle.com, which was presented by Cheng et al. [18]. The dataset is of 233 patients fetched from Nanfang Hospital, Guangzhou, and General Hospital, the Tianjing Medical University of China during the year 2005-2010. Dataset consists of 3064 T1 weighted improved contrast slices of three common types of tumors, Meningioma, Glioma, and Pituitary Tumor in sagittal, coronal, and axial views. Table 2 represents the number of slices with respect to the number of patients corresponding to each tumor type.

Table 2. Details of the Dataset

Dataset includes	Type of Tumors			Total
	Meningioma	Glioma	Pituitary	
Number of patients	82 patients	89 patients	62 patients	233 patients
Number of slices	708 slices	1426 slices	930 slices	3064 slices

3.2 PRE-PROCESSING

As CNN uses fewer pre-processing techniques as compared to other algorithms, data augmentation techniques are considered in pre-processing to improve the dataset and to avoid overfitting of the model and better generalization. Various data augmentation techniques like flipping, shifting, scaling, rotating, Grid and optical distortion, resizing, and random cropping on images are performed to increase data variability and flexibility. The dataset is randomly split into a training set, testing set, and validation set with the proportion of 0.80: 0.12: 0.08 respectively. With this proportion, the complete dataset is divided into a training set consisting of 2479 slices, a validation set consisting of 246 slices, and a test set consisting of 339 slices. During the training process, after every epoch, testing on the validation set is done to observe the model performance, by comparing the DSC score of the train and validation set. Here if they seem to divert from each other which eventually causes overfitting can be prevented by changing the model hyperparameters. The dataset images are in the size of 512x512. This size of the image is reduced to 128x128 before giving it as input to the architecture. The images are color normalized to have the intensities lying between 0 to 1 using batch normalization which ultimately causes a reduction in the bit depth hence reducing the processing time and cost.

3.3 NETWORK STRUCTURE

In the proposed system of tumor segmentation and classification, the type of tumor is identified, and also finds the exact location of the tumor in the given MRI images. To achieve this objective, improvised UNet architecture with embedded ResNet 50, ResNet 101, and

ResNext 50 is designed. UNet architecture is specifically designed for the segmentation of medical images with a small dataset and typically consists of encoding and decoding layers [19]. Instead of using traditional UNet encoding layers three variants of ResNet like ResNet 50, ResNet 101, and ResNext 50 are used. As shown in Fig. 1., the decoding layers are designed in such a way that they complement the encoding layers.

In the decoding layer, the upsampling is done through transpose convolution. Optimization is done using an ADAM optimizer with a learning rate of 1e-4 for training. Model is built on Kaggle using Python Programming Language. As a free resource, Kaggle is having execution time limitations and even cannot be run for larger epochs for experiments.

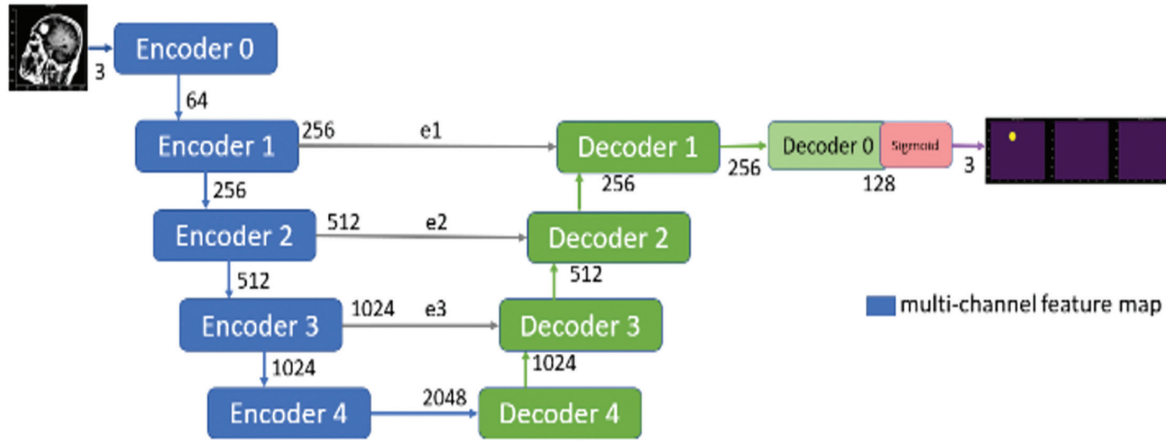


Fig. 1. Proposed modified UNet Architecture with ResNet/ResNext as a backbone architecture

4. EXPERIMENTS AND RESULT ANALYSIS

4.1 PERFORMANCE EVALUATION METRICS

For semantic segmentation to find the performance of the model the most popular metric is the Dice Similarity Coefficient (DSC). DSC is represented in Eq. (1) and computes spatial overlap between predicted segmentation and available ground truth to quantify the performance of image segmentation methods.

$$DSC = \frac{2|A \cap B|}{(|A| + |B|)} \quad (1)$$

Where A represents the ground truth and B represents the predicted segmentation. Metric values range between 0 and 1. 0 means no overlapping between predicted segmentation and available ground truth, while 1 means perfectly overlapping between predicted segmentation and available ground truth.

$$IoU = J(A, B) = \frac{|A \cap B|}{|A \cup B|} \quad (2)$$

Another most commonly used metric for the evaluation of a model is Jaccard Index or Intersection over Union (IoU) represented in Eq. (2). IoU is calculated as the area of overlap to the area of union between the predicted segmentation and available ground truth. The Mean IoU (MIoU) is calculated by taking an average of IoU of each class which is used in performance measurement in segmentation algorithms [20].

4.2 EXPERIMENT 1 (FOR HYPERPARAMETER TUNING)

The Deep Learning model has a set of parameters and hyperparameters. Parameters are updated at every backpropagation step using an optimization al-

gorithm. Hyperparameters need to be set for deciding model structure and training strategy. For manual finding evaluation of the best hyperparameters for the model is a difficult task. The first experiment is carried out by considering ResNet 101 as the backbone architecture for transfer learning with 10 epochs to decide on the proper tuning of hyperparameters like gamma, learning rate, optimizer, step size, and batch size to achieve the best performance. An epoch consists of a cycle to train complete data. The learning algorithm will work a number of times through the entire training dataset equal to a number of epochs.

4.2.1. Gamma

With 1e-4 learning rate, Adam Optimizer, 64 Batch Size, 80 Step Size training time required for various values of gamma are almost the same, and mean loss on the train (MLT) is minimum at gamma=0.1 is shown in Table 3. So, Gamma 0.1 is considered for further experiment as it also gives better metric values for individual tumor types as illustrated in Fig. 2(a).

Table 3. Comparison of training time and MLT for different values of Gamma

Gamma	Training Time	MLT
0.05	00:33:04	0.384912
0.075	00:32:56	0.371084
0.1	00:32:59	0.343684
0.15	00:32:43	0.344272
0.2	00:32:43	0.349402
0.75	00:33:16	0.47495

4.2.2. Learning rate

The most important hyperparameter to tune for best results is the learning rate. With gamma 0.1, Adam Optimizer, 64 Batch Size, and 80 Step Size extremely poor performance for very lower and higher values of learning rate is observed. Table 4 compares different metrics like MIoU, DSC and individual class dice score for Meningioma, Glioma, and Pituitary type of tumor (PT). It is observed that the learning rate 1e-4 gives better results with less training time. Very poor performance is observed for learning rates 1e-2 and 1e-5 are not considered for comparison as shown in Fig. 2 (b).

Table 4. Comparison of metrics for various learning rates

Learning Rate	MIoU	DSC	Meningioma	Glioma	Pituitary Tumor
1e-2	Very Poor Performance all readings zero				
1e-3	60%	59.88%	71.15%	57.38%	64.08%
1e-4	74%	73.69%	79.32%	66.85%	67.55%
1e-5	Very Poor Performance all readings zero				

4.2.3. Optimizer

For loss reduction, different optimizers of adaptive learning rate like Adam, Adagrad, RMSprop, and Adamax are tried for the selection of the best optimizer as shown in Table 5. Adam optimizer gives the best results as illustrated in Fig. 2(c) with a similar mean loss in train and training time as compared to other optimizers.

Table 5. Comparison of metrics for various optimizers

Optimizer	MIoU	DSC	Meningioma	Glioma	Pituitary Tumor
Adam	74%	73.69%	79.32%	66.85%	67.55%
Adagrad	15%	15.14%	33.04%	26.87%	17.43%
RMS Prop	72%	71.59%	77.27%	64.74%	80.29%
Adamax	55%	54.81%	55.79%	49.67%	37.08%

4.2.4. Batch size

A number of samples used to make predictions that are compared with expected output variables to calculate error is known as Batch size.

Table 6. Comparison of metrics for different batch size

Batch Size	MIoU	DSC	Meningioma	Glioma	Pituitary Tumor
8	71%	70.83%	86.30%	60.70%	76.34%
16	71%	70.68%	83.26%	61.43%	66.47%
32	76%	75.79%	82.01%	68.30%	76.74%
64	74%	73.69%	79.32%	66.85%	67.55%

A large batch size decreases the quality of the model to generalize while requiring more memory space and

too small batch size makes learning too stochastic. In this experiment batch sizes, 32 and 64 give better metric values on the test dataset as shown in Table 6 and graphically illustrated in Fig. 2 (d). A batch size greater than 64 is not supported by available resources.

4.2.5. Step size

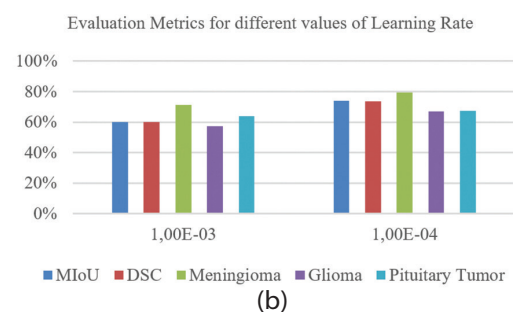
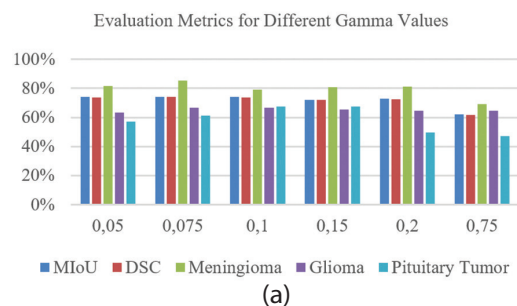
Step size consists of several iterations required to train the complete available dataset. Step size varies concerning batch size for the training process. For batch size 64, step size 80 gives a maximum MIoU of 74% shown in Fig. 2(e) and for batch size 32, step size 240 gives a maximum MIoU of 77% shown in Fig. 2(f) as listed in Table 7 and Table 8 respectively.

Table 7. Comparison of metrics for different step sizes with batch size 64

Step Size	MIoU	DSC	Meningioma	Glioma	Pituitary Tumor
20	67%	67.07%	76.97%	63.31%	60.50%
40	70%	70.02%	81.59%	65.79%	56.61%
60	62%	61.55%	72.91%	65.86%	39.81%
80	74%	73.69%	79.32%	66.85%	67.55%
120	73%	73.04%	77.91%	68.68%	70.34%
150	71%	71.00%	83.69%	64.47%	61.11%

Table 8. Comparison of metrics for different step sizes with batch size 32

Step Size	MIoU	DSC	Meningioma	Glioma	Pituitary Tumor
120	73%	72.76%	83.15%	64.76%	68.13%
180	73%	73.32%	82.08%	66.44%	77.49%
240	77%	76.70%	86.48%	69.01%	79.91%
280	72%	71.70%	83.13%	67.88%	70.52%
320	73%	73.14%	83.51%	64.52%	77.04%
360	72%	72.02%	84.54%	65.29%	79.02%



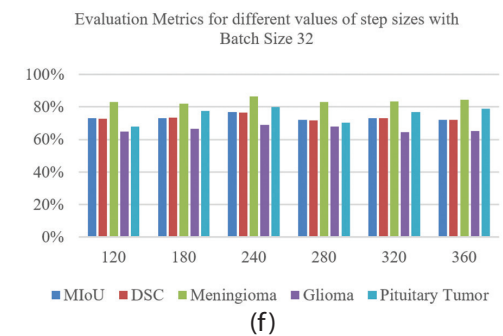
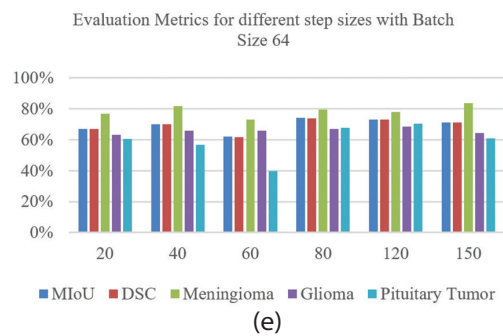
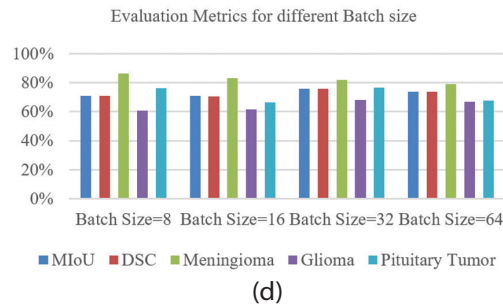
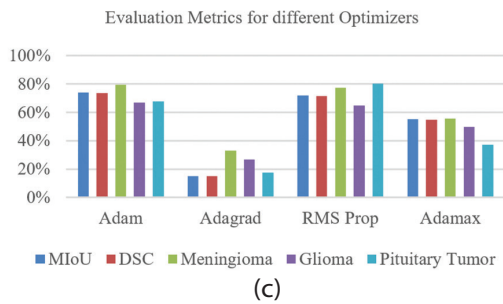


Fig. 2. Comparison of Evaluation Metrics for Hyperparameter Tuning using ResNet 101 as the backbone for UNet with 10 Epochs, for different: (a) Gamma (b) Learning Rate (c) Optimizer (d) Batch Size (e) Step Size with Batch Size 64 (f) Step Size with Batch Size 32

4.3 EXPERIMENT 2 (FOR LARGER STEP SIZE)

From the results of the first experiment, the second experiment is designed for ResNet 101 with batch size 32 and step size 240 considering gamma 0.1, learning rate as $1e-4$ using ADAM optimizer for 10, 20, 30, 50, and 100 epochs as shown in Table 9. With different values of epochs, metric performance is not improved as expected as illustrated in Fig. 3

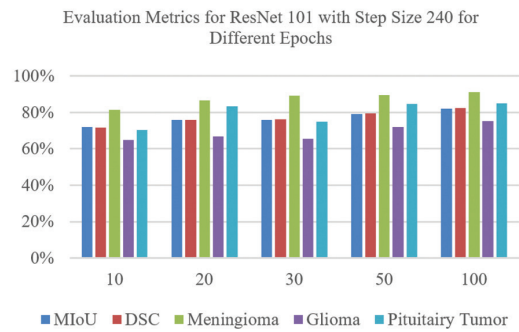


Fig. 3. Comparison of Evaluation Metrics for ResNet 101 with step size 240 for a different number of epochs

Table 9. Comparison of metric values for ResNet101 with step size 240 for a different number of epochs.

Epochs	MIOU	DSC	Meningioma	Glioma	Pituitary Tumor
10	72%	71.64%	81.37%	64.80%	70.25%
20	76%	75.94%	86.59%	66.86%	83.44%
30	76%	76.04%	89.29%	65.44%	75.04%
50	79%	79.33%	89.53%	71.99%	84.75%
100	82%	82.32%	91.23%	75.24%	85.10%

Table 10. Comparison of proposed architectures

Network	Backbone architecture	Number of Convolutional layers	Training Time in hours (for 100 epochs)
ResUNet1	ResNet50	53	03:59:49
ResUNet2	ResNet101	104	05:27:13
ResUNet3	ResNext50	53	07:35:30

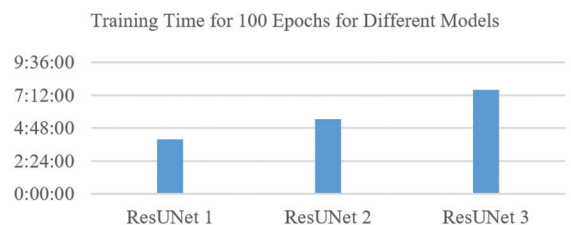


Fig. 4. Comparison of Training Time for different models evaluated at 100 epochs

4.4 EXPERIMENT 3 (COMPARISON OF BRAIN TUMOR SEGMENTATION AND CLASSIFICATION USING DIFFERENT MODELS)

These architectures as listed in Table 10, experimented with 10, 15, 20, 30, 50, and 100 epochs. It is observed that we must increase the number of epochs to reduce the mean loss on training to improve on metrics like DSC and MIOU, while training time goes on increasing. ResUNet2 and ResUNet3 for 100 epochs give maximum MIOU of 85% and 84% respectively as listed in Table 11. While training time required for ResUNet3 is very huge as compared to ResUNet2 as illustrated in Fig. 4. From

Fig. 5, ResUNet2 for 100 epochs should be preferred with a DSC of 83.69% and Mean IoU of 85%. Fig. 6. Illustrates how the proposed architecture reached very fast to its maximum performance and demonstrates consistency between training DSC score, validation DSC score, and loss. Due to hardware and time limitations on the Kaggle model with ResNext 101 using batch size 64 is not able to execute even for 10 or lesser epochs. A model with ResNext 101 executed with batch size 32 is not further evaluated due to the very large training time as compared with other models for 10 epochs.

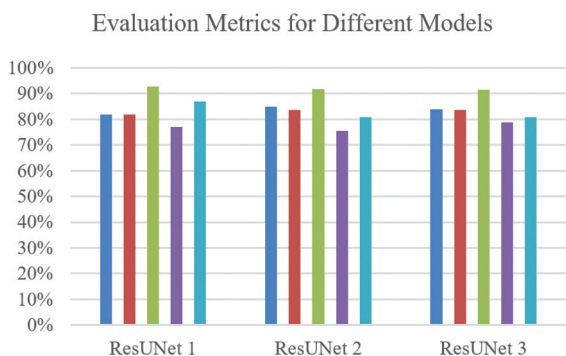


Fig. 5. Comparison of Evaluation Metrics for different models

Evaluation metrics are determined for three types of tumors namely Meningioma, Glioma, and Pituitary Tumor. Comparative analysis is presented in Table 12 for evaluating the effectiveness of the proposed model. It is evident from Table 12 that the proposed ResUNet 2 architecture outperforms other existing models on the same dataset in terms of DSC and Mean IoU.

Table 11. Comparison of metric values for different models

Different Models	MIoU	DSC	Meningioma	Glioma	Pituitary Tumor
ResUNet1	82%	81.84%	92.81%	77.18%	87.02%
ResUNet2	85%	83.69%	91.67%	75.45%	80.91%
ResUNet3	84%	83.68%	91.42%	78.87%	80.81%

Visual results of our model performance for three types of tumors are shown in Fig. 7. Tumor is segmented and classified for random test samples for Meningioma, Glioma, and Pituitary Tumor. The region detected is shown in yellow and it is compared with the ground truth available. The images of brain tumors acquired from Nanavati Super Speciality are applied to the proposed Model ResUNet2 trained on the online available dataset using Command Line Interface (CLI). Segmentation results and performance obtained are verified and demonstrated in Fig. 8. Execution time at different instances varies between 14 to 20 seconds.

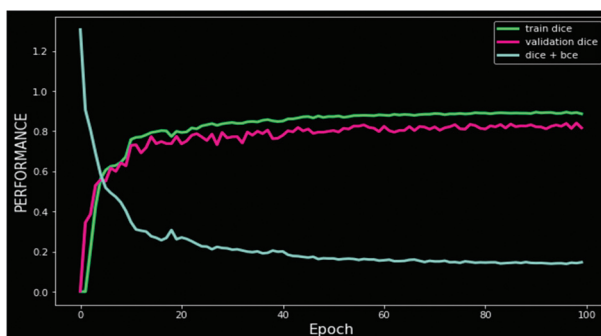


Fig. 6. Proposed architecture performance

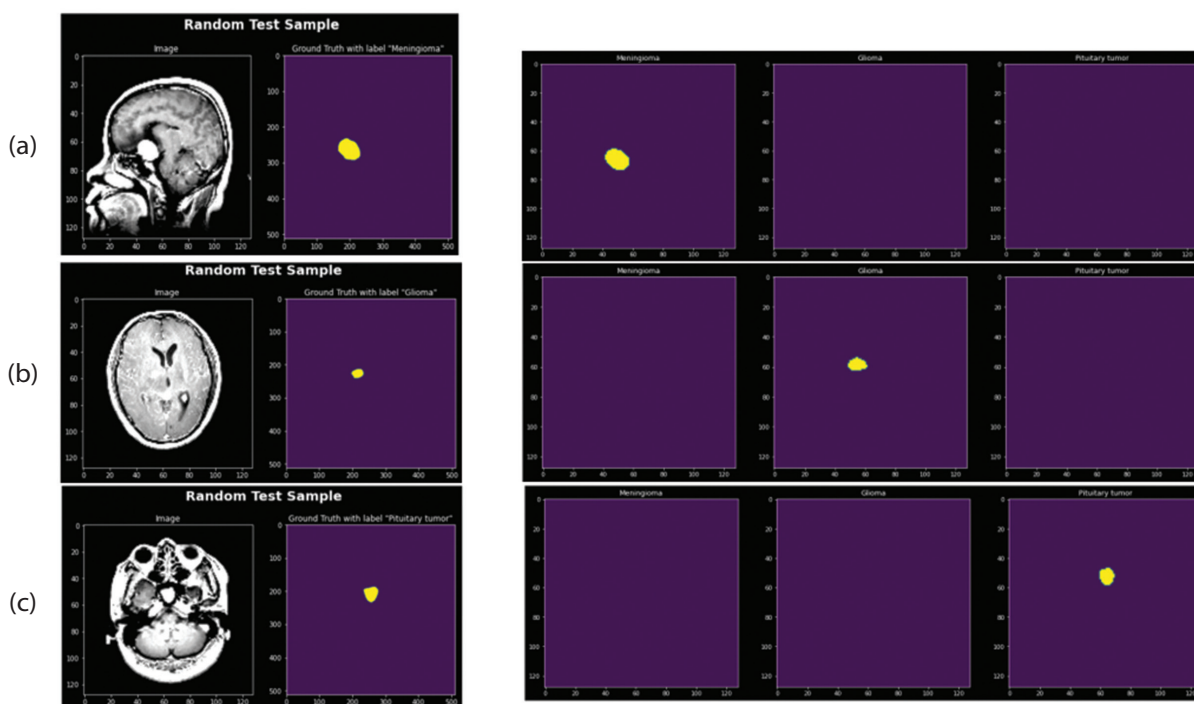


Fig.7. Ground truth versus Segmented and classified image for (a) Meningioma (b) Glioma and (c) Pituitary Tumor

Table 12. Comparison of proposed architecture with other architectures evaluated on same data

Author/ Architecture	DSC	Mean IoU
Francisco Javier et. al. [10] Multi-pathway CNN 2021	82.8%	-
Benjamin Maas et. al [11] Quick Tumor Net 2021	74.4%	-
Zahra Sobhaninia et. al [21] 2018 Single LinkNet for all directions	73%	-
Zahra Sobhaninia et. al [21] 2018 Separately trained Linknet networks for each direction	76%	-
Zahra Sobhaninia et. al. [22] 2020 Cascaded Dual-Scale LinkNet	80.03%	-
Ahmad Thias et.al. [23] 2019 morphological geodesic active contour (MGAC)	-	72.66%
Proposed Architecture (ResUnet2)	83.69%	85%

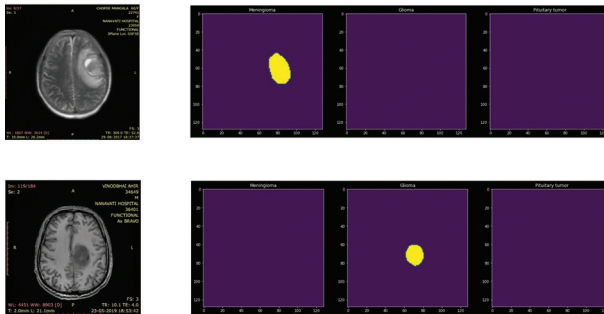


Fig. 8. Segmentation of Brain Tumor images obtained from Nanavati Super Speciality Hospital

5. RESULTS DISCUSSION

Proposed an improved UNet architecture by embedding three architectures ResNet 50, ResNet 101, and ResNext 50 which inherently has the advantage of UNet and ResNet architecture. Also, Various data augmentation techniques on images are performed to increase data variability and flexibility. A Pre-trained model helps in a significant reduction in training time because it just needs to fine-tune the weights of the model instead of learning them from scratch.

The experimental results were obtained for tumor segmentation and classification on the tumor dataset. The first experiment is designed for proper tuning of hyperparameters which helps in finding suitable hyperparameters like gamma, learning rate, type of optimizer, batch size, and step size. With extensive experimentation, we settle to gamma as 0.1, 1e-4 as learning rate, Adam optimizer for batch size 32 or 64 with a number of step sizes to train model through the available dataset. In the second experiment, performance is evaluated for backbone ResNet101 on batch sizes 32 and 64. Though batch size 32 with step size 240 gives the best MIoU 77% for 10 epochs, performance is not improved as we increase epochs towards 100. From the analysis of the first two experiments, we concluded

that the best batch size is 64 with step size 80. The third experiment shows and compares the effectiveness of the use of transfer learning with ResNet 50, ResNet 101, and ResNext 50 in segmentation using deep learning. From the analysis of this experiment, ResUnet2 gives the best results in important performance evaluation metrics with average training time. ResUnet2 gives a Mean Test DSC Score of 83.69% and a Mean IoU Test of 85% which is significantly better than existing methods. A maximum number of slices present in glioma type of tumor, but MRI images obtained from these scans are having variation in intensities throughout the dataset, because of this, the DSC score obtained for meningioma and pituitary type of tumor is better as compared to glioma type of tumor. The best-pretrained model is used for the segmentation of tumor images obtained from Nanavati Super Speciality Hospital, the same validated by expert radiologists. The average execution time is 17 seconds.

6. CONCLUSION

In this paper, we proposed a unique fully automatic encoder-decoder architecture for brain tumor segmentation and classification which lead to better results and is a step ahead of improvisation over basic UNet architecture. The three extensive experiments with three proposed architectures on a publicly available MRI dataset were executed and tested through standard performance metrics and compared with previously published results on the same dataset, the best performance was achieved using ResNet2 architecture for 100 epochs with freely available resources with Dice Similarity Coefficient of 83.69% and Mean Intersection over Union of 85% and thereby assisting in better tumor analysis.

7. REFERENCES:

- [1] "Types of Cancer, Brain tumor", Brain Tumor: Statistics, <https://www.cancer.net/cancer-types/brain-tumor/statistics> (accessed: 2022)
- [2] Z. Ullah, M. Farooq, S. Lee, D. An, "A hybrid image enhancement based brain MRI images classification technique", Medical Hypotheses, Vol. 143, 2020.
- [3] M. Razzak, S. Naz, A. Zaib, "Deep Learning for Medical Image Processing: Overview, Challenges and Future", Book on Classification in BioApps, SpringerLink, 2017, pp 323-350.
- [4] A. Buslaev, V. Iglovikov, E. Khvedchenya, A. Parinov, M. Druzhinin, A. Kalinin, "Albumentations: Fast and Flexible Image Augmentations", Information, Vol. 11, No. 2, 2020.
- [5] A. Krizhevsky, I. Sutskever, G. Hinton, "ImageNet Classification with Deep Convolutional Neural

- Networks", *Communications of the ACM*, Vol. 60, No. 6, 2017, pp. 84-90.
- [6] J. Wacker, M. Ladeira, J. Nascimento, "Transfer Learning for Brain Tumor Segmentation", arXiv:1912.12452v2, 2019.
- [7] S. Pereira, A. Pinto, V. Alves, and C. Silva, "Brain Tumor Segmentation Using Convolutional Neural Networks in MRI Images", *IEEE Transactions on Medical Imaging*, Vol. 35, No. 5, 2016, pp. 1240-1251,
- [8] S. Hussain, S. Anwar, M. Majid, "Brain Tumor Segmentation using Cascaded Deep Convolutional Neural Network", *Proceedings of the Annual International Conference of the IEEE Engineering in Medicine and Biology Society, Jeju, Korea, 11-15 July 2017*, pp. 1198-2001.
- [9] M. Havaei, A. Davy, D. Warde-Farley, A. Biard, A. Courville, Y. Bengio, C. Pal, P. Jodoin, H. Larochelle, "Brain tumor segmentation with Deep Neural Networks", *Medical Image Analysis*, Vol. 35, 2017, pp.18-31
- [10] F. Pernas, M. Martínez-Zarzuela, M. Antón-Rodríguez, D. González-Ortega, "A Deep Learning Approach for Brain Tumor Classification and Segmentation Using a Multiscale Convolutional Neural Network", *Healthcare*, Vol. 9, 2021, pp. 1-14.
- [11] B. Maas, E. Zabeh, S. Arabshahi, "QuickTumorNet: Fast Automatic Multi-Class Segmentation of Brain Tumors", *Proceedings of the International IEEE/EMBS Conference on Neural Engineering, Italy, 4-6 May 2021*, pp.81-85.
- [12] M. Naser, M. Deen, "Brain tumor segmentation and grading of lower-grade glioma using deep learning in MRI images", *Computers in Biology and Medicine*, Vol. 121, 2020.
- [13] M. Naceur, R. Saouli, M. Akil, R. Kachouri, "Fully Automatic Brain Tumor Segmentation using End-to-End Incremental Deep Neural Networks in MRI images", *Computer Methods and Programs in Biomedicine*, Vol. 166, 2018, pp. 39-49.
- [14] Y. Guan, M. Aamir, Z. Rahman, A. Ali, W. Abro, Z. Dayo, M. Bhutta, Z. Hu, "A framework for efficient brain tumor classification using MRI images", *Mathematical Biosciences and Engineering*, Vol. 18, No. 5, 2021, pp. 5790-5815.
- [15] A. Sajjad, S. Khan, M. Khan, W. Wu, A. Ullah, S. Baik, "Multi-Grade Brain Tumor Classification using Deep CNN with Extensive Data Augmentation", *Journal of Computational Science*, Vol. 30, 2019, pp. 1-13.
- [16] A. Khan, S. Khan, M. Harouni, R. Abbasi, S. Iqbal, Z. Mehmood, "Brain tumor segmentation using K-means clustering and deep learning with synthetic data augmentation for classification", *Wiley Periodicals LLC*, 2021, pp. 1-11.
- [17] J. Kang, Z. Ullah, J. Gwak, "MRI-Based Brain Tumor Classification Using Ensemble of Deep Features and Machine Learning Classifiers", *Sensors*, Vol. 21, 2022.
- [18] J. Huang, S. Cao, R. Yang, W. Yang, Z. Yun, Z. Wang, Q. Feng, "Enhanced Performance of Brain Tumor Classification via Tumor Region Augmentation and Partition", *PLOS ONE*, 2015.
- [19] O. Ronneberger, P. Fischer, T. Bro, "U-net: Convolutional networks for biomedical image segmentation", *Proceedings of the International Conference on Medical image computing and computer-assisted intervention*, 2015, pp. 234-241.
- [20] S. Minaee, Y. Boykov, F. Porikli, A. Plaza, N. Kehtarnavaz, D. Terzopoulos, "Image Segmentation Using Deep Learning: A Survey", *IEEE Transactions Pattern Analysis and Machine Intelligence*, Vol. 44, No. 7, 2021, pp. 3523-3542.
- [21] Z. Sobhaninia, S. Rezaei, A. Noroozi, M. Ahmadi, H. Zarrabi, N. Karimi, A. Emami, S. Samavi, "Brain Tumor Segmentation Using Deep Learning by Type Specific Sorting of Images", arXiv:1809.07786v1, 2018.
- [22] Z. Sobhaninia, S. Rezaei, N. Karimi, A. Emami, S. Samavi, "Brain Tumor Segmentation by Cascaded Deep Neural Networks Using Multiple Image Scales", *Proceedings of the 28th Iranian Conference on Electrical Engineering*, 2020.
- [23] A. Thias, A. Mubarak, A. Handayani, D. Danudirdjo, T. Rajab, "Brain Tumor Semi-automatic Segmentation on MRI T1-weighted Images using Active Contour Models", *Proceedings of the International Conference on Mechatronics, Robotics and Systems Engineering, Bali, Indonesia, 4-6 December 2019*, pp. 217-221.

An improved Gaussian Mixture Model with post-processing for multiple object detection in surveillance video analytics

Original Scientific Paper

Fancy Joy

Department of Computer Science
Sri Ramakrishna College of Arts and Science, Coimbatore
fancyjoy1@gmail.com

V. Vijayakumar

Department of Computer Science
Sri Ramakrishna College of Arts and Science, Coimbatore
Veluvijay20@gmail.com

Abstract – Gaussian Mixture Model (GMM) is an effective method for extracting foreground objects from video sequences. However, GMM fails to detect the object in challenging scenarios like the presence of shadow, occlusion, complex backgrounds, etc. To handle these challenges, intrinsic and extrinsic enhancement is required in traditional GMM. This paper presents a novel framework that combines improved GMM with postprocessing for multiple object detection. In the proposed system, GMM with parameter initialization is considered an intrinsic improvement. Video preprocessing and postprocessing are considered extrinsic improvements. Integration of morphological operation with GMM helps for better segmentation than traditional GMM, and it also helps to increase detection performance by reducing false positives. Video preprocessing is the process of noise removal that prepares input video ready for further processing. In the final step gradient of morphological operations is used for postprocessing. The proposed approach was tested on challenging surveillance video sequences from benchmark datasets such as PETS 2009 and CD 2014(Change Detection). The experimental results are compared using ground truth and performance evaluation metrics. The results show that the proposed approach performs better than GMM, and the method can detect the object effectively even in illumination variation and partial occlusion.

Keywords: gaussian mixture model, background subtraction, multiple object detection, postprocessing

1. INTRODUCTION

In this era, video surveillance systems have a prime role in implementing public safety and security. Even though intelligent surveillance analytics systems exist, peoples still rely on humans for monitoring surveillance systems. The object detection process in surveillance video plays a significant part in video analytics. In this real-world, detection of objects has a wide variety of applications, such as theft detection, street monitoring, intruder detection, traffic monitoring etc. [1]. The significant challenges involved in object detection are the sudden illumination variation [2], presence of shadow, long-term occlusion [3], and dynamic background due to natural phenomena (wind, rain, moving trees etc.) [4]. An intelligent surveillance system requires an efficient object detection approach to segment the foreground from the background. The main objective of the proposed method is to integrate the

proposed approach with the surveillance system for object detection without human intervention. This paper presents a robust object detection method that can apply in real-world scenarios. The technique uses the Gaussian Mixture Method (GMM) [5] with updated parameters and gradient filter technique as advanced filtering. This approach can detect the object in surveillance videos even with challenging scenarios.

A simplified block diagram of the proposed method shows in Fig.1. The proposed approach introduces a hybrid object detection framework that consists of video preprocessing, background subtraction and postprocessing. GMM has been chosen here as the backbone for detection. Background subtraction uses the gaussian mixture method (GMM) to determine the background from video frames, which helps to segment the foreground object from the background model. The approach modifies the GMM by integrating both intrinsic and extrinsic enhancement.

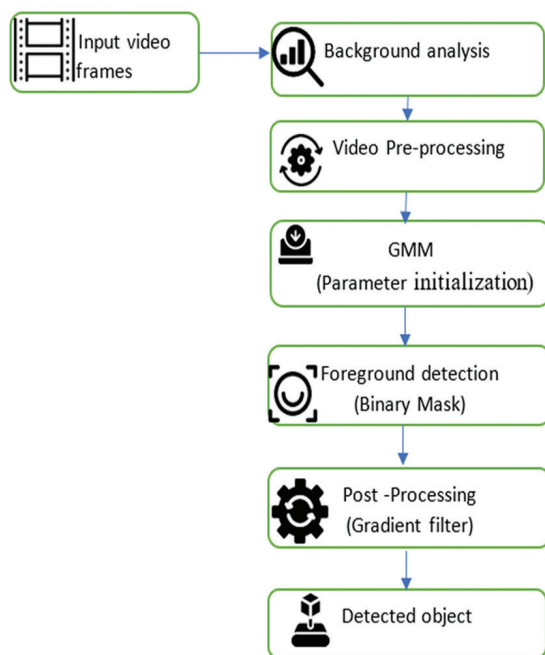


Fig. 1. Block diagram of proposed gradient GMM for object detection

Here GMM with parameter initialization technique as intrinsic improvements. Both preprocessing and postprocessing parts consider extrinsic modifications. GMM initializes its parameters by performing the histogram analysis of training frames. Preprocessing video frames is an essential task that makes the video frames noise-free and ready for advanced processing like detection and tracking. The proposed method uses a bilateral edge-preserving method for preprocessing. Advanced filtering is one of the relevant tasks in proposed GMM-based object detection. A gradient-based morphological filter introduces here, which helps effectively segment objects from the background. The postprocessing phase applies an advanced filter in segmented results from the gaussian mixture model (GMM) and boosts the detection of multiple objects more accurately. In most challenging scenarios, background subtraction and segmentation play a vital role in GMM-based object detection.

The significant contribution of this paper is a fast and improved method for object detection in surveillance monitoring with an advanced filtering process. Advanced filtering introduces a gradient filter mechanism for better segmentation. Hence, the proposed method can detect foreground objects efficiently in various challenging scenarios. The rest of the paper organizes as follows: Section 2 examines the literature regarding object detection and the proposed method discussed in section 3. Section 4 presents the experimental results, and the conclusion is in section 5.

2. REVIEW OF LITERATURE

Object detection is one of the major research areas in computer vision. The simplest method for object

detection is background subtraction. Background subtraction includes deriving a background reference image for a video, subtracting each new video frame from the reference image and outputting the result [6]. Many researchers have focused on background subtraction methods to deal with different challenges in object detection. Background estimation, kernel density estimation, subspace learning, background clustering and statistical models are some background modelling methods. Statistical models maintain an excellent balance between performance and computational cost. Gaussian Mixture model [6], kernel density estimation [7] and subspace learning [4] are the commonly used statistical models. Subspace learning methods work with the idea of dimensionality reduction [4] and perform well in varying illumination. Kernel density estimation [7] uses the kernel function to estimate the density of pixels. Gaussian Mixture Model is the most used background subtraction approach. Some researchers improved the GMM to handle the challenges faced by the video surveillance system. The following part reviews various background subtraction approach based on Gaussian Mixture Model and its variations.

Stauffer and Grimson [5] introduced adaptive background mixture models for real-time tracking. This method models each pixel as a mixture of Gaussians and updates the model with an online approximation. The authors also discussed learning patterns of activity used in real-time tracking [8]. The main drawback of their method was that approach learns very slowly in the beginning. To overcome the limitation of the above technique, KaewTraKulPong and Bowden [6] improved the adaptive background mixture model with shadow detection. They applied the expectation-maximization method to update the parameters of the existing GMM. But this method also suffers a slow learning rate.

Lee[9] presented adaptive learning rate-based GMM for background subtraction. A dynamic learning rate helps the GMM to achieve convergence faster. The method shows better performance, but it takes more computational time. Zivkovic and Heizden [10] suggested adaptive Gaussians to each pixel to improve GMM. This approach achieves fast execution than GMM. Its single learning nature causes an increased number of false positives and false negatives. Shah et al. [11] also built an adaptive local learning rate for GMM. They proved that this method is efficient in both memory and time, but it is computationally expensive due fixed number of Gaussians. Shah et al. [12] again modify the GMM with an adaptive learning rate. The method derived the learning rate from the dynamic nature of the image. The algorithm uses YUV color space and SURF features for better segmentation. R. Chavan et al. [13] modified GMM by parameter tuning. The authors used EIR with the expectation-maximization algorithm to choose the value for parameters such as threshold and learning rate. The method performs better detection in the dynamic background with sudden illumination variation.

Del Blanco et al. [14] used GMM with postprocessing to improve detection accuracy. They used parametric background subtraction for detecting moving regions in video data. Estimating and fitting ellipses apply here as postprocessing to refine the foreground. Pathan et al. [15] proposed a Gaussian mixture model with a median filter and morphological operation for moving object detection. The method assures complete detection of moving objects. Chen and Ellis [16] improved the gaussian mixture model with varying learning rates and the number of Gaussians. The authors proved that the approach performs well in illumination variation and dynamic background.

Fradi and Dugelay [17] proposed a new approach based on incorporating on uniform motion model into GMM background subtraction. The authors combined improved GMM background subtraction with a uniform motion model and proposed a single framework. The approach has improved accuracy even in complex backgrounds. Video object detection based on GMM was discussed by Fu and Wang [18]. They introduced the combination of foreground and background gaussian distribution for efficient segmentation.

Xiaofeng Lu and Caidi Xu[19] built an improved gaussian mixture model based on mean block images. The approach improves accuracy using a wavelet-based denoising method with a semi-soft threshold used in the foreground detection stage. The author's used mean images of image blocks as background modelling and wavelet-based denoising for foreground detection to improve the speed of GMM.

Chen et al. [20] developed a spatiotemporal gaussian mixture model based on pixel hierarchy. The method used optical flow, spanning trees and super-pixel segmentation. The approach worked well even with sudden or frequent changes in pixel values. Ghedia and Vithalani [21] modified the GMM with parameter initialization and adaptive thresholding. They used intrinsic and extrinsic improvements to GMM for efficient object detection.

From the literature reviews, it is clear that the Gaussian Mixture model requires both intrinsic and extrinsic improvements. Intrinsic improvements aim the parameter optimization and tuning. Extrinsic enhancement such as preprocessing and postprocessing reduces the noise and improves the performance of detection. Hence both intrinsic and extrinsic modification to the GMM is required.

3. PROPOSED METHOD

The proposed object detection method has a hybrid object detection method that uses modified GMM. The gaussian mixture model is the flexible foreground detection approach introduced by Stauffer et al. [8]. To handle the multimodality of the background, the GMM represents each frame pixel using a mixture of normal distributions. GMM first generate the background

model and then subtracts the background model from the current frame pixel-by-pixel. Surveillance video background may vary due to various constraints such as illumination, presence of shadow, dynamic background etc. The intrinsic and extrinsic enhancement makes the GMM that handle different conditions. Modified GMM depicts in Fig 2. The proposed object detection method has a hybrid framework that consists of preprocessing, object detection and postprocessing. Preprocessing and postprocessing are extrinsic improvements. Here parameter initialization of the GMM is the intrinsic modification.

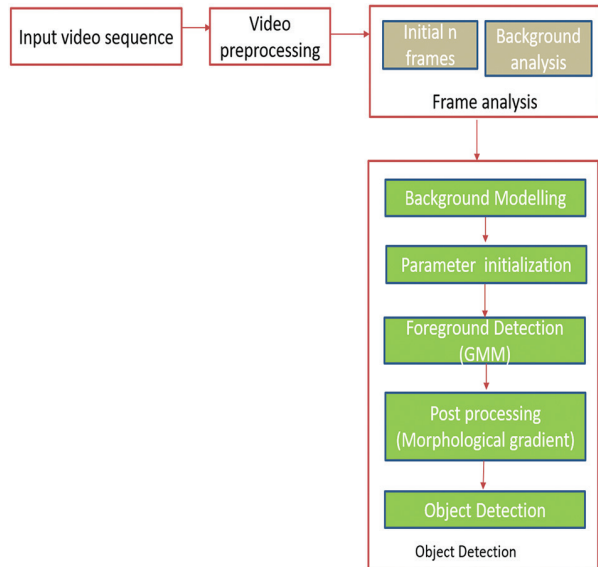


Fig. 2. Proposed Gradient GMM approach

3.1. PRE-PROCESSING

Pre-processing is one of the significant tasks in video processing. Video pre-processing improves the quality of video frames, thereby reducing or eliminating noise. Hence it can increase the performance of further video processing applications such as object detection, tracking and monitoring etc. In the proposed system bilateral filter is used for preprocessing. A bilateral filter converts the video frames into a smoother version by removing noise and fine details[22]. The main advantage of this filter is that it can preserve the edges of objects without blurring.

Let 'I' be the input image, then the bilateral filter output image I^{filtered} is defined as

$$I^{\text{filtered}}(q) = \frac{1}{w_s} \sum_{q_i \in \rho} I(q_i) r_k (\| I(q_i) - I(q) \|) s_k (\| q_i - q \|) \quad (1)$$

Here the intensity values of each pixel in the input image are replaced with a weighted average of intensity values of the adjacent pixel. The bilateral filter uses spatial and range kernel intensity values to preserve the sharp edges. In the equation w_s denotes weight normalization and can be defined as

$$w_s = \sum_{q_i \in \rho} r_k (\| I(q_i) - I(q) \|) s_k (\| q_i - q \|) \quad (2)$$

Here I and $I^{filtered}$ indicate input image and filtered image respectively and q' denotes the coordinates of the current pixel to be filtered. ρ indicates the window that is centred in q i.e. $q \in \rho$ refers to another pixel in the image. r_k is the range kernel, which performs smoothing differences in intensities of pixels. s_k is the spatial kernel which performs smoothing differences in spatial coordinates of pixels[22].

3.2. OBJECT DETECTION

Object detection in the proposed system divides into two tasks: frame analysis with parameter initialization and background subtraction. The flowchart of frame analysis with parameter initialization depicts in figure 3. This step analyzes the initial training frames of the video dataset. Analyze various frame intensities using histogram analysis to understand the nature of the background and declare the set of parameter vectors according to it. Here the approach considers two significant parameters: α (learning rate) and T (threshold). Here α is the learning constant for background subtraction, and T is the threshold, which means the minimum proportion of the frame that regards the background. Initial training using GMM started using default parameters and then compares its binary mask results with ground truth. If the parameter gives a better result, initialize the GMM with the same α and T or check the next set of parameters. Repeat the steps until the final set of parameter values. Histogram analysis and background model comparison use here to choose the parameters for a particular dataset.

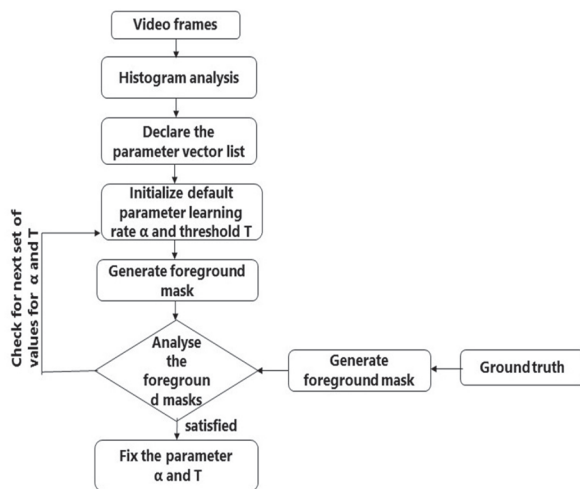


Fig. 3. Flowchart of frame analysis with parameter initialization

The significant task in this object detection step is background subtraction. For background subtraction, the proposed method uses a statistical probability-based approach. Gaussian Mixture Model (GMM) is the widely used background subtraction method. Here probability density function of the gaussian mixture model is used to represent each pixel of video frames. GMM used a mixture of gaussian distribution to model

the $\{Q_1, Q_2, \dots, Q_s\}$ of each pixel. To model the history of each pixel, GMM uses the mixture of K Gaussian distribution.

The probability of the current pixel is represented as

$$P(Q_s) = \sum_{i=1}^K w_{i,s} * \eta(Q_s, \mu_{i,s}, \Sigma_{i,s}) \quad (3)$$

Where

K - number of gaussian distribution

$w_{i,s}$ - weight of i^{th} gaussian in the mixture at time s

$\mu_{i,s}$ -mean of pixel intensities

$\Sigma_{i,s}$ -covariance matrix of pixel intensities

η refers the gaussian probability density function which is defined by

$$\eta(Q_s, \mu_{i,s}, \Sigma) = \frac{1}{\frac{1}{m} e^{-1/2(Q_s - \mu_s)^T \Sigma^{-1} (Q_s - \mu_s)}} \quad (4)$$

Here $w_{i,s}$ can be defined as

$$w_{i,s} = (1 - \alpha)w_{i,s} + \alpha(\mu_{i,s}) \quad (5)$$

Where α is the learning rate and $\mu_{i,s}$ is the mean value. Every new pixel Q_{s+1} is compared against the previous K gaussian distribution of the pixel until a match is found. Mean μ is set to 1 if the background model matches otherwise μ assigned to 0.

$$\mu_{i,s} = \begin{cases} 1, & \text{If the background model matches} \\ 0, & \text{otherwise} \end{cases} \quad (6)$$

If the distribution is found unmatched then the μ_s and σ_s^2 parameters remain the same. If the distribution finds a match, then the parameters μ_s and σ_s^2 are updated based on previous distribution values.

$$\mu_s = (1 - \rho)\mu_{s-1} + \rho(Q_s) \quad (7)$$

$$\sigma_s^2 = (1 - \rho)\sigma_{s-1}^2 + \rho(Q_s - \mu_s)^T (Q_s - \mu_s) \quad (8)$$

Where ρ is the second learning rate. It can be represented as

$$\rho = \alpha \eta\left(\frac{Q_s}{\mu_i}, \sigma_i\right) \quad (9)$$

The primary step in every background subtraction model is background modelling. This step compares the current frame to the background frame and then classifies the pixels as foreground and background. Here the first 'M' distribution is used for background modelling. 'M' can be defined as

$$M = \operatorname{argmin}_m \left(\sum_{i=1}^m w_i > T \right) \quad (10)$$

Where T is the threshold value, which is the measure of the minimum portion of data that should be considered as background.

3.3. POST-PROCESSING

The vital role in the proposed architecture lies in the postprocessing phase. Gradient morphological operations use here to process the video frames according to their shapes. There are mainly two kinds of morphological operations; dilation and erosion. The structuring element is the essential element of both dilation and erosion. The structuring element is a matrix that processes the pixel of the image and its neighbourhood.

Dilation operation adds the pixel to an image boundary, whereas erosion removes the pixel from the image boundary[21]. In this morphological gradient operation, the gradient is the difference between dilation and erosion of the image. The gradient operation of an image results in the contrast intensity in adjacent pixels, which will help for better segmentation and edge detection of an object. Hence the integration of gradient operation with the gaussian mixture model can improve the object detection performance. Let $I(x,y)$ be the input image and $S(x,y)$ be the structuring elements. Erosion of I by structuring element S produces $I \ominus S$. Dilation of the image I by structuring element S is given by $I \oplus S$. Hence the gradient G is defined as

$$\text{Gradient } G = (I \oplus S) - (I \ominus S) \quad (11)$$

4. EXPERIMENTAL RESULTS

4.1. EXPERIMENTAL SETUP

Implementation of proposed method Matlab 2017 with 8GB RAM have used. The datasets used for evaluation were the video sequences from the datasets VISOR [23], CD 2014(Change Detection) [24] and PETS 2009[25] and used several existing methods [8][21][26][27] for comparison were used. The terminologies used in the evaluation matrix were TP, TN, FP and FN. TP indicates the correct object detection, TN denotes the correct object rejection, false positive or false detection of an object represented by FP and FN measures the detection failure. Root Mean Square Error (RMSE) is the difference between the source and result image. Precision measures the ratio between true positives to overall positives. Recall calculates true positives to actual objects. The following evaluation metrics uses here to evaluate the performance of the proposed method.

$$RMSE = \sqrt{\frac{1}{mn} \sum_{i=1}^m \sum_{j=1}^n (x_{ij} - y_{ij})^2} \quad (12)$$

$$\text{Precision} = \frac{TP}{TP+FP} \quad (13)$$

$$\text{Recall} = \frac{TP}{TP+FN} \quad (14)$$

4.2. EXPERIMENTAL RESULTS

The results in table 1 indicate the comparison of existing GMM [5] and gradient GMM (proposed) in the as-

pect of foreground detection. Here benchmark GMM is used for comparison. Column 3 represents the ground truth frame. The results of GMM and gradient GMM has shown in column 4, column5 respectively. From the results, it becomes apparent that the gradient GMM performs better than GMM. RMSE(Root Mean Square Error) of the binary mask results of the GMM and the gradient GMM with the actual image has shown in Fig.4. The RMSE value of Gradient GMM is less when compared to GMM, which means that the gradient GMM results more similar to the actual image than other.

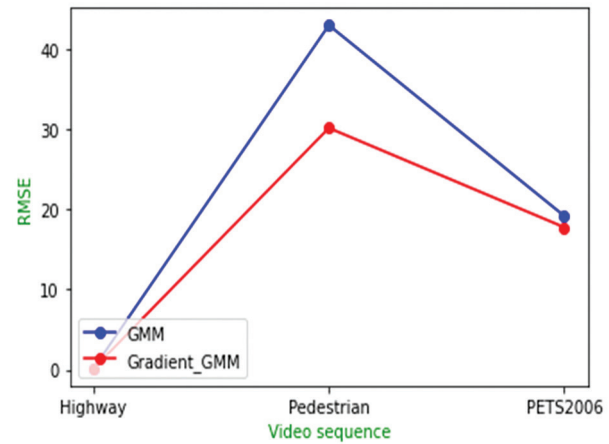


Fig.4. RMSE between the resultant frame of GMM [5] and the proposed method

Fig.5 and Fig.6 represent precision and recall graphs. The precision and recall of Nguyen [26], Poppe's method [27] and the proposed method have displayed in these graphs. The methods Nguyen [26] and Poppe's method [27] used the non-GMM method and used the same dataset for their experiment. The authors used change detection video sequences with various challenges for comparison. According to the precision graph Fig.5, the proposed method outperforms when compared to the other two approaches. But all methods result in almost the same precision value in PETS2006 video sequences due to high reflection in the video.

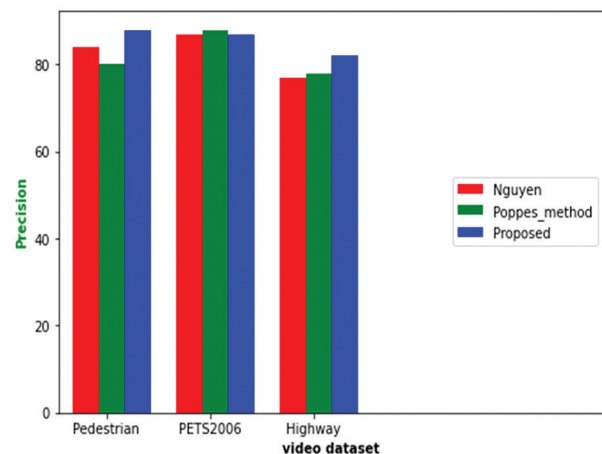


Fig. 5. Precision graph of Nguyen method [26], Poppe's method [27] and the proposed method

Table 1. Comparison of GMM with the proposed system

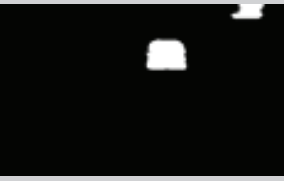



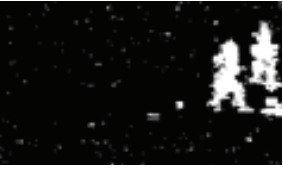

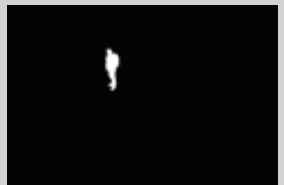

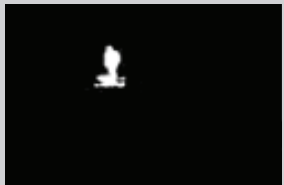
Dataset name	Frame number	Ground Truth	GMM	Gradient GMM (Proposed)
Highway	100			
Pedestrian	420			
PETS2006	300			

Table 2. Comparison of Foreground mask generated by self-adaptive GMM [21] and Gradient GMM(Proposed)

	Original frame and challenges	Background	Foreground Mask N S Ghedia [21]	Foreground Mask (Proposed)
clutter				
high illumination				
high reflection				
surveillance				
Far Field				

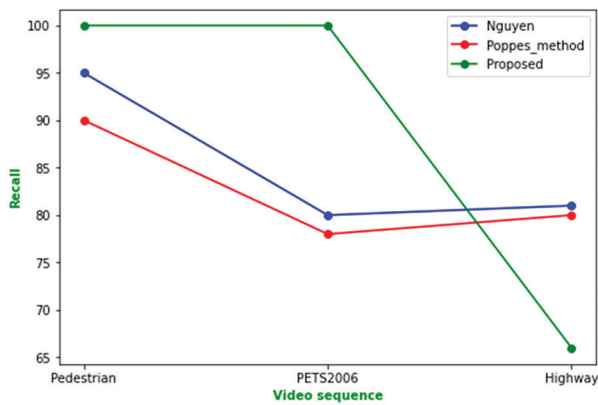


Fig. 6. Recall graph of Nguyen method [26], Poppe's method [27] and the proposed method

The recall is the measure of the true positives towards actual positives. Fig. 6 shows the recall comparison of the proposed system performance with Nguyen [26] and Poppe's method [27].

The proposed method performs well in pedestrian and PETS 2006 video sequences compared to the other two methods [26][27]. But recall is very low in Highway sequences (dynamic background). The complex background motions may lower the recall value of the proposed method.

Table 2 represents the foreground mask comparison of various frames with the improved GMM method Ghedia [21]. The method Ghedia [21] used a self-adaptive improved GMM method with the same experimental dataset. The table represents the frames from various challenging scenarios such as illumination variation, presence of shadow and clutter etc. In table 2, column 1 represents the original frame, column 2 shows the background frame, column 3 displays the foreground mask of the self-adaptive GMM method Ghedia [21] and the last column shows the foreground mask of the proposed system. The table evidence that the foreground mask of the proposed method is better than the method of Ghedia [21]. From the above comparisons and results, it is clear that Gradient GMM performs more correctly than GMM. But Gradient GMM is less accurate in the case of high reflection.

5. CONCLUSIONS

This paper introduced a gradient GMM method for multiple object detection in surveillance videos. The Proposed gradient GMM for object detection performs better under various challenging circumstances. Gaussian Mixture Model is the backbone of the proposed system. Contributions to GMM classifies into intrinsic and extrinsic enhancement. Parameter initialization of gradient GMM is the intrinsic improvement and helps the proposed method for better background subtraction. The preprocessing and postprocessing are extrinsic enhancements to GMM. The morphological gradient filter plays a critical role in foreground detec-

tion and eliminating the noise in foreground objects. Integration of the gradient filter adds to the efficiency and robustness of the proposed GMM method. The experimental results proved that the proposed technique performs better than GMM. Gradient GMM can detect the object even in illumination variation, shadows, occlusion, and dynamic background to a range. But the method results in false positives in the case of moving backgrounds such as high reflection, high dynamic motion etc. A further modification is required to handle complex backgrounds and long-lasting occlusion.

6. ACKNOWLEDGEMENT

We thank Sri Ramakrishna College of Arts and Science for giving support for doing this research work.

7. REFERENCES:

- [1] J. Fancy, V. Vijayakumar, "A Review on Multiple Object Detection and Tracking in Smart City Video Analytics", *International Journal of Innovative Technology and Exploring Engineering*, Vol. 8, No. 2S2, 2018, pp. 2278-3075.
- [2] D. Zhou, V. Frémont, B. Quost, Y. Dai, H. Li, "Moving object detection and segmentation in urban environments from a moving platform", *Image and Vision Computing*, Vol. 68, 2017, pp. 76-87.
- [3] S. Li, C. Zeng, Y. Fu, S. Liu, "Optimizing multi-graph learning based salient object detection", *Signal Processing: Image Communication*, Vol. 55, 2017, pp. 93-105.
- [4] T. Bowmans, "Subspace learning for background modelling: a survey", *Recent Patents on Computer Science*, Vol. 2, No. 3, 2009, pp. 223-234.
- [5] C. Stauffer, W. Eric L. Grimson, "Adaptive background mixture models for real-time tracking", *Proceedings of the IEEE computer society conference on computer vision and pattern recognition*, Vol. 2, Fort Collins, CO, USA, 23-25 June 1999.
- [6] P. KaewTraKulPong, R. Bowden, "An improved adaptive background mixture model for real-time tracking with shadow detection", *Proceedings of the 2nd European workshop on advanced video-based surveillance systems: AVBS01*, September 2001.
- [7] A. Elgammal, D. Harwood, L. Davis, "Non-parametric model for background subtraction", *Lecture Notes in Computer Science*, Springer Berlin, 2000, pp. 751-767.

- [8] C. Stauffer, W. Eric L. Grimson, "Learning patterns of activity using real-time tracking", *IEEE transactions on pattern analysis and machine intelligence*, Vol. 22, No. 8, 2000.
- [9] D. S. Lee, "Effective Gaussian mixture learning for video background subtraction", *IEEE Transaction on Pattern Analysis Machine Intelligence*, Vol. 27, Issue.5, 2005, pp.827-832.
- [10] Z. Zivkovic Z, F. van der Heijden, "Efficient adaptive density estimation per image pixel for the task of background subtraction," *Pattern Recognition Letters*, Vol. 27, No. 7, 2006, pp. 773-780.
- [11] M. Shah, J. Deng, B. Woodford B, "Localized adaptive learning of mixture of Gaussians models for background extraction", *Proceedings of the Image and Vision Computing Conference, New Zealand, 2010*, pp.1-8.
- [12] M. Shah, J. Deng, B Woodford, "Video background modelling: recent approaches, issues and our proposed techniques", *Machine Vision application*, Vol. 25, No. 5, 2014, pp.1105-1119.
- [13] R Chavan, S. R. Gengaje, S. Gaikwad, "Multi-Object Detection Using Modified GMM-Based Background Subtraction Technique", *Proceedings of the International Conference on ISMAC in Computational Vision and Bio-Engineering ISMAC, 2019*, pp.945-954.
- [14] C. R del-Blanco, F Jaureguizar, N. García, "An efficient multiple object detection and tracking framework for automatic counting and video surveillance applications", *IEEE Transaction on Consumer Electronics*, Vol. 58, No. 3, 2012.
- [15] I. Pathan, C. Chauhan, P. Kathiriya, "Real-time moving object detection and tracking using adaptive gaussian mixer model and Lucas -Kanade Method", *International Journal of Engineering Science and Computing*, Vol. 6, No. 5, 2016.
- [16] Z. Chen, T. Ellis, "A self-adaptive gaussian mixture model", *Computer Vision and Image Understanding*, Vol. 122, 2014, pp. 35-46.
- [17] H. Fradi, J. L. Dugelay, "Robust foreground segmentation using improved gaussian mixture model and optical flow", *Proceedings of the International Conference on Informatics, Electronics & Vision, Dhaka, Bangladesh, 18-19 May 2012*, pp. 248-253.
- [18] Z. Fu, L. Wang, "Video object detection algorithm based on gaussian mixture models", *Advanced Materials Research*, Vol. 721, 2013, pp. 587-590.
- [19] X. Lu, C. Xu, "Novel Gaussian mixture model background subtraction method for detecting moving objects", *Proceedings of the IEEE International Conference of Safety Produce Informatization, Chongqing, China, 10-12 December 2018*, pp. 6-10.
- [20] M. Chen, X. Wei, Q. Yang, Q. Li, G. Wang, M.-H. Yang, "Spatiotemporal GMM for Background Subtraction with Superpixel hierarchy", *IEEE Transactions on Pattern Analysis and Machine Intelligence*, Vol. 40, No. 6, 2018.
- [21] N. S. Ghedia, C. H. Vithalani, "Outdoor object detection for surveillance based on modified GMM and adaptive thresholding", *International Journal of Information Technology*, Vol. 13, 2020, pp.185-193.
- [22] S. Paris, P. Kornprobst, J. Tumblin, F. Durand, "Bilateral filtering: Theory and applications", *Foundations and trends in Computer graphics and Vision*, Vol. 4, No. 1, 2008, pp. 1-73.
- [23] Visordataset, https://aimagelab.ing.unimore.it/visor/video_categories.asp (accessed:2022)
- [24] Change detection dataset, <https://www.kaggle.com/datasets/fc82cc044b7e90db502e947e3a4d301a0ff2c498a38b75522543304a40c764f5> (accessed: 2022)
- [25] PETS 2009 dataset, <http://cs.binghamton.edu/~mrldata/pets2009> (accessed: 2022)
- [26] M. H Nguyen, T. L. Vuong, D. N. Nguyen, D. V. Nguyen, H. Le, T. Nguyen, "Moving object detection in compressed domain for high-resolution videos", *Proceedings of the Eighth International Symposium on Information and Communication Technology, 2017*.
- [27] S Bruyne, C. Poppe, S Verstockt, P Lambert, R V D Walle, "Estimating motion reliability to improve moving object detection in the H.264/AVC domain", *Proceedings of the IEEE International Conference on Multimedia and Expo, New York, NY, USA, 28 June - 3 July 2009*, pp. 290-299.

Real-time object detection and selection with the LabVIEW program

Original Scientific Paper

Nihat Pamuk

Zonguldak Bulent Ecevit University,
Faculty of Engineering, Department of Electrical and Electronics Engineering
Zonguldak, Turkey
nihatpamuk@beun.edu.tr

Abstract – Nowadays, the demand for production is increasing due to the increase in the human population. For this reason, different developing technologies are used to meet the required production. In developing technologies, image processing techniques are used to save manpower and time and to minimize possible errors. In this study, image processing techniques were used to detect and select the colors and shapes of the objects coming over the conveyor belt system. Real-time images were preferred in the study. In the implemented system, the selection process was carried out by using the LabVIEW program to define the colors and shapes of the objects. LabVIEW NI-IMAQdx was used to find the colors of the objects. To facilitate the definition of shapes, the images taken from the Vision Assistant module in the LabVIEW program were converted to HSL format, and shape definitions were made using different algorithms. After these processes were done, the servo motors in the conveyor belt system were enabled to communicate with each other with the help of the Arduino program and the selection of the objects was carried out. According to the results obtained, the average accuracy rate for three-dimensional objects was 95.349 %. This rate is considered to be a very high rate for object detection of correct color and shape.

Keywords: Color and shape detection, Conveyor belt system, Image processing, LabVIEW

1. INTRODUCTION

One of the most important factors for increasing the level of welfare in human life is the increase in the level of production in the industry. This increase is made possible by the advancement of technology. With the advancement of technology, simple operations where people spend their time intensively are carried out with the use of appropriate machinery and equipment. One of these machines is the conveyor belt system, which is used in the rapid transportation, detection, and selection of products in the industrial industry.

The selection process in the conveyor belt system is made using image processing technology. Before the development of image processing technology, all the steps of detecting suitable objects were done by humans. For this reason, it was not possible to prevent time loss and human-induced errors in production. The use of image processing technology in the industry and industrial processes is also aimed to solve the working problems in areas that are risky for human health.

Scientists have used a technique to automatically detect and track objects using the color feature in their studies. In this way, they enabled the identification of

objects, their monitoring, and obtaining information about objects [1]. In 2013, camera-assisted image processing methods were used to analyze the surfaces of tomatoes in motion on the conveyor belt system. In the study, the cracks and colors on the tomatoes were analyzed and the damaged tomatoes were selected [2]. Studies have been carried out to find the coordinates, dimensions, and shapes of objects on a real-time image using the LabVIEW program [3].

In some studies, real-time images were taken and measurements were made from apple, orange, and lemon samples using the LabVIEW program. Caliper measurements were also taken from the samples obtained together with the measurements. With the results obtained, it has been shown that the measurement values used in determining the size of agricultural products can be used more effectively [4]. In some studies, using the LabVIEW program, the age factor of tomatoes was calculated with image processing techniques. While determining the age factor, the transformation stages of tomatoes from green to red were followed and it was determined when the harvest time would be [5]. Designed to meet the evolving needs of Industry 4.0, such systems are easily used to categorize objects with different properties. Objects to be determined with the help of image

processing techniques are selected at lower costs. As a result of the observations and research, image processing techniques have been used because they are faster, healthier, and more practical.

In addition, studies have been carried out to define the colors and edges of images for patients with color blindness. In such studies, the wireless camera from which the image will be taken and the computer are paired, and the resulting image is processed using the LabVIEW IMAQ image assistant and displayed on the screen [6]. By using image processing techniques and the LabVIEW program, cancer cells in the human body were identified and classified. By performing automatic detection, segmentation, and classification steps with image analysis, normal cells were distinguished from cancerous cells [7]. In a study published in 2011, a bolt and nut identification study was performed on the conveyor belt system using artificial neural networks, and a 92% recognition success was achieved [8]. Image processing techniques are used to perform quality control in the glass production system.

LoG, Canny, wavelet transform, cellular neural network, and Gabor bank algorithms were applied to the images obtained to detect defects such as broken, cracked, scratched, and bubbled glass. Errors on the glass were detected and the results obtained were compared with the reference images. At the end of this study, the researcher determined that the most successful models were cellular neural networks with 91.46% and Gabor bank applications with 89.55% [9]. In another study, fault detection and classification of objects passing over a belt system were performed with a robot arm with three degrees of freedom. It has benefited from Artificial Neural Network algorithms for the detection of objects [10].

2. MATERIALS AND METHOD

In this study, the process of selecting objects in motion according to their different colors and shapes was made using real-time images. After determining the color and shape of the object coming over the conveyor belt system, the selection process was carried out with the help of the arms connected to the servo motors. In the conveyor belt system, 2 servo motors and 2 DC motors with a voltage level of 5V are used.

LabVIEW program was used to control servo motors and communication was provided between LabVIEW and Arduino UNO R3. The appropriate Package Manager VI was used for Arduino to be recognized by the LabVIEW program. Afterward, LINX software was loaded so that the information sent by the LabVIEW program can be used by Arduino. In this way, servo motors were controlled with the software platform developed in the LabVIEW program.

The hybrid model structure is used in the article. Since the methods used in the article have a hybrid structure, the deficiency in one model is reduced as a result of

the combination of another model. For this reason, it can show its effect in industrial applications at the rates where the color separation can be made sensitively. The relationship of mobile technology with the environment can become much more compatible with color distribution models. Color segmentation is the first step for industrial applications. The environments in which industrial applications interact with the real world often change dynamically. In addition, technological developments in recent years have made sensor technology and automation systems available to react to many options in daily life. Automation systems use color model algorithms to further improve environmental adaptation and consider this a good option.

As the object to be defined, cube and cylinder-shaped objects were determined in 4 different color types and the evaluation phase was started. A webcam camera with a resolution of 640x480 and 5-megapixel was used to obtain object images. Color and shape selection was made with the buttons created in the system interface. Objects are detected according to the specified boundary selection values.

Objects are directed to appropriate parts of the conveyor belt system if they conform to predetermined specifications. To determine the color and shape of the object correctly, 2 different functions are used in the block diagram. The first of these functions were used to perform the color test correctly, and the second to make the shape detection correct. The color spectrum obtained from the NI-IMAQdx color learning function was used to find the color. After the correct color of the object has been determined, special algorithm structures have been created with the Vision Assistant module. With the help of the algorithms used, the shape of the object whose correct color was determined was determined. The block diagram structure of the system is shown in Fig. 1.

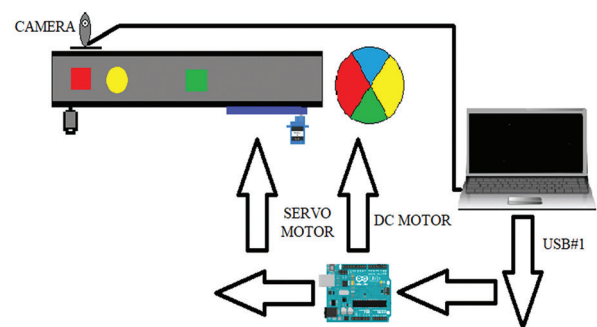


Fig. 1. Block diagram structure of the system

3. DEFINING OBJECT COLORS

Examining the block diagram of the application, there are four icons representing the USB webcam driver. These icons are IMAQ USB Unit for the initialization unit, IMAQ USB Grab Setup for the configuration unit, IMAQ USB Grab Acquire for the image acquisition unit, and IMAQ USB Close for the drive shutdown unit [11]. There

are two icons on the LabVIEW Vision platform. These are the IMAQ Create and IMAQ Color Learn functions that calculate the color spectrum [12]. These symbols carry out similar mathematical calculations as in other software programs. To define the color, the color information in the predetermined images is used by making use of the color spectrum. Color information is encoded in the index array tab in the block diagram in the LabVIEW program, and then the threshold values of the color pixels are determined. Minimum and maximum pixel values are used to determine the full dynamic range of the image. The minimum and maximum values of the pixels determine the appearance of the image. The z coordinate value in the LabVIEW program is calculated with the formula given in equation 1.

$$z = \frac{s - y}{v - y} x 255 \quad (1)$$

In Equation 1, where the z value is an 8-bit pixel value, the x value is a 16-bit pixel value. The minimum intensity value is defined as y and the maximum intensity value as v [13]. While converting the pixel values in the program input to the actual coordinate values, some errors occur. The error values of the pixel coordinate points show the largest estimated position value for the actual coordinate values. The error value in the LabVIEW program is calculated with the formula given in equation 2. This technique applied minimizes possible errors when changing light, angle and other parameters change [14].

$$e(i, j) = f \sqrt{(s - s_{reas})^2 + (y - y_{reas})^2} \quad (2)$$

Colors are represented by three different components: hue, saturation, and lightness (HSL) [15]. In HSL, the colors of each hue are obtained by placing neutral colors ranging from black to white in a radial slice around a central axis [16]. Hue indicates the base color in degrees or numbers [17]. Saturation can be defined as the ratio of color to brightness and is always expressed as a percentage, with 100% saturation meaning that the color is fully saturated. Luminance is defined by the brightness of the illuminated white color and is expressed as a percentage. 100% of the brightness defines the white color and 0% defines the black color [18]. Color and tonal values are shown in Table 1.

Table 1. Color and tonal values.

Color	Tonal (Degree)	Tonal (Value)
Red	0 or 360	0 or 6
Yellow	60	1
Green	120	2
Cyan	180	3
Blue	240	4
Magenta	300	5

The HSL color space handles color processing functions such as color matching, color positioning, and color pattern matching. This situation makes HSL the best choice for many image processing applications, such as color matching. In the literature, it is necessary to determine the color tone components, which are the basic idea of brightness, in the calculation of brightness, saturation, and hue components. Equation 3 is used to determine the color components.

$$H = \begin{cases} \arccos \frac{0.5[(R - G) - (R - B)]}{\sqrt{(R - G)^2 + (R - B) \cdot (G - B)}} & B > G \\ 360 - \arccos \frac{0.5[(R - G) - (R - B)]}{\sqrt{(R - G)^2 + (R - B) \cdot (G - B)}} & G \geq B \end{cases} \quad (3)$$

In Equation 3, H is expressed in degrees. To get results faster, it is necessary to reduce the number of multiplications and avoid subtracting the square root. The results that allow accelerated application is shown in equation 4.

$$H = \begin{cases} Undefined & R = G = B \\ \frac{\pi}{3} + \arctan \left(\frac{\sqrt{3} \cdot (G - R)}{G + R - 2B} \right) & \min(R, G, B) = B \\ \pi + \arctan \left(\frac{\sqrt{3} \cdot (B - G)}{G + B - 2R} \right) & \min(R, G, B) = R \\ \frac{5\pi}{3} + \arctan \left(\frac{\sqrt{3} \cdot (R - B)}{B + R - 2G} \right) & \min(R, G, B) = G \end{cases} \quad (4)$$

It does not need trigonometric functions because the mathematical area can be calculated simply. Therefore, the expression can be reduced to equation 5.

$$H = \begin{cases} Undefined & R = G = B \\ \frac{G - B}{3 \cdot (G + R - 2B)} & \min(R, G, B) = B \\ \frac{B - R}{3 \cdot (G + B - 2R)} & \min(R, G, B) = R \\ \frac{R - G}{3 \cdot (B + R - 2G)} & \min(R, G, B) = G \end{cases} \quad (5)$$

Therefore, the image taken from the camera in the Red, Green Blue (RGB) form has been converted to the HSL form. The mathematical equations for converting from RGB to HSL are shown in equation 6. Equation 6 is obtained if the saturation component is added to equation 5 in addition to two equivalent formulations. In the equations, the value of H varies in the range of $[-180^\circ, +180^\circ]$ [19].

In Equation 6, the intensity value decreases the saturation of the color as it approaches the limit values. This allows the best classification of the components of a surface in the absolute and visual field, which increases its perceptibility and allows for selectivity. In the study,

the method used for matching is normalized cross-correlation and the square of the Euclidean distance between the two images is used as a measure of similarity [20]. The template image on which the correlation application was applied is shown in Fig. 2. In the correlation application, the $w(x,y)$ pixel dot in the (k,l) size template image transforms into a target image shape of $(x+y)mxn$ size. The target image to be obtained at the end of the correlation process is calculated with equation 7 [21].

$$H = \begin{cases} \max(R,G,B)=0, & 0^0 \\ \max(R,G,B)=R, & \frac{G-B}{\max(R,G,B)-\min(R,G,B)} \\ \max(R,G,B)=G, & 2+\frac{B-R}{\max(R,G,B)-\min(R,G,B)} \\ \max(R,G,B)=B, & 4+\frac{R-G}{\max(R,G,B)-\min(R,G,B)} \end{cases}$$

$$L = \begin{cases} \frac{\max(R,G,B)+\min(R,G,B)}{2} \end{cases} \quad (6)$$

$$L = \begin{cases} \frac{\max(R,G,B)+\min(R,G,B)}{2} \end{cases}$$

$$S = \begin{cases} \frac{\max(R,G,B)-\min(R,G,B)}{\max(R,G,B)+\min(R,G,B)}, & L < 0.5 \\ \frac{\max(R,G,B)-\min(R,G,B)}{2-\max(R,G,B)+\min(R,G,B)}, & L > 0.5 \end{cases}$$

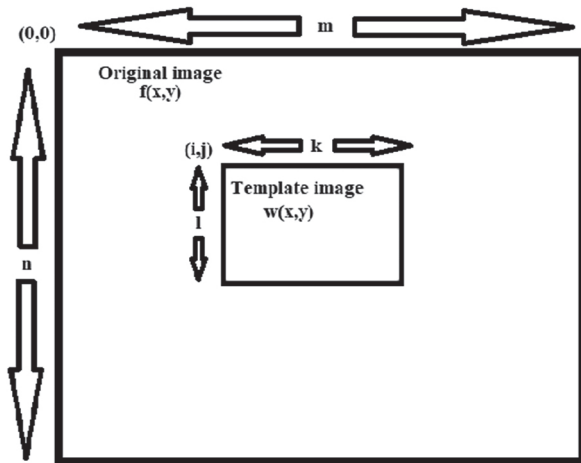


Fig. 2. Correlation process image

$$d^2(i,j) = \sum_{x=0}^{l-1} \sum_{y=0}^{k-1} [w(x,y) - f(x+i,y+j)]^2 \quad (7)$$

Considering the total energy of the template image as constant and it is calculated by equation 8.

$$\sum_{x=0}^{l-1} \sum_{y=0}^{k-1} w(x,y)^2 \quad (8)$$

$$\sum_{x=0}^{l-1} \sum_{y=0}^{k-1} f(x+i,y+j)^2 \quad (9)$$

As a result, the original and template image values are superimposed. The obtained cross-correlation expression is given in equation 10.

$$C(i,j) = \sum_{x=0}^{l-1} \sum_{y=0}^{k-1} w(x,y)f(x+i,y+j) \quad (10)$$

If the original and template image values obtained are superimposed on the (i,j) coordinate value, the obtained images are similar. If the image energy position changes, the matching fails. In such cases, a normalized correlation term is calculated. The mean intensity in the template and the mean intensity value of the target image in the region overlapping the template are expressed as $t(i,j)$. The normalized correlation function is calculated by equation 11 [22].

$$t(i,j) = \frac{\sum_{x=0}^{l-1} \sum_{y=0}^{k-1} (w(x,y) - \bar{w})(f(x+i,y+j) - \bar{f}(i,j))}{\sqrt{\sum_{x=0}^{l-1} \sum_{y=0}^{k-1} (w(x,y) - \bar{w})^2 \sum_{x=0}^{l-1} \sum_{y=0}^{k-1} (f(x+i,y+j) - \bar{f}(i,j))^2}} \quad (11)$$

The pyramid matching model used in color detection is divided into two methods. These methods are the gray value method and the gradient method. While normalized pixel values are used in the gray value method, filtered edge pixels are used in the gradient method. In addition, the vector correlation method is used instead of normalized cross-correlation in the gradient method. Since the gradient method uses less data, it gives faster results than the gray method. However, at very low-resolution values, since the strength and reliability values of the edges decrease, the gradient method works at a higher resolution than the gray value method.

Each interval value in the color spectrum is expressed as a percentage of color pixels in the image. A spectrum of colors with more divisions represents higher color resolution. There are three different color sensitivities as low, medium, and high [23]. In the study, using low color sensitivity values, the tonal color space is divided into seven tabs. In this case, a total of 16 color spectrum ranges were obtained. Each range represents different color pixels, with the first range value being saturation.

If there are n ranges in the color space, the color spectrum array contains the range values of $n+2$ color spectra [24]. The color spectrum ranges to be applied using the LabVIEW program are shown in Fig. 3. The colors of the objects taken from the real-time images were compared concerning the measured color pixel values to find the range values of the colors in the spectrum. The pixel values taken from the color spectrum range are shown in Table 2.

Table 2. Color pixel values in the color spectrum range.

Colors	Color Spectrum Range															
	0	1	2	3	4	5	6	7	8	9	10	11	12	13	14	15
Red	0,00	1,00	0,00	0,00	0,00	0,00	0,00	0,00	0,00	0,00	0,00	0,00	0,00	0,00	0,00	0,00
Blue	0,00	0,00	0,00	0,00	0,00	0,00	0,00	0,00	0,00	0,78	0,00	0,22	0,00	0,00	0,00	0,00
Green	0,00	0,00	0,00	0,00	0,00	0,00	0,98	0,00	0,02	0,00	0,00	0,00	0,00	0,00	0,00	0,00
Yellow	0,00	0,00	0,05	0,95	0,00	0,00	0,00	0,00	0,00	0,00	0,00	0,00	0,00	0,00	0,00	0,00

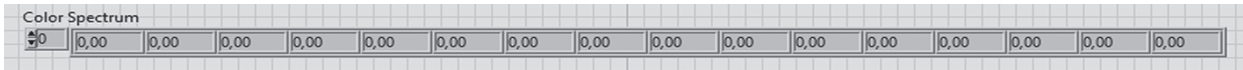


Fig. 3. The color spectrum of the image

4. DEFINING OBJECT SHAPES

The Vision Assistant algorithm in the Vision Development Module is used to detect shape. The Vision Assistant algorithm is shown in Fig. 4. The Vision Acquisition module was used to take the shape image of the object, and the Vision Assistant module was used to

operate the image processing part. The real-time image is transmitted to the Vision Assistant module and the image is processed with the help of the algorithm used. In the LabVIEW program, 2 different objects are defined as a cube and a circle. Different algorithms are used to identify objects. The block diagram designed in the LabVIEW program is shown in Fig. 5.

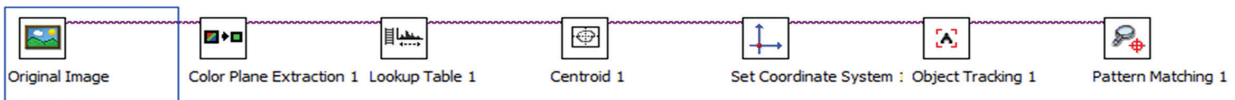


Fig. 4. Vision assistant algorithm

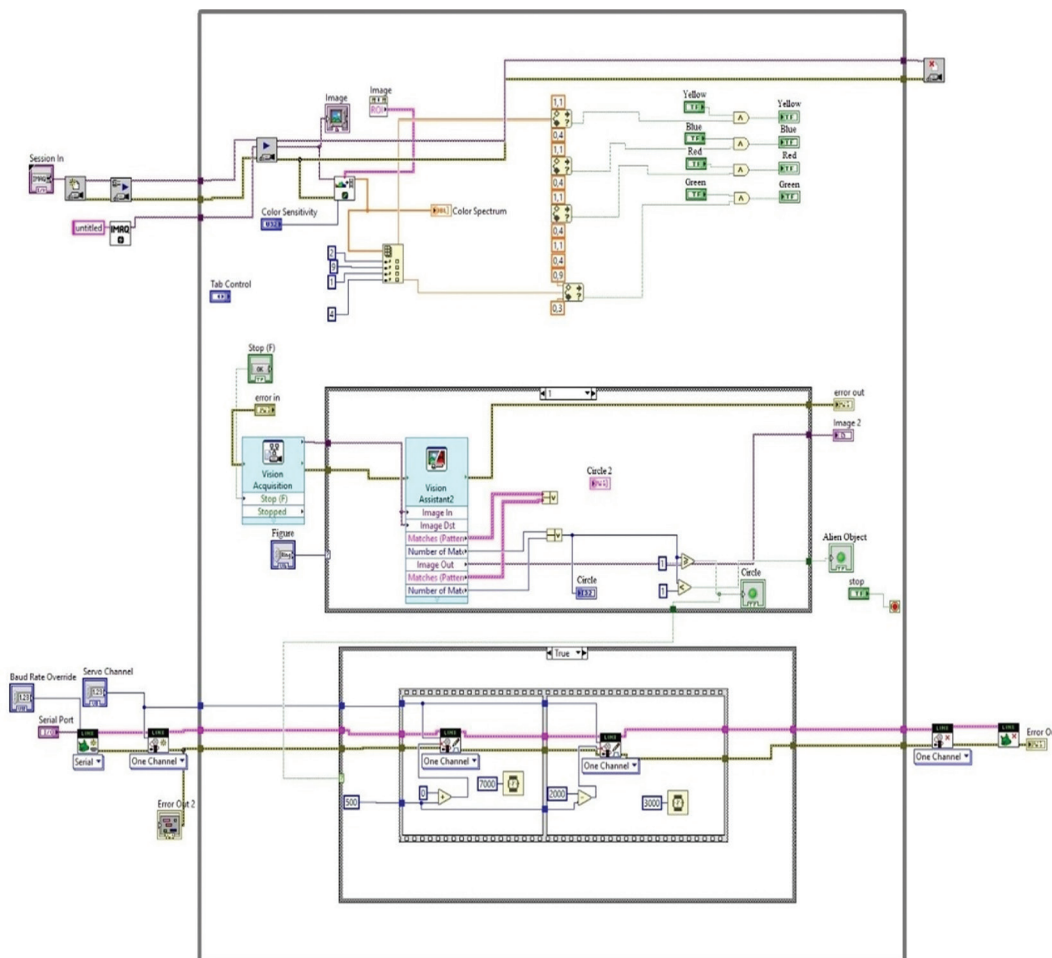


Fig. 5. Block diagram structure in the LabVIEW program

The original image obtained was converted from a color plane extraction RGB color model to an HSL color model. With this process, the hue, saturation, and lightness components of the color image are revealed. To determine the shape of the displayed object more easily, the color definition of the image was made with the lookup table 1 tab. In the next step, the energy center of the image is selected with the centroid tab. The coordinate values of the object are calculated by determining the reference value with a set coordinate system. Then, the object tracking feature was used to follow the object on the conveyor belt system and pattern matching was performed to define the shape.

5. DETERMINING THE COLORS AND SHAPES OF OBJECTS

In the program created with LabVIEW, shape, and color detection work simultaneously and independently of each other. The color and shape of the object to be detected are selected on the user interface screen. After the selection process made on the buttons, the color determination is made when the object in the conveyor belt system appears on the fixed camera screen. Color and shape detection images obtained from the LabVIEW program are shown in Fig. 6.

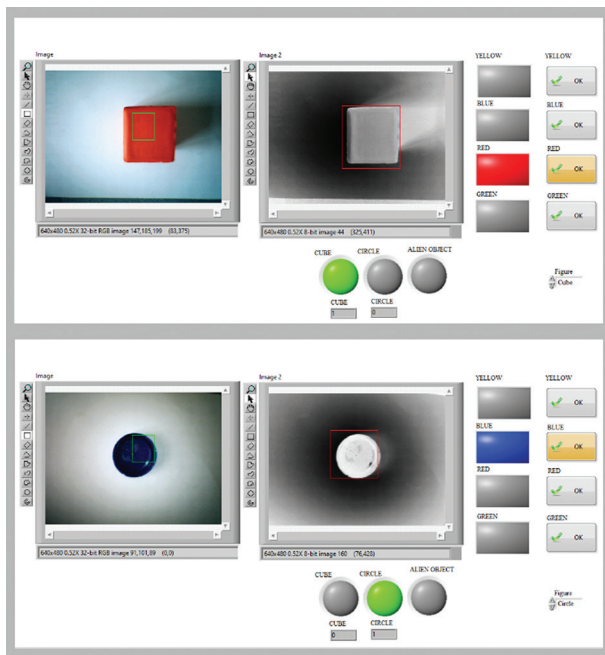


Fig. 6. Color and shape detection

During color detection, the color pixels falling on the camera's focal point are in the range of the color spectrum, and the relevant color is detected and displayed in the user interface. The case structure block is used to detect objects in the block diagram designed in the LabVIEW program. If the object to be detected on the conveyor belt is a cube, the section with a default value of zero becomes active. If the object is a circle, the section with a default value of one becomes active. For the object to be detected more easily, the image is con-

verted to gray color so that the object is different from the background color. In this way, the detection of the moving object is made quickly and easily.

6. IMPLEMENTED CONVEYOR BELT SYSTEM STRUCTURE

Conveyor belt systems are mechanical transport vehicles that allow objects to be transferred from one location to another. In the study, the transfer of objects was successfully carried out using the conveyor belt system. The conveyor belt system is manufactured using plastic-coated Styrofoam. The length of the conveyor belt system is 80 cm and the width is 25 cm. The movement of the conveyor belt system is provided by 2 DC motors with a voltage of 5V. The movement of the arms that provide the selection process in the conveyor belt system is provided by 2 servo motors used in the system. For the belt rollers in the system to rotate easily, 2 bearing structures of 7x8x22 mm were used. The LINX interface in the LabVIEW program was used for programming the Arduino. In this way, the program developed in the LabVIEW environment is processed by Arduino and the servo motors used in the system are controlled. The image of the conveyor belt system structure is shown in Fig. 7.

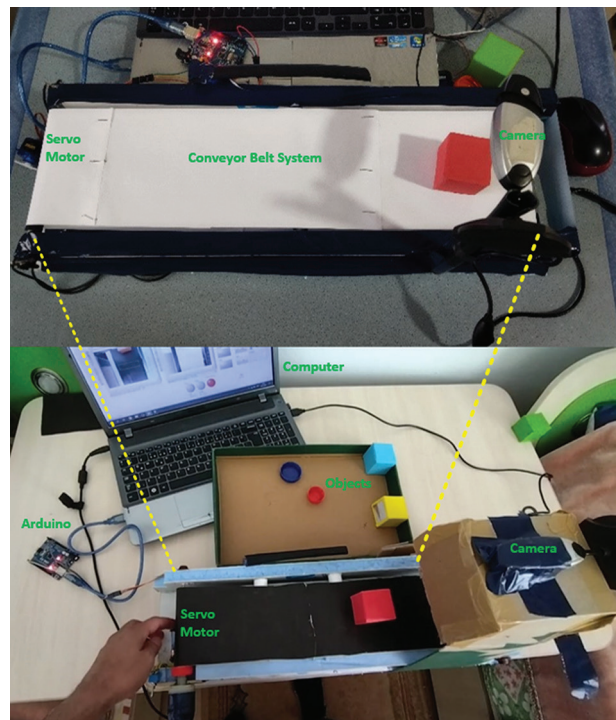


Fig. 7. Image of conveyor belt system structure

7. FINDINGS AND RESULTS

In the study, four different colors red, blue, yellow, and green, and two different shapes cube and circle were used. The colors and shapes of the objects to be defined on the conveyor belt system were successfully determined and the selection process was carried out. Some problems occurred in identifying the

object when the environment was not properly illuminated. For this reason, the importance of the lighting system used during the identification process has been revealed. In addition, the resolution value of the camera used in the study had a great effect on the success of the study. This effect caused a decrease in the detection time of the object. A webcam camera with a resolution of 640x480 was used in the study. By using cameras with higher resolution and making light angle adjustments clearly, the problems that may be encountered in detecting objects will be eliminated. Shape and color determination was carried out by deducing the front faces of the 3D objects in the conveyor belt system. Then, the color, shape, coordinate values, and accuracy rates of these objects were determined on the computer screen. The colors, shapes, coordinate information, and accuracy rates of 3D objects in the conveyor belt system are shown in Table 3.

Table 3. Colors, shapes, coordinate information, and accuracy rates of objects.

Colors	Shapes	Coordinate	Accuracy Rates
Red	Cube	250.43, 175.45, 224.87	89.941 %
Red	Circle	366.97, 241.29, 247.39	96.153 %
Blue	Cube	270.31, 232.68, 347.14	89.688 %
Blue	Circle	366.32, 230.92, 197.88	97.617 %
Green	Cube	273.44, 272.75, 162.63	98.835 %
Green	Circle	265.87, 220.45, 201.15	97.563 %
Yellow	Cube	348.14, 289.54, 252.99	97.721 %
Yellow	Circle	379.71, 246.08, 238.43	95.274 %

8. CONCLUSIONS

LabVIEW is a programming language that can provide graphical results, unlike other text-based programming languages. The most important feature that distinguishes this study from other studies in the literature is that it was developed with LabVIEW programming in real-time. Image processing techniques used to detect objects are systems with a very complex structure. However, such systems consist of maintenance-free and highly efficient structures.

The established system has many advantages. The most important of these advantages is that it can work with a webcam. It is possible to communicate with the webcam via USB by using the appropriate drivers in the system. Otherwise, expensive cameras must be used to communicate between the LabVIEW program and Ethernet. Another advantage is that it uses the color spectrum in real-time and can simply identify colors. In the system, the color of the object is defined by the camera's detection of the object. Illumination of the object is very important when using image processing techniques at the time of identification. In case of a large amount of light falls on the object, shadow or reflection events occur on the image. If the light value falling on the object is low, it becomes difficult for the camera to detect the object.

The identification process in the study was made for the colors blue, red, yellow, and green. With the color definitions to be made on the LabVIEW program, objects with different colors can be selected. Appropriate modules are used for the communication between the LabVIEW program and the Arduino. Servo motors are controlled via Arduino LIFA base in the LabVIEW program. In addition, since the Arduino LIFA Base interface causes a slowdown in the data rate to be transmitted to the servo motors, the LINX interface is also used in the study. Thanks to the additional program add-ons, the color, and shape of the object were instantly detected in real-time and the selection process was carried out. As a result, various algorithms were applied in the LabVIEW program using the webcam, the colors and shapes of different objects were determined and the selection process was carried out successfully. When the results were compared with similar studies in the literature, the average accuracy rate in other studies was around 93%, while the average accuracy rate in this study was 95.349%.

9. REFERENCES

- [1] P. Singh, B. B. V. L. Deepak, T. Sethi, M. D. P. Murthy, "Real-Time Object Detection and Tracking Using Color Feature and Motion", Proceedings of the International Conference on Communication and Signal Processing, India, 2-4 April 2015, pp. 1252-1257.
- [2] Md. Rokunuzzaman, H. P. W. Jayasuriya, "Development of a Low Cost Machine Vision System for Sorting of Tomatoes", Agricultural Engineering International: CIGR Journal, Vol. 15, No. 1, 2013, pp. 173-180.
- [3] S. Kos, Z. Vrhovski, D. Vidić, "Detection, Localization and Recognition of Objects Using LabVIEW", Tehnički Glasnik, Vol. 9, No. 3, 2015, pp. 245-250.
- [4] A. Beyaz, "Agricultural Product Dimension Determination by Using Video Analysis at Labview Platform", Journal of Agricultural Faculty of Gaziosmanpasa University, Vol. 33, No. Supplement 1, 2016, pp. 1-9. (in Turkish)
- [5] B. R. Navada, K. V. Santhosh, S. Prajwal and H. B. Shetty, "An Image Processing Technique for Color Detection and Distinguish Patterns with Similar Color: An Aid for Color Blind People", Proceedings of the International Conference on Circuits, Communication, Control and Computing, Bangalore, India, 21-22 November 2014, pp. 333-336.
- [6] M. J. A. Aviso, A. M. S. Cabao-an, N. A. P. Niverba and R. M. Anacan, "Age Factor Identification of Tomato Using Labview via Image Processing", Pro-

- ceedings of the TENCON 2018 - 2018 IEEE Region 10th Conference, Jeju, South Korea, 28-31 October 2018, pp. 66-71.
- [7] H. G. Zadeh, S. Janianpour, J. Haddadnia, "Recognition and Classification of the Cancer Cells by Using Image Processing and LabVIEW", *International Journal of Computer Theory and Engineering*, Vol. 5, No. 1, 2013, pp. 104-107.
- [8] T. M. Johan, A. S. Prabuwo, "Recognition of Bolt and Nut Using Artificial Neural Network", *Proceedings of the International Conference on Pattern Analysis and Intelligence Robotics*, Kuala Lumpur, Malaysia, 28-29 June 2011, pp. 165-170.
- [9] Ş. Öztürk, "Glass Defect Detection with Image Processing", Selçuk University, Faculty of Electrical and Electronics Engineering, Konya, Turkey, Master Thesis, 2015. (in Turkish)
- [10] T. Erdoğan, "Object Recognition with Camera Images on Moving Conveyor and Pick and Place Application the Objects", *Dokuz Eylül University, Faculty of Mechatronics Engineering*, Izmir, Turkey, Master Thesis, 2012. (in Turkish)
- [11] National Instruments Corporation, "NI Vision Concepts Manual", https://zone.ni.com/reference/en-XX/help/370281AG-01/nivisionconcepts/color_spectrum (accessed: 2022)
- [12] H. Jia, Y. L. Murphey, J. Shi, T. S. Chang, "An Intelligent Real-Time Vision System for Surface Defect Detection", *Proceedings of the 17th International Conference on Pattern Recognition*, Cambridge, UK, 2004, pp. 239-242.
- [13] T. Kilinger, "Image Processing with LabVIEW and IMAQ Vision", First Edition, National Instruments Virtual Instrumentation Series, Prentice Hall Professional Technical Reference, 2003.
- [14] M. Mahmoodi, L. A. James, T. Johansen, "Automated Advanced Image Processing for Micro-model Flow Experiments; An Application Using LabVIEW", *Journal of Petroleum Science and Engineering*, Vol. 167, 2018, pp. 829-843.
- [15] R. P. Gómez, O. O. S. González, A. M. Sibaja, O. P. Rodríguez, G. A. Hernández, "Digital Image Processing Using LabVIEW", *Practical Applications and Solutions Using LabVIEW Software*, InTech, 2011, pp. 297-316.
- [16] G. Vishali, H. Meghana, M. A. Kumar, N. Rajesha, "An Investigation on Image Conversions and Edge Detection Patterns in Image Processing", *Proceedings of the International Conference on Emerging Trends in Science and Engineering*, Hyderabad, India, 18-19 September 2019, pp. 1-8.
- [17] N. A. Ibraheem, M. M. Hasan, R. Z. Khan, P. K. Mishra, "Understanding Color Models: A Review", *ARPN Journal of Science and Technology*, Vol. 2, No. 3, 2012, pp. 265-275.
- [18] P. Ferrand, "GPScan.VI: A General-Purpose LabVIEW Program for Scanning Imaging or any Application Requiring Synchronous Analog Voltage Generation and Data Acquisition", *Computer Physics Communications*, Vol. 192, 2015 pp 342-347.
- [19] P. Qiao, H. Liu, X. Yan, Z. Jia, X. Pi, "A Smart Capsule System for Automated Detection of Intestinal Bleeding Using HSL Color Recognition", *Plos One*, Vol. 11, No. 11, 2016, pp. 1-14.
- [20] M. A. Sutton, J. J. Orteu, H. Schreier, "Image Correlation for Shape, Motion and Deformation Measurements: Basic Concepts, Theory and Applications", Springer Science & Business Media, 2009.
- [21] J. Im, J. R. Jensen, J. A. Tullis, "Object-based Change Detection Using Correlation Image Analysis and Image Segmentation", *International Journal of Remote Sensing*, Vol. 29, No. 2, 2008, pp. 399-423.
- [22] S. H. Tsai, Y. H. Tseng, "A Novel Color Detection Method Based on HSL Color Space for Robotic Soccer Competition", *Computers & Mathematics with Applications*, Vol. 64, No. 5, 2012, pp. 1291-1300.
- [23] S. V. Levoniuk, L. A. Ginis, "Objects Selection and Recognition During Remote Sensing Images Digital Processing by means of LabVIEW", *IOP Conference Series: Materials Science and Engineering*, Vol. 698, No. 4, 2019, pp. 1-6.
- [24] Y. Guan, B. Shen, Y. Zhang, Z. Fu, "Design of Color Mixing 3D Printing System Based on LabVIEW", *Journal of Computers*, Vol. 28, No. 6, 2017, pp. 277-287.

Spatio-Temporal Information for Action Recognition in Thermal Video Using Deep Learning Model

Original Scientific Paper

P. Srihari

School of Computer Science and Engineering,
VIT-AP University, Amaravathi 522237, India
psrihari851@gmail.com

J. Harikiran

School of Computer Science and Engineering,
VIT-AP University, Amaravathi 522237, India
harikiranj@vit.in

Abstract – Researchers can evaluate numerous information to ensure automated monitoring due to the widespread use of surveillance cameras in smart cities. For the monitoring of violence or abnormal behaviors in smart cities, schools, hospitals, residences, and other observational domains, an enhanced safety and security system is required to prevent any injuries that might result in ecological, economic and social losses. Automatic detection for prompt actions is vital and may help the respective departments effectively. Based on thermal imaging, several researchers have concentrated on object detection, tracking, and action identification. Few studies have simultaneously extracted spatial-temporal information from a thermal image and utilized it to recognize human actions. This research provides a novelty based on frame-level and spatial and temporal features which combines richer context temporal information to address the issue of poor efficiency and less accuracy in detecting abnormal/violent behavior in thermal monitoring devices. The model can locate (bounded box) video frame areas involving different human activities and recognize (classify) the actions. The dataset on human behavior includes videos captured with infrared cameras in both indoor and outdoor environments. The experimental results using the publicly available benchmark datasets reveal the proposed model's efficiency. Our model achieves 98.5% and 94.85% accuracy on IITR Infrared Action Recognition (IITR-IAR) and Thermal Simulated Fall (TSF) datasets, respectively. In addition, the proposed method may be evaluated in more realistic conditions, such as zooming in and out etc.

Keywords: Action Recognition, Activity Classification, Complex-Valued Deep Fully Convolutional Network, Deep Learning, Deeplabv3+Net, Fall Detection, Mask R-CNN, Thermal Cameras, Violence.

1. INTRODUCTION

Human action recognition (HAR) is a method for identifying a continuous action in a video clip that has grasped a lot of attention in recent years because of its various applications, which include gaming

and sports, healthcare, security, autonomous vehicles, automated assisted living systems, human-machine interaction, video surveillance cybernetics analysis. Substantial improvement has been achieved in action detection over the last several decades, and the majority of existing techniques for action classification have been used in visible image clips. [1–3]. In addition, several visible light action datasets, such as UCF101, KTH and HMDB51 have been developed for action detection. HAR in visible light has been widely studied and effectively used in various domains. Still,

occlusion, background clutter, shadow and illumination variation continue to be serious obstacles for visible light AR [4-7].

Thermal infrared cameras, rather than visible light cameras, can capture human activities due to the advancement of vision-based technologies. Infrared (IR) action recognition, as contrasted to visible light AR, can address the aforementioned issues [8,9]. IR thermal imagery can capture individuals accurately in low light while they are difficult to see that in visible light recordings. This is particularly useful for nighttime monitoring or human-computer interaction (HCI) under dim illumination. Since the occlusion, background clutter and temperatures of the shadow are very low compared to those of individuals or moving objects in IR movies, these obstacles may be effectively reduced [10,11]. With these

characteristics, infrared AR is useful in a wider range of applications outperforming visible light.

Several current approaches essentially adhere to the process of raw feature extraction, feature encoding, and classifier training [12,13]. In this process, the feature map is widely regarded as the most crucial component, and its capability to represent the fundamental information beneath the video typically influences the efficiency of AR techniques [14,15]. Many well-established feature descriptors, such as STIP, HOG3D, and 3DSIFT, have been developed and utilized in action recognition (AR). Several approaches based on convolutional neural networks (CNN) have been developed for action identification in visible videos, motivated by the effective use of CNNs in other classification of image tasks. The existing two-stream convolutional architecture can effectively integrate motion and appearance data for AR [16, 17]. Yet, the complexity of CNN models and the high computational cost of the back propagation training process reduce the deep network's efficiency in tackling video AR challenges [18]. Furthermore, the existing CNN architectures models are built to analyze 2D raw frames; thus, they cannot be used directly to learn temporal information from input videos.

Recently, the computer vision industry has paid great importance to the timely detection of falls in home video surveillance and violent activities [19,20]. To analyze behavior performance, introduced a dataset of thermal images and videos that replicate violent motions and abnormal activity in outdoor and indoor environments. Recording conditions vary from simple to complicated backgrounds, occlusions and random camera angles. But, researchers faced enormous challenges in accurate and precise identification of these activities in thermal environments due to key factors like diversity in lighting conditions, background complexity and occlusions, HAR is complicated by similar acts performed by several individuals.

To the aforementioned issues, this paper focus on vision-based approaches for automatically detecting violence and abnormal activities in thermal cameras. The framework is designed based on frame-level and extraction of both temporal and spatial information. Additionally, to perform experiments, IITR-IAR and Thermal Simulated Fall datasets are considered as two benchmark datasets to compare the proposed method with existing methods. The simulation results show that the proposed method is helpful for the operators who supervise in several monitoring services since the safety and security of our daily life is so serious in society. The proposed framework's modules are visualized to demonstrate their efficiency. The contributions of the research paper are as follows:

- A unique deep learning technique is proposed for multimodal activity detection in thermal video.
- The proposed method can localize regions and recognize the multiple individual activities.

- The proposed framework can recognize more than 30 behaviors based on spatiotemporal information.
- Contrast limited adaptive histogram equalization (CLAHE) is implemented to enhance the quality of low-resolution images.
- To propose Gaussian – Adaptive Bilateral Filter (GABF) for removing the noise from the thermal image and handling the occlusion problem.
- For obtaining ROI proposed a deep learning method Mask-RCNN with the backbone as Densenet-41.
- For extracting the spatial and temporal information DeepLabv3+Net is adopted.
- Finally, the activity of the human is classified by the complex-valued fully convolutional network. For performance evaluation, implemented on IITR-IAR and TSF datasets.

This paper is organized as follows: Section 2 presents a comprehensive literature review. Section 3 presents the challenges and overviews of the proposed architecture and its main components. Section 4 reports the experiments conducted and analyzes the results. In Section 5, the conclusion and future work are presented.

2. LITERATURE SURVEY

During the last decade, various approaches for detecting violence or abnormal in different applications have been developed. This section examines efforts in the area of abnormality identification and fall detection that are conceptually similar to the present work research.

Manssor et al. [21] developed a deep person detector that recognizes nighttime pedestrians from TIR pictures. To accomplish the aim, Tiny-convolutional yolov3's layers are contrast-enforced at the channel level. A network design employing PDM-Net and TIE-Net with an Up-Sampling layer was demonstrated. The TIE-Net optimizes and processes TIR images by eliminating information loss between initial convolution layers. Darknet-53 and PDL-Net make up PDM-Net. The TIR image's features are retrieved by Darknet-53 and classified by PDL-Net.

Imran et al. [22] developed a four-stream network based on BiLSTM and CNN models to integrate global and local motion data. SSDIs may improve action identification accuracy coupled with SDFDI dense optical flow-based pictures. CNN uses ResNet, whereas RNN uses BiLSTM. Finally, two CNN streams are trained using a single SSDI and a single SDFDI to collect global Spatio-temporal knowledge. To collect local temporal and spatial information, the clip is divided into eight segments and eight SSDIs and SDFDIs are created. These SSDIs and SDFDIs train two CNN-BiLSTM streams. Late fusion combines all four streams to analyze the class label.

Krito et al. [23] employed CNN models for RGB pictures to recognize people in thermal photos. They examined the performance of state-of-the-art object detectors and retrained them using a dataset of thermal images collected from movies simulating unauthorized movements along the border and in protected regions. Nighttime videos are captured in fog, rain and clear weather at varied ranges, and with various movement patterns. YOLOv3 was quicker than other detectors and had equivalent performance, therefore it was employed in investigations.

Batchuluun et al. [24] suggested a technique to extract joints and skeletal information by transforming a 1-channel thermal picture into a 3-channel thermal image and utilizing it as input for Joint-GAN. Using the collected joints and skeletal information, CNN-LSTM was used to recognize human activities. To test the suggested approach, 3-channel and 1-channel thermal pictures were compared.

Ding et al. [25] designed a system for identifying airport-ground activities based on an infrared video stream. First, they create a seven-class action dataset based on airport-goer behavior. Considering the limitations of infrared surveillance photos, they used a tracking technique to separate the target from the background and constructed short-term Spatio-temporal feature vectors. Finally, they built an action classification network with two LSTM layers to extract long-term spatial and temporal data and a fully connected classifier.

Hei et al. [26] introduced an infrared AR framework called REWS to reweight training set samples to overcome limited IR action data. They first translate IR action video data to low-dimensional feature space and then calculate the score of the training data set samples based on the similarity measures between the training and testing set feature data. Each sample of a training set has its weight. The weighted training sets are then used to train a support vector machine (SVM) to detect

infrared actions.

De Boissiere et al. [27] suggested that a pre-trained 3D CNN is employed as an IR module for extracting visual data from recordings. Using a multilayer perceptron, both feature vectors are then combined and used cooperatively. RoI from IR videos are cropped using 2D skeletal coordinates. This work integrates infrared and skeletal data. They assessed their system using the biggest dataset for HAR from depth cameras, the NTU RGB+D dataset. They conduct substantial ablation research.

3. METHODOLOGY

Recognizing human activities in thermal cameras is a crucial task. Figure 1 depicts the architecture of the proposed method. In this part, some of the research obstacles are discussed initially. Then, a DL-based approach is presented for the task of localization and action recognition.

3.1. CHALLENGES

Our framework highlights the issue of human behavior recognition, which involves the investigation of a few distinct actions. As a result, the approach will handle the following major issues:

- Intra-class and Inter-class Variations. Changes in internal or external stimuli cause people to react in different ways. For a particular movement, such as "walking," a person might exhibit multiple stances, speeds, and even occluded body parts while doing the same activity. In other words, a single motion may include numerous distinct movement patterns. Also, high levels of occlusion posed by other people or scenario objects make it difficult to view the whole movement area. There are parallels between activities such as "walking" and "running." These actions with tiny changes provide difficulty for deep learning systems as well.

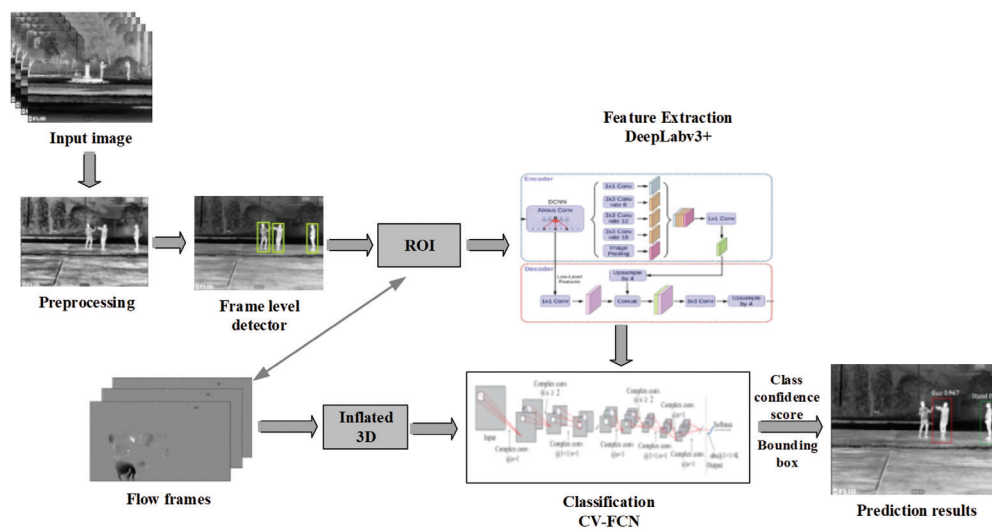


Fig. 1. Proposed framework

- Background and Time-Period. The proposed method seeks to identify various behaviors that occur at various times and the whole day. Therefore, the recordings were done at varying moments, including daytime and nighttime views. Even if the background in these videos may be the same, the intensity of light varies and the activities are distinct. Despite the difficulty of evaluating these conditions, the data collected from these tests would allow for more accurate monitoring of human activity.
- Early fall detection. A reliable fall detection system is required to limit the impacts of falling. The fall detection issue is considered an abnormal detection problem since falling is an irregular behavior. Even though many existing training models are focused on detecting falls, they are nevertheless susceptible to false positives. To eliminate false positives and achieve high accuracy, developing a reliable fall detection system is the major issue.

3.2. DATA ACQUISITION

To collect the IITR-IAR dataset, a FLIR T1020 camera is used. Its focal length is 8.4 mm and it shoots video at 1024 × 768 in a format MPEG-4 at 30 fps. This camera has a spectral range of 7.5–14 μm. The temperature range is between –15°C and 50°C, and the field of vision (FOV) is 12°.

The second dataset (Thermal Simulated Fall) is comprised of videos acquired from FLIR ONE thermal camera placed on an Android mobile in a single-view room environment. The frame rates of the videos are either 15 or 25 fps, which was determined by analyzing the attributes of every video.

3.3. DATA ANNOTATION

Based on the following criteria, created the annotation approach to identify 38 distinct kinds of actions: Normal, Violent and Abnormal activities.

Normal activities: This activity includes clap, crouch, hop, run, walk, wave1, wave2, drop, recording video, selfie, throw, handshake, hug, passing object, sit, eat, drink, making the bed, Transfers from wheelchair to chair, Removing and putting on shoes, changing clothes, getting into and out of bed, sleep, read, cough, sneeze, bend.

Violent activities: This activity includes pointing a gun, chase, fight, kick, punch, push

Abnormal activities: This activity includes slow falls, fast falls such as falling from chain, falling while walking, falling when changing from chair to bed etc.

3.4. PREPROCESSING

The thermal video taken under different conditions is given as the input to the proposed method. The Gauss-

ian-Adaptive Bilateral Filter is used to reduce noise from the input images as part of the pre-processing. These procedures will be described in detail below.

3.4.1. Selecting the Input and Frame splitting

In video format, a dataset for HAR based on thermal images is gathered. Preprocessing is performed in the IITR-IAR Dataset after video capture. Because the video is 30 frames per second, skipping every 12 frames in the collected dataset to gain one frame for training and testing the detection model. The attributes of the input videos are as follows:

Type	: VLC media file (.avi)
Dimensions	: 1024 x 768
Frame rate	: 30 frames per second

The video input is divided into frames. The frame rate is measured in frames per second. Frame rate is the number of visible frames per second.

The properties of the Thermal Simulated Fall input videos are,

Type	: VLC media file (.avi)
Dimensions	: 640 × 480
Frame rate	: 25 frames per second

It includes 9 non-fall scenario video portions and 35 fall scenario video portions. Other pre-processing methods are described in the following subsections.

3.4.2. Contrast limited adaptive histogram equalization

CLAHE is used to enhance the low image quality. This method improves image resolution by reducing amplification and clipping certain histogram thresholds. It is used to precisely improve the inverse of picture intensity. It is a superior approach for picture enhancement in comparison to adaptive histogram equalization (AHE) and other histogram equalization techniques due to its exceptional performance.

3.4.3. Gaussian – Adaptive Bilateral Filter

GABF is used to effectively eliminate the image's noise and provide improved edge preservation and smoothing. The proposed method may significantly increase infrared image quality. Input image I and Guidance g differ from the bilateral filter and is stated in eqn. (1):

$$f(x) = \sum_y W_{x,y}^g(g) I_y \quad (1)$$

Where, the center position of the input image is represented as I , $W_{x,y}^g$ is given as:

$$W_{x,y}^g = \frac{1}{k_x} \exp\left(-\frac{\|x-y\|^2}{\sigma_s^2}\right) \quad (2)$$

Where the normalizing factor is k_x . In Eqn. (2), the Gaussian spatial kernel is represented by second term

$\exp\left(-\frac{\|x-y\|^2}{\sigma_s^2}\right)$, the sizes of the window is denoted by. The

GAB kernel is expressed as:

$$W_{x,y}^{gab}(I, \bar{g}) = \frac{1}{kx} \exp\left(-\frac{\|x-y\|^2}{\sigma_s^2}\right) \exp\left(-\frac{\|I_x - \bar{g}\|^2}{\sigma_r^2}\right) \quad (3)$$

Where \bar{g} is obtained by eqn. (1). In eqn. (3), the third term $\exp\left(-\frac{\|I_x - \bar{g}\|^2}{\sigma_r^2}\right)$ is the range kernel. Variation in intensities is de by σ_r . The final output $f(x)$ of the GABF can be expressed as,

$$f(x) = \sum_y W_{x,y}^{gab}(I, \bar{g}) I_y \quad (4)$$

The entire process of our preprocessing output is shown in figure 2.

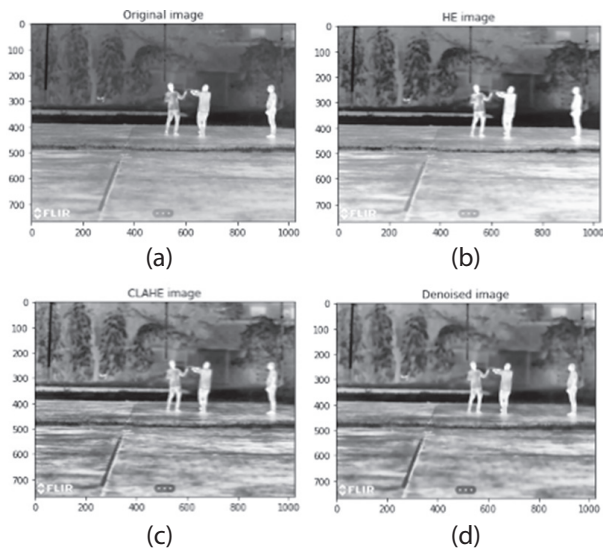


Fig. 2. Preprocessing results: (a) Original, (b) Enhance IR after HE, (c) CLAHE, (d) GABF

3.4.4. Handling Occlusion

Even though target monitoring has a wide variety of applications, it, however, poses challenges. Object or self-occlusion is the second most prevalent difficulty in target tracking applications, behind the noise. In some frames, the person is fully occluded by other things or people in the area. In addition, issues like changes in lighting, size variation, background clutter, etc. have a detrimental impact on the robustness of object tracking. For this reason, monitoring is based on a Gaussian – Adaptive Bilateral filter. These filters must be updated at every frame, even frames in which the target is obscured, therefore it is likely that background information is utilized to update the filter, which reduces the filters' discriminative power.

3.5. PROPOSED FRAMEWORK

The proposed technique recognizes human actions in thermal videos. Consequently, our objective is to address the issue of activity identification of various

persons in a scenario. To this goal, we offer a paradigm influenced by recent development in deep learning-based Spatio-temporal recognition. The system consists of three distinct components: a) ROI detection frame-based, b) temporal-context extraction of feature and c) Spatial and temporal recognition.

3.5.1. ROI frame-level detector

This section is motivated by recent developments in object recognition [28]. Here, the DL method Mask-RCNN is employed for both person recognition and segmentation of pixels. It is the expansion of Faster RCNN that can localize and classify along with segmentation. It has two parts: (1) Convolutional backbone part: Convolutional backbone extracts image features; (2) Head part: It does bounding-box identification and mask prediction. A network for extracting key points must have a large number of convolution layers to learn more accurate and discriminative features. This research has employed Densenet-41 with Mask-RCNN. The backbone network Densenet-41 is utilized to obtain the important features. However, DenseNet-41 contains 24 channels on the first convolution layer and the size of the kernel is 3×3 . In addition, numerous hidden layers within each dense block are adjusted for the computational complexity. The RPN network is fed the feature map generated from feature extraction to obtain ROIs. Figure 6 depicts an example of the ROIs extracted from the preprocessed thermal images.

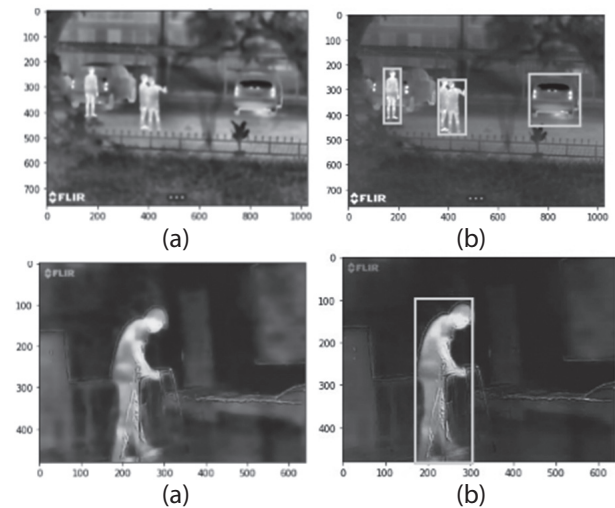


Fig. 3. (a) Preprocessed image, (b) ROI obtained

3.5.2. Temporal context-based feature extraction

To acquire temporal-context features of the targets in the image, employed the representation of different frames. The network is used for extracting temporal attributes in this sort of convolution. As a result, in the action recognition process, proposed DeepLabv3+Net as the backbone network for feature extraction. An encoding and decoding module comprises the architecture of deeplabv3+Net. The encoding module's goal is to extract temporal characteris-

tics from video frames in each video sequence step by step or layer by layer. Feature maps produced by deep layers acquire more abstract as layers are added, and they incorporate deeper semantic information that is useful to the pixel categorization. However, due to the stride of convolution, the temporal resolution of the feature maps reduces. This implies that local information such as borders and other features are removed from the feature map. As a result, a decoding module must be included. To construct a new feature map, the decoding module combines high- and low-resolution feature maps from shallow and deep layers. This new feature map comprises the borders of the action performers which are included in the feature set, as well as the semantics information that is useful for categorization. These characteristics are then fed into the classifier.

3.5.3. Spatio-temporal action prediction

This section aims to enhance the framework's Spatio-temporal features. Spatio-temporal characteristics strive to capture video motion patterns and give additional temporal information across frames. In fact, the frame-level detector employs Mask RCNN to extract Region of Interests. Using CV-FCNN of k successive frames ($k = 10$), we got the features from the temporal context. The motion characteristics are extracted by optical flow. Using the interim frames, the optical flow is calculated. The Spatio-temporal characteristics and ROIs are integrated to provide a more accurate representation of the scenes and their objects. Particularly the complex feature vector of size $1 \times K$, where K is the total number of classes, may be derived from the final convolution layer. As a result, at the feature map level, average pooling is employed to merge the ROI extracted component with the optical flow portion. The magnitude of the complex feature vector is computed at the output layer for bounding box prediction and confidence scores, and the softmax function is then applied to the final prediction.

3.5.4. Magnitude Operation

According to [29], the final convolution output in the hidden layer has complex values. Therefore, targeting is often a real-valued label. By transforming either label or output, the complex-valued output is compared with the real-valued label. In the output layer of CV-FCNN, the magnitude operation is performed to transform complex values into real numbers prior to softmax classification. Assume the last hidden layer convolution produces a $1 \times K$ complex feature vector, then the magnitude is calculated by,

$$o_k^L = \sqrt{\left(\Re(o_k^{L-1})\right)^2 + \left(\Im(o_k^{L-1})\right)^2} \quad (5)$$

Where complex feature vector for k th component is represented as o_k^{L-1} .

3.5.5. Softmax Classification

In multiclass classification, Softmax is always used. It can transfer each real-valued vector component to 0–1, and the total equals 1, meeting the probability criteria. In the output layer of CV-FCNN, the softmax function is employed for action recognition. From eqn. (6), a real-valued vector with a size $1 \times K$ can be obtained. Then the output of softmax classification is formulated by,

$$p_k = \frac{\exp(o_k^L)}{\sum_{m=1}^K \exp(o_m^L)} \quad (6)$$

Where, k^{th} class probability for one complicated visual or training sample is represented by p_k .

Training the classification model end-to-end attempts to eliminate loss functions as in Eqn. (7). Cross-entropy is used as a loss function.

$$Loss = - \sum_{k=1}^k q_k \ln p_k \quad (7)$$

Where, the true classification result of one training sample is represented as q_k . That is if k is the training sample label is, then q_k is equal to 1; otherwise, q_k is equal to 0.

4. EXPERIMENTAL SETUP AND RESULTS

In this part, we discuss the research observations and assessments of the objective of human action recognition using frame-level and spatiotemporal information. The proposed system is capable of operating in both the image and video fields. To evaluate the performance of the proposed framework, provided with qualitative and quantitative outcomes. This technique will be evaluated using two commonly used action datasets (IITR-IAR and TSF) to assess HAR methods. The implemented model's efficacy is further shown by the results.

4.1. DATASETS

As seen in Figure 4, the IITR-IAR dataset contains 21 action types that may be generally categorized into three groups. They are (1) individual actions: two hand wave (wave2), one hand wave (wave1), walking (walk), running (run), hopping (hop), crouching (crouch) and clapping (clap). (2) person-object interaction: throwing object (throw), clicking selfie (selfie), recording video (video), picking up an object (pickup), carrying/pointing a gun (gun), dropping object (drop) and (3) person-person interaction: pushing (push), punching (punch), passing object (pass), kicking (kick), hugging (hug), handshaking (handshake), fighting (fight) and chasing (chase). For each action class, 70 videos containing 35 distinct individuals aged 8 to 37 have been gathered. As shown in Figure 5, a total of 44 videos are gathered, with 35 videos including a fall in addition to typical ADL and 9 videos simply containing ADL. There are several empty frames in the dataset, i.e. scenarios in which no human is present. It also includes shots of individuals attempting to enter from the left and right.

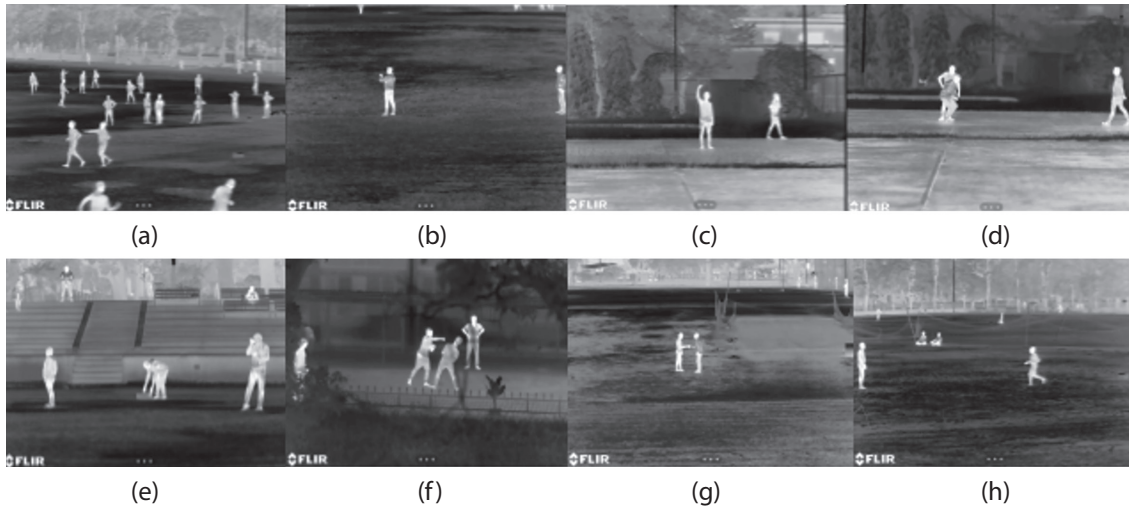


Fig. 4. IITR-IAR dataset a) chase, b) clap, c) Taking selfie, d) crouch, e) drop object, f) fight, g) handshaking, h) run



Fig. 5. Sample images from the Thermal ADL dataset

4.2. ANALYSIS METRICS

We evaluated the proposed model using the most standard metrics, including Accuracy, Precision, Recall, and F1-score. These are mathematically in equations (8) to (11)

$$Precision = \frac{TP}{TP + FP} \quad (9)$$

$$Accuracy = \frac{TP + TN}{TP + TN + FP + FN} \quad (10)$$

$$Recall = \frac{TP}{TP + FN} \quad (11)$$

$$F1\text{-score} = 2 \times \frac{Precision \times Recall}{Precision + Recall} \quad (12)$$

True positive (TP) refers to violent action accurately detected, whereas false positive (FP) refers to nonviolent or normal activity wrongly forecasted as violent. True negative (TN) represents accurately determined nonviolent activity statistics. False negatives (FN) are violent events misclassified as nonviolence.

4.3. IMPLEMENTATION AND PARAMETER SETTINGS

Before training the model, appropriate adjustments of parameters are necessary. Here, chose 128 as the default sliding window size and 25 as the default stride for all experimental datasets, which is a tradeoff between classification performances. Furthermore, Adam is utilized to update CV-FCN parameters with a momentum of 0.9. The learning rate η is 0.0001. The mini-batch size is fixed at 30. Until the model converges, the training epoch number is 200. In addition, dropout regularization is used to reduce dimensionality. Experiments were performed on a personal workstation with an Intel Core i7 8th edition CPU, 4 GB GPU driver providing CUDA, 64 bits processor, RAM capacity of 8 GB, and Windows 10 operating system. The deep architecture has been implemented in Python.

We initially built the frame-level detector to recognize human actions using a single utilizing the key-frames taken from the clips. A frame is used as the detector's input in this portion. These qualities help identify activities by integrating contextual information in the boxes. Then temporal context attributes

(DeepLabV3+ and CV-FCN) are added and motion information (optical flow) to the frame-level framework as an initial point. These characteristics are designed to capture video motion patterns and give additional temporal information across frames.

4.4. TRAINING AND TESTING ON IITR-IAR DATASET

The proposed IITR-IAR dataset includes 21 action types. Each image is taken at a 1024×768 resolution. We chose 45 videos from each class at random as training images and the remaining 25 for testing. All of the tests are carried out multiple times.

4.4.1. Performance analysis of proposed method on IITR-IAR dataset

We provide demonstrations of qualitative outcomes for many sorts of situations in videos captured at various times. Adopting the frame-level and Spatio-temporal frameworks, these outcomes are produced. Figure 6 illustrates various sample outcomes of HAR in sequential video frames. In other instances, aggressive activities such as fighting, shooting, pursuing, and kicking are also seen. Individuals, on the other hand, exhibit normal activities such as sitting, standing, taking selfies, and sometimes walking at night. It is also observed that it is complicated to distinguish partial activities. It is correlated to the object's size. Also noted is that the integration of Spatio-temporal data enables the combination of motion and appearance characteristics across frames. Consequently, the proposed method distinguishes between normal and violent behavior.

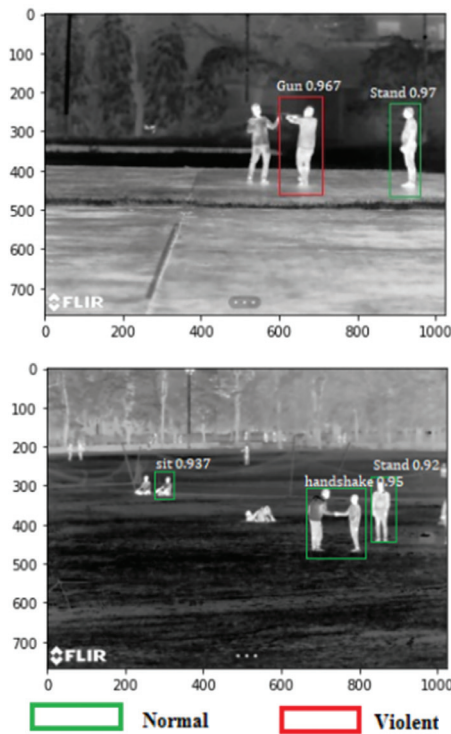


Fig. 6. Recognition results of normal and violent actions in an infrared video

Figures 7 and 8 depict the confusion matrices for the two distinct cases. It is evident from the data that the majority of complicated action examples are accurately identified. The minimum recognition accuracy (93%) is attained for routine outdoor activities that record actions. While the highest accuracy (96%) is attained for maximum normal actions and 97 percent for violent acts in an outdoor scenario. Only the punch and push classes are unclear. This is because both acts entail two people approaching one another and then utilizing either two hands (for a push) or a single hand (for a punch) to achieve the desired action. Overall, we reach a baseline average precision of 98.5% throughout the whole dataset. Figure 9 demonstrates that the ROC curves for both the normal and abnormal categories have desirable qualities and that the classification impact and generalizability are rather robust.

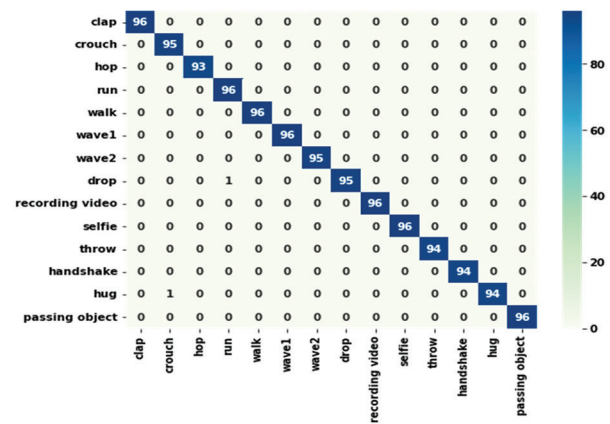


Fig. 7. Confusion matrix for Non-Violent activities

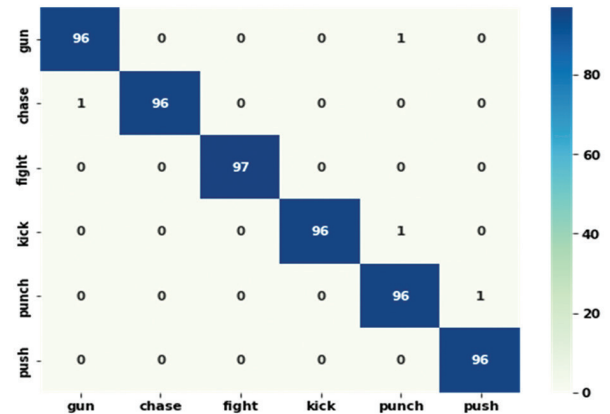


Fig. 8. Confusion matrix for violent activities

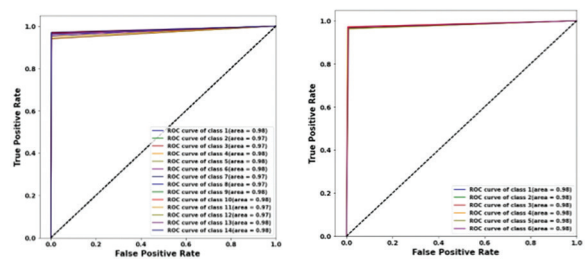


Fig. 9. ROC for normal activities and violent activities

4.4.2. Comparison with existing methods

To examine the role of Spatio-temporal characteristics in the network, we compared the outcomes of our experiment to earlier research. The quantitative outcomes of this comparison are shown in Table 1. The performance of the proposed method is compared to the RGB data set [30]. Table 2 demonstrates that the proposed technique outperforms the Hockey-Fight dataset. Overall, performance increased in all categories, but particularly in those with increased movement in terms of greater displacements. This makes it easier to acquire motion data using optical flow.

Table 1. Accuracy of action recognition

Actions	Existing [22] (%)	Proposed (%)
Gun	74	86.9
Chase	91.3	89.27
Clap	98.6	89.76
Selfie	74	94.82
Crouch	82	89.11
Drop	48.6	95.17
Fight	86.6	98.45
Handshake	76	90.26
Hop	90.67	94.35
Hug	77.33	96.67
Kick	64	96.57
Pass	60	90.21
Pickup	50	95.92
Punch	53.3	96.97
Push	60	94.76
Video	80.67	96.84
Run	83.33	91.14
Throw	89.33	93.17
Walk	76.67	87.92
Wave 1	93.33	97.87
Wave 2	81.33	98.21

Table 2. Comparison in different dataset

Dataset	Actions	Precision	Recall	F1-Score	Accuracy
Proposed (Thermal)	Violent Activity	0.97	0.98	0.98	98.5%
	Normal Activity	0.98	0.97	0.97	
Hockey-Fight Dataset (RGB) [30]	Violent Activity	0.96	0.97	0.97	96%
	Normal Activity	0.97	0.96	0.96	

4.5. TRAINING AND TESTING ON TSF DATASET

For the training phase, only standard ADL clips are utilized. The video clips are utilized to train the models were not labelled since they all represented as normal ADL. During the testing phase, fall videos with both normal and fall frames are employed. In these videos,

the fall frames were labelled manually. The calculation of a test error may be used as an anomalous score to designate a fall frame as an abnormality. Quantitative findings are obtained by evaluating the proposed framework on 30% samples of the dataset.

4.5.1. Performance analysis of proposed method on TSF dataset

We provide an example of qualitative indoor environment outcomes. Figure 10 illustrates various sample findings of HAR in sequential video frames. In other instances, abnormal behaviors such as falling from standing, falling from a chair, and falling from a seated position are also recognized. Individuals, on the other hand, exhibit normal behaviors such as sitting, walking, laying down, bending, etc. Also, noted that partial activities are complex to recognize.

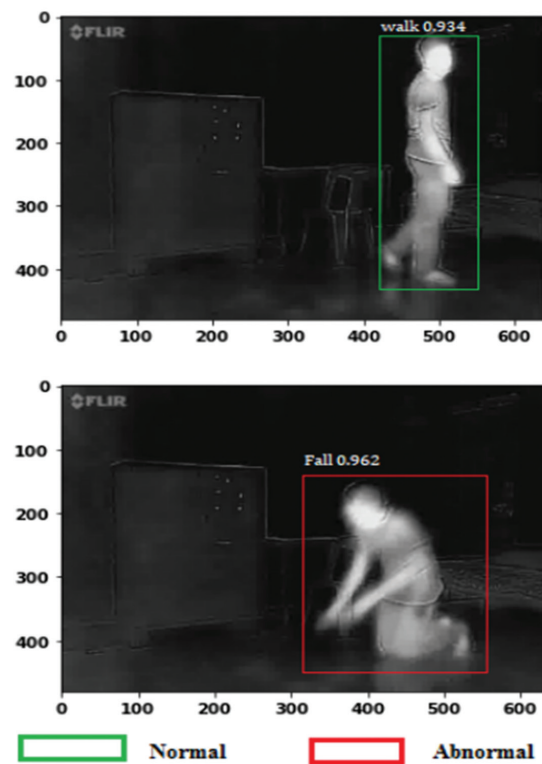


Fig. 10. Recognition results of normal and abnormal actions in an infrared video

Figures 11 and 12 illustrate the confusion metrics for indoor scenarios. It is evident from the data that the majority of complicated action examples are accurately identified. The lowest recognition accuracy (92%) is attained for routine indoor activities that capture actions. Maximum regular acts have the most accuracy (95%), whereas abnormal actions have the highest accuracy (97%). Only walk and stand classes confuse with each other since they have only minor changes. On the whole dataset, we reach 94.85% accuracy. Figure 13 demonstrates that the ROC curves for both the normal and abnormal categories have desirable qualities and that the classification impact and generalizability are rather robust.

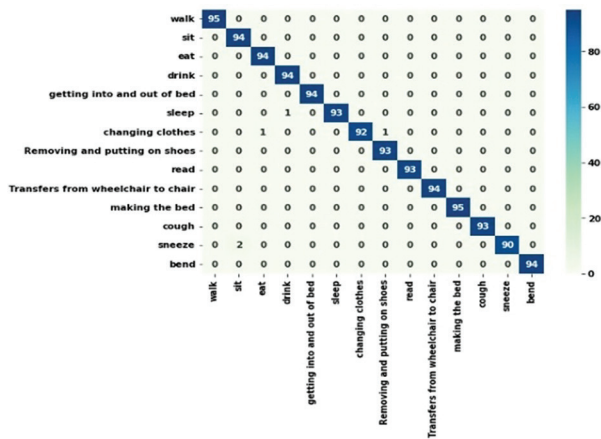


Fig.11. Confusion matrix for Normal activities

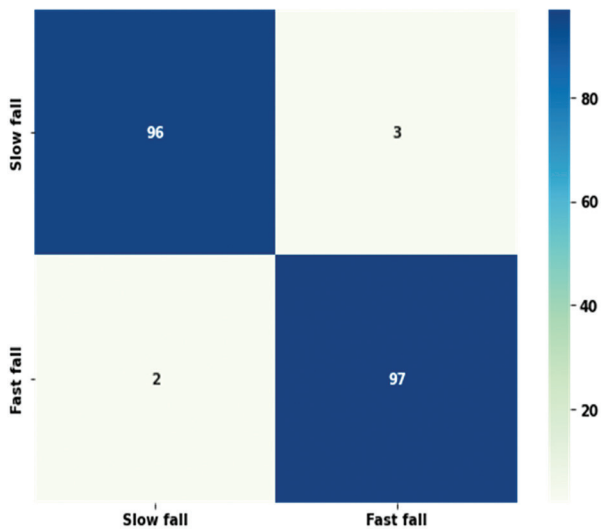


Fig. 12. Confusion matrix for abnormal activities

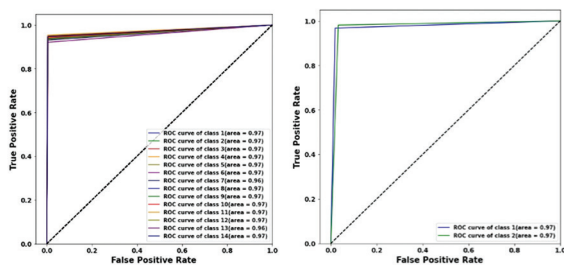


Fig. 13. ROC for normal activities and abnormal activities

Figure 14 depicts accurate predictions with their highest confidence ratings for a single action video based on our proposed system. A set of frames for each action is also provided for readers' convenience. It is noted from the experiments that the complex actions such as "kneel down" and "fall" which has a minor difference in the same action have more than 90% accuracy. The confidence score for normal actions like walking, sitting, kneeling, lying, sleeping, making the bed, bend show 86.88%, 92.17%, 93.3%, 95.48%, 95%, 97.22% and 90.08% respectively. The abnormal action like falls shows about 95.96% which reveals an effective result.

Sequence of frames representing an action					Predictions	Confidence score (%)
					walk	86.88
					sit	92.17
					Kneel down	93.3
					lying on the table	95.48
					sleep	95
					making the bed	97.22
					bend	90.08
					fall	95.96

Fig.14. Some prediction results on the TSF dataset with a maximum confidence score

4.5.2. Comparison with existing methods

The proposed model is compared with Deep Spatio-Temporal Convolutional Autoencoders (DSTCAE) [31] since they too are implemented on a similar dataset. The results for comparison of existing with the proposed method are shown in Table 3. It is noted that the proposed model performs better than the DSTCAE model. This is because the proposed approach extracts both spatial and temporal characteristics from videos that are essential for fall detection.

Table 3. Comparison with existing methods

Methods	Precision	Recall	F1-Score	Accuracy
Proposed	94.12	94.14	94.14	94.85%
DSTCAE [31]	-	-	-	93%

In conclusion, the findings demonstrated that the approach provided by this research is effective in recognizing activities in complicated indoor and outdoor scenarios.

5. CONCLUSION AND FUTURE SCOPE

Human activity detection is a complex issue with a wide range of applications in entertainment, autonomous driving, human-computer interaction and visual surveillance. This research proposes a deep learning strategy for recognizing human behavior using Spatio-temporal data. The framework includes frame-level appearance attributes and spatial and temporal information with temporal-context features. The proposed work identifies multiple regions containing human activities, unlike single-action approaches. The experiment is conducted on IITR-IAR and TSF datasets. The system can distinguish 38 sequential behaviors divided

into normal, abnormal and violent activities. Qualitative and quantitative findings illustrate our framework's monitoring effectiveness. This research reveals new issues in detecting human behavior for optimum conditions. Future work of this research may include control appliances, yoga analysis, sports actions through human body poses etc. In addition, the proposed method may be evaluated in more realistic conditions, such as zooming in and out etc.

6. REFERENCES

- [1] V. John, S. Mita, A. Lakshmanan, A. Boyali, S. Thompson, "Deep Visible and Thermal Camera-Based Optimal Semantic Segmentation Using Semantic Forecasting", *Journal of Autonomous Vehicles and Systems*, Vol. 1, 2021, pp. 106-119.
- [2] F. S. Leira, H. H. Helgesen, T. A. Johansen, T. I. Fossen, "Object detection, recognition, and tracking from UAVs using a thermal camera", *Journal of Field Robotics*, Vol. 38, 2021, pp. 242-267.
- [3] M. Kristo, M. Ivasic-Kos, M. Pobar, "Thermal object detection in difficult weather conditions using YOLO", *IEEE Access*, Vol. 8, 2021, pp. 125459-125476.
- [4] J. Kim, J. Cho, "Low-cost embedded system using convolutional neural networks-based spatiotemporal feature map for real-time human action recognition", *Applied Sciences*, Vol. 11, 2021, p. 4940.
- [5] V. Parameswari, S. Pushpalatha, "Human Activity Recognition using SVM and Deep Learning", *European Journal of Molecular & Clinical Medicine*, Vol. 7, 2020, pp. 134-144
- [6] A. B. Sargano, X. Gu, P. Angelov, Z. Habib, "Human action recognition using deep rule-based classifier", *Multimedia Tools and Applications*, Vol. 79, 2020, pp. 30653-30667.
- [7] M. E. N. Gomes, D. Macêdo, C. Zanchettin, P. S. G. de Mattos-Neto, A. Oliveira, "Multi-human fall detection and localization in videos", *Computer Vision and Image Understanding*, Vol. 1, 2022, pp. 103442.
- [8] F. S. Leira, H. H. Helgesen, T. A. Johansen, T. I. Fossen, "Object detection, recognition, and tracking from UAVs using a thermal camera", *Journal of Field Robotics*, Vol. 38, 2021, pp. 242-267.
- [9] C. Dhiman, D. K. Vishwakarma, "View-invariant deep architecture for human action recognition using two-stream motion and shape temporal dynamics", *IEEE Transactions on Image Processing*, Vol. 29, 2020, pp. 3835-3844.
- [10] H. Liu, Y. Chen, W. Zhao, S. Zhang, Z. Zhang, "Human pose recognition via adaptive distribution encoding for action perception in the self-regulated learning process", *Infrared Physics & Technology*, Vol. 114, 2021, p. 103660.
- [11] R. Kapoor, R. Goel, A. Sharma, "Deep learning based object and railway track recognition using train mounted thermal imaging system", *Journal of Computational and Theoretical Nanoscience*, Vol. 17, No. 11, 2020, pp. 5062-5071.
- [12] M. A. Khan, Y. D. Zhang, S. A. Khan, M. Attique, A. Rehman, S. Seo, "A resource conscious human action recognition framework using 26-layered deep convolutional neural network", *Multimedia Tools and Applications*, Vol. 80, 2021, pp. 35827-35849.
- [13] K. Thapa, A. Al, Z. Md, B. Lamichhane, S. H. Yang, "A deep machine learning method for concurrent and interleaved human activity recognition", *Sensors*, Vol. 20, 2020, p. 5770.
- [14] D. Zhou, S. Qiu, Y. Song, K. Xia, "A pedestrian extraction algorithm based on single infrared image", *Infrared Physics & Technology*, Vol. 105, 2020, p. 103236.
- [15] Q. Kang, H. Zhao, D. Yang, H. S. Ahmed, J. Ma, "Lightweight convolutional neural network for vehicle recognition in thermal infrared images", *Infrared Physics & Technology*, Vol. 104, 2020, p. 103120.
- [16] P. Kovács, B. Lehner, G. Thummerer, G. Mayr, P. Burgholzer, M. Huemer, "Deep learning approaches for thermographic imaging", *Journal of Applied Physics*, Vol. 128, 2020, p. 155103.
- [17] M. Awais, X. Long, B. Yin, S. F. Abbasi, S. Akbarzadeh, C. Lu, W. Chen, "A hybrid DCNN-SVM model for classifying neonatal sleep and wake states based on facial expressions in video", *IEEE Journal of Biomedical and Health Informatics*, Vol. 25, No. 5, 2021, pp. 1441-1449.
- [18] C. Dhiman, D. K. Vishwakarma, "View-invariant deep architecture for human action recognition using two-stream motion and shape temporal dynamics", *IEEE Transactions on Image Processing*, Vol. 29, 2020, pp. 3835-3844.

- [19] D. K. Vishwakarma, "A two-fold transformation model for human action recognition using decisive pose", *Cognitive Systems Research*, Vol. 61, 2020, pp. 1-13.
- [20] H. Liu, X. Wang, W. Zhang, Z. Zhang, Y. F. Li, "Infrared head pose estimation with multi-scales feature fusion on the IRHP database for human attention recognition", *Neurocomputing*, Vol. 411, 2020, pp. 510-520.
- [21] S. A. Manssor, S. Sun, M. Abdalmajed, S. Ali, "Real-time human detection in thermal infrared imaging at night using enhanced Tiny-yolov3 network", *Journal of Real-Time Image Processing*, Vol. 19, 2022, pp. 261-274.
- [22] J. Imran, B. Raman, "Deep residual infrared action recognition by integrating local and global spatio-temporal cues", *Infrared Physics & Technology*, Vol. 102, 2019, pp. 103014.
- [23] M. Krišto, M. Ivasic-Kos, M. Pobar, "Thermal object detection in difficult weather conditions using YOLO", *IEEE Access*, Vol. 8, 2020, pp. 125459-125476.
- [24] G. Batchuluun, J. K. Kang, D. T. Nguyen, T. D. Pham, M. Arsalan, K. R. Park, "Action recognition from thermal videos using joint and skeleton information", *IEEE Access*, Vol. 9, 2021, pp. 11716-11733.
- [25] M. Ding, Y. Y. Ding, X. Z. Wu, X. H. Wang, Y. B. Xu, "Action recognition of individuals on an airport apron based on tracking bounding boxes of the thermal infrared target", *Infrared Physics & Technology*, Vol. 117, 2021, p. 103859.
- [26] H. Hei, X. Jian, E. Xiao, "Sample weights determination based on cosine similarity method as an extension to infrared action recognition", *Journal of Intelligent & Fuzzy Systems*, Vol. 40, 2021, pp. 3919-3930.
- [27] A. M. De Boissiere, R. Noumeir, "Infrared and 3d skeleton feature fusion for rgb-d action recognition", *IEEE Access*, Vol. 8, 2020, pp. 168297-168308.
- [28] S. Ren, K. He, R. Girshick, J. Sun, "Faster R-CNN: towards real-time object detection with region proposal networks", *IEEE Transactions on Pattern Analysis and Machine Intelligence*, Vol. 39, No. 6, 2017, pp. 1137-1149.
- [29] L. Yu, Y. Hu, X. Xie, Y. Lin, W. Hong, "Complex-valued full convolutional neural network for SAR target classification", *IEEE Geoscience and Remote Sensing Letters*, Vol. 17, 2019, pp. 1752-1756.
- [30] S. Habib, A. Hussain, W. Albattah, M. Islam, M. S. Khan, R. U. Khan, Khan, K. "Abnormal Activity Recognition from Surveillance Videos Using Convolutional Neural Network", *Sensors*, Vol. 21, 2021, p. 8291.
- [31] J. Nogas, S. S. Khan, A. Mihailidis, "Deepfall: Non-invasive fall detection with deep spatio-temporal convolutional autoencoders", *Journal of Healthcare Informatics Research*, Vol. 4, 2020, pp. 50-70.

The effect of quantized ETF, grouping, and power allocation on non-orthogonal multiple accesses for wireless communication networks

Original Scientific Paper

Amir F. Banob

Faculty of Engineering
Mansoura University
marioneta_mero@yahoo.com

Fayez W. Zaki

Faculty of Engineering
Mansoura University
fwzaki2017@gmail.com

Mohammed M. Ashour

Faculty of Engineering
Mansoura University
mohmoh2@yahoo.com

Abstract – Nonorthogonal multiple access (NOMA) is a significant technology in radio resource sharing and it has been recognized as a favorable method in fifth-generation (5G) wireless networks to meet the requirements of system capacity, service latency, and user connectivity. Many schemes for NOMA have been proposed in the last few years. such as transmitter linear spreading-based NOMA as a code domain, as well as a linear minimum mean square error (LMMSE), parallel interference cancellation (PIC), and serial interference cancellation (SIC) with power allocation and grouping as a power domain at the receiver side for uplink NOMA. This work aims to evaluate the performance of multiple types of linear spreading-based NOMA schemes. Simulations are achieved for the error-rate performance evaluation of these NOMA schemes, received signal after detection, and received signal and effect of every user on the other. Evaluating the performance of these technologies with comparison is also achieved through using grouping and power allocation. Simulations are achieved for the sum rate and spectral efficiency. For the future, 5G NOMA development, an equiangular tight frame (ETF) is suggested for improving performance and suggests grouping with 64qam-quantized Grassmannian for improving performance favorite about grouping with Generalized welch-bound equality (GWBE)

Keywords: Non-orthogonal multiple access (NOMA), fifth-generation (5G), equiangular tight frame (ETF), and generalized WBE (GWBE) sequences.

1. INTRODUCTION

Non-orthogonal multiple access (NOMA) has been introduced for both uplink and downlink transmission schemes to provide the need for higher connectivity and data rate in wireless communications that participated in the development of 5G[1]. The power and code domains are the two major categories of NOMA schemes. Diverse power levels are allocated to users to permit interference cancellation at the receiver side, in the power domain NOMA[2]. The spreading-based NOMA techniques that are essential for the code domain can be accomplished by using sequence-based spreading [3],[4]. The commonly

used receiver structure for symbol-based spreading is the parallel interference cancellation (PIC) receiver by uplink NOMA schemes, and grouping enhancement of multilevel average received powers can be combined with all existing NOMA schemes [5]. As part of the NOMA studies for 5G, several sequence-based spreading schemes are used, such as Grassmannian[6], [7], 64QAM-quantized Grassmannian[6], [7], pattern division multiple access (PCMA) [8], Welch-bound spreading multiple access (WSMA) [7], and generalized welch-bound equality (GWBE) sequences[7]. The spreading sequences with the lowest cross-correlation are supposed to be the preferable solution for NOMA transmission[9]. This work

aims to investigate and evaluate the performance of sequence-based spreading uplink NOMA for the above techniques compared with equiangular tight frame (ETF) matrix (4,8), and matrix (6,12) constructs by Paley's conference matrix. To gain further insight into spreading sequence design. The combination of power and code domain should be taken into consideration as well; more precisely, in addition to seeking sequences with low cross-correlations.

This paper is organized as follows: In Section II the system model provides 8 or 12 active detected users for six MA sequence spreading-NOMA as the code domain, and power allocation and grouping as the power domain are illustrated. Section III proposes strategies for NOMA improvements uplink performance. In section IV, the simulation results are presented.

2. LITERATURE REVIEW

To develop the mobile communication frameworks from the initial generation until 5G networks and beyond systems, many attempts have been developed to provide an increase in data rate requirements [10]. The recommendation of the International Telecommunication Union (ITU) for the IMT-2020 system, and the use of scripts for 5G and beyond frameworks included massive machine-type communications (mMTC), enhanced mobile broadband (eMBB), and reliable and self-contained communications Low latency (URLLC) [11]. Modern requirements become 1000 x average data rate for 4G with a response time of 1 ms, and 106 connections/km²[12]. With NOMA, users can be served with substantial resources such as frequency and/or time together with the use of sophisticated receivers. The 1st proposal of NOMA was to be applied to downlink to improve system capacity [13]. However, depending on the power variation among users, capabilities for uplink and downlink can grow by the NOMA field, which can achieve a 1.5x increase in system capacity [14]. Therefore, user association, energy allocation, and scheduling are studied extensively in many kinds of literature [15]. Various NOMA schemes, such as interleaved-division multiple access (IDMA), sparse code multiple access (SCMA) and multi-user shared access (MUSA) were introduced [16]. In Release 14, other multiple access (MA) (such as sequences, codebook, mapping pattern and interleaved) are used to group doubled users and simplified multi-user detection (MUD) at the receiver [17]. Due to the limited time in Release 14, NOMA was not completed [18]. Release 15 focused on the uplink However, power is not hard done by Releases 14 or 15, which assumed equal power at the receiver without enhancing the performance by power difference, which is an important issue of uplink NOMA [10]. The trade-off between complexity and performance by sequence-based NOMA schemes was explained in [19]. There are a variety of topics in Release 16 studies, including Multimedia Priority

Service, Vehicle-to-everything (V2X) application layer services, access to 5G satellites, support local area network in 5G, 5G wireless and wired convergence, terminal positioning and location, vertical domains communications and automation for network and techniques for novel radio [20].

3. SYSTEM MODEL

Some M users in uplink NOMA were spreading sequence (SS) vector s_k to the base station (BS), let b_M be the transmitted symbol that balances a unit norm. The additive white Gaussian noise (AWGN) signal model may be given as $y= Sb+z$, where z is the zero-mean AWGN vector with a covariance matrix I , i.e., an identity matrix. The in general SS matrix with an SS codeword (CW) in each of its columns is S , and the transmit symbol vector is b . It begins with the received power of each user being set to unity. A unit norm receives filter f_k , such as a linear minimum mean squared error (MMSE) filter, which may be employed by the receiver to obtain an estimate \hat{b}_k for the transmitted symbol b_k . [21]

$$y(t) = \sum_{k=1}^M \sqrt{P_M} h_M s_M(t) + n(t) \quad (1)$$

Come from synchronization NOMA.

$$y(t) = \sum_{k=1}^M A_M b_M [i] S_M(t - iT - \tau_M) + n(t) \quad (2) [21]$$

where, $s(t)$ is the superposition of the data signals for the M-users each having different power, where T is the bit period, $b_k \{-1,1\}$ is the information bit transmitted by user k during the time interval T , A_k is the amplitude of data received from user K , $\tau_k=0$ for synchronization, $n(t)$ is the AWGN with unit power spectral density (which models the thermal noise and all other noise sources unrelated to the transmitted signals) and σ is the standard deviation of the noise. σ^2 variance. $A_k=\sqrt{P_k}$, where h_i is the channel coefficient between m_{th} users and the base station (BS). [21]

Fig. 1. represents the transceiver uplink NOMA power domain

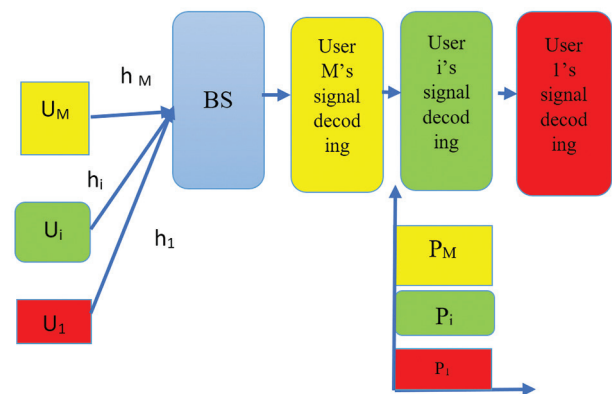


Fig. 1. transceiver uplink NOMA power domain

3.11 TRANSMITTER

3.1.1 MA SIGNATURES SEQUENCE

Comparing performance between six transmitted signals x_i has spreading-based NOMA schemes in 5G, namely, Grassmannian, 64QAM-quantized Grassmannian, PCMA, WSMA, GWBE, and ETF construct by Paley conference matrix. f_m is a unit norm receive filter, s_m is a unit norm spreading sequence (SS) vector, trace (.) represents the trace operator, v_m represents the noise component in the SINR γ_m , and w is the zero-mean AWGN vector with a covariance matrix I , i.e., an identity matrix, where s_m is employed by the receiver to obtain the estimation of the received signals. The postprocessing $SINR_m \gamma_m$ can be expressed as follows

$$\gamma_m = \frac{|f_m^H s_m|^2}{\sum_{i=1, i \neq m}^M |f_m^H s_i|^2 + |f_m^H w|^2} = \frac{f_m^H (s_m s_m^H) f_m}{f_m^H (\sum_{i=1, i \neq m}^M s_i s_i^H + I) f_m},$$

$$\xrightarrow{f_m = s_m}, SINR_m = \frac{1}{\text{trace}((ss^T)^2) - 1 + v_m} \quad (3) \quad [22] \quad [23]$$

The trace(.) term in the denominator is the total squared correlation (TSC). If the postprocessing noise is white, the noise power of each v_m is the same. It is known that reducing the denominator or comparably increasing $SINR_m$, where TSC can be particularly used as a performance metric and it is expressed as follows: after $\sum_{i=1}^m \sum_{j=1}^m |s_i^H s_j|^2$ Let $R_m = (\sum_{i=1, i \neq m}^m s_i s_i^H + I)$ is the correlation matrix of the interference plus noise for the m th user, R_m it can be identified that minimizing the denominator or equivalently maximizing γ_m is a well-known Rayleigh-quotient problem [22][23]

Fig. 2. represents the NOMA transmitter

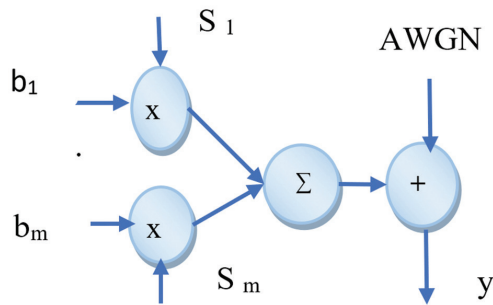


Fig. 2. NOMA transmitter

Sequence-based spreading NOMA schemes are considered 5G and rely on short-length sequences. Since the number of users is usually larger than the spreading factor, i.e., $N > K$, there will always be some cross-correlation among the sequences. Selecting the right codebook for a spreading-based NOMA is the key to achieving high performance, that is, the NOMA code domain

A finite unit-norm frame over the field C^m is a sequence of N vectors $f_i \in C^m$; $1 \leq i \leq N$; that satisfies $\|f_i\| = 1$ and $\alpha \|v\|_2^2 \leq \sum_{i=1}^N |f_i^H v|^2 \leq \beta \|v\|_2^2, \forall v \in C^m$. The paper introduces the frame synthesis matrix $F \in C^{m \times N}$ consist-

ing of the concatenated frame vectors $F = [f_1 \ f_2 \ f_3 \ f_4 \ \dots \ f_N]$. Constants of $\alpha, \beta \in R$ with $0 < \alpha \leq \beta < \infty$ are called the lower and upper bounds of the frame. If $\alpha = \beta$ then the frame is called tight.

3.2. SPREADING-CODE NOMA SCHEMES IN 5G

In this section, six spreading-based NOMA schemes Grassmannian, 64QAM-quantized Grassmannian, PCMA, WSMA, and GWBE, compared with the constructing Equiangular tight frame (ETF) are investigated, and the sequence and quantized version of the sequence can be obtained as follows.

GRASSMANNIAN SEQUENCE [24]

The chordal Distance method supposes we have two k -dimensional subspaces S, T in $G(k, n)$, and the columns of $S, T \in R^{n \times k}$ form orthonormal bases for S, T , respectively. The chordal distance between S and T , as a function of (S, T) , is given by

$$d_{chord}(S, T) = \sqrt{\sin^2 \theta_1 + \dots + \sin^2 \theta_k} = [k - \|S \times T\|_F^2]^{\frac{1}{2}} \quad (4)$$

principal angles between S and T is $\{\theta_1, \dots, \theta_k\} \in [0, \pi/2]$. Based on the SVD decomposition, $S^T T = U \Sigma V^T$, $\Sigma_{ii} = \cos \theta_i, i \in [k]$, and the second equation comes from $\|S^T T\|_F^2 = \sum_{i=1}^k \cos^2 \theta_i$. Given the Grassmannian manifold $G(k, n)$ of k -dimensional subspaces of the real Euclidean n -dimensional space R^n , find a set of N k -dimensional subspaces $\{S_1, \dots, S_N\} \subseteq G(k, n)$ spanned by the matrices $F = \{F_1, \dots, F_N\}$, that solves the mathematical program

$$\max_{F: |F| = N} \min_{F_i, F_j \in F, i \neq j} d_{chord}(F_i, F_j) \quad (5)$$

64QAM-QUANTIZED GRASSMANNIAN [25]

Constrain by Grassmannian spreading codebooks are normalized by multiplying $P_{no, N, K}$ which is $(K \times K)$ normalized matrix for the power constraints,

$$P_{no, N, K} = \begin{bmatrix} P_{no, 1} & 0 & 0 & 0 \\ 0 & P_{no, 2} & 0 & 0 \\ 0 & 0 & \ddots & 0 \\ 0 & 0 & 0 & P_{no, K} \end{bmatrix}$$

Here, $P_{no, N, K} = (1/|c^{(k)}|) \times \sqrt{N}$, for $k=1, \dots, K$. quantized via coefficients from 64QAM modulation.

The mapping function for the 64-point modulated symbol sequence of length 2 is listed in table 1. The constellation of output symbols is shown in fig (3), where x can be either 0 or 1 which means four-bit sequences are mapped to the same symbol.

Table 1 Mapping function for the 64-point modulated symbol sequence of length 2 shows the relation between the corresponding bit sequence and output symbol sequence. This table explains how to construct the 64QAM-quantized Grassmannian from the Grassmannian spreading sequence.

Table 1. Mapping function for the 64-point modulated symbol sequence of length 2

000 000	000 001	000 010	000 011	000 100	000 101	000 110	000 111
$\begin{bmatrix} 1+j \\ 1+j \end{bmatrix}$	$\begin{bmatrix} 1+3j \\ 1+3j \end{bmatrix}$	$\begin{bmatrix} 1-j \\ 1+j \end{bmatrix}$	$\begin{bmatrix} 1-3j \\ 1+3j \end{bmatrix}$	$\begin{bmatrix} 3+j \\ 3+j \end{bmatrix}$	$\begin{bmatrix} 3+3j \\ 3+3j \end{bmatrix}$	$\begin{bmatrix} 3-j \\ 3+j \end{bmatrix}$	$\begin{bmatrix} 3-3j \\ 3+3j \end{bmatrix}$
001 000	001 001	001 010	001 011	001 100	001 101	001 110	001 111
$\begin{bmatrix} -1+j \\ 1+j \end{bmatrix}$	$\begin{bmatrix} -1+3j \\ 1+3j \end{bmatrix}$	$\begin{bmatrix} -1-j \\ 1+j \end{bmatrix}$	$\begin{bmatrix} -1-3j \\ 1+3j \end{bmatrix}$	$\begin{bmatrix} -3+j \\ 3+j \end{bmatrix}$	$\begin{bmatrix} -3+3j \\ 3+3j \end{bmatrix}$	$\begin{bmatrix} -3-j \\ 3+j \end{bmatrix}$	$\begin{bmatrix} -3-3j \\ 3+3j \end{bmatrix}$
010 000	010 001	010 010	010 011	010 100	010 101	010 110	010 111
$\begin{bmatrix} 1+j \\ 1-j \end{bmatrix}$	$\begin{bmatrix} 1+3j \\ 1-3j \end{bmatrix}$	$\begin{bmatrix} 1-j \\ 1-j \end{bmatrix}$	$\begin{bmatrix} 1-3j \\ 1-3j \end{bmatrix}$	$\begin{bmatrix} 3+j \\ 3-j \end{bmatrix}$	$\begin{bmatrix} 3+3j \\ 3-3j \end{bmatrix}$	$\begin{bmatrix} 3-j \\ 3-j \end{bmatrix}$	$\begin{bmatrix} 3-3j \\ 3-3j \end{bmatrix}$
011 000	011 001	011 010	011 011	011 100	011 101	011 110	011 111
$\begin{bmatrix} -1+j \\ 1-j \end{bmatrix}$	$\begin{bmatrix} -1+3j \\ 1-3j \end{bmatrix}$	$\begin{bmatrix} -1-j \\ 1-j \end{bmatrix}$	$\begin{bmatrix} -1-3j \\ 1-3j \end{bmatrix}$	$\begin{bmatrix} -3+j \\ 3-j \end{bmatrix}$	$\begin{bmatrix} -3+3j \\ 3-3j \end{bmatrix}$	$\begin{bmatrix} -3-j \\ 3-j \end{bmatrix}$	$\begin{bmatrix} -3-3j \\ 3-3j \end{bmatrix}$
100 000	100 001	100 010	100 011	100 100	100 101	100 110	100 111
$\begin{bmatrix} 1+j \\ -1+j \end{bmatrix}$	$\begin{bmatrix} 1+3j \\ -1+3j \end{bmatrix}$	$\begin{bmatrix} 1-j \\ -1+j \end{bmatrix}$	$\begin{bmatrix} 1-3j \\ -1+3j \end{bmatrix}$	$\begin{bmatrix} 3+j \\ -3+j \end{bmatrix}$	$\begin{bmatrix} 3+3j \\ -3+3j \end{bmatrix}$	$\begin{bmatrix} 3-j \\ -3+j \end{bmatrix}$	$\begin{bmatrix} 3-3j \\ -3+3j \end{bmatrix}$
101 000	101 001	101 010	101 011	101 100	101 101	101 110	101 111
$\begin{bmatrix} -1+j \\ -1+j \end{bmatrix}$	$\begin{bmatrix} -1+3j \\ -1+3j \end{bmatrix}$	$\begin{bmatrix} -1-j \\ -1+j \end{bmatrix}$	$\begin{bmatrix} -1-3j \\ -1+3j \end{bmatrix}$	$\begin{bmatrix} -3+j \\ -3+j \end{bmatrix}$	$\begin{bmatrix} -3+3j \\ -3+3j \end{bmatrix}$	$\begin{bmatrix} -3-j \\ -3+j \end{bmatrix}$	$\begin{bmatrix} -3-3j \\ -3+3j \end{bmatrix}$
110 000	110 001	110 010	110 011	110 100	110 101	110 110	110 111
$\begin{bmatrix} 1+j \\ -1-j \end{bmatrix}$	$\begin{bmatrix} 1+3j \\ -1-3j \end{bmatrix}$	$\begin{bmatrix} 1-j \\ -1-j \end{bmatrix}$	$\begin{bmatrix} 1-3j \\ -1-3j \end{bmatrix}$	$\begin{bmatrix} 3+j \\ -3-j \end{bmatrix}$	$\begin{bmatrix} 3+3j \\ -3-3j \end{bmatrix}$	$\begin{bmatrix} 3-j \\ -3-j \end{bmatrix}$	$\begin{bmatrix} 3-3j \\ -3-3j \end{bmatrix}$
111 000	111 001	111 010	111 011	111 100	111 101	111 110	111 111
$\begin{bmatrix} -1+j \\ -1-j \end{bmatrix}$	$\begin{bmatrix} -1+3j \\ -1-3j \end{bmatrix}$	$\begin{bmatrix} -1-j \\ -1-j \end{bmatrix}$	$\begin{bmatrix} -1-3j \\ -1-3j \end{bmatrix}$	$\begin{bmatrix} -3+j \\ -3-j \end{bmatrix}$	$\begin{bmatrix} -3+3j \\ -3-3j \end{bmatrix}$	$\begin{bmatrix} -3-j \\ -3-j \end{bmatrix}$	$\begin{bmatrix} -3-3j \\ -3-3j \end{bmatrix}$

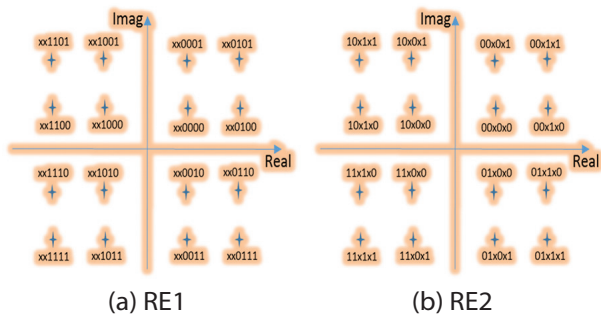


Fig. 3. 64 Point modulation constellation, x can be either 0 or 1.

PDMA [26] TYPE OF SPARSE SEQUENCE.

The transmitter side processing of PDMA with single-layer transmission is illustrated in Fig. 4. K users share the same time-frequency resources. For each UE, after channel coding and modulation, the modulated symbols are spread with a specific PDMA pattern, weighted by a given scaling factor, and then subjected to RE mapping. The details of the PDMA pattern, scaling factor, and RE mapping are given in the remainder of this section.

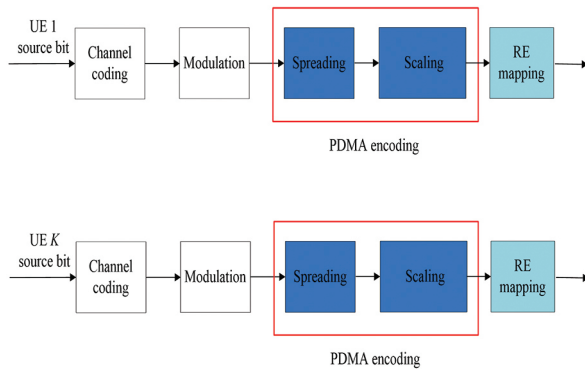


Fig. 4. PDMA with single-layer transmission

To support data transmission with higher spectral efficiency, PDMA with multiple-layer transmission can be supported. After channel coding and modulation,

the modulated symbols are divided into multiple layers. For different layers, the modulated symbols are spread with different PDMA patterns separately, and then weighted by independent scaling factors. Then, data from different layers are summed up and subjected to RE mapping. The PDMA pattern defines the sparse symbol-level spreading sequence in Figure 4. PDMA pattern g_k is an $N \times 1$ binary vector with elements "0" and "1", where N denotes the spreading factor and "1" can also be replaced by complex values. The K users' a PDMA patterns construct the PDMA pattern matrix $G^{[N \times K]}_{PDMA}$ with the dimension of $N \times K : G^{[N \times K]}_{PDMA} = [g_1, g_2, \dots, g_K]$. The scaling factor can be the power factor and/or phase factor. For PDMA with single-layer transmission, the scaling factor can be the power factor. $factor_{scaling}(K)$ for the PDMA pattern g_k , which achieves normalizing each RE power to be 1, can be calculated as follows:

$$factor_{scaling}(k) = \sqrt{\frac{N}{\sum (abs(g_k))^2}} \quad (6)$$

For PDMA with multiple-layer transmission, the scaling factor can be both a power factor and a phase factor. The different PDMA patterns for a single UE should be orthogonal.

RE mapping is two types of PDMA: type 1) Localized, and type 2) distributed. where 4 PRB and $g_2 = [1 \ 1 \ 0 \ 0]^T$ are assumed. Given a sufficiently large number of PRB and frequency selective channels with a large delay spread, distributed RE mapping can provide more frequency diversity than localized RE mapping.

WSMA [27]

The design metric for the signature vectors is the total squared cross-correlation $T_c \triangleq \sum_{i,j} |s_i^H s_j|^2$. The lower bound on the total squared cross-correlation of any set of K vectors of length N is $K^2/N \leq T_c$. The WBE sequences are designed to meet the bound on the total squared cross-correlations of the vector set with equality $B_{WBE} \triangleq K^2/N$.

GENERALIZED WBE (GWBE) SEQUENCES [28]

When $\sum_{k=1}^K P_k \geq N \cdot \max\{P_1, P_2, \dots, P_K\}$, the powers of multiple users are close enough and there are no oversized users; i.e., $K = \varphi$.

In this case, it reduces to $\lambda^* = \frac{\sum_i P_i}{N} \mathbf{1}_N$, and the optimal sequences satisfy $S^* P (S^*)^H = \frac{\sum_i P_i}{N} I_N$. It can be easily found that when $P_k = P \forall k$, $P = P I_{K^r}$ the optimal sequences satisfy $S^* (S^*)^H = \frac{K}{N} I_N$ [10]

3.1.2.

To find the optimal power allocation for MA signatures NOMA which enhances performance. It is necessary to assign different powers to each user's signals in a realistic communication system. For unequal received powers, the cross-correlations become $R_m = S^H P S$, where $P = \text{diag}\{P_1, \dots, P_m\}$ is a diagonal matrix, whose diagonal elements are the received powers of M users. Then, the optimal sequences satisfy

$$\min_{s_m^H, s_m=1 \forall k} R_m = \|S^H P S\|_F^2 = \sum_{i=1}^m \sum_{j=1}^m P_i P_j |s_i^H s_j|^2 \quad (7) \quad [29]$$

where P_j is the received power of user j . We use offset power between users =2 dB, 3 dB, 5 dB. From equation (7) using power allocation to enhance performance is a well-known Rayleigh quotient problem in equation (3).

Apply this method for 64QAM-quantized Grassmanian and GWBE.

It is a natural phenomenon, that a near-far effect exists in cellular networks. Applying the power allocation method for all MA signatures NOMA schemes are arranged to descend the detected users by calculating total squared correlation $= \sum_{i=1}^m \sum_{j=1}^m |S_i^H S_j|^2$ for every user. Then assuming that $\check{p}_1 \geq \check{p}_2 \geq \dots \geq \check{p}_m$, there is a constant offset power between every user and the total power remains constant.

$$\frac{1}{m} \sum_{i=1}^m p_i = \frac{1}{m} \sum_{i=1}^m \check{p}_i = P \quad (8)$$

where equal power $p_i=1$, m = numbers of users, $P=p_i \times m$, offset power = 1 dB, 3 dB, 5 dB. \check{p}_i is the new power for every user after using the offset power. Then, we study the effect of the power allocation method on the performance of MA signature NOMA schemes.

3.1.3

The third sequence with grouping enhances performance. In grouping with power allocation: For any sequence pool with L sequences, the sequence pool can be divided into G groups for interference reduction and performance enhancement. Only the cross-correlations among sequences in groups with lower received powers matter. Therefore, the optimal sequences in a group g should satisfy [29].

$$\min_{s_m^H, s_m=1 \forall k} R_m = \min_{S_g} \sum_{m,n \geq g} \sum_{i \in \mathcal{K}_m} \sum_{j \in \mathcal{K}_n} \check{P}_m \check{P}_n |s_i^H s_j|^2 \quad (9)$$

where S_g is composed of sequences for group g , \mathcal{K}_m and P_m denote the set of sequence indices and average received power of group m , respectively, and $\check{P}_1 \geq \dots \geq \check{P}_G$ we will use offset power between groups =5 dB. From equation (21) using grouping with power allocation to enhance performance is a well-known Rayleigh quotient problem which in equation (3)

To enhance performance, apply the grouping method for all MA signatures NOMA schemes, first arrange to descend the detected users by calculating total squared correlation $= \sum_{i=1}^m \sum_{j=1}^m |S_i^H S_j|^2$ for every user, then compose the number of groups from descending users then assume $\check{p}_{G1} \geq \check{p}_{G2} \geq \check{p}_{G3}$, there is a constant offset power between every group and the total power remains constant; where

$$\frac{1}{m} \sum_{i=1}^m p_i = \frac{1}{n} \sum_{G=1}^G \sum_{n=1}^n \check{p}_G = P \quad (10)$$

Where $p_i=1$, m =numbers of users, $P=p_i \times m$, n =number of users in the group= no of groups, offset power = 1 dB, 3 dB, 5 dB, and the low power was given with the

low total squared correlation group. The first trial divides users into two groups.

Fig. 5. represents the grouping method FIG (5) represents the grouping method apply this method for Grassmannian sequence, WSMA spreading, 64 QAM-quantized Grassmannian sequences, GWBE sequences, sparse sequences, and ETFs.

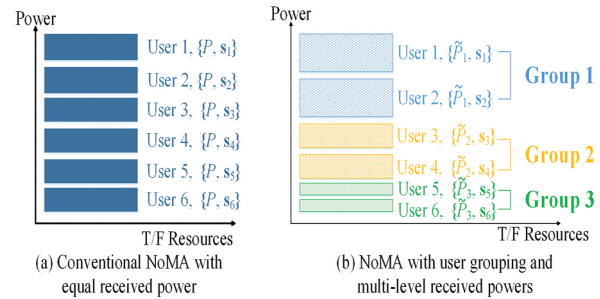


Fig. 5. grouping method

3.3 RECEIVER DETECTOR

Linear minimum mean square error (LMMSE), interference cancellation (parallel and serial) PIC, SIC.

Fig. 6. represents linear minimum mean square error (LMMSE)

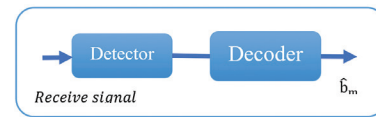


Fig. 6. Linear minimum mean square error (LMMSE)

$$\hat{b}_m = \text{sgn} \left(\frac{1}{A_m} ([R + \sigma^2 A^{-2}]^{-1} y)_m \right) = \text{sgn}([R + \sigma^2 A^{-2}] y)_m \quad (11) \quad [21]$$

Where R is normalized cross correlation, A is received amplitudes, and σ is the noise

PARALLEL INTERFERENCE CANCELLATION (PIC)

Fig (7) represents parallel interference cancellation (PIC)

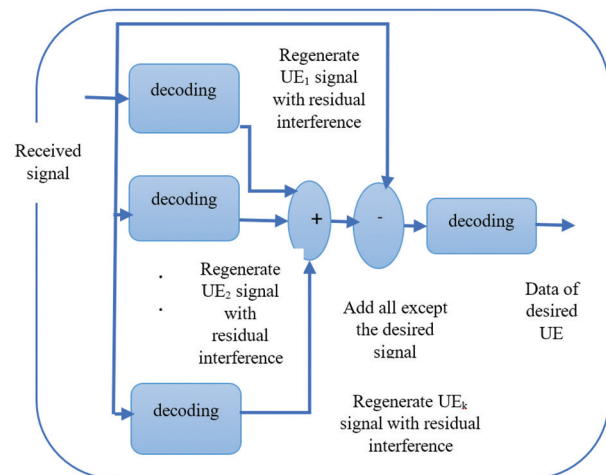


Fig. 7. Parallel interference cancellation (PIC)

An index n represents the iteration $n=0, 1, 2, \dots$, the user ($m=1, 2, \dots, M$), Let the symbol estimate \hat{x}_m^n . Those estimates from iteration n , updated estimate at iteration $n+1$ is

$$\hat{x}^{(n+1)} = A^{-1}(y - (R - I)A\hat{x}^{(n)}) \quad (12) [30]$$

SERIAL INTERFERENCE CANCELLATION (SIC)

Let the strictly lower triangular part be L of $R=L + L^t + I$. Then the vector form is Estimates $\hat{x}^{(n)}$, and received vector y .

$$\hat{x}^{n+1} = A^{-1}(y - LA\hat{x}^{(n-1)} - L^t A\hat{x}^{(n)}) \quad (13) [30]$$

Fig. 8. represents serial interference cancellation (SIC)

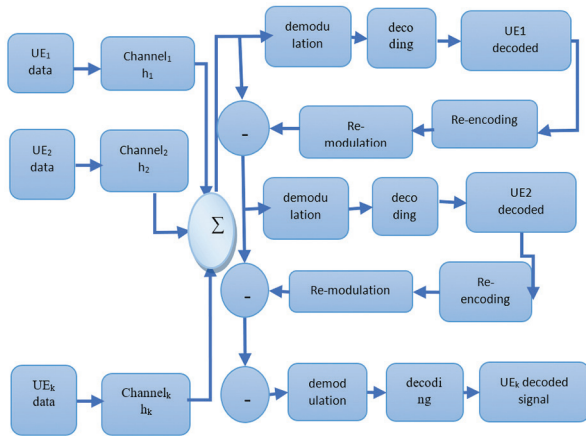


Fig. 8. Serial interference cancellation (SIC)

LINEAR MINIMUM MEAN SQUARE ERROR (LMMSE), PARALLEL INTERFERENCE CANCELLATION (PIC).

Fig (9) represents linear minimum mean square error (LMMSE) with parallel interference cancellation (PIC).

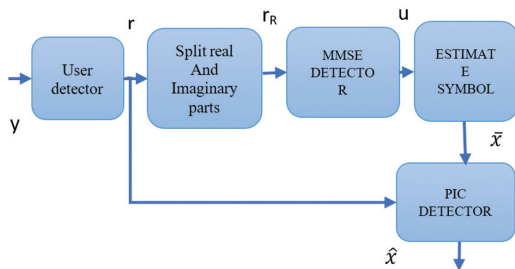


Fig. 9. Linear minimum mean square error (LMMSE) with parallel interference cancellation (PIC).

3.4 MATCHING BETWEEN ANALYTIC AND SIMULATION [31]

The corresponding general analytic synchronization bit error rate in NOMA for MF was calculated as the follows:

$$P_{em} = \frac{1}{2^{N-1}} \sum_{j \neq m}^{N-1} Q\left(\frac{A_m + \sum A_j \rho_{1j}}{\sigma}\right) + Q\left(\frac{A_m - \sum A_j \rho_{1j}}{\sigma}\right), j \neq m \quad (14)$$

where ρ is the cross correlation, p is probability of error, A is received amplitudes and σ is the noise

$$\begin{aligned} & \text{real}(\rho_{ij}) \text{ used, imaginary}(\rho_{ij}) \\ & = 0, \text{ also neglects the first part} \\ & 0 \leq |\rho_1 \pm \rho_{12} \pm \rho_{13} \pm \rho_{14} \pm \rho_{15} \pm \rho_{16} \pm \rho_{17} \pm \rho_{18}| \leq 1 \end{aligned}$$

The corresponding general analytic synchronization bit error rate in NOMA for the correlator was calculated as the follows:

$$P_{em} = \frac{1}{2^{N-1}} \sum_{j \neq m}^{N-1} Q\left(\frac{1 + \sum A_j \rho_{1j}}{\sigma}\right) + Q\left(\frac{1 - \sum A_j \rho_{1j}}{\sigma}\right), \quad (15)$$

$$\begin{aligned} & \text{real}(\rho_{ij}) \text{ used, imaginary}(\rho_{ij}) \\ & = 0, \text{ also neglects the first part} \end{aligned}$$

3.5. ACHIEVABLE SUM-RATE ANALYSIS

For comparison among different CD NOMA schemes. evaluate in this section the achievable rates and the spectral efficiency. Compute the capacities of the continuous-input-continuous-output memoryless channel (CCMC)

3.5.1. CCMC CAPACITY

As a result, the ergodic CCMC capacity at the j -th user for the described NOMA system is generally (regardless of the employed scheme ETF, GWBE, PDMA, 64QAM-quantized Grassmannian, Grassmannian, and WSMA where $SNR = JN_0, \frac{1}{K} = \text{frame gain}$, k is the width dimension of the frame, $E_{H_j, F}$ is ergodic capacity, and N_0 is the spectral power density at each j receiver given by[32]

$$C_j^{CCMC} = E_{H_j, F} \left[\log_2 \det \left(I_K + \frac{1}{JN_0} H_j F F^H H_j^H \right) \right] \quad (16)$$

The instances of the matrix F and the channel H_j greatly, influence the sum-rate performance.

4. PROPOSED NONORTHOGONAL MULTIPLE ACCESS (NOMA) ENHANCES UPLINK PERFORMANCE

In this section, three enhancements for uplink NOMA are proposed. The first at transmitter constrain ETF matrix (4,8), matrix (6,12) by Paley's conference matrix, where this transmitted matrix enhances performance compared with Grassmannian sequence, WSMA spreading, 64 QAM-quantized Grassmannian Sequence, GWBE sequences, and sparse sequence. The second proposed using power allocation with grouping to achieve the best performance for 64 QAM-quantized Grassmannian sequence, and GWBE sequences better than using only power allocation. The third proposed using grouping with 64QAM-quantized Grassmannian with a power offset of 5 dB enhances performance more than using grouping with GWBE with a power offset of 5 dB.

4.1 CONSTRUCT ETF MATRIX (4,8), AND MATRIX (6,12) BY PALEY'S CONFERENCE MATRIX ENHANCE PERFORMANCE COMPARE WITH USING POWER ALLOCATION OR GROUPING WITH POWER ALLOCATION FOR THESE MATRICES (GRASSMANNIAN SEQUENCE, WSMA SPREADING, 64 QAM-QUANTIZED GRASSMANNIAN SEQUENCE, GWBE SEQUENCES, AND PDMA SEQUENCE)

ETF for construction Conference matrix of size $n \times n$, Let ψ be a quadratic character of F . For different matrix $x, y \in F$ we write $Q = (\psi(x - y))$, The diagonal elements of Q are all 0 and the other elements are in $\{1, -1\}$. The matrix Q satisfies, $Q^T = \begin{cases} Q & \text{if } q \equiv 1 \pmod{4} \\ -Q & \text{if } q \equiv 3 \pmod{4} \end{cases}$

conference matrix 8x8

$$\begin{bmatrix} 0 & +1 & +1 & +1 & +1 & +1 & +1 & +1 \\ -1 & 0 & +1 & +1 & -1 & +1 & -1 & -1 \\ -1 & -1 & 0 & +1 & +1 & -1 & +1 & -1 \\ -1 & -1 & -1 & 0 & +1 & +1 & -1 & +1 \\ -1 & +1 & -1 & -1 & 0 & +1 & +1 & -1 \\ -1 & -1 & +1 & -1 & -1 & 0 & +1 & +1 \\ -1 & +1 & -1 & +1 & -1 & -1 & 0 & +1 \\ -1 & +1 & +1 & -1 & +1 & -1 & -1 & 0 \end{bmatrix}$$

S (4x8)

$$\begin{bmatrix} -0.00 - 0.00i & 0.30 - 0.78i & 0.07 + 0.20i & 0.28 + 0.10i \\ -0.20 - 0.26i & 0.53 + 0.49i & -0.38 + 0.16i & -0.60 + 0.10i, \dots \\ -0.00 - 0.00i & -0.16 - 0.10i & -0.03 + 0.23i & 0.22 - 0.67i \\ 0.29 + 0.59i & 0.03 + 0.27i & -0.80 - 0.08i & 0.46 - 0.25i, \dots \\ 0.00 - 0.00i & 0.27 - 0.22i & 0.57 + 0.65i & -0.41 + 0.33i \\ -0.54 + 0.16i & -0.01 - 0.51i & -0.20 - 0.06i & 0.31 - 0.35i, \dots \\ -1.00 - 0.00i & 0.00 - 0.38i & -0.00 - 0.38i & -0.00 - 0.38i \\ -0.00 - 0.38i & -0.00 - 0.38i & -0.00 - 0.38i & -0.00 - 0.38i \end{bmatrix}$$

conference matrix 12x12

$$\begin{bmatrix} 0 & +1 & +1 & +1 & +1 & +1 & +1 & +1 & +1 & +1 & +1 & +1 \\ -1 & 0 & +1 & -1 & +1 & +1 & -1 & -1 & -1 & +1 & -1 & -1 \\ -1 & -1 & 0 & +1 & -1 & +1 & +1 & +1 & -1 & -1 & +1 & +1 \\ -1 & +1 & -1 & 0 & +1 & -1 & +1 & +1 & +1 & -1 & -1 & -1 \\ -1 & -1 & +1 & -1 & 0 & +1 & -1 & +1 & +1 & +1 & -1 & -1 \\ -1 & -1 & -1 & -1 & +1 & -1 & 0 & +1 & -1 & +1 & +1 & +1 \\ -1 & +1 & -1 & -1 & -1 & +1 & -1 & 0 & +1 & -1 & +1 & +1 \\ -1 & +1 & +1 & -1 & -1 & -1 & +1 & -1 & 0 & +1 & -1 & +1 \\ -1 & +1 & +1 & +1 & -1 & -1 & -1 & +1 & -1 & 0 & +1 & -1 \\ -1 & -1 & +1 & +1 & +1 & -1 & -1 & -1 & +1 & -1 & 0 & +1 \\ -1 & +1 & -1 & +1 & +1 & +1 & -1 & -1 & -1 & +1 & -1 & 0 \end{bmatrix}$$

S (6x12)

$$\begin{bmatrix} -0.00 + 0.00i & -0.034 - 0.01i & 0.18 + 0.60i & -0.08 - 0.05i \\ 0.45 - 0.17i & -0.52 + 0.14i & -0.39 - 0.45i & 0.21 + 0.33i \\ -0.10 + 0.19i & 0.28 - 0.44i & 0.31 - 0.18i & -0.31 + 0.03i, \dots \\ 0.00 + 0.00i & -0.017 + 0.017i & -0.41 + 0.09i & 0.04 - 0.48i \\ 0.52 + 0.30i & -0.13 + 0.15i & -0.07 - 0.11i & -0.01 - 0.30i \\ 0.36 + 0.40i & -0.58 + 0.37i & 0.06 - 0.47i & 0.22 + 0.02i, \dots \\ -0.00 + 0.00i & 0.15 + 0.02i & 0.30 + 0.05i & 0.38 - 0.46i \\ 0.01 + 0.17i & -0.47 - 0.19i & 0.39 + 0.49i & -0.22 + 0.51i \\ 0.25 - 0.32i & -0.13 - 0.13i & -0.34 - 0.27i & -0.32 + 0.14i, \dots \\ -1.00 - 0.00i & 0.00 - 0.30i & 0.00 - 0.30i & 0.00 - 0.30i \\ -0.00 - 0.30i & 0.00 - 0.30i & 0.00 - 0.30i & 0.00 - 0.30i \\ -0.00 - 0.30i & -0.00 - 0.30i & -0.00 - 0.30i & -0.00 - 0.30i, \dots \\ 0.00 - 0.00i & -0.14 + 0.16i & -0.12 + 0.23i & -0.35 - 0.15i \\ -0.43 - 0.19i & -0.20 - 0.46i & 0.19 - 0.07i & 0.20 - 0.35i \\ 0.61 - 0.07i & 0.04 + 0.02i & 0.36 + 0.17i & -0.16 + 0.70i, \dots \\ -0.00 - 0.00i & 0.87 - 0.27i & -0.09 + 0.40i & -0.26 - 0.27i \\ -0.05 + 0.22i & 0.08 + 0.24i & -0.07 + 0.29i & -0.09 - 0.42i \\ -0.07 - 0.13i & -0.17 - 0.28i & 0.14 + 0.42i & -0.28 - 0.19i \end{bmatrix}$$

ii) $Qe = 0, QJ = 0$, iii) $QQ^T = qI - J$, where J is the matrix with all entries 1. $M = \begin{bmatrix} 0 & e^T \\ \psi(-1)e & Q \end{bmatrix}$, the conference matrix created by Paley different sets SVD for the conference matrix to construct the complex matrix size $n \times n$, extract a tight frame from C via SVD size $n \times k$ by nonzero eigenvalues are the first d elements on the diagonal of V , then $f^k = \frac{\sqrt{N}}{\sqrt{d}} \{V_{k,i}\}_{i=1}^d, P$ for $k = 1, \dots, N$ form an ETF in this example $\sqrt{2}$.

Let $R_k = (\sum_{j=1}^K s_j s_j^H + I)$, which is the correlation matrix of the interference plus noise $\sum_{j=1}^K s_j s_j^H$

For (4,8), the maximum cross-correlation is different for each sequence: Grassmannian 0.5772, WSMA 0.6845; 64QAM-quantized Grassmannian 0.7217; GWBE sequences 0.7502; sparse spreading 0.8165, ETF= 0.3780 and R_k ETF=16, GWBE=17.2060, Grassmannian=18.047, WSMA=18.165, 64QAM-quantized Grassmannian=19.19, and sparse=22. For (6,12), the maximum cross-correlation is different for each sequence; Grassmannian 0.3904; WSMA 0.7027; 64QAM-quantized Grassmannian 0.5459, and ETF= 0.3015, ETF achieve less maximum cross-correlation ρ and R_k ETF=24, 64QAM-quantized Grassmannian=29.104, and Grassmannian=29.5231, ETF achieve less R_k .

4.2. PROPOSES GROUPING [4,4] FOR MA SIGNATURE WITH A POWER OFF SET BETTER THAN ONLY POWER ALLOCATION

Where equation(9) obtain enhance than for equation(7)

For our example with Grouping [4,4] with offset 5 dB mathematical calculation for R_x to 64QAM-quantized Grassmannian=16.8615, GWBE=17.068, 64QAM-quantized Grassmannian, R_x for 0 dB = 19.19, for 2 dB = 19.757, for 3 dB = 19.975, for 5 dB = 20.2668, For GWBE, R_x for 0 dB = 17.206, for 2 dB = 17.367, for 3 dB = 17.450, for 5 dB = 17.538

Notice that grouping enhances performance more than only using power location between users where power allocation does not give tangible enhancement in performance

4.3. PROPOSES GROUPING [4,4] WITH OFFSET POWER FOR 64QAM-QUANTIZED GRASSMANNIAN ENHANCES PERFORMANCE COMPARED TO GWBE

Grouping with Power allocation division of the 8 users into two groups [4, 4], power = 5 dB, LMMSE-PIC detector the optimal sequences in group g should satisfy equation(9) for all other types of MA signatures. ETF=16.758, 64QAM-quantized Grassmannian=16.8615, GWBE=17.068, Grassmannian=17.247, WSMA=17.356, and sparse=18.0908.

5. SIMULATION RESULTS AND DISCUSSION

In this section, we display our assessment of different sequence-based spreading NOMA schemes, namely, Grassmannian, 64QAM-quantized Grassmannian, PCMA, WSMA, GWBE, and ETF. The detailed simulation assumptions are provided in table (2), using MATLAB in simulations.

Table 2. Simulation parameters

Parameter	Value or assumption
Programming	MATLAB
Modulation	BPSK
Signature allocation	Fixed
Channel estimation	Ideal
Number of B.S antenna	1
Frame length (N)	4,6
Number of users(K)	8, 12, 16, 24,64
Offset power	1 dB, 3 dB, 5 dB
Interference cancelation	PIC, SIC
Noise	AWGN
S/N	0:2:18 dB
Receiver type	LMMSE-PIC

5.1 ON THE EFFECT OF SPREADING CODE SEQUENCES ON AVERAGE BER

comparison between analytic and simulation to 8 users for matched filter and correlator

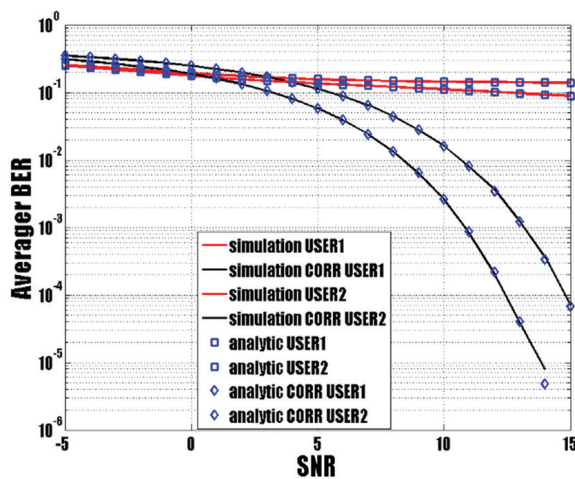


Fig. 10. GWBE spreading sequence relation between Average BER and SNR, Number of users =2

Fig (10) shows the relation between the average BER and SNR, where the number of users =2. A comparison between the analysis and simulation was carried out to ensure the used equations. The GWBE spreading sequence signal was applied using the MF detector and the correlation detector; there was a match between the analysis and simulation. The corresponding general analytic synchronization bit error rate in NOMA for MF was calculated as the follows.

Fig. (11,12,13,14,15) represent the BER versus the signal-to-noise ratio (SNR)

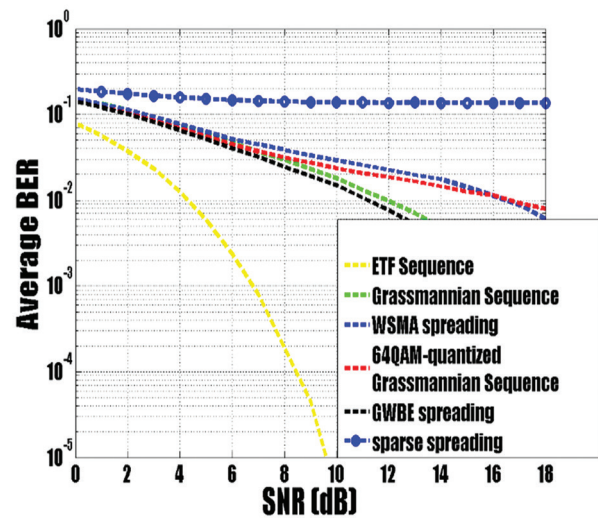


Fig. 11. Comparing the performance between different types of transmitted signals N=4

As shown in fig (11), where ETF NOMA spreading code where N=4, K=8, Grassmannian N=4, K=12, WSMA N=4, K=12, 64QAM-quantized Grassmannian N=4, K= 24, GWBE sequences N=4, K=16, PCMA K=64. assuming power for all users unity, receiver type is LMMSE-PIC, where $R = (\sum_{i=1, i \neq n}^N s_i s_i^H + I)$, compare the values of R for ETF=16, GWBE=17.2060, Grassmannian=18.047, WSMA=18.165, 64QAM-quantized Grassmannian=19.19, and sparse=22, by MATLAB simulation find that SNR will be enhanced for ETF than GWBE with gain in detection all 8 users and gain in performance, the figure shown that GWBE best than all other sequences which compact with 3GPP which considered GWBE sequence as a candidate for MA SIGNATURE sequence. Therefore, minimize the denominator $R = (\sum_{i=1, i \neq n}^N s_i s_i^H + I)$ or equivalently maximize $SINR_m$.

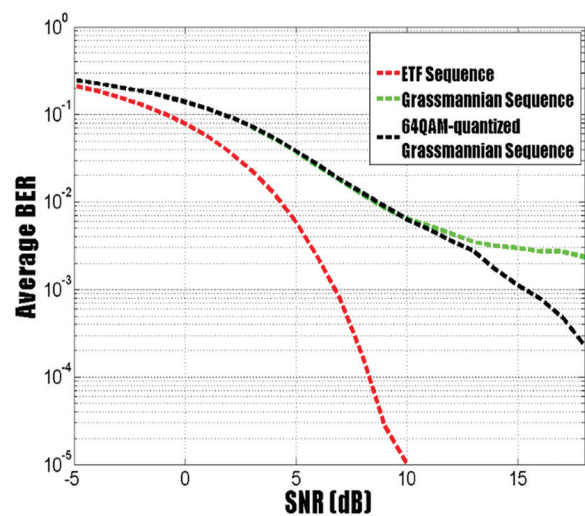


Fig. 12. Comparison between the performances of different types of transmitted signals N=6

Fig (12), where ETF NOMA spreading code $N=6$, $K=12$ for, Grassmannian $N=6$, $K=24$, 64QAM-quantized Grassmannian $N=6$, $K=24$, detection for 12 users, with equal power, In figure 9 Calculate the value $R = (\sum_{i=1}^N s_i s_i^H + I)$ for ETF, Grassmannian, and 64QAM-quantized Grassmannian, ETF=24, 64QAM-quantized Grassmannian=29.104, and Grassmannian=29.5231, MATLAB simulation finds that SNR will be enhanced for ETF than 64QAM-quantized Grassmannian or Grassmannian. This figure confirms equation (3) where minimizing the denominator maximizes $SINR_{n'}$ and proves the idea performance enhancement with ETF compared to other MA SIGNATURE sequences.

Fig. 11, and 12 illustrate that ETF spreading code enhancement performance gains 8 dB more than any other MA signature. Additionally, GWBE was better than all other sequences with 3GPP, which considered the GWBE sequence as a candidate for MA SIGNATURE sequence. This result was achieved by mathematic calculation and MATLAB simulation.

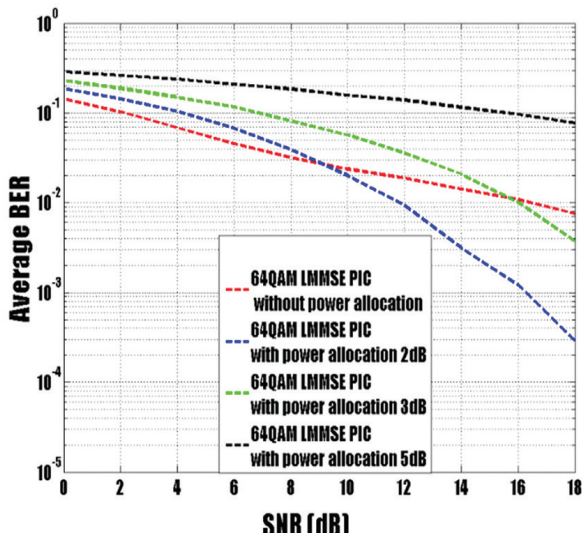


Fig. 13. Power allocation for 64QAM the spreading sequence code signal with offset power between users

Fig. 13 presents a try to obtain the optimal power allocation, where transmitted signal 64QAM spreading sequence code, where $N=4$ and $k=24$, detector LMMSE-PIC, detection for 8 users with different power offset between users =0 dB, 2 dB, 3 dB, and 5 dB. By mathematical calculation for equation(8) $\min_{s_k^H, s_k=1 \forall k} R_x = \|S^H P S\|_F^2 = i=1Kj=1KPiPjSiSj^H/2, R_x$ for 0 dB =19.19, for 2 dB =19.757, for 3 dB =19.975, for 5 dB =20.2668, compact with MATLAB simulation, shows that the best BER performance at 0 dB, then BER performance goes from bad to worse when using power allocation with power offset between users = 2 dB, 3 dB, and 5 dB for 64QAM-quantized Grassmannian spreading sequence code.

Fig. 14 presents attempt to obtain the optimal power allocation, transmitted signal GWBE spreading sequence code, where $N=4$ and $k=16$, detector LMMSE-

PIC, detection for 8 users with different power offsets between users =0 dB, 2 dB, 3 dB, and 5 dB. Then, by mathematical calculation for equation(7), R_x for 0 dB =17.206, for 2 dB =17.367, for 3 dB =17.450, for 5 dB =17.538, compact with the MATLAB simulation where the best BER performance at 0 dB, the BER deteriorates when using power allocation with power offset between users = 2 dB, 3 dB, and 5 dB. for GWBE spreading sequence code.

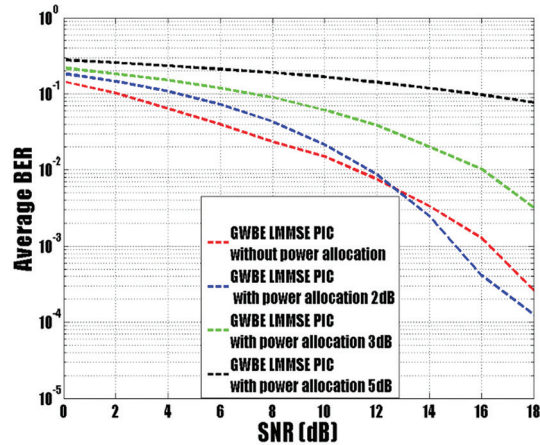


Fig. 14. Power allocation for THE GWBE spreading sequence code signal with offset power between users

Fig. 13, and 14 prove that $\min_{s_k^H, s_k=1 \forall k} R_x = \|S^H P S\|_F^2 = \sum_{i=1}^K \sum_{j=1}^K P_i P_j |s_i^H s_j|^2$ is the controller for optimal sequences using power allocation for the MA SIGNATURE sequence.

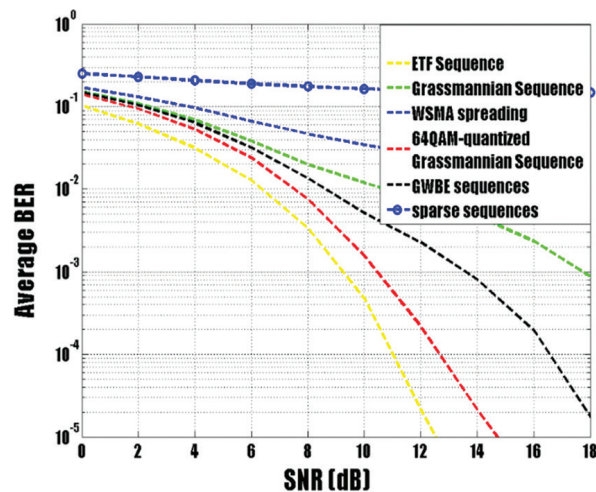


Fig. 15. Comparing the performance of different transmitted signals with grouping

Fig. 15. compares the performance of the transmitted signals (Grassmannian sequence $N=4$, $k=12$, WSMA spreading $N=4$, $k=12$, 64 QAM-quantized Grassmannian Sequence $N=4$, $k=24$, GWBE sequences $N=4$, $k=16$, and sparse sequence $N=4$, $k=64$) with a division of the 8 users into two groups [4, 4], power = 5 dB, LMMSE-

PIC detector the optimal sequences in group g should satisfy equation(9), the mathematical calculation for R_x to ETF=16.758, 64QAM-quantized Grassmannian=16.8615, GWBE=17.068, Grassmannian=17.247, WSMA=17.356, and sparse=18.0908. Comparing these values with mathematical calculation ETF=16, GWBE=17.2060, Grassmannian=18.047, WSMA=18.165, 64QAM-quantized Grassmannian=19.19, and PCMA =22 in figure 4, we observe that grouping for GWBE with power allocation enhances performance more than without grouping, which agrees with 3GPP, which assumes that grouping for GWBE is a candidate for enhanced performance for MA SIGNATURE. Additionally, from a comparison for 64QAM-quantized Grassmannian, we conclude that grouping of 64QAM-quantized Grassmannian enhances performance more than without grouping, grouping for 64QAM-quantized Grassmannian enhances performance more than GWBE grouping, and ETF grouping still gives better performance than grouping for 64QAM-quantized Grassmannian and GWBE grouping. These results achieved by mathematic calculation and MATLAB simulation. Also comparing results for figure 8 with results for figure 6 which mathematical values R_x for 0 dB =19.19, for 2 dB =19.757, for 3 dB =19.975, for 5 dB =20.2668 for 64QAM-quantized Grassmannian and with results for figure 12 which mathematical values R_x for 0 dB =17.206, for 2 dB =17.367, for 3 dB =17.450, for 5 dB =17.538 for GWBE. From the comparison, it can be concluded that grouping enhances performance more than without grouping or with only power allocation.

5.2 ON THE EFFECT OF SPREADING CODES ON THE RECEIVED SIGNAL AFTER DETECTION

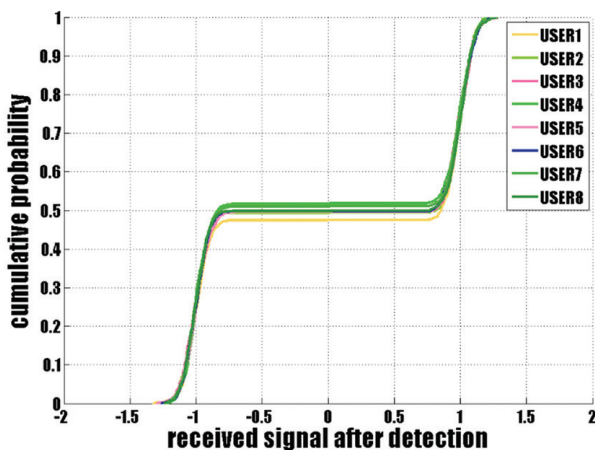


Fig. 16. CDF for ETF NOMA code

Fig. 16. illustrates detection for the ETF signal, detection for 8 users randomly with equal received power, where $N=4$, $K=8$, the empirical CDF presents in y-axis straight line increases begin near 1 and end near -1 for all 8 users mean that all users have received well after detection.

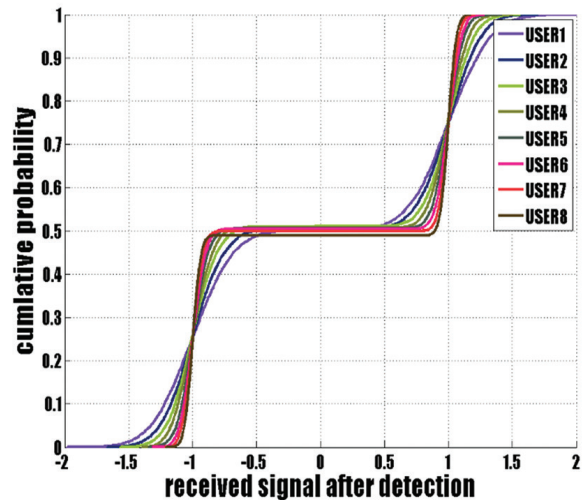


Fig. 17. CDF for GWBE NOMA code.

Fig. 17 shows the CDF for the GWBE spreading sequence, 8 users randomly received equal power. It illustrates that some users have straight-line increases beginning near 1 and ending near -1, and others have the straight line beginning near 0.5 and ending near -0.5, that is mean some users have received good detection, and others do not. The detection for all users is not similar; some are not perfect like the others

Compare figs (16,) and (17) by cumulative distribution function for 8 active users detected, which have been sent by ETF and GWBE NOMA spreading sequence, ETF better-received signal after detection than GWBE.

5.3 ON THE EFFECT OF SPREADING CODES ON THE RECEIVED SIGNAL AND THE EFFECT OF EVERY USER ON THE OTHER

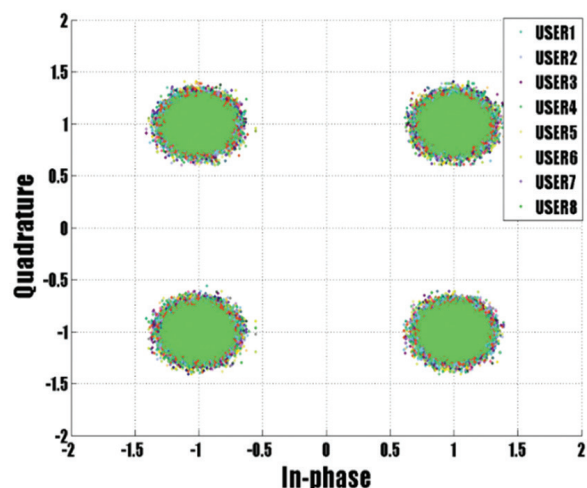


Fig. 18. Scatter diagram (constellation diagram), ETF NOMA spreading code

Fig (18) shows constellation diagrams for ETF sequence signals where $N=4$, $K=8$, and there are 8 users to detect. In MATLAB code we display the relation be-

tween any two users randomly, so here $\frac{k(k-1)}{2}$ relations among all users in the x-y plane (quadrature and in-phase). This reveals that the amount of data was more concentrated at approximately -1, -1. which means that the inter-symbol interference (ISI) is not too high.

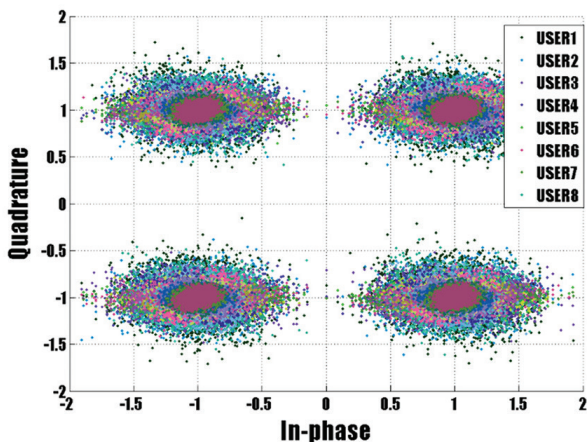


Fig. 19. Scatter diagram (constellation diagram), GWBE spreading code.

Fig (19) shows constellation diagrams for the GWBE sequence signal where $N=4$, $K=8$, and there are 8 users to detect with equal received power. In MATLAB code, we display the relation between any two users randomly, so here $\frac{k(k-1)}{2}$ relations among all users in the x-y plane (quadrature and in-phase). The data got dispersed far away from approximately (-1, 1), which means that there is inter-symbol interference (ISI) between users for GWBE transmitted signal.

Figs (18,) and (19) illustrate that GWBE clouds in the constellation have a higher spreading tendency than ETF, which causes higher performance degradation that illustrates ETF's better performance than GWBE. Constellation diagrams could be considered one of the major performance metrics for the NOMA design in NR.

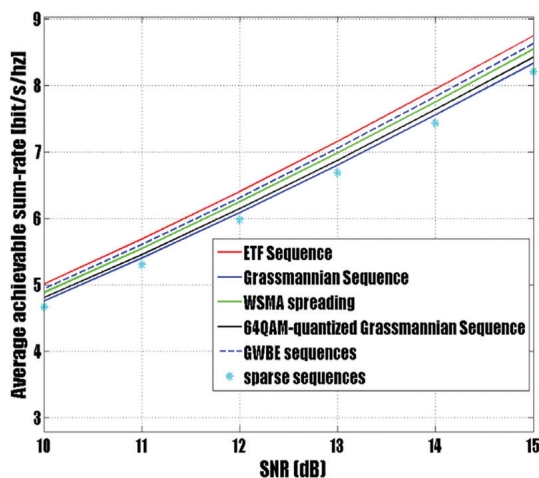


Fig. 20. CCMC capacity between ETF, GWBE, Grassmannian, WSMA, 64QAM-quantized Grassmannian, and sparse with $j=4$, $K=8$

Fig. 20 shows the CCMC capacity for ETF, GWBE, Grassmannian, WSMA, 64QAM-quantized Grassmannian, and sparse. The results indicate that ETF obtains a higher spectrally normalized sum rate than the other NOMA schemes.

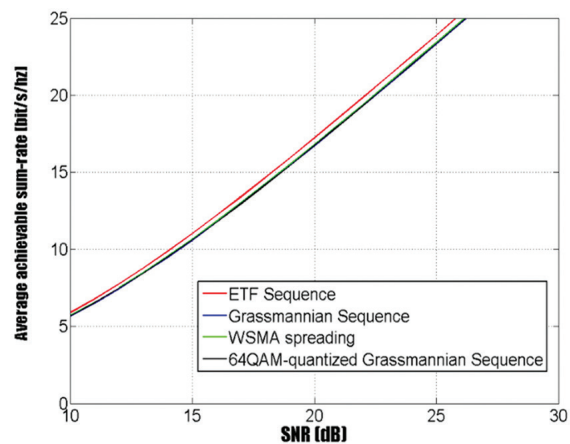


Fig. 21. CCMC capacity between ETF, Grassmannian, WSMA, and 64QAM-quantized Grassmannian with $j=6$, $K=12$

Fig (21) simulation shows the CCMC capacity for ETF, Grassmannian, WSMA, and 64QAM-quantized Grassmannian. The results indicate that ETF obtains a higher spectrally normalized sum rate than the other NOMA schemes

6. CONCLUSION

ETF enhances performance more than the Grassmannian sequence, WSMA spreading, 64 QAM-quantized Grassmannian sequence, GWBE sequence, and PDMA sequence, proving that by the effect of spreading code sequences on average BER, the effect of spreading codes on the received signal after detection and the effect of spreading codes on received signal and the effect of every user on the other. Grouping enhances performance more than using power allocation. 64 QAM-quantized Grassmannian sequence with grouping is better than GWBE sequences with grouping for enhancement performance. Simulation for the continuous-input-continuous-output memoryless channel capacity proves that ETF is optimal in achieving sum rates compared to other NOMA schemes

7. REFERENCE

- [1] Z. Ding, M. Peng, H. V. Poor, "Cooperative non-orthogonal multiple access in 5G systems", IEEE Communications Letters, Vol. 19, No. 8, 2015, pp. 1462-1465.
- [2] Z. Yang, Z. Ding, P. Fan, N. Al-Dhahir, "A general power allocation scheme to guarantee quality of service in downlink and uplink NOMA systems",

- IEEE Transactions on Wireless Communications, Vol. 15, No. 11, 2016, pp. 7244-7257.
- [3] 3GPP R1-1805840, "Key processing modules at transmitter side for NOMA, ZTE, RAN1 #93."
- [4] 3GPP R1-1809434, "Transmitter Side Signal Processing Schemes for NOMA", Qualcomm Incorporated, RAN1 #94.
- [5] 3GPP R1-1809148, "Transmitter design for uplink NOMA, Gothenburg, Sweden", TSG RAN WG1 Meeting #94.
- [6] 3GPP R1-1808499, "Transmitter side signal processing schemes for NCMA", TSG RAN WG1 Meeting #94."
- [7] 3GPP R1-1809844, "Email discussion to collect detailed description of the NOMA schemes", TSG RAN WG1 Meeting #94."
- [8] 3GPP R1-1808386, "NOMA transmitter side signal processing", TSG RAN WG1 Meeting #94."
- [9] J. H. Mott, "An algebraic method for the construction of families of sequences with good Hamming cross-correlation properties", Proceedings of the Twentieth Southeastern Symposium on System Theory, 1988, pp. 328-329.
- [10] W. Liu, X. Hou, L. Chen, "Enhanced uplink non-orthogonal multiple access for 5G and beyond systems", Frontiers of Information Technology & Electronic Engineering, Vol. 19, No. 3, 2018, pp. 340-356.
- [11] I. M. T. Vision, "Framework and overall objectives of the future development of IMT for 2020 and beyond", Radiocommunication Study Groups, 2015.
- [12] J. G. Andrews et al. "What will 5G be?", IEEE Journal on Selected Areas in Communications, Vol. 32, No. 6, 2014, pp. 1065-1082.
- [13] Y. Saito, Y. Kishiyama, A. Benjebbour, T. Nakamura, A. Li, K. Higuchi, "Non-orthogonal multiple access (NOMA) for cellular future radio access", Proceedings of the IEEE 77th vehicular technology conference, Dresden, Germany, 2-5 June 2013, pp. 1-5.
- [14] D. Lopez-Perez et al. "A Survey on 5G Energy Efficiency: Massive MIMO, Lean Carrier Design, Sleep Modes, Machine Learning", arXiv2101.11246, 2021.
- [15] X. Chen, A. Benjebbour, A. Li, A. Harada, "Multi-user proportional fair scheduling for uplink non-orthogonal multiple access (NOMA)", Proceedings of the IEEE 79th Vehicular Technology Conference, Seoul, Korea, 18-21 May 2014, pp. 1-5.
- [16] Z. Yang, Z. Ding, P. Fan, G. K. Karagiannidis, "On the performance of non-orthogonal multiple access systems with partial channel information", IEEE Transactions on Communications, Vol. 64, No. 2, 2015, pp. 654-667.
- [17] 3GPP TR 38.802, "Study on new radio access technology physical layer aspects." 3GPP Valbonne, France, 2017.
- [18] A. Hoglund et al. "Overview of 3GPP release 14 enhanced NB-IoT", IEEE Networks, Vol. 31, No. 6, 2017, pp. 16-22.
- [19] R. Ratasuk, N. Mangalvedhe, Z. Xiong, M. Robert, D. Bhatoolaul, "Enhancements of narrowband IoT in 3GPP Rel-14 and Rel-15", Proceedings of the IEEE Conference on Standards for Communications and Networking, Helsinki, Finland, 18-20 September 2017, pp. 60-65.
- [20] T.-K. Le, U. Salim, F. Kaltenberger, "An overview of physical layer design for Ultra-Reliable Low-Latency Communications in 3GPP Release 15, 16, 17", IEEE Access, Vol. 9, 2020. pp. 433-444.
- [21] S. Halunga fratru, O. Fratu, "MULTIUSER DETECTION ALGORITHMS", 2005.
- [22] K. Long, D. Chen, S. Duan, P. Wang, F. Wu, "Improved uplink NOMA performance through adaptive weighted factors aided PIC and MA signature", IEEE Access, Vol. 7, 2019, pp. 35908-35918.
- [23] 3GPP R1-1806241, "Signature design for NoMABusan", TSG-RAN WG1 Meeting #93.
- [24] T. Zheng, J. Guthrie, E. Mallada, "Inner Approximations of the Positive-Semidefinite Cone via Grassmannian Packings", arXiv2105.12021, 2021.
- [25] 3GPP R1-1808151, "Transmitter side designs for NOMA", 3GPP TSG RAN WG1 Meeting #94."
- [26] 3GPP R1-1808386, "NOMA transmitter side signal processing", TSG RAN WG1 Meeting #94.
- [27] R.-1806241 3GPP, "Signature design for NoMA", Ericsson, RAN1#93.

- [28] "3GPP TR 38.812., "" Study on Non-Orthogonal Multiple Access (NOMA) for NR"
- [29] 2018v1. 3GPP, "Transmitter design for uplink NOMA", Technical Report R1-1809148, 2018."
- [30] M. L. Honig, "Advances in multiuser detection", John Wiley & Sons, 2009.
- [31] S. Verdu, "Multiuser detection. Cambridge university press, 1998.
- [32] Hara, Takanori, et al. "On the Sum-Rate Capacity and Spectral Efficiency Gains of Massively Concurrent NOMA Systems", Proceedings of the IEEE Wireless Communications and Networking Conference, Marrakesh, Morocco, 15-18 April 2019.

Design of Sparse Uniform Linear Array Beamformer using Modified FRM Structure for Varied Applications

Original Scientific Paper

Parvathi Ammothum Kandy

Department of Electronics and Communication Engineering, National Institute of Technology Calicut
Kerala, India
parvathi_p180072ec@nitc.ac.in

Sakthivel Vellaisamy

Faculty of Department of Electronics and Communication Engineering, National Institute of Technology Calicut, Kerala, India
sakthi517@nitc.ac.in

Abstract – This paper presents a method to generate antenna patterns for a Uniform Linear Array (ULA) having narrow beamwidth and low sidelobe levels (SLL) using the recently proposed Modified FRM (ModFRM) architecture. This allows it to direct the beams to specific ground cells for communications while mitigating inter-cell interference. The sharpness of the beam pattern defines the spatial discriminating performance of a ULA beamformer, while the SLL dictates the interference and noise suppression capabilities. Typically, a conventional ULA beamforming will demand high computational complexity and a large number of sensors to satisfy these requirements. Hence to reduce the system cost, using the ModFRM technique a sparse array is developed. With this strategy, the total number of sensors is drastically reduced compared to conventional ULA beamformers. The designed beamformers can be used in applications with stringent requirements where cost and size are concerned.

Keywords: Spatial filtering, Beamformer, Uniform Linear Array (ULA), Frequency response masking (FRM), Spatial interpolation

1. INTRODUCTION

Beamforming is one of the most common forms of distinguishing different signals depending on their physical location. Communication, sonar, radar, medical diagnostics, seismology, and speech acquisition for teleconferencing are just a few examples of real-world applications [1-3]. It is primarily used to identify the existence of the desired signal by filtering both interference and noise signals. These requirements necessitate beamformers with sharp beams having low sidelobes. Tapered beamformers in [4] can fulfill these criteria, but only with a trade-off between a narrow beam and a low sidelobe level (SLL). Furthermore, specifying the main beamwidth and SLL requirements is problematic for tapered beamformers.

A beamformer can be considered a spatial filter that processes sensor array outputs to generate the required beam (directivity) pattern [2]. Two sub-processes make up a spatial filtering operation: synchronization and weight-and-sum. Although both processes are essential in controlling the array beam pattern (the synchronization part governs the steering direction

and the weight-and-sum process governs the main lobe beamwidth and sidelobe characteristics), the second step is given more attention.

Among the various techniques, array beamformer synthesis is closely associated with the design of digital finite-impulse-response (FIR) filters, in which the tapped delay line is transformed by spatial delay, and the filter length is proportional to the number of antennas. The Uniform Linear Array (ULA) is the most widely used array geometry because of its simplicity, superior directivity, and realization of the narrow beamwidth in a given direction [5,6]. In the ULA beamformer, the spatially sampled sequences from each sensor are linearly combined in the same way the temporally sampled data are linearly combined by an FIR filter [7]. It is well known that the passband and stopband ripples, as well as the transition bandwidth, are the crucial aspects of a typical FIR filter design problem. Likewise, the most significant beam pattern characteristics are main beamwidth, SLL, and null-to-null beamwidth. A narrow transition width and low sidelobes beamformer are desirable as the sharp transition impacts the spatial discriminating performance, and the SLL determines the

interference and noise removal capability. However, designing an appropriate beam pattern with narrow transition bands and minimal sidelobes using traditional FIR filter design approaches such as windowing methods would require many sensors, resulting in high cost and high computational complexities. Hence, the objective is to achieve this with the fewest sensors possible.

Sparse array models distribute sensors optimally, thus obtaining desired beamforming attributes while lowering overall hardware costs and simplifying data processing. There-forth, sparse arrays have received much attention from system designers to save costs [8-12]. In sparse array beamforming, interpolation techniques are frequently used [5,13-15]. FIR filter design techniques, such as Frequency response masking (FRM) proposed by Lim [16,17] and interpolated FIR [18], have lately been investigated to see if they may be used in array processing [19-21]. Rosen et al. [22] recently proposed beamformers with constant beamwidths based on FIR. The primary idea behind this method is to adjust the effective array aperture to keep the beamwidth constant over the specified frequency band. Although this method has reduced computational complexity, it cannot modify the sidelobe level.

This paper presents a framework for designing active sparse linear arrays useful for radar/sonar applications using Modified FRM (MoFRM) approach proposed in [23]. This approach designs a pencil beam pattern with a specified maximum SLL which allows it to discriminate between two objects in proximity and avoid inter-cell interference. Owing to the low computational cost and ease of implementation, this technology is well suited for real-time digital beamforming scenarios such as satellite and high-altitude platform systems that need many array components.

The following is an overview of the structuring of this paper. Section 2 provides a brief overview of the analogy between the ULA and the FIR filter. The ModFRM approach for array pattern design is discussed elaborately in Section 3. The design of the desired antenna radiation pattern and the proposal outcomes are presented in Section 4. Section 5 brings the paper to a close-by reviewing the benefits of the proposed ModFRM beamformer and outlining future research prospects.

2. ANALOGY BETWEEN ULA BEAMFORMING AND FIR FILTER

Beamforming is a method that confines a signal on a specific receiving device as opposed to having it spread out in all directions and also attenuating signals from other locations [24,25]. In the cases, when the desired signal and interference are from the same frequency band, temporal filtering is typically ineffective in separating the two. However, the targeted and undesired signals are usually generated from different spatial points. Using a spatial filter at the receiver,

this spatial separation may be used to isolate the desired signal from other interference. In the same way, as temporal filter processes the data acquired across a temporal range, spatial filter processes data gathered over a spatial aperture. The magnitude response of an FIR filter is analogous to the beam pattern of an antenna array. Likewise, the sine of the direction of arrival (DOA), $\sin \theta$, and the temporal frequency f_i of the FIR filter input have an analogy. The DOA refers to the general direction from which a wave that is propagating typically arrives at a region where typically a group of sensors are placed [26,27]. As ULA and the FIR filter have a correspondence, a theorem that applies to the FIR filter in the time domain will also apply to the ULA in the space domain.

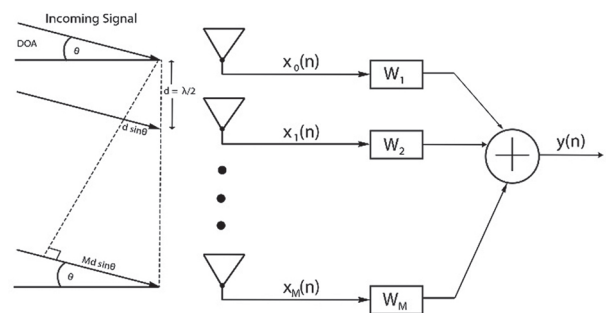


Fig. 1. Narrowband beamformer using ULA.

The frequency response of an N^{th} order FIR filter with impulse response $h(n)$ to a signal of frequency ω is,

$$H(\omega) = \sum_{n=0}^{N-1} h(n)e^{-j\omega n} \quad (1)$$

The beamformer response for an N-sensor beamformer with an aperture function $b(n)$ is,

$$B(\theta, \omega) = \sum_{n=0}^{N-1} b(n)e^{-j\omega t_n(\theta)} \quad (2)$$

where $t_n(\theta), 0 \leq n \leq N - 1$ is the propagation delay concerning the first sensor. In a nutshell, the sine of the direction in a narrowband, linear equi-spaced beamformer is the same as the temporal frequency in a FIR filter.

From the classical ULA beamformer depicted in Fig. 1, its resemblance with the FIR filter can be better understood.

3. PROPOSED SPARSE ULA BEAMFORMER USING MODIFIED FRM STRUCTURE

3.1 MODIFIED FRM STRUCTURE

Fig. 2 is the layout of designing a ModFRM filter. A prototype filter, $H_a(z)$ of lower order with an adequate passband and transition width is modulated throughout the spectrum for a set of bandpass filters covering the entire range of frequencies. All of these modulated versions are then interpolated by a factor L. The sum of interpolated even modulated channels and the sum of odd modulated channels plays the role of the $H_a(z^L)$ and $H_c(z^L)$ in traditional FRM [16]. The sum of interpolated even modulated channels is called even band-edge shaping filter bank (even BES-FB) and the sum of odd

modulated channels is called odd band-edge shaping filter bank (odd BES-FB). The number of modulations of the prototype filter has to be odd so that alternately they can be added to form the even and odd BES-FBs. Also, full spectral coverage by the prototype filter and its modulated versions is ensured by the condition:

$$(m + 1)(\rho + \varphi) = 2\pi \quad (3)$$

where ρ and φ denotes the passband and stopband edge frequencies of the prototype filter respectively. The number of modulated filters, m must be odd such that the frequency response occurs alternately when the modulated filters are recombined. Therefore,

$$m = 2p + 1; p = 0, 1, 2, \dots \quad (4)$$

Finally, the ModFRM filter is created by cascading the even BES-FB and odd BES-FB with the masking filters $H_{Ma}(z)$ and $H_{Mc}(z)$ respectively, as in Fig. 2.

The transfer function of the ModFRM filter can be expressed as [23]:

$$H(z) = [H_{a,0}(z^L) + H_{a,2}(z^L) + \dots + H_{a,2p}(z^L)]H_{Ma}(z) + [H_{a,1}(z^L) + H_{a,3}(z^L) + \dots + H_{a,2p+1}(z^L)]H_{Mc}(z) \quad (5)$$

where $H_{a,q}(z^L)$ is the q^{th} DFT modulated prototype filter interpolated by L . Equation (5) can be rewritten as:

$$H(z) = \sum_{i=0}^p H_{a,2i}(z^L)H_{Ma}(z) + \sum_{i=0}^p H_{a,2i+1}(z^L)H_{Mc}(z) \quad (6)$$

where,

$$\sum_{i=0}^p H_{a,2i}(z^L) \text{ represents the even BES - FB}$$

$$\sum_{i=0}^p H_{a,2i+1}(z^L) \text{ represents the odd BES - FB}$$

Both the even BES-FB or odd BES-FB can be used to determine the frequency response of the ModFRM filter around the transition band. Accordingly, the masking filter design may be done in two ways as follows [23]:

Case I

$$\omega_{p,Ma1} = \frac{3\rho+2\varphi}{L}; \omega_{s,Ma1} = \frac{4\rho+3\varphi}{L}; \quad (7)$$

$$\omega_{p,Mc1} = \frac{\rho+2\varphi}{L}; \omega_{s,Mc1} = \frac{2\rho+3\varphi}{L}; \quad (8)$$

Case II

$$\omega_{p,Ma2} = \frac{\varphi}{L}; \omega_{s,Ma2} = \frac{\rho+2\varphi}{L}; \quad (9)$$

$$\omega_{p,Mc2} = \frac{2\rho+\varphi}{L}; \omega_{s,Mc2} = \frac{3\rho+2\varphi}{L}; \quad (10)$$

For higher values of L , the masking filter's complexity is significant, as can be interpreted from (15). Therefore, the masking filters are built using the interpolated FIR (IFIR) method [4], a simpler counterpart of FRM used for designing narrow passband sharp filters. The IFIR structure comprises two filters: the IFIR modal filter and

the image-suppressor filter. For minimal multipliers, the optimal interpolation factor, L_{IFIR} , is determined as follows:

$$L_{IFIR} = \frac{2\pi}{\omega_{p,Ma} + \omega_{s,Mc} + \sqrt{2\pi(\omega_{s,Mc} - \omega_{p,Ma})}} \quad (11)$$

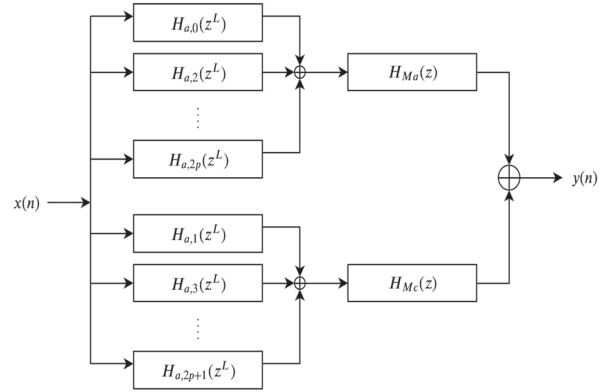


Fig. 2. Proposed ModFRM structure [23]

3.2 SPARSE ULA BEAMFORMER USING MODFRM TECHNIQUE

Assume we know the source is in a specific area between angles ϕ_1 and ϕ_2 . So, we intend to create a beamformer that receive signals from a range of ϕ_1 to ϕ_2 but attenuates signals from other directions. Mathematically, the directional response $B_d(\phi)$ is written as:

$$B_d(\phi) = \begin{cases} 1 & \text{if } \phi_1 \leq \phi \leq \phi_2 \\ 0 & \text{otherwise} \end{cases} \quad (12)$$

As the main lobe width reduces, the number of antenna elements increases, whereas the number of nulls keeps growing. This will suppress a significant proportion of interference, but the computational complexity of the beamformer shoots up drastically. In this work, a Modified FRM (ModFRM) architecture is suggested for designing hardware efficient sparse ULA beamformers having sharp beamwidth of better angular resolution. For the design of spatial filters, three attributes are required:

- 3-dB main beamwidth in the direction of ϕ_0 of the intended beamformer (and its associated 3-dB spatial frequency).
- Intended beamformer's null-to-null main beamwidth in the direction of ϕ_0 (and its associated null-to-null spatial frequency).
- The intended beamformer's SLL.

With the ModFRM technique, initially, a prototype beamformer is synthesized. It is then modulated and spatially interpolated by an appropriate expansion factor to increase the inter-element spacing. The even and odd modulated versions of the prototype beamformer that are spatially interpolated are subsequently grouped to constitute the two spatial shaping filters, namely, the even spatial shaping filter and the odd spatial shaping filter. To reduce grating lobes that appear due to changes in spacing, the beam pattern of spatial shaping filters is cascaded with the spatial masking fil-

ters (B_{Ma} and B_{Mc}) as in Fig. 2. If the masking beamformers are created using the IFIR approach, the antenna components will be reduced even further. This is because IFIR decomposes the design of a sharper beam pattern into the design of two spatial filters having beam patterns of broader beam width. These two spatial filters are modal beamformer and image-suppressor beamformer, respectively.

When compared to the traditional approach, the suggested method has the following merits:

- The aperture functions of the ULA beamformer formed with the ModFRM filter synthesis can provide a very narrow main beamwidth and low SLL.
- It can separate two closely spaced objects with minimal elements, resulting in a considerable decrease in the number of components utilized.
- The main beam width and the SLL can be specified individually without making a trade-off.

Table 1. FRM subfilter parameters for narrow beam ULA synthesis.

	FRM Subfilter	3-dB Beamwidth	3-dB Spatial frequency	Null-to-Null Beamwidth	Null-to-Null Spatial frequency	No: of Antenna Elements
1.	Prototype Beamformer	5.8°	0.1696	21°	0.3304	42
2.	Spatial masking filter, Ma	3°	0.0551	10.5°	0.1384	87
3.	Spatial masking filter, Mc	3°	0.1116	10.5°	0.1949	87

4. DESIGN EXAMPLE

A ULA beamformer with a 3-dB main beamwidth of 1° at direction 90° (3-dB spatial frequency is 0.1116), a null-to-null beamwidth of 3.5° (null-to-null spatial frequency is 0.1384) and the desired SLL of -60dB is taken as an example. In this work, the Dolph-Chebyshev model is a popular weighting method used for pattern synthesis [28, 29]. Using this model, uniformly spaced linear arrays oriented to broadside with specified SLL and null-null beam width can be established. The total number of elements for desired beamformer design using the direct-form FIR method is found to be 255. To design the desired beam pattern using conventional FRM structure, the 3-dB and null-to-null beamwidth required by the prototype beamformer and the spatial masking beamformer are given in Table 1. The FRM beamformer output is then given by Equation (13) [20].

$$y(n) = B_a(M\phi)B_{ma}(\phi) + B_c(M\phi)B_{mc}(\phi) \quad (13)$$

As seen from (13), the FRM beamformer is the sum of Here, M represents the spatial interpolation factor and $B_c(\phi)$ corresponds the complementary spatial filter of the prototype beamformer, $B_a(\phi)$. In this scenario, the prototype beamformer and the two spatial masking beamformers will require 216 antenna elements (42+87+87). Table 2 lists the frequency specifications for the various ModFRM subfilters and the corresponding number of antenna elements required for the proposed ModFRM beamformer synthesis. Thus, 157 antenna elements (25+49+18+49+16) are sufficient for attaining the intended beam pattern using the newly proposed ModFRM technique. Fig. 3 shows the prototype beamformer and Fig. 4 is the IFIR modal beamformer for the design of spatial masking beamformer, B_{Ma} . In Fig. 5, the modal beamformer of $B_{Ma}(\phi)$ is spatially interpolated and is masked with an image-suppressor

beamformer, according to the principle of the IFIR technique. Similarly, the modal beamformer and the image-suppressor beamformer of $B_{Mc}(\phi)$ are designed. Finally, the intended beamformer with a 3-dB main beamwidth of 1° and a null-to-null beamwidth of 3.5° is generated using Equation (5). The obtained ModFRM beamformer is given in Fig. 6.

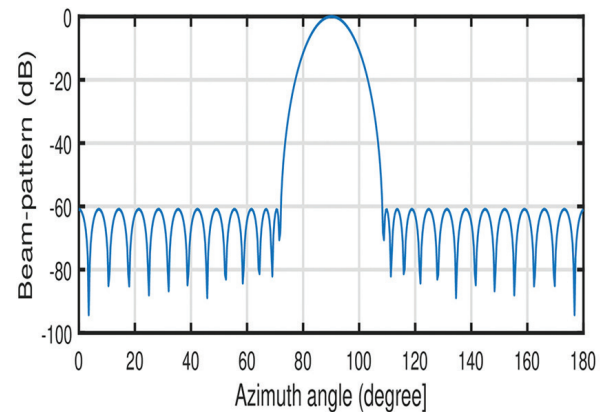


Fig. 3. Prototype Beamformer

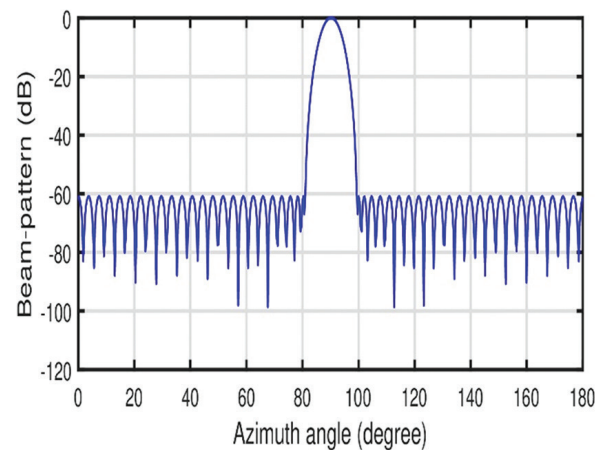


Fig. 4. Spatial modal filter of $H_{Ma}(z)$.

Table 2. ModFRM subfilter parameters for narrow beam ULA synthesis.

	ModFRM Subfilter	3-dB Beamwidth	3-dB Spatial frequency	Null-to-Null Beamwidth	Null-to-Null Spatial frequency	No: of Antenna Elements
1.	Prototype Beamformer	10°	0.1157	36°	0.3843	25
2.	Modal beamformer for spatial masking filter, B_{Ma}	5.4°	0.3348	18.4°	0.4848	49
3.	Image-suppressor beamformer for spatial masking filter, B_{Ma}	15°	0.1116	50°	0.5051	18
4.	Modal beamformer for spatial masking filter, B_{Mc}	5.4°	0.2652	18.4°	0.4152	49
5.	Image-suppressor beamformer for spatial masking filter, B_{Mc}	15°	0.0884	50°	0.5283	16

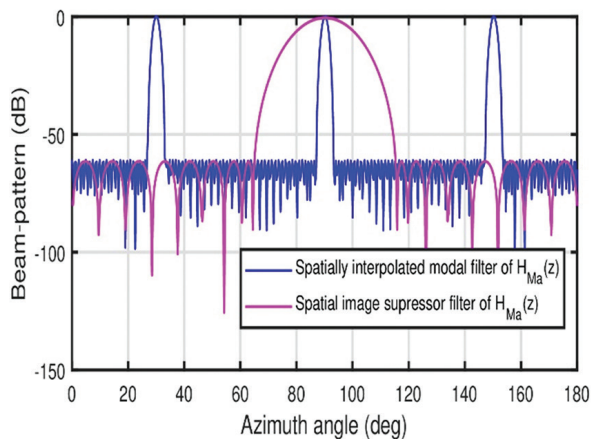


Fig. 5. Spatially interpolated modal filter and image-suppressor filter for $H_{Ma}(z)$.

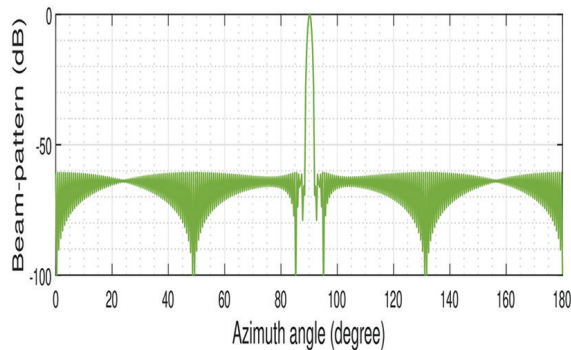


Fig. 6. ModFRM Beamformer

As an outcome, a beam pattern with a narrow main beamwidth (due to increased spacing) and low SLL (attributable to the attenuation of the spatial masking filter) is created without expanding the number of antenna elements. To put it another way, using a spatially interpolated beamformer allows one to lower the number of antenna elements while maintaining the same main beamwidth and SLL as the classic beamforming approach, which requires a more significant number of elements. Furthermore, because of the wider inter-element separation, mutual coupling amongst antenna elements can be reduced, which is an essential concern in practicality.

5. CONCLUSION

In this paper, a ModFRM-based narrowband beamforming architecture is introduced. With this technology, a beamformer may be designed to produce a sharp beam with low SLL that can point to specific cells and prevent inter-cell interference. Computer simulations demonstrate that the proposed beamformer provides a more directive main lobe with fewer sensor elements compared to the sparse array beamformer designed using conventional FRM technique. Hence, the suggested method may be used in a wide range of scenarios where a sharp beam with low sidelobe level is required, which otherwise demands a massive antenna array.

6. REFERENCES

- [1] N. Dey, A. S. Ashour, "Direction of arrival estimation and localization of multi-speech sources", Springer, 2018.
- [2] B. D. Van Veen, K. M. Buckley, "Beamforming: A versatile approach to spatial filtering". IEEE ASSP Magazine, Vol. 5, No. 2, 1988, pp. 4-24.
- [3] R. Kokila, K. Chithra, R. Dhilsha, "Wideband beamforming using modified farrow structure FIR filtering method for sonar applications". Proceedings of the International Symposium on Ocean Technology, 2019, pp. 21-28.
- [4] K. Schuler, W. Wiesbeck, "Tapering of multitransmit digital beamforming arrays". IEEE Transactions on Antennas and Propagation, Vol. 56, No. 7, 2008, pp. 2125-2127.
- [5] L. J. Gudino, S.N. Jagadeesha, J. X. Rodrigues, "A novel design of sharp transition fir filter for digital beamforming", Proceedings of the 6th International Symposium on Communication Systems, Networks and Digital Signal Processing, 2008, pp. 247-250.
- [6] L. J. Gudino, S.N. Jagadeesha, J. X. Rodrigues, "A novel filter design for spatially interpolated beamform-

- er”, Proceedings of the International Symposium on Intelligent Signal Processing and Communications Systems, 2009, pp. 1-4.
- [7] Y. Zhang et al, “Flat topped radiation pattern synthesis based on FIR filter concept”, Proceedings of the IEEE Asia Pacific Microwave Conference, 2017, pp. 751-754.
- [8] M. B. Hawes, W. Liu, “Sparse array design for wide-band beamforming with reduced complexity in tapped delay-lines”, IEEE/ACM Transactions on Audio, Speech, and Language Processing, Vol. 22, No. 8, 2014, pp. 1236-1247.
- [9] Z. Zheng, Y. Fu, W.-Q. Wang, “Sparse array beamforming design for coherently distributed sources”, IEEE Transactions on Antennas and Propagation, Vol. 69, No. 5, 2020, pp. 2628-2636.
- [10] Q. Lu et al. “Cognitive wideband beamforming for sparse array”, Proceedings of the IEEE Radar Conference, 2020, pp. 1-6.
- [11] S. A. Hamza, M. G. Amin, “Sparse array design for transmit beamforming”, Proceedings of the IEEE International Radar Conference, 2020, pp. 560-565.
- [12] M. Ruan, L. W. Hanlen, M. C. Reed, “Spatially interpolated beamforming using discrete prolate spheroidal sequences”, Proceedings of the IEEE International Conference on Acoustics Speech and Signal Processing Proceedings. Vol. 3, 2006.
- [13] T. Do-Hong, P. Russer, “A new design method for digital beamforming using spatial interpolation”, IEEE Antennas and Wire-less Propagation Letters, Vol. 2, 2003, pp. 177-181.
- [14] R. G. Pridham, R. A. Mucci, “Digital interpolation beamforming for low-pass and bandpass signals”, Proceedings of the IEEE, Vol. 67, No. 6, 1979, pp. 904-919.
- [15] C. Sun, Q.L. Guo, Y.X. Yang, “Design broadband beamformers via interpolation techniques”, OCEANS, 2007, pp. 1-4.
- [16] Y. Lim, “Frequency-response masking approach for the synthesis of sharp linear phase digital filters”, IEEE Transactions on Circuits and Systems, Vol. 33, No. 4, 1986, pp. 357-364.
- [17] Y. C. Lim et al, “FPGA implementation of digital filters synthesized using the FRM technique”, Circuits, Systems and Signal Processing, Vol. 22, No. 2, 2003, pp. 211-218.
- [18] Y. Neuvo, D. Cheng-Yu, S. Mitra, “Interpolated finite impulse response filters”, IEEE Transactions on Acoustics, Speech, and Signal Processing, Vol. 32, No. 3, 1984, pp. 563-570.
- [19] Y. Liu, Z. Lin, “On the applications of the frequency response masking technique in array beamforming”, Circuits, Systems and Signal Processing, Vol. 25, No. 2, 2006, pp. 201-224.
- [20] Y. Liu, Z. Lin, “Active array beamforming using the frequency-response masking technique”, Proceedings of the IEEE International Symposium on Circuits and Systems, Vol. 3, 2004.
- [21] P. P. Vaidyanathan, C.-C. Weng, “Active beamforming with interpolated FIR filtering”, Proceedings of the IEEE International Symposium on Circuits and Systems, 2010, pp. 173-176.
- [22] O. Rosen, I. Cohen, D. Malah, “FIR-based symmetrical acoustic beamformer with a constant beamwidth”, Signal Processing, Vol. 130, 2017, pp. 365-376.
- [23] A.K. Parvathi, V. Sakthivel, “Low complexity reconfigurable modified FRM architecture with full spectral utilization for efficient channelizers”, Engineering Science and Technology, Vol. 28, 2022, p. 101022.
- [24] W. Kellermann, “Beamforming for speech and audio signals”, Handbook of Signal Processing in Acoustics, Springer, 2008, pp. 691-702.
- [25] H. L. Van Trees, “Optimum array processing: Part IV of detection, estimation, and modulation theory”, John Wiley & Sons, 2004.
- [26] J. G. Ryan, R. A. Goubran, “Array optimization applied in the near field of a microphone array”, IEEE Transactions on speech and Audio Processing, Vol. 8, No. 2, 2000, pp. 173-176.
- [27] L. C. Godara, “Application of antenna arrays to mobile communications. II. Beam-forming and direction-of-arrival considerations”, Proceedings of the IEEE, Vol. 85, No. 8, 1997, pp. 1195-1245.
- [28] R.C. Hansen, “Dolph-Chebyshev array directivity against spacing”, Electronics Letters, Vol. 32, No. 12, 1996, pp. 1050-1051.
- [29] N. Fadlallah et al. “Antenna array synthesis with Dolph-Chebyshev method”, Argument, Vol. 2, 2011, p. 3

Fuzzy Controller Based DTC of SRM Drive Fed by Common High Side Asymmetric Switch Converter

Original Scientific Paper

Ashok Kumar Kolluru

Koneru Lakshmaiah Education Foundation,
Department of Electrical and Electronics Engineering,
Vaddeswaram, Guntur-522502, A.P, India
kolluruashok206@gmail.com

Kiran Kumar Malligunta

Koneru Lakshmaiah Education Foundation,
Department of Electrical and Electronics Engineering,
Vaddeswaram, Guntur-522502, A.P, India
Kiran.malligunta@gmail.com

Abstract – The switched reluctance motor (SRM) is recently gaining huge popularity in electric vehicle (EV) applications due to its control flexibility, simple structure, lower cost and high efficiency than the synchronous and induction motors. Among all the controllers, the direct torque control (DTC) is the most preferred due to its higher efficiency, lower losses and superior control characteristics. In this paper, a 6/4 pole SRM with fuzzy logic based DTC has been proposed for the EV application along with a converter with reduced switch counts to reduce the torque ripples and enhance the performance of the system under steady and transient state conditions. The proposed system is tested and validated under various scenarios that include load torque and speed variations and compared with the vector control method. From the investigation it has been found that the proposed technique reduces ripples from the system during all the scenarios with a resultant flux of less than 0.5pu.

Keywords: Switched Reluctance Motor, high side switch asymmetric converter, direct torque control, fuzzy logic controller

1. INTRODUCTION

Switched reluctance motor (SRM) has gained popularity among the industries for various inherent characteristics such as low cost, simple design, a wider range of speed, flexible control, higher starting torque and fault tolerance [1,2]. The advancement of power electronics converters and their control algorithms has additionally improved the performance of SRM [3]. The growing industrialization has led to the application of the SRM in various sectors like aviation, textile factories, robotics and electric vehicles [4-6]. However, the SRM encounters reliability and safety issues due to presence of doubly salient and switching power properties that added several demerits of higher torque ripples generation, noise and non-linear magnetic characteristics [7-9]. Also, nowadays, more research is going to design new control strategies to enhance the performance of the SRM as traditional techniques lag in terms of accuracy [10-15].

The most complex control strategies proposed in the wide range of literature include direct torque control (DTC), torque sharing function (TSF), advance torque control (ATC) and feedback control that can reduce the ripples in the SRM drives [16-19]. The torque ripples suppression of 12/8 SRM along with an investigation of the response of speed and load torque has been done by using both the TSF and DTC techniques in the literature [16]. Additionally, a predictive DTC strategy for torque and speed response improvement of SRM has been proposed and proved to be more effective than the conventional DTC in the literature [17]. An ATC-based control technique that maintains desired torque of the motor at the desired speed of the SRM has been proposed in [18] which is further improved by using the control parameters based on multi-objective optimization [19]. The low-frequency oscillations of the output torque in SRM torque have been compensated using a sliding mode control strategy in the literature [20]. Another technique based on the optimal com-

mutation has been proposed for the SRM to reduce the torque ripple and enhance the torque-producing capacity of the motor [21]. A state-of-the-art literature review on various advanced control, current regulation and torque control strategies of the SRM drives has been conducted in [22].

Various research based on the utilization of simple PID controllers with optimization techniques has been conducted recently to meet the optimal torque and speed response of the SRM [23-25]. Some examples of optimization based PID controller technique includes ant colony optimization [23] and genetic algorithm [24] that have been applied to the 8/6 pole SRM that enhanced the speed regulation by tracking the set points in a faster way. Similarly, another particle swarm optimization based optimal PID controller has been proposed that achieved a minimum integral quadratic error of the speed by tuning the parameters [25]. Also, the torque and speed profile enhancement of a 6/4 SRM has been done by using ant lion optimization in a fractional order PID controller [26]. In [27], the performance of the speed and torque has been improved by using an optimal design for the parameters of the SRM. Also, the performance of SRM has been enhanced in [28] by replacing the material of the core with a soft magnetic composite.

Over the past few years, the current regulation of SRM has been carried out through numerous control strategies as investigated in [29] among which the current chopping control technique [30] has gained importance due to its independence in model and faster dynamic response. Moreover, as an alternative to the hysteresis controller, a controller with intelligence based on iterative learning has been proposed [31, 32]. Also, various complex control strategies has been proposed that include model prediction [33, 34], sliding mode [35, 36], dead-beat [37, 38] and adaptive [39] control strategies. However, the mentioned strategies have various vulnerabilities in terms of complexity, cost, slow response, sensitivity, higher ripples in current, etc. Recently, a PID controller based on the adaptive fuzzy concept has been proposed but, the system shows poor performance in terms of torque and speed regulation [40].

Hence, in this paper, a fuzzy logic based direct torque control (DTC) strategy for the SRM has been proposed that can reduce the torque ripples and enhance the performance and efficiency of the system during any scenario. The strategy has been applied to a 6/4 pole SRM along with a converter topology with a reduced number of switches that minimizes the cost and losses in the system. The performance of the proposed technique has been compared to the system with vector control DTC using various scenarios such as load and speed variation. The proposed work has been successfully implemented using MATLAB simulation environment. Further in addition, the same technique can also be implemented in real-time scenario as a future contribution of article.

The rest of the paper includes the description of the

system modelling in section 2, the proposed control strategy in section 3, followed by the results and discussion in section 4 and the conclusion in section 5.

2. SYSTEM MODELLING

The proposed system has been shown in Fig.1 which comprises a novel converter configuration with only four switches, a 6/4 pole SRM, and an appropriate controller. The SRM is a doubly salient machine which has variable reluctance in the stator as well as the rotor. The following equations have been used to model the motor.

$$V = \frac{(\lambda_a - \lambda_u)i}{\lambda_u} \frac{(L^s_a - L_u) \times i}{t} \quad (1)$$

$$\text{Where } t = \frac{\beta_s}{\omega_r}$$

$$\sigma_s = \frac{T^s_a}{L_a} \quad \text{and} \quad \sigma_u = \frac{T^s_u}{L_u}$$

$$V = \frac{\omega_r}{\beta_s} L^s_a i \left(1 - \frac{1}{\sigma_s \sigma_u} \right) \quad (2)$$

$$L^s_a i = \phi T_{ph} = B \times A_{sp} \times T_{ph} = B \times D \times L \times \beta_s \times T_{ph} / 2 \quad (3)$$

$$A_s = \frac{2T_{ph}im}{\pi D} \quad (4)$$

$$P_d = k_d k_d V_{in} \quad (5)$$

$$k_d = \frac{\theta_i q P_r}{360} \quad (6)$$

In the case of 6/4 SRM having short pitch winding, a phase is mainly formed from the series connection of coils with physically opposing poles. Hence, to avoid negative torque components, only one phase of the SRM is excited as a result, there is a simultaneous operation of the two phases during the commutation period. This cause the current of the ongoing phase to zero four which there is an increase in the current of the next incoming current. Hence, the developed power during one phase conduction (P_d) has been calculated as

$$P_d = k^d k_e \left(\frac{\pi^2}{120} \right) \left(1 - \frac{1}{\sigma_s \sigma_u} \right) B A_s D^2 L N_r$$

$$T = k_d k_e k_3 k_2 (B A_s) D^2 L$$

$$\text{with } k_2 = 1 - \frac{1}{\sigma_s \sigma_u} \quad \text{and} \quad k_3 = \frac{\pi}{4}$$

L^s_a : per phase aligned inductance

L_u : unaligned inductance

t : time required by the rotor to turn from aligned to unaligned

L^u_a : unaligned unsaturated inductance

β_s : arc of stator pole

φ : aligned flux

A_{sp} : stator pole area

D : bore diameter
 L : length of stator pole inductance
 B : flux density of stator pole
 T_{ph} : number of turns per pole per phase
 m : active number of phases
 k_d : duty cycle
 q : number of stator phases i.e. $P_s/2$
 θ_r : current conducting per phase
 P_d : power developed by the SRM (as only one phase conducts at a time)
 P_s : number of poles in the stator
 P_r : number of poles in the rotor

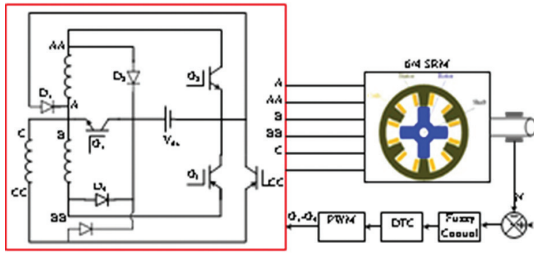


Fig. 1. Speed control of SRM

Also, it can be viewed from Fig.1 that one DC supply, four PWM-based switches and four diodes have been used and applied to the three phases of the SRM. The proposed system is less expensive and can be easily implemented in SRM as compared to the conventional converters. Also, due to lesser switch counts involved in the power conversion, the ripples from the system get reduced.

3. CONTROL STRATEGY

Direct torque control (DTC) is a strategy that controls the PWM converter fed drives by controlling the torque and flux of the SRM without requiring any complicated algorithms like vector control. Also, it requires only the stator resistance in which torque and flux components can directly regulate within the limits so that it can regulate torque under less ripples compared to vector control. The block diagram of DTC for the proposed system has been represented in Fig.2. The Fuzzy controller generates the reference torque signal by using Fuzzy memberships and the Fuzzy block diagram has been represented in Fig.3.

Also, the fuzzy rule base table used in the proposed concept has been tabularized in Table 1.

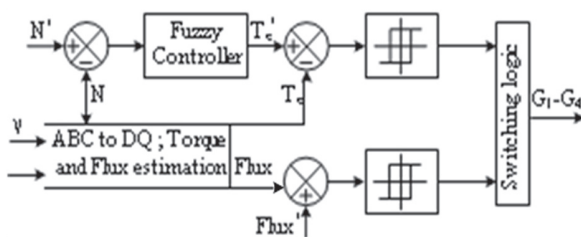


Fig. 2. Direct torque control (DTC) for the proposed system

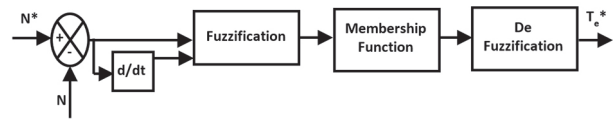


Fig. 3. Block representation of the fuzzy controller

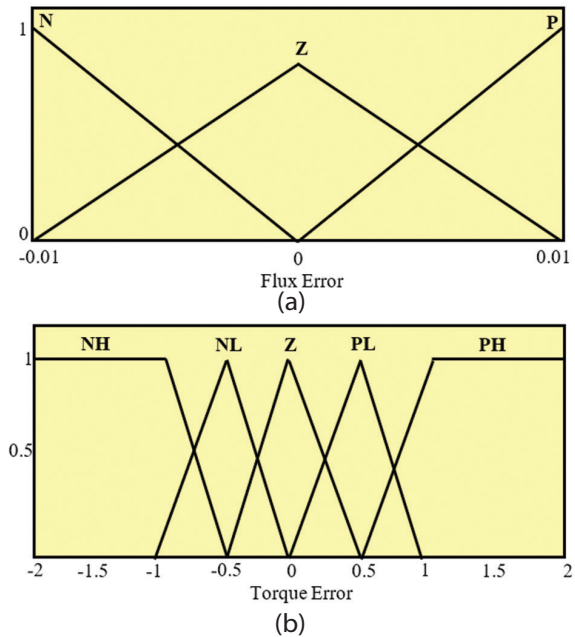


Fig. 4. Membership function of (a) flux, and (b) torque

The trapezoidal membership function has been used in this work for Fuzzification. Based on two inputs and a single output, three membership function groups with each group having many subsets have been used. The torque error (T_e) and stator flux error (F_e) are considered the inputs of the fuzzy system. The T_e has five categories whereas the F_e has three. From the fuzzy rule base table given in Table 1, three linguistic variables i.e. positive (P), negative (N) and zero (Z) has been used to represent the error in the stator flux. Similarly, five linguistic variables i.e. positive high (PH), positive low (PL), negative high (NH), negative low (NL) and zero has been used to represent the torque error. The membership function of flux and torque have been represented in Fig.4 (a) and (b) respectively. The actions that will be decided by the fuzzy controller include torque and flux increase ($TIFI$), torque increase and flux decrease ($TIFD$), torque hold (TH), torque decrease and flux increase ($TDFI$) and torque decrease flux decrease ($TDFD$). In this work, the maximum method of fuzzification has been considered to achieve smooth control and switching where the membership functions are distributed to the entire range of fuzzy range through the crossing.

Table 1. Fuzzy rule base table

$T_e \backslash F_e$	NH	NL	Z	PL	PH
N	TDFD	TDFD	TH	TIFD	TIFD
Z	TDFI	TH	TH	TIFD	TIFD
P	TDFI	TDFI	TH	TIFI	TIFI

Table 2. Switching sequence of the converter

G1	G2	G3	G4	Torque	Flux
On	On	On	On	High	High
On	On	On	Off	High	Low
On	On	Off	Off	Low	Low
On	Off	Off	Off	Zero	High

The switching sequence of the proposed converter to torque and flux has been given in Table 2. The reference torque is compared with the estimated torque and the error signal is sent to torque controller. Similarly, the reference flux is compared with the estimated value and the respective signal is fed to the flux controller. The d-q reference frame representation of the torque and flux has been given below.

$$\begin{bmatrix} i_a \\ i_b \\ i_c \end{bmatrix} = \sqrt{\frac{2}{3}} \begin{bmatrix} \cos 2\theta & \cos(2\theta - \frac{2\pi}{3}) & \cos(2\theta + \frac{2\pi}{3}) \\ -\sin 2\theta & -\sin(2\theta - \frac{2\pi}{3}) & -\sin(2\theta + \frac{2\pi}{3}) \\ \frac{1}{\sqrt{2}} & \frac{1}{\sqrt{2}} & \frac{1}{\sqrt{2}} \end{bmatrix} \begin{bmatrix} i_d \\ i_q \\ i_0 \end{bmatrix} \quad (9)$$

$$\begin{bmatrix} V_d \\ V_q \\ V_o \end{bmatrix} = R \begin{bmatrix} i_d \\ i_q \\ i_0 \end{bmatrix} + \begin{bmatrix} L_{dc} + \frac{L_{ac}}{2} \cos 6\theta & -\frac{L_{ac}}{2} \sin 6\theta & L_{ac} / \sqrt{2} \\ -\frac{L_{ac}}{2} \sin 6\theta & L_{dc} + \frac{L_{ac}}{2} \cos 6\theta & 0 \\ L_{ac} / \sqrt{2} & 0 & L_{ac} \end{bmatrix} \begin{bmatrix} i_d \\ i_q \\ i_0 \end{bmatrix} \quad (10)$$

The torque created is proportional to the current in the q-axis and given as

$$T_e = k_t i_q \quad (11)$$

where $k_t = \sqrt{2} P L_{ac} i_d$

The d-q reference components have been used to design the direct torque controller. The pulse generator generates four pulses for each of the four switches. The specification of the SRM considered in the study has been given in Table 2.

The switching logic block will generate only 4 pulses which are required for the proposed converter to drive the 6/4 pole SRM. The fuzzy logic controllers will help to generate smooth reference signals to make less ripples in the electromagnetic torque of the SRM.

Table 2. Specification of the SRM

Parameter	Ratings
Stator resistance	3.1Ω
Inertia	0.0089 N ^m
Friction coefficient	0.01
Unaligned inductance	5.9 e ⁻³
Aligned inductance	23.6e ⁻³
Saturated aligned inductance	0.15e ⁻³

4. RESULTS AND DISCUSSIONS

The performance of the proposed system has been evaluated in the MATLAB/Simulink environment and tested under various scenarios such as load torque and speed variation. Also, the ripples generation of the pro-

posed technique has been compared with the artificial neural network vector control DTC technique.

4.1. TORQUE RIPPLES COMPARISON

The performance of the proposed system has been validated by comparing it with the ANN-based vector control technique in terms of torque ripples generation. The graph represented in Fig.5 represents the torque ripples generated by the SRM with ANN vector control and the proposed control technique and it can be observed that the ripples are less in the case of the proposed fuzzy-based converter compared to the ANN vector control technique. Due to the direct control of torque and flux, the torque gets stabilizes quickly with a very less ripple content and this type of response is very important in case of electric vehicle application.

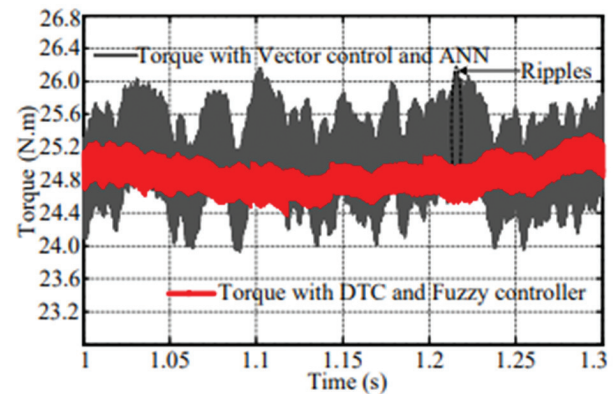


Fig. 5. Response of torque in vector control, ANN and proposed fuzzy based DTC

The load torque considered in this study is of value 25Nm and it can be visualised from the graph that the proposed technique controller can stabilize the electromagnetic torque with reduced ripples in the system. Also, the reduced count of switches in the converter provides a smooth power conversion between the batteries and motor windings.

4.2. SPEED VARIATION

In this study, the proposed controller is tested under a speed variation scenario in which the speed of the motor has been increased at time $t=3s$ from 1000rpm to 1500rpm. During this case, the proposed controller attempts to raise the reference torque of the system. As the speed of the SRM depends on the generated electromagnetic torque hence, the controller enhances the torque of the motor to increase the speed and maintain it to the reference value.

The response of speed of the SRM during this case has been depicted in Fig. 6 in which it is visible that the proposed controller stabilizes the speed to the set reference value. The response of the electromagnetic torque has been shown in Fig.7 from which it can be seen that the torque increases temporarily before stabilizing at its usual value which is equal to the load torque.

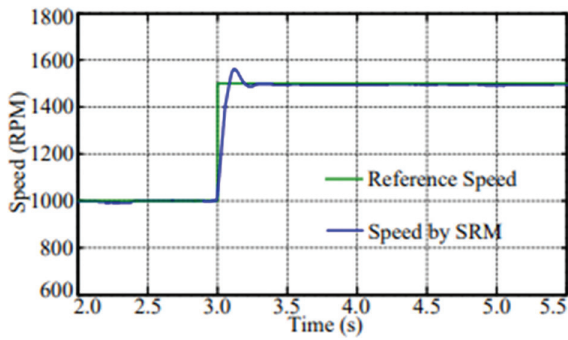


Fig. 6. Response of speed

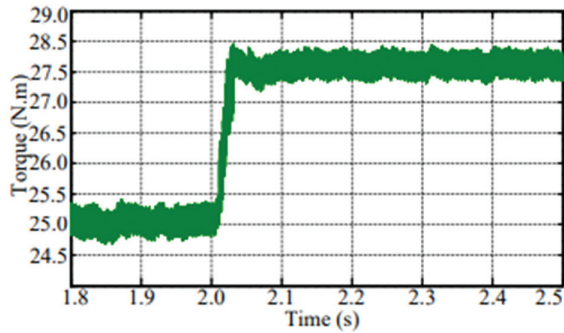


Fig. 7. Response of electromagnetic torque

4.3. LOAD TORQUE VARIATION

The performance of the proposed fuzzy logic based controller has been tested under load torque variation. In this scenario, the load torque has been increased from 25Nm to 27Nm at time $t=2s$. During this scenario, it has been observed that there is a reduction in the speed of the SRM due to increased load torque. The proposed fuzzy controller then increases the reference electromagnetic torque to increase the speed of the motor. This operation is carried out by the controller that sends the required signal to the switches of the converter to increase electromagnetic torque of motor. The response of electromagnetic torque and speed of the system during this scenario has been recorded in Fig.8 and Fig.9 respectively in which it can be observed that when electromagnetic torque reached near the reference value, the speed of the SRM reduced temporarily which has been managed by the proposed controller.

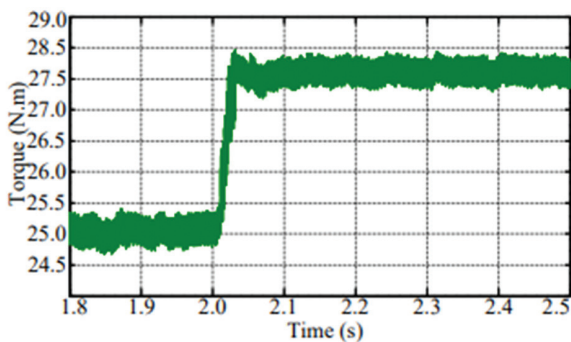


Fig. 8. Response of electromagnetic torque under load torque variation

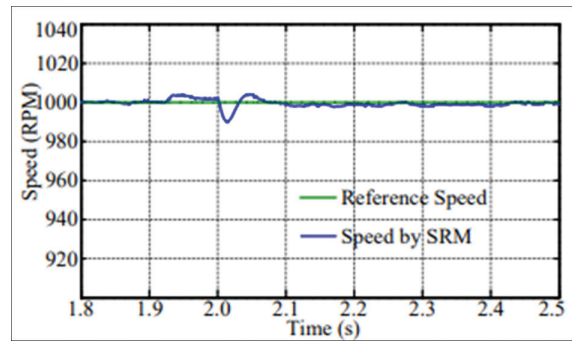


Fig. 9. Response of speed under load torque variation

4.4. RAPID REFERENCE SPEED VARIATION

The rapid speed variation is one of the common case noticed among the SRM applications such as electric vehicles. Hence, to study the efficacy of the controller, a scenario where the reference speed of the motor has been varied from time $t=1s$ to $2.2s$. The response of the reference speed with the variation has been shown in Fig.10 in which it can be observed that the controller can track the changing reference value effectively and allows the motor to run according to the reference speed. This scenario is most useful for the case of electric vehicles in which the reference speed varies continuously. The controller is capable of tracking all types of reference speed variation in the system.

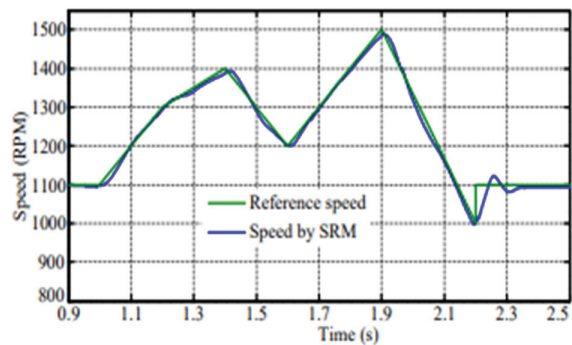


Fig. 10. Response of speed of SRM with rapid reference speed variation

4.5. FLUX TRAJECTORY

The trajectory between the flux of the direct axis and quadrature axis is very important to analyzing the flux status under the operation of the motor. This trajectory can examine both flux weakening and saturation mode of the core. The response of trajectory has been shown in Fig.11 for changing the speed and torque. From the graph, it can be observed that the resultant flux is less than 0.5 per unit (pu), hence the flux is under the limit to avoid saturation mode.

Hence, from the results, it can be concluded that the proposed fuzzy logic based DTC technique for SRM works effectively by smoothing the system's operation along with reducing the ripples. The main advantage

of the proposed technique is the requirement of less switches in the converter and higher torque reduction capability than vector control methods and simple structure. But, the demerit lies in switching frequency variation and the dependence on the flux of the stator along with the hysteresis band comparator.

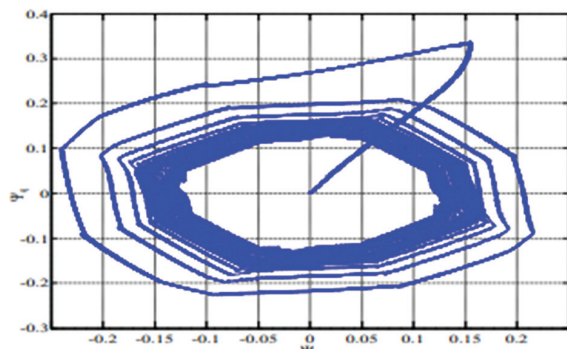


Fig. 11. Response of flux trajectory in pu

5. CONCLUSION

In this paper, a fuzzy logic based direct torque control for the 6/4 poles switched reluctance motor has been proposed that can be used in the electric vehicle application. Also, a new converter with reduced switch counts has been designed to reduce the associated cost and losses from the system. The proposed technique has been tested under various steady-state and transient state scenarios that include load torque variation and speed variation of SRM and compared with the vector control technique. The results clearly state that the proposed technique is capable of reducing the torque ripple and increasing efficiency. Also, it has been noted that during load torque and speed variation scenarios, the proposed technique can stabilize the system with very less generated ripples. Also, during speed variation of the motor, the fuzzy logic-based controller can enhance the speed and maintain it to the reference value. From the conducted analysis, it has been established that the proposed system has a resultant flux of less than 0.5pu. The main advantages of using the proposed control technique lie in its efficient torque reduction, simple structure and reliability. Also, the proposed advanced technique does not generate negative torques like conventional DTC resulting in no reduction of the torque-ampere ratio of the motor. The future scope of this work can be the implementation of the proposed technique in the four-phase and five-phase SRM along with applying the concept in sliding mode control. The same can also be implemented in a real-time scenario with development of hardware prototype as a future scope of the article.

6. REFERENCES:

- [1]. J. Ye, B. Bilgin, A. Emadi, "An offline torque sharing function for torque ripple reduction in switched reluctance motor drives", *IEEE Transactions on energy conversion*, Vol. 30, No. 2, 2015, pp. 726-735.
- [2]. Y. Cai, C. Wang, C. Ju, "Research on torque model based on pretreatment method for switched reluctance motor", *Proceedings of the 13th IEEE Conference on Industrial Electronics and Applications*, Wuhan, China, 31 May 2018 - 2 June 2018, pp. 1881-1885.
- [3]. N. Saha, S. Panda, "Speed control with torque ripple reduction of switched reluctance motor by Hybrid Many Optimizing Liaison Gravitational Search technique", *Engineering science and technology, an international journal*, Vol. 20, No. 3, 2017, pp. 909-921.
- [4]. C. Gan, J. Wu, Q. Sun, W. Kong, H. Li, Y. Hu, "A review on machine topologies and control techniques for low-noise switched reluctance motors in electric vehicle applications", *IEEE Access*, Vol. 6, 2018, pp. 31430-31443.
- [5]. G. F. Lukman, X. S. Nguyen, J. W. Ahn, "Design of a low torque ripple three-phase SRM for automotive shift-by-wire actuator", *Energies*, Vol. 13, No. 9, 2020, p. 2329.
- [6]. P. Bogusz, "A switched reluctance motor control method limiting the maximum dc source current in the low-speed range", *Bulletin of the Polish Academy of Sciences: Technical Sciences*, Vol. 1, 2016.
- [7]. J. Liang et al. "Prediction of acoustic noise and vibration of a 24/16 traction switched reluctance machine", *IET Electrical Systems in Transportation*, Vol. 10, No. 1, 2020, pp. 35-43.
- [8]. Y. Qin et al. "Vibration mitigation for in-wheel switched reluctance motor driven electric vehicle with dynamic vibration absorbing structures", *Journal of Sound and Vibration*, Vol. 419, 2018, pp. 249-267.
- [9]. A. Rezig, W. Boudendouna, A. Djerdir, A. N'Diaye, "Investigation of optimal control for vibration and noise reduction in-wheel switched reluctance motor used in electric vehicle", *Mathematics and Computers in simulation*, Vol. 167, 2020, pp. 267-280.
- [10]. M. Elamin et al. "Effects of windows in stator and rotor poles of switched reluctance motors in reducing noise and vibration", *Proceedings of the IEEE International Electric Machines and Drives Conference*, Miami, FL, USA, 21-24 May 2017, pp. 1-6.

- [11]. M. Le Guyadec, L. Gerbaud, E. Vinot, V. Reinbold, C. Dumont, "Use of reluctance network modelling and software component to study the influence of electrical machine pole number on hybrid electric vehicle global optimization", *Mathematics and Computers in Simulation*, Vol. 158, 2019, pp. 79-90.
- [12]. Z. Omac, C. Cevahir, "Control of switched reluctance generator in wind power system application for variable speeds", *Ain Shams Engineering Journal*, Vol. 12, No. 3, 2021, pp. 2665-2672.
- [13]. E. I. Mbadiwe, E. B. Sulaiman, "Design and optimization of outer-rotor permanent magnet flux switching motor using transverse segmental rotor shape for automotive applications", *Ain Shams Engineering Journal*, Vol. 12, No. 1, 2021, pp. 507-516.
- [14]. C. Labiod, K. Srairi, B. Mahdad, M. T. Benchouia, M. E. H. Benbouzid, "Speed control of 8/6 switched reluctance motor with torque ripple reduction taking into account magnetic saturation effects", *Energy Procedia*, Vol. 74, 2015, pp. 112-121.
- [15]. X. Ai-de, Z. Xianchao, H. Kunlun, C. Yuzhao, "Torque-ripple reduction of SRM using optimised voltage vector in DTC", *IET Electrical Systems in Transportation*, Vol. 8, No. 1, 2018, pp. 35-43.
- [16]. H. A. Maksoud, "Torque ripple minimization of a switched reluctance motor using a torque sharing function based on the overlap control technique", *Journal of Engineering, Technology & Applied Science Research*, Vol. 10, No. 2, 2020, pp. 5371-5376.
- [17]. R. Abdel-Fadil, L. Számel, "Predictive direct torque control of switched reluctance motor for electric vehicles drives", *Periodica Polytechnica Electrical Engineering and Computer Science*, Vol. 64, No. 3, 2020, pp. 264-273.
- [18]. M. Jamil, W. Kongprawechnon, N. Chayopitak, "Average torque control of a switched reluctance motor drive for light electric vehicle applications", *IFAC-PapersOnLine*, Vol. 50, No. 1, 2017, pp. 11535-11540.
- [19]. M. Hamouda, A. Abdel Menaem, H. Rezk, M. N. Ibrahim, L. Számel, "Numerical estimation of switched reluctance motor excitation parameters based on a simplified structure average torque control strategy for electric vehicles", *Mathematics*, Vol. 8, No. 8, 2020, p. 1213.
- [20]. X. Gao, X. Wang, Z. Li, Y. Zhou, "A review of torque ripple control strategies of switched reluctance motor", *International Journal of Control and Automation*, Vol. 8, No. 4, 2015, pp. 103-116.
- [21]. P. Ren, J. Zhu, Z. Jing, Z. Guo, A. Xu, "Minimization of torque ripple in switched reluctance motor based on MPC and TSF", *IEEJ Transactions on Electrical and Electronic Engineering*, Vol. 16, No. 11, 2021, pp. 1535-1543.
- [22]. G. Fang et al. "Advanced control of switched reluctance motors (SRMs): A review on current regulation, torque control and vibration suppression", *IEEE Open Journal of the Industrial Electronics Society*, Vol. 2, 2021, pp. 280-301.
- [23]. H. Kotb, A. H. Yakout, M. A. Attia, R. A. Turkey, K. M. AboRas, "Speed control and torque ripple minimization of SRM using local unimodal sampling and spotted hyena algorithms based cascaded PID controller", *Ain Shams Engineering Journal*, Vol. 13, No. 4, 2022, p. 101719.
- [24]. N. Saha, S. Panda, "Speed control with torque ripple reduction of switched reluctance motor by Hybrid Many Optimizing Liaison Gravitational Search technique", *Engineering Science and Technology*, Vol. 20, No. 3, 909-921.
- [25]. K. K. Nimisha, R. Senthilkumar, "Optimal tuning of PID controller for switched reluctance motor speed control using particle swarm optimization", *Proceedings of the International Conference on Control, Power, Communication and Computing Technologies*, Kannur, India, 23-24 March 2018, pp. 487-491.
- [26]. C. Zhang, Z. Ming, Z. Su, Z. Cai, "An advanced robust method for speed control of switched reluctance motor", *Review of Scientific Instruments*, Vol. 89, No. 5, 2018, p. 054705.
- [27]. A. C. F. Mamede, J. R. Camacho, R. E. Araújo, G. C. Guimarães, "Effects analysis of design parameters on three-phase 6/4 and four-phase 8/6 switched reluctance machines performance", *Proceedings of the International Conference on Electrical Machines*, Gothenburg, Sweden, 23-26 August 2020, pp. 441-447.
- [28]. K. Vijayakumar et al. "Influence of iron powder core on the switched reluctance motor performance enhancement", *Materials Today: Proceedings*, 33, 2020, pp. 2255-2263.

- [29]. G. Fang et al. "Advanced control of switched reluctance motors (SRMs): A review on current regulation, torque control and vibration suppression", *IEEE Open Journal of the Industrial Electronics Society*, Vol. 2, 2021, pp. 280-301.
- [30]. F. Peng, J. Ye, A. Emadi, "A digital PWM current controller for switched reluctance motor drives", *IEEE Transactions on Power Electronics*, Vol. 31, No. 10, 2015, pp. 7087-7098.
- [31]. E. El-Kharahi, M. El-Dessouki, P. Lindh, J. Pyrhönen, "Toward including the effect of manufacturing processes in the pre-estimated losses of the switched reluctance motor", *Ain Shams Engineering Journal*, Vol. 6, No. 1, 2015, pp. 121-131.
- [32]. C. Lai, Y. Zheng, A. Labak, N. C. Kar, "Investigation and analysis of iterative learning-based current control algorithm for switched reluctance motor applications", *Proceedings of the International Conference on Electrical Machines*, Berlin, Germany, 2-5 September 2014, pp. 796-802.
- [33]. S. S. Ahmad, G. Narayanan, "Linearized modeling of switched reluctance motor for closed-loop current control", *IEEE Transactions on Industry Applications*, Vol. 52, No. 4, 2016, pp. 3146-3158.
- [34]. H. N. Huang, K. W. Hu, Y. W. Wu, T. L. Jong, C. M. Liaw, "A current control scheme with back EMF cancellation and tracking error adapted commutation shift for switched-reluctance motor drive", *IEEE Transactions on Industrial Electronics*, Vol. 63, No. 12, 2016, pp. 7381-7392.
- [35]. X. Li, P. Shamsi, "Inductance surface learning for model predictive current control of switched reluctance motors", *IEEE Transactions on Transportation Electrification*, Vol. 1, No. 3, 2015, pp. 287-297.
- [36]. X. Li, P. Shamsi, "Model predictive current control of switched reluctance motors with inductance auto-calibration", *IEEE transactions on Industrial Electronics*, Vol. 63, No. 6, 2015, pp. 3934-3941.
- [37]. X. Zhang, Q. Yang, M. Ma, Z. Lin, S. Yang, "A switched reluctance motor torque ripple reduction strategy with deadbeat current control and active thermal management", *IEEE Transactions on Vehicular Technology*, Vol. 69, No. 1, 2019, pp. 317-327.
- [38]. S. S. Ahmad, G. Narayanan, "Predictive control based constant current injection scheme for characterization of switched reluctance machine", *IEEE Transactions on Industry Applications*, Vol. 54, No. 4, 2018, pp. 3383-3392.
- [39]. B. Ganji, M. Heidarian, J. Faiz, "Modeling and analysis of switched reluctance generator using finite element method", *Ain shams Engineering Journal*, Vol. 6, No. 1, 2015, pp. 85-93.
- [40]. E. S. Prasad, B. S. Ram, "Ant-lion optimizer algorithm based FOPID controller for speed control and torque ripple minimization of SRM drive system", *Proceedings of the International Conference on Signal Processing, Communication, Power and Embedded System*, Paralakhemundi, India, 3-5 October 2016, pp. 1550-1557.

A quadratic boost converter derived multi output converter for electric vehicles application

Original Scientific Paper

I. S. Sree Devi

Noorul Islam Centre for Higher Education
Kumarakovil, TamilNadu, India
issredevieeee@gmail.com

D. M. Mary Synthia Regis Prabha

Noorul Islam Centre for Higher Education
Kumarakovil, TamilNadu, India
regisprabha@gmail.com

Abstract – A novel Solar Photo Voltaic Powered dual output DC to DC converter with the Quadratic Boost Converter as the core element, typically for Electrical Vehicle applications has been proposed and validated in this work. The proposed system harvests the solar power and charges a 12 V battery, supplies power to a 12 V load, using the buck feature of the proposed converter. A second channel of 48 V output is derived using the boost channel and the 48 V output is meant for driving the traction motor as well as any other load that requires a regulated 48 V. The proposed converter can operate in three different modes. For the purpose of voltage regulation at the 48 V and 12 V output channels and for the Maximum Power Point Tracking, applicable to the Solar Photo Voltaic source, individual Sliding Mode Controllers are used. The proposed idea has been validated using simulations in the MATLAB SIMULINK environment and an experimental prototype.

Keywords: harvesting solar photo voltaic energy, quadratic boost derived converter, multiple output dc to dc converters, sliding mode controllers, dual output converter

1. INTRODUCTION

Electrically powered vehicles of all ranges of power ratings are encouraged globally. The EV sector includes all transportation systems from the E bike to the electrically actuated city buses and so on. EVs are also included in the fleet of garbage management systems in big and smart cities as well as industrial transportation systems. The electrically actuated two wheeler bikes, which can carry two persons, use BLDC motors which require 48 V DC. The three wheeler type garbage collecting EVs used in major cities use the BLDC motor or the DC motor as the drive element and it is rated at 48 V. In the case of three wheeler type garbage collection and transportation system the main source of power is the Solar Photo Voltaic (SPV) panels mounted on the top and sides of the body of the vehicles. There is a standard battery backup of voltage rating 12 V and of nickel ion or lead acid type. These vehicles also have charging facility using which the battery can be charged directly from the utility AC source when the vehicle is parked in the standby condition. [1 – 4] Essentially these systems have three entities namely the SPV source, the battery and the BLDC motor. Although the SPV panels have a certain rated voltage and cur-

rent, because of the changes in the solar irradiance and temperature the terminal voltage of the SPV panel will have to be maintained at the optimal voltage for enabling maximum power point tracking system. Thus the SPV panel becomes a variable voltage, variable power output source. This variable DC voltage source is used by a DC to DC converter to charge the battery that is nominally rated at 12 V. The required operating voltage of the BLDC motor is 48 V. The BLDC motor may use either a voltage controlled speed control mechanism or a current controlled PWM scheme for the speed control. Thus three different voltages are involved in the system. Therefore a DC to DC power conversion system converter that can deliver the required voltage to the 12 V battery from the SPV panel or from the utility source and the required 48 V to the BLDC motor drive system is required.

In [5] the authors have developed an off line battery charging system and in [6] the authors have developed an electric vehicle for a typical school bus application. Since an automobile, especially an electrical vehicle uses a number of electrical systems which require different voltage levels, DC to DC converters with multi input multi output features are required. The main drive

system may use a higher DC voltage while the control systems, lights, AC, video monitors, navigational systems etc. may require diversified DC voltage levels.

Since many of the electrical vehicles use drives which require at least 48 V, when the backup source is a 12 V DC battery, high voltage gain DC to DC converters are required. In [7] a switched reluctance motor based drive system has been developed and the system uses a high voltage gain DC to DC converter. In [8 -9] the authors have adopted a hybrid DC to DC conversion system that combines the topologies of the Quadratic Boost converter and the Cuk or with the SEPIC converter. The Quadratic Boost Converter (QBC) has also evolved as a high voltage gain DC to DC converter. The authors in [10] have developed and validated the concept of QBC.

Considering the non linearity and the variable structure nature of the power electronic converters the Sliding Mode Controller (SMC) is encouraged. Several researchers have used the SMC for parameter regulation as well for maximum power point tracking of the renewable resources [11 - 13].

A proliferation of multiport DC to DC conversion systems are available and the authors in [14] and [15] have presented multiport DC to DC conversion systems using hybrid energy sources.

The authors in [16] have presented a bidirectional power conversion scheme that has proved to be comparatively more efficient. The authors in [17] have developed a non-isolated high step- up DC-DC converter featuring soft switching for hybrid energy systems. Quadratic boost converter is discussed in detail in [18]-[21]. A combination of an isolated and a non isolated multiple output topology was proposed and validated by the authors in [22]. A multi input SPV energy harvesting system with a DC to DC converter has been demonstrated in [23]. The authors in [23] have also included an MPPT feature in this work. An interesting power flow control scheme for a dual input interleaved converter with buck and boost features has been demonstrated by the authors in [24]. An AC link converter topology for a solar powered inverter was proposed and validated by the authors in [25]. The high frequency resonant AC link enables zero voltage switching leading to reduced switching losses and increased power conversion efficiency. The authors in [26] have proposed and validated a battery charging system for the nanogrid using a set of multiple sources governed by a common control. Further in [27] a two stage bidirectional AC/DC converter that uses a renewable energy source governed by a suitable control loop design has been proposed and validated. In a similar development, a bidirectional micro inverter with a dual active bridge scheme with ultra capacitor based energy storage system powered by modular SPV source was proposed and validated in [28]. In the article [29] a novel bidirectional converter for the support of a residential DC distribution system with a grid interface for the SPV source has been presented. The same authors

as in [29] have made another contribution [30] wherein a novel grid interface with a two stage power conversion scheme has been promoted.

To this end, a review of the literature suggests that a solar power harvesting system with high voltage gain, bidirectional power transaction, energy storage and backup feature and multiport outputs are an absolute necessity in the modern electric vehicle industry. In this work a novel Quadratic Boost Derived Multi Output Converter(QBDMOC) is designed and is used to deliver a 48 V boost output and 12 V stepdown output. . The control scheme adopted uses the Sliding Mode Controller (SMC) and this ensures the harvest of maximum power from the solar PV system for the given solar irradiation.

The paper is arranged as follows. Next to this brief introduction, in section 2, an outline of the proposed system is presented. The state space averaged model of the QBC is presented in section 3. The realization of the proposed system in MATLAB SIMULINK environment is given in section 4. The details of the experimental verification and the results obtained in simulations and in the experimental verifications have been discussed about in section 5. The conclusion and the references section follow.

2. OUTLINE OF THE PROPOSED SYSTEM

The general structure of the proposed system is shown in Fig. 1. It draws power from the SPV source and optionally the utility source can be used. There are two output voltages and they are maintained at 12 V (LV) and 48 V (MV). Fig. 1 shows the configuration in which the 12 V battery, a load for the LV bus and a load for the MV bus are used. Across the MV bus bar, an R or RL load is used or as shown in Fig. 2, typically a BLDC motor can be used. The features of the proposed system are it can generate a 48 V DC supply from a battery or from the SPV source or from the Utility source. Depending upon the availability and the strength of the different sources and the requirement of the load, the different modes are selected. The topology of the core power electronic converter used in the proposed system is similar to a Quadratic Boost Converter.

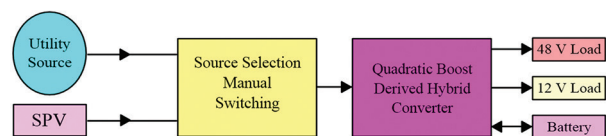


Fig. 1. Proposed dual output DC to DC converter

In addition, the system uses an additional power electronic switch for delivering a stepped down voltage output, typically 12 V for either charging the battery or for delivering power for the 12 V load. With reference to the circuit diagram shown in Fig. 3 there are two individual switches SW_1 and SW_2 and a set of switches grouped as GS. SW_1 can connect or discon-

nect the external source to the converter unit. The switch SW_2 can be used to connect or disconnect the 48 V load denoted as Load 2.

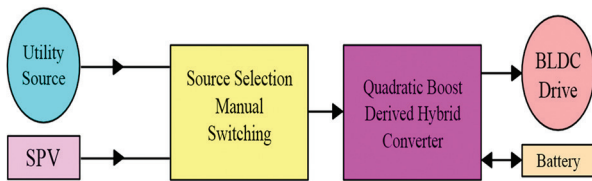


Fig. 2. An Application of the proposed system

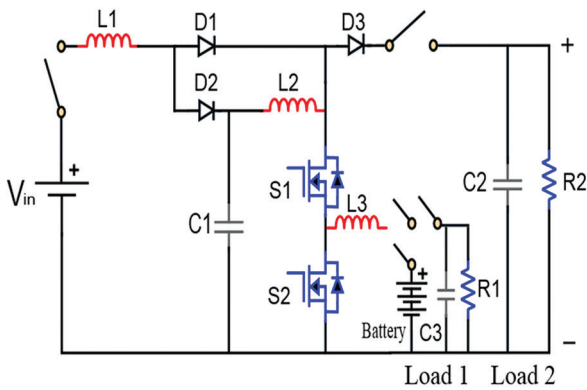


Fig. 3. Schematic of the proposed system

The switch group GS can be used to connect the battery to the rest of the circuit for charge or discharge modes of operation. Using the switch group GS, the low voltage load, denoted as Load1, can be connected or disconnected to the battery or to the converter. Some of the important modes of operation which could be realized using these are,

Mode. 1. The input source voltage is available. (Buck Mode) (SW_1 On; SW_2 Off; GS: Battery connected to converter). In this mode only the battery gets charged.

Mode. 2. The source voltage is not available. (SW_1 Off; SW_2 On; GS: battery connected to converter). The boost converter draws power from the 12 V battery and drives Load 2 with 48 V regulated supply. The battery is now discharging.

Mode. 3. The main input source is available. (Buck and Boost (QBC))

Load 1 and load 2 are operational. The battery can also be charged.

3. THE DETAILS OF THE SUBSYSTEMS

3.1 STATE SPACE ANALYSIS OF THE QUADRATIC BOOST CONVERTER

Since the QBC is the heart of the system the state space analysis of the QBC is developed and considering the steady state condition from the state equation the voltage gain of the QBC is derived. The voltage gain of the GBC and the QBC are shown in equations (1) and (2) respectively

$$V_o = \frac{V_{in}}{(1-D)} \quad (1)$$

$$V_o = \frac{V_{in}}{(1-D)^2} \quad (2)$$

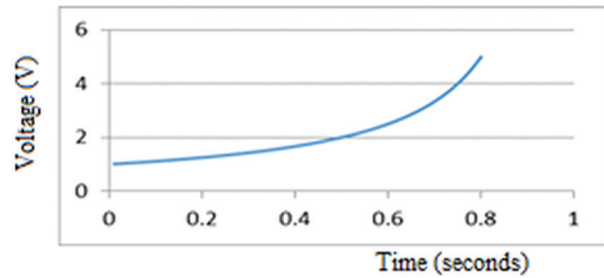


Fig. 4. Voltage gain variation of boost converter

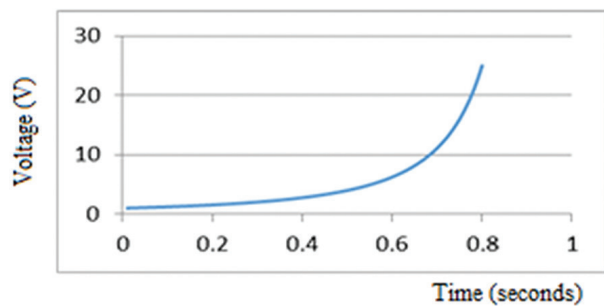


Fig. 5. Voltage gain variation of proposed converter

Fig.4 and Fig. 5 shows the duty cycle D versus voltage gain of the generic boost converter and proposed converter respectively. With reference figures 4 and 5 it can be seen that the voltage gain of the QBC is much higher than that of the GBC.

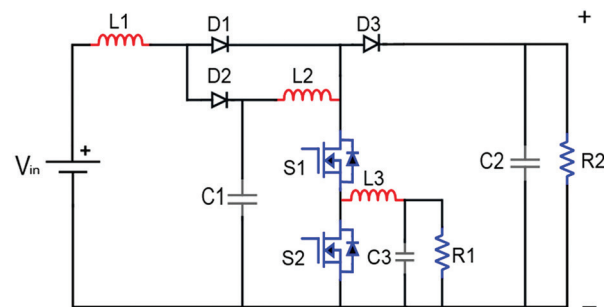


Fig. 6. Topology of the Quadratic boost derived hybrid converter

The topology of the proposed system is given in Fig.6

3.2 THE SOLAR PHOTO VOLTAIC SOURCE

Here, the SPV source is the primary source of power. Six numbers of similar panels are used in parallel. The VI and the VP characteristics of one of the SPV panel are shown in Fig. 7.

With reference to Fig. 7 it is clear that the solar power output will be maximum, for any given solar irradiation, if and only if the terminal voltage of the SPV subsystem is maintained at a specific value while it delivers a spe-

cific current as well. In this work the SMC technique is used for MPPT. The advantage of the SMC technique is that, unlike the perturb and observe algorithm and the incremental conductance algorithm for MPPT, the SMC based MPPT scheme requires only the terminal voltage of the SPV unit need to be monitored.

In MPPT system, as applied to SPV systems, the set or the desired value of the controlled parameter is a dynamic one. Since the power electronic switches can be switched at high frequencies the SMC can track the desired level easily.

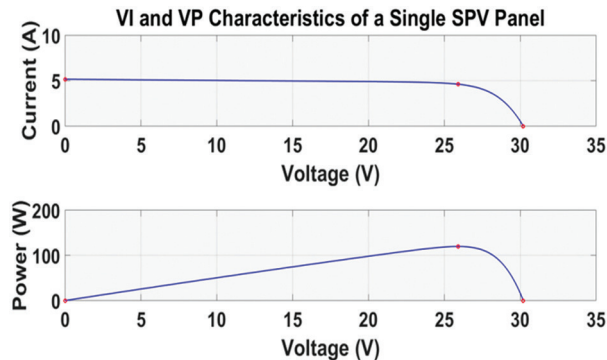


Fig.7. VI and VP characteristics of one of the SPV panels

3.3 SMC AS A MPPT CONTROLLER

The ratio between V_{pmax} and V_{oc} is a constant of the panel, which we denote as G , and the operating terminal voltage of the SPV panel should be adjusted in real time that the constant G is always maintained.

The algorithm for the SMC based MPPT is as follows.

1. Keep the power converter in the OFF state.
2. Measure the Open Circuit Terminal Voltage of the SPV unit. (V_{oc})
3. Turn on the power converter.
4. Measure the Terminal Voltage of the SPV unit (V_{pv}).
5. Is $(V_{pv} / V_{oc}) < G$ (G is the constant and is V_{pmax} / V_{oc}).
6. If yes, turn OFF the power converter and go to step 1.
7. Else keep power converter ON and go to step 4.

3.4 SCHEME OF CONTROL

There are some operational modes selected manually, as given earlier in the outline section. Besides, there are some requirements to be fulfilled automatically by the proposed control systems. The automatic closed loop control schemes have been built to satisfy the following requirements or objectives.

- There must be a provision for MPPT.
- The voltage across Load 2 should be maintained at 48 V

- The load across Load 1 should be maintained at 12 V.

In the proposed system the switch S_1 is primarily meant for buck operation to deliver a 12 V supply across Load1 or charge the 12 V battery. The switch S_2 is primarily meant for the boost operation. There are two control sub systems and they are meant for the buck and the boost converter switches S_1 and S_2 respectively. For the boost converter a fixed duty cycle of 0.6 is used. This will provide a voltage gain of $(1 / (1 - 0.6)^2) = 6.25$. If the source voltage is as low as 10 V the maximum possible output voltage could be 62.5 V. The duty cycle of the buck converter is 0.8 and if the source voltage is as low as 15 V the output voltage could be 12 V.

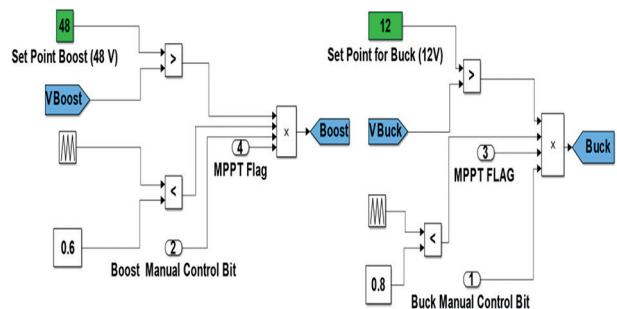


Fig. 8. Control subsystems.

Fig. 8 shows the control scheme adopted as realized in the MATLAB SIMULINK environment.

3.5. INTERLOCKING CONTROL SCHEME

In the proposed system, for the QBC based boost mode of operation the switches S_1 and S_2 should be operational. It is possible that the voltage across load 1 reaches the 12 V level earlier than the instant the voltage across Load 2 reaches 48 V. In this scenario according to the control scheme logic switch S_1 will be turned off. This will stop the functioning of the QBC and the voltage across Load 2 cannot be built up to the required 48 V level. According to the control system, only S_2 will be getting the required switching pulses. This will enable the capacitor across Load 1 to act as a source and the S_2 along with the inductor L_3 and the diode of S_1 will form a generic boost converter trying to pump power to the 48 V load. This causes the voltage across the Load1 to become little less than 12 V level bringing again S_1 also to be functional and the QBC comes back to form. This process continues until the voltage across Load1 and Load2 reach 12 V and 48 V level respectively.

3.6. DIFFERENT MODES OF OPERATION AND POWER BALANCE

Mode 1: The different modes of operations and the corresponding circuit arrangements are shown in Fig.9 to 11. Fig. 9 shows the battery charging mode or the 12 V load driving mode. In this mode the 48 V load is turned off. The power control switch S_1 is operational in

the buck mode. The diode inside S_2 is used as the free-wheeling diode. The control system regulates the load side voltage at 12 V. In the same mode of operation, if an SPV is used for the source and a battery is used for the load then the battery is charged satisfying the MPPT requirement.

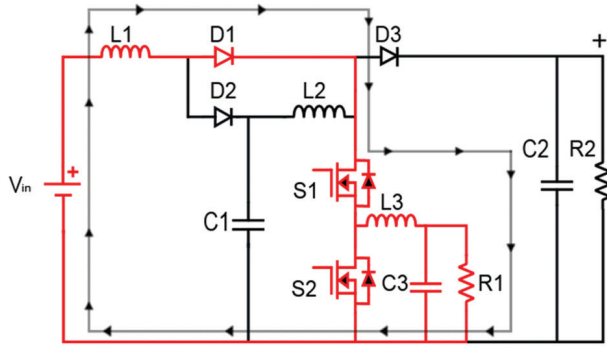


Fig. 9. Buck mode of operation

Fig. 10 gives the circuit arrangement of the buck and the boost mode of operation. The S_1 and S_2 are operational and the load side voltages of 12 V and 48 V are regulated across the respective loads.

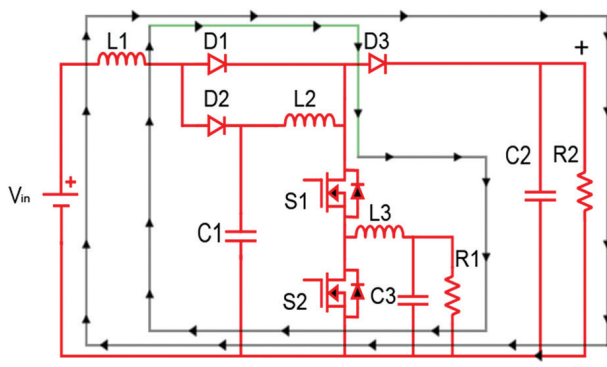


Fig. 10. Buck and boost modes of operations

Fig. 11 shows the scenario when the external source is absent and the 48 V load is operational. The battery supplies the required power to the 48 V load. The circuit obeys the voltage gain equation of the generic boost converter.

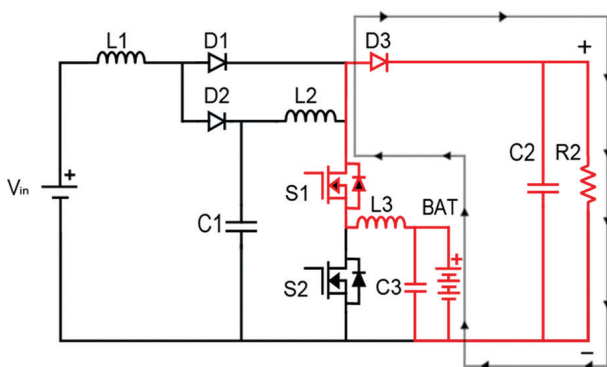


Fig. 11. Boost mode powered from the battery

4. REALIZATIONS IN MATLAB SIMULINK AND THE RESULTS

The proposed system has been realized in MATLAB SIMULINK and the various subsystems are presented in Fig.12 to 14. Fig. 12 shows the SPV and the MPPT subsystems. Fig. 13 shows the internal structure of the SMC based MPPT scheme. The constant 0.857 is the constant of the solar panel used and it has been derived using equation (3)

$$G = \frac{V_{pmax}}{V_{oc}} = \frac{25.9}{30.2} = 0.857 \quad (3)$$

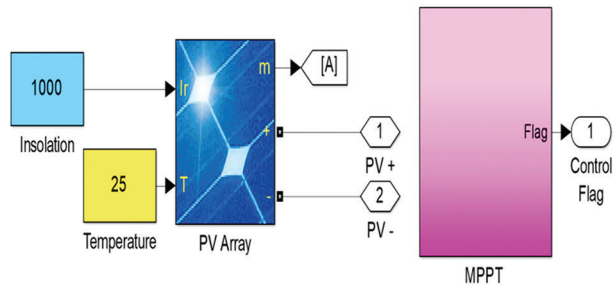


Fig. 12. SPV Subsystem

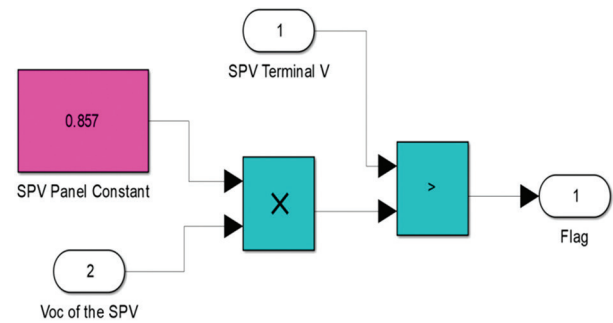


Fig. 13. MPPT subsystem

Fig. 13 shows the MPPT subsystem. To start with, the control system monitors the open circuit voltage of the SPV and calculates the required voltage to be maintained across the SPV subsystem. Then the power converter is actuated until the terminal volts falls down to the V_{pmax} level from the V_{oc} level. Once the terminal voltage across the SPV falls just below the V_{pmax} level the converter is switched off. The SPV voltage now rises back to the same V_{oc} level or a new V_{oc} level depending upon the current solar irradiance. The V_{oc} is noted down, the new V_{pmax} is estimated and then the converter is again turned on. The process continues and the required voltage across the SPV panel is thus maintained with a mild chattering and the maximum power harvest is achieved.

Fig. 14 shows the implementation of the proposed system in the MATLAB SIMULINK environment. The two MOSFETs S_1 and S_2 get the required switching pulses from the control system discussed in the earlier section and shown in Fig. 8. The results of the simulations have been recorded for different modes of operation and are presented herein.

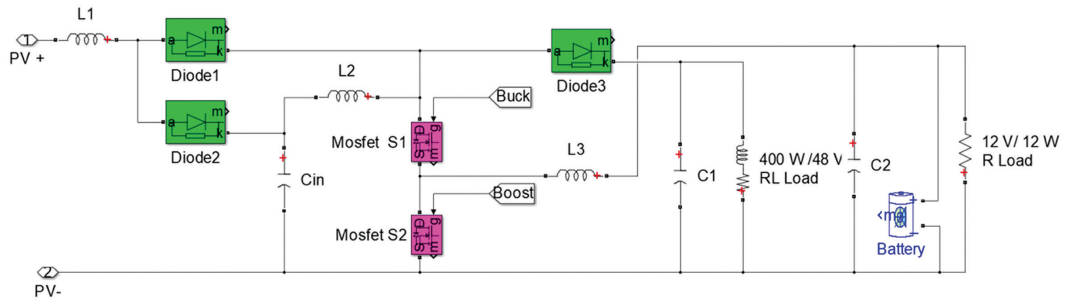


Fig. 14. MATLAB SIMULINK realization of the proposed system

4.1 MODE 1 OPERATION: BATTERY CHARGING FROM EXTERNAL SOURCE

In this mode of operation the battery is charged from the external source. The active part of the circuit is highlighted and is shown in Fig. 9. As a result of a solar irradiance of 1000 W/m^2 , the battery is charged. The related waveforms are shown in Fig. 15 to 21. Fig. 15 shows the solar irradiance of 1000 W/m^2 . The corresponding terminal voltage across the SPV panel is shown in Fig. 16. The terminal voltage across the SPV panel which is nearly 25 V is buck converted to charge the 12 V battery and the battery gets charged with charging current shown in Fig. 18. As a result the State Of Charge of the battery gets increased and is shown in Fig. 19. The voltage across the battery is nearly 12.5 V and is as shown in Fig. 20.

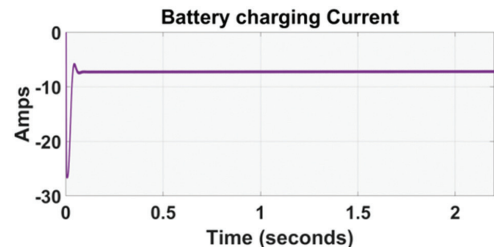


Fig. 18. Battery Charging current

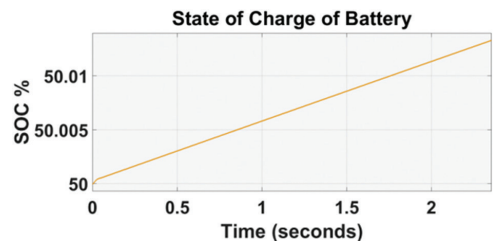


Fig.19. Rise of SOC while charging

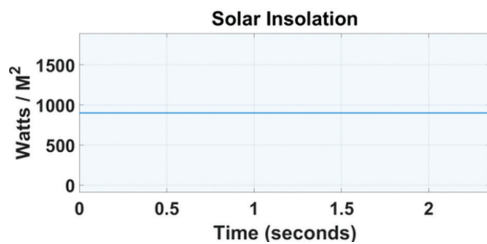


Fig. 15. Solar irradiance of 1000 W/m^2 .

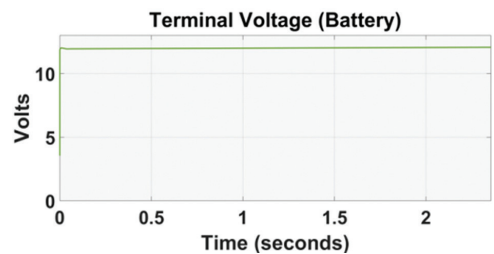


Fig. 20. Battery charging current

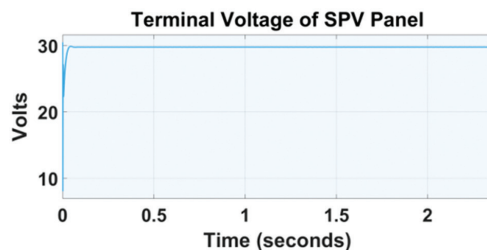


Fig. 16. Terminal voltage across the SPV

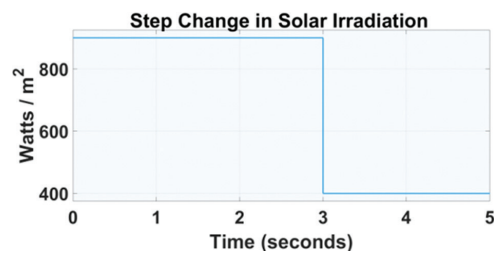


Fig. 21. Step change in solar irradiance

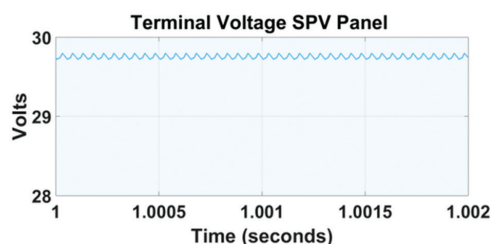


Fig. 17. Ripple in the SPV terminal voltage

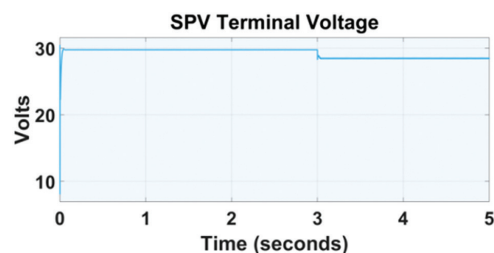


Fig. 22. SPV terminal voltage

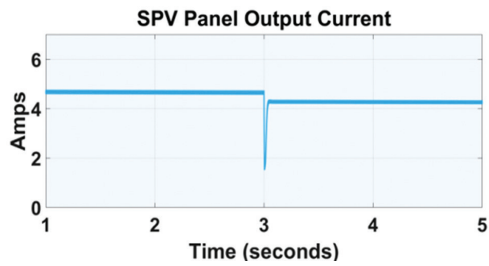


Fig. 23. SPV panel output current

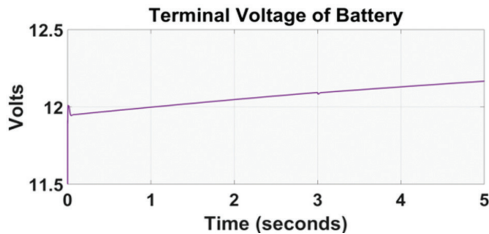


Fig. 24. Rise of Battery voltage

Fig. 21 shows the case of a step change in the solar irradiance from 900W/m^2 to 400W/m^2 . All the related waveforms have been recorded and the important waveforms are shown in Fig. 21 to 24. The change in solar irradiance occurs at time instant 3 sec. and correspondingly the other waveforms reflect. It is observed that there is negligible impact on the loads when there is a step change in input. The transient response of the SPV reflected in terms of the SPV voltage and the SPV output current have been recorded and are as shown in figures 22 and 23. The fall in the solar irradiance results in a fall of the terminal voltage across the SPV terminals and the sudden dip in the SPV current at 3 seconds while the solar irradiance suddenly falls.

4.2 MODE 2: DELIVERING POWER TO THE 48 V LOAD

In this mode of operation corresponds to the circuit arrangement shown in Fig. 11. The external source is not used. The battery supplies the required power for the 48 V load. The SOC of the battery falls with time. The terminal voltage across the load and the battery discharge current are shown in Fig.25- 27. The discharge current from the battery is positive.

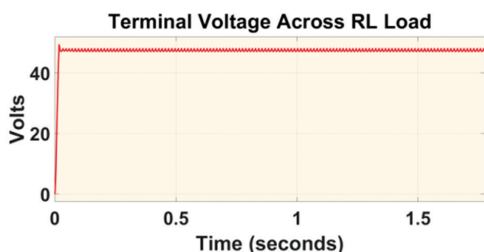


Fig. 25. Terminal voltage across Load2

The proposed system is intended to deliver an output voltage of 48 V in the high voltage output channel. The transient response of the output voltage, when a command is given at time instant 0 is given, is shown in fig-

ure 25. the rise time of the output voltage was observed to be 0.02 second. The peak overshoot was observed to be 49.5 V and the steady state error was found to be 0.05 as the output voltage was regulated at 48.05 V.

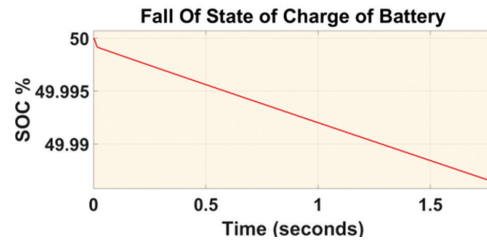


Fig. 26. SOC of battery

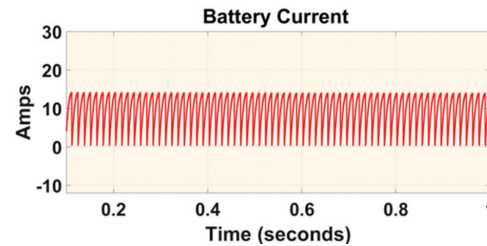


Fig. 27. Battery current (Discharging)

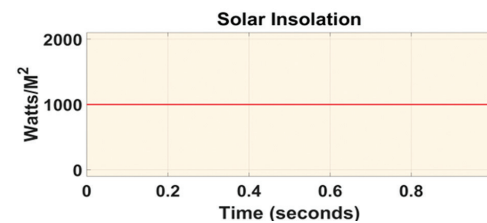


Fig. 28. Solar irradiation

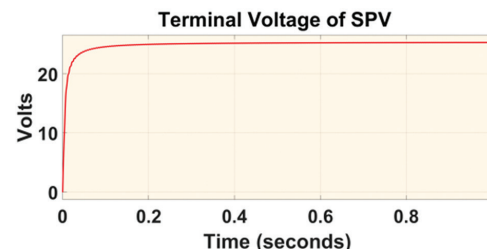


Fig. 29. Terminal voltage of SPV

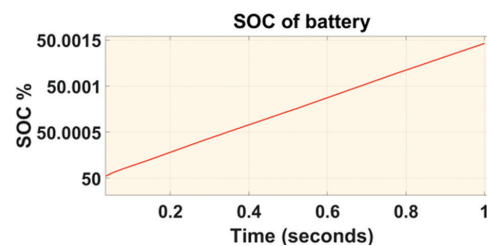


Fig. 30. SOC of the battery

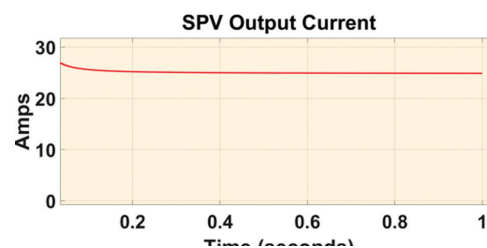


Fig. 31. Output current of SPV

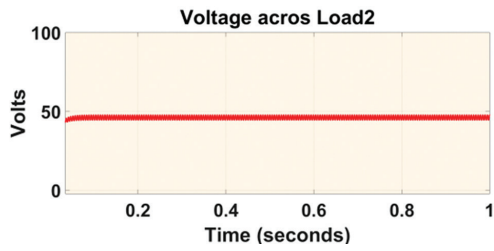


Fig. 32. Voltage across Load 2

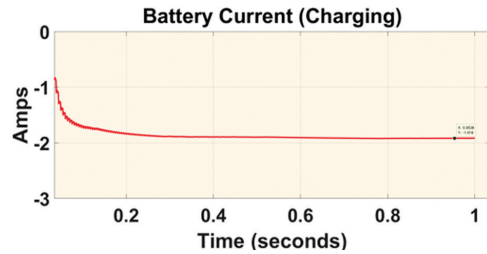


Fig. 33. Battery charging current

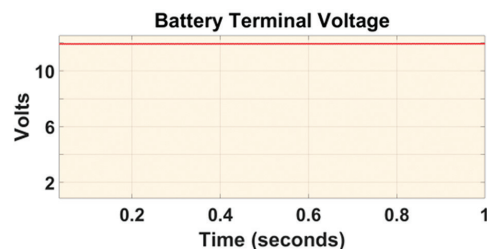


Fig. 34. Battery terminal voltage

4.3 MODE 3: BUCK AND BOOST MODE OF OPERATION

In this mode both the loads are operational. Fig. 29 to 34 correspond to the case of the external source delivering power to the 48 V load as well the battery is charged. The circuit arrangement shown in fig. 10 corresponds to this mode of operation. With a solar irradiance of 1000 W/m^2 , the maximum power harvested is shared among the loads without any wastage. Table 1 & 2 gives the specifications of the components used and the values of some important parameters.

Table 1. Nominal parameters and specifications of components

Parameter / Component	Specification
Power Electronic Switches	MOSFET
Inductor L_1	500 μH
Inductor L_2	500 μH
Capacitor C_1	2200 μF
Capacitor C_2	2200 μF
Nominal Input voltage	12 to 19 V
Buck output for Battery	12 V
Boost output for Load	48 V
Nominal load @ 48 V	500 W
Nominal load @ 12 V	300W

Table 2. Specifications of the SPV Panel and the battery

SPV panel	Specification
Max. Power rating of panel	120 W
Open Circuit Voltage	30.2 V
Short Circuit Current	5.15 A
Voltage at P_{max}	25.9 V
Current at P_{max}	4.63 A
Number of panels in series	1
Number of panels in Parallel	6
Storage Battery	
Type	Lead Acid
Nominal Terminal Voltage	12 V
Capacity	35 Ah

5. HARDWARE DESCRIPTION

The major components of the setup include the SPV panel, the battery the proposed converter system and the resistive loads for the 12 V and 48 V channels of loads. The SPV system can deliver a maximum power output of 125 W at a solar irradiance of 1000 W/m^2 and 25°C . The battery is rated 12 V and 35 Ah. An R load of $50 \Omega / 50\text{W}$ is powered by the system. The excess energy harvested is stored in the battery. When the SPV is not available the battery supplies the load. The system therefore has a buck mode of operation and a boost mode of operation happening simultaneously. The buck converter charges the battery while the boost converter supplies the required 48 V to the load. The proposed system uses an SMC for the maintenance of the 48 V across the load. The switching pulses produced by the SMC drives the MOSFET through the opto coupler.

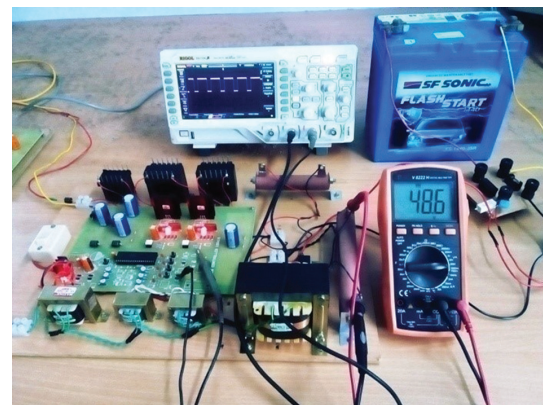


Fig. 35. Photograph of the proposed system

The algorithm can be implemented in the PIC Micro controller. The PIC Micro Controller 16F877 A has built in ADCs using which the terminal voltage of the panel and any other analog quantities to be considered could be read into. In the case of the quadratic boost derived hybrid converter topology, it is necessary that the power electronic switch be applied with a square pulse of a

fixed duty cycle that can produce the required output voltage and MPPT.

The power electronic switches used in the buck and the boost sections are of type IRF 540 and they are protected with snubber circuits. The hardware prototype uses an optical isolation between the control circuit and the power circuit. The control circuit consists of the micro controller. The power circuit consists of the main source of power, the load, the battery and the power electronic switches and the storage elements like L and C which form the topology.

The specifications of the system under consideration are shown in table 3.

Table 3. Specifications of the Proposed System

Parameters	Specifications
Capacity of SPV Source	125 W
Open circuit voltage	22.2 V
Short Circuit Current	7.75 A.
Voltage at Pmax	17.2 V
Current at Pmax	7.25 A.
The MOSFETs	IRF 540
Opto Coupler	MCT2E

The wave forms of the various currents and the voltages have been recorded and are presented herein. Fig. 35 shows the terminal voltage of the SPV panel when there is no load on the SPV panel. It has been observed that for the given climatic conditions the open circuit voltage of the SPV panel is 9.1 V. With the battery as the load, for the available solar irradiance the battery gets charged. The switching pulses applied to the buck converter switch SW1 is shown in Fig. 37. The charging current is shown in Fig. 38.

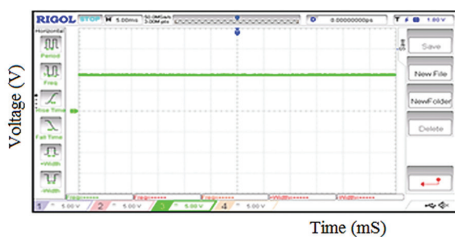


Fig. 36. SPV panel terminal Voltage with No load on the SPV (Low Solar Irradiance; $V_{pv} = 9V$)

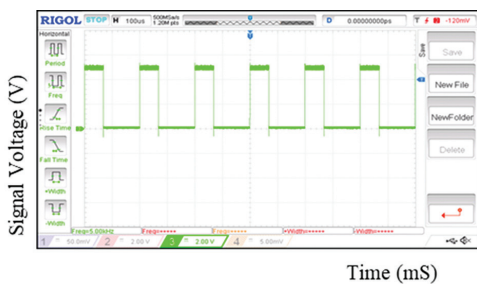


Fig. 37. Switching pulses applied to the buck converter.

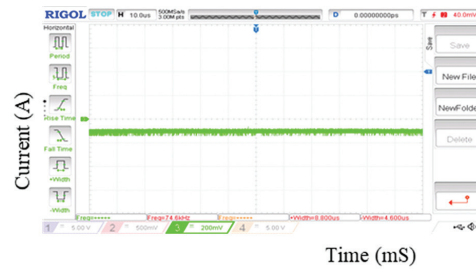


Fig. 38. Battery while charging. (Scenario 1)

When the quadratic boost converter is in action the two inductors L_1 and L_2 play important role in boosting up the voltage from the SPV panel which is as low as 15.2 V as shown in Fig. 39, to a load side voltage of 48 V. Fig.41 shows the load side voltage of 48 V when the system is fed directly from the SPV panel, without the support of the battery. In this mode of operation switches S_1 and S_2 should work and the voltage across the series combination of S_1 and S_2 is shown 40.

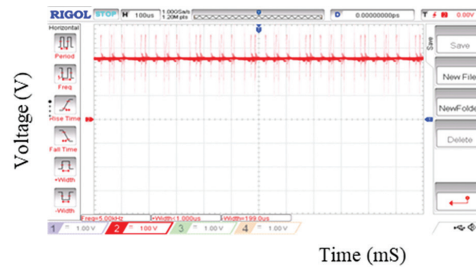


Fig. 39. SPV terminal voltage

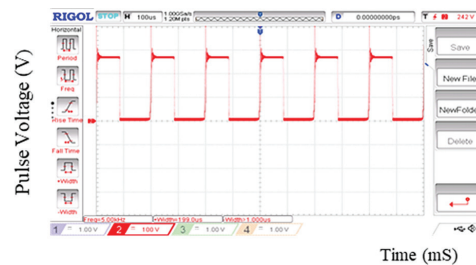


Fig. 40. Voltage across the switch S1 and S2

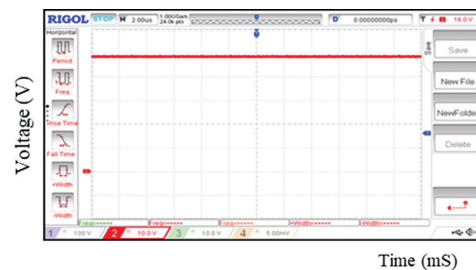


Fig. 41. Voltage across the load = 48 V

When the SPV source is not available, the battery is the only source and it gets discharged while supplying power to the 48 V load. In this mode of operation, the generic boost converter operation takes place with L_3 as the boost inductor and SW_2 as the power control switch. The inductor current L_3 current has a continu-

ous component and a pulsating component. The inductor L_3 current is the input current now, and it is the battery discharge current also as shown in Fig. 42.

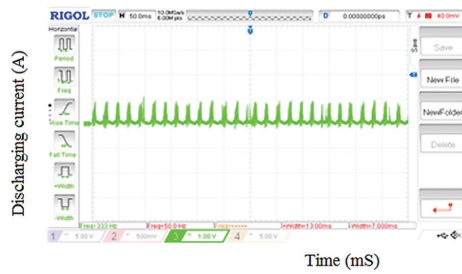


Fig. 42. Battery discharging while no SPV (Scenario 2)

The proposed system can be operated in standby mode also when the SPV power is just used for charging the battery. During this period the loads will not be operational. The power electronic switch S_1 alone works and the internal diode in S_2 acts as the free-wheeling diode. The buck action charges the battery and the battery terminal voltage rises. The battery terminal voltage is as shown in Fig. 43.

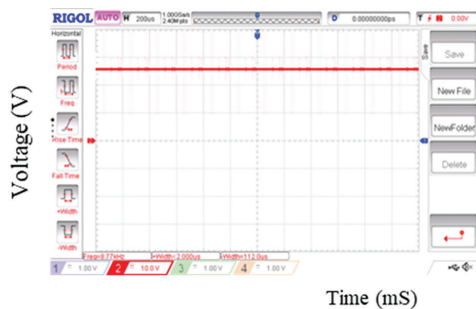


Fig. 43. Voltage across the battery while charging

The control system meant for regulating the output voltage for load 2 at 48 V can be used to regulate any desired load side voltage by just changing the set point. A typical case of regulating the voltage across load 2 at 30 V is shown in Fig. 44.

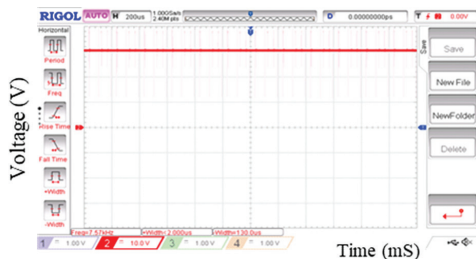


Fig. 44. Voltage across the load when the set value is 30 V

Different scenarios are shown in table 4.

With reference to the tables showing the different scenarios it is clear that when the SPV power is available and if it is more than the demand of the load the

excess power available is routed to the battery through the buck converter. The battery gets charged. It was observed that, for the case when the SPV power generated is 43 W with a terminal voltage of the SPV panel is 14.7 V the SPV current is 2.96 A. Out of this power, the battery is being charged with a terminal voltage across the battery being 12.72 V and the charging current is 3.27A and the total power harvested is routed to the battery.

Table 4. Scenario 1: SPV available Load 48 W Connected.

Source	Power	Voltage	Current
SPV	116 W	19.2 V	6.04 A
Battery	50 W	12.2 V	4.03 A (Charging)
Load2	48 W	48 V	1 A
Load 1	12.4 W	12.2 V	1.016 A
Efficiency	95.19%		

Table 5. Scenario 2: No SPV Source but Load Connected

Source	Power	Voltage	Current
SPV	0 W	0 V	0 A
Battery	65.8 W	11.9 V	5.53 A (Discharging)
Load2	48 W	48 V	1 A
Load 1	11.8 W	11.9 V	0.991 A
Efficiency	90.87%		

Table 6. Scenario 3 SPV Source Available but No Load

Source	Power	Voltage	Current
SPV	43 W	14.7 V	2.96 A
Battery	40 W	12.72 V	3.27 A (Charging)
Load2	0 W	48 V	0 A
Load 1	0 W	0 V	0 A
Efficiency	95.5%		

With reference to the tables showing the different scenarios it is clear that when the SPV power is available and if it is more than the demand of the load the excess power available is routed to the battery through the buck converter.

The battery gets charged. It was observed that, for the case when the SPV power generated is 43 W with a terminal voltage of the SPV panel is 14.7 V the SPV current is 2.96 A. Out of this power, the battery is being charged with a terminal voltage across the battery being 12.72 V and the charging current is 3.27A and the total power harvested is routed to the battery.

6. CONCLUSION

A novel dual output DC to DC converter built around a QBC has been presented. The mathematical modeling using the State Space averaging technique has been presented. The open circuit behavior of the proposed QBDMOC has been studied. The proposed converter has been powered by an SPV source. SMC scheme has been used for the MPPT as well as for regulating the output voltages. The different modes of operations have been simulated and the proposed idea has been validated. An experimental prototype has also been developed and the proposed idea has been verified successfully. It has been observed that both in the simulation and in the experimental verification the proposed topology exhibited the expected functionality by delivering a regulated 48 V output at the high voltage channel and a regulated 12 V output at the low voltage channel. The MPPT scheme using the SMC has proved to track the changes in the solar irradiance and helps to harvest the maximum power at all solar irradiances. Efficiency can be improved by designing advanced controller. Novel converter can be designed by interfacing n number of converters to get n number of multilevel outputs.

7. REFERENCES

- [1] J. Malan, M. J. Kamper, "Performance of a hybrid electric vehicle using reluctance synchronous machine technology", *IEEE Transactions on Industry Applications*, Vol. 37, No. 5, 2001, pp. 1319-1324.
- [2] F. Musavi, W. Eberle, W. G. Dunford, "A high-performance single-phase AC-DC power factor corrected boost converter for plug in hybrid electric vehicle battery chargers", *Proceedings of the IEEE Energy Conversion Congress and Exposition*, Atlanta, GA, USA, 12-16 September 2010, pp. 3588-3595.
- [3] Z. Chen, Z. Nie, Y. Fu, C. C. Mi, "A bidirectional power converter for battery of plug-in hybrid electric vehicles", *Proceedings of the IECON 36th Annual Conference on IEEE Industrial Electronics Society*, Glendale, AZ, USA, 7-10 November 2010, pp. 3049-3053.
- [4] S. Ketsingsoi, Y. Kumsuwan, "An Off-line Battery Charger Based on Buck-Boost Power Factor Correction Converter for Plug-in Electric Vehicles", *Energy Procedia*, vol. 56, 2014, pp. 659-666.
- [5] P. H. Kydd, C. A. Martin, K. J. Komara, P. Delgoshaei, D. Riley, "Vehicle-Solar-Grid Integration II: Results in Simulated School Bus Operation", *EEE Power and Energy Technology Systems Journal*, Vol. 3, No. 4, 2016, pp. 198-205.
- [6] M. A. Mingyao, Z. Chang, Y. hu, C. Gan, W. Cao, "An Integrated Switched Reluctance Motor Drive Topology with Voltage-Boosting and On-Board Charging Capabilities for Plug-In Hybrid Electric Vehicles (PHEVs)", *IEEE Access*, Vol. 6, 2017, pp. 1550-1560.
- [7] V. Fernao Pires, A. Cordeiro, D. Foito, J. F. Silva, "High step-up DC-DC converter for fuel cell vehicles based on merged quadratic boost-cuk", *IEEE Transactions on Vehicular Technology*, Vol. 68, No. 8, 2019, pp. 7521-7530.
- [8] S. Natchimuthu, M. Chinnusamy, A. P. Mark, "Experimental Investigation of PV Based Modified SEPIC Converter Fed Hybrid Electric Vehicle (PV-HEV)", *International Journal of Circuit Theory and Applications*, Vol. 48, No. 6, 2020, pp.1-17.
- [9] D. S. Wijeratne, G. Moschopoulos, "Quadratic power conversion for power electronics: principles and circuits", *IEEE Transactions on Circuits and Systems I: Regular Papers*, Vol. 59, No. 2, 2011, pp. 426-438.
- [10] S. H. Chincholkar, C. Y. Chan, "Design of fixed-frequency pulsewidth-modulation-based sliding-mode controllers for the quadratic boost converter", *IEEE Transactions on Circuits and Systems II: Express Briefs*, Vol. 64, No. 1, 2019, pp. 51-55.
- [11] S. W. Lee, H. L. Do, "Quadratic Boost DC-DC Converter with High Voltage Gain and Reduced Voltage Stresses", *IEEE Transactions on Power Electronics*, Vol. 34, No.3, 2019, pp. 1-7.
- [12] G. Li, X. Jin, X. Chen, X. Mu, "A Novel Quadratic Boost Converter with Low Inductor Currents", *CPSS Transactions on Power Electronics and Applications*, Vol. 5, No. 1, 2020, pp. 1-10.
- [13] Y. M. Chen, A. Q. Huang, X. Yu, "A high step-up three-port DC-DC converter for stand-alone PV/battery power systems", *IEEE Transactions on Power Electronics*, Vol. 28, No. 11, 2013, pp. 5049-5062.

- [14] B. R. Lin, C. W. Chu, "Hybrid DC–DC Converter with High Efficiency, Wide Zvs Range, and Less Output Inductance", *International Journal of Circuit Theory and Applications*, Vol. 44, No. 5, 2016, pp. 996-1011.
- [15] N. A. Dung, P. P. Hieu, Y. C. Hsieh, J. Y. Lin, Y. C. Liu, H. J. Chiu, "A Novel Low-Loss Control Strategy For Bidirectional DC–DC Converter", *International Journal of Circuit Theory and Applications*, Vol. 45, No.11, 2017, pp. 1801-1813.
- [16] R. Faraji, H. Farzanehfard, "Soft-Switched Non-Isolated High Step-Up Three-Port Dc-Dc Converter for Hybrid Energy Systems", *IEEE Transactions on Power Electronics*, Vol. 33, No. 12, 2018, pp. 10101-10111.
- [17] J. Leyva-Ramos, M. G. Ortiz-Lopez, L. H. Diaz-Saldierna, J. A. Morales-Saldana, "Switching Regulator Using a Quadratic Boost Converter for Wide DC conversion ratios", *IET Power Electronics*, Vol. 2, No. 5, 2009, pp. 605-613.
- [18] J. A. Morales-Saldana, R. Galarza-Quirino, J. Leyva-Ramos, E. Carbajal-Gutierrez, M. G. Ortiz-Lopez, "Multiloop Controller Design for a Quadratic Boost Converter", *IET Electric Power Applications*, Vol. 1, No. 3, 2007, pp. 362-367.
- [19] J. A. Morales-Saldana, R. Loera-Palomo, E. Palacios-Hernandez, J. L. Gonzaz-Martinez, "Modelling and Control of a DC-DC Quadratic Boost Converter with R2P2", *IET Power Electronics*, Vol. 7, No. 1, 2014, pp. 11-22.
- [20] O. Lopez, L. G.Vicuna, M. Castilla, J. Matas, M. Lopez, "Sliding-Mode-Control design of a High-Power-Factor Buck-Boost Rectifier", *IEEE Transactions on Industrial Electronics*, Vol. 46, No. 3, 1999, pp. 604-612.
- [21] O. Ray, S. Mishra. "A Multi-Port Converter Topology with Simultaneous Isolated and Non-Isolated Outputs," *Proceedings of the 39th Annual Conference of the IEEE Industrial Electronics Society*, Vienna, Austria, 10-13 November 2013, pp. 7118-7123.
- [22] O. Ray, S. Mishra, "and Ac Outputs", *IEEE Transactions on Industry Applications*, Vol. 50, No. 2, 2014*, pp. 1082–1093.
- [23] S. Poshtkouhi, O. Trescases, "Multi-Input Single-Inductor Dc-Dc Converter for MPPT in Parallel-Connected Photovoltaic Applications", *Proceedings of the Twenty-Sixth Annual IEEE Applied Power Electronics Conference and Exposition*, Fort Worth, TX, USA, 2011, pp. 41-47.
- [24] M. C. Mira, Z. Zhang, A. Knott, M. A. E. Andersen, "Power Flow Control of A Dual-Input Interleaved Buck/Boost Converter With Galvanic Isolation For Renewable Energy Systems", *Proceedings of the IEEE Applied Power Electronics Conference and Exposition*, Charlotte, NC, USA, 2015, pp. 3007-3012.
- [25] H. Keyhani, H. A. Toliyat, "Single-Stage Multistring PV Inverter With an Isolated High-Frequency Link and Soft-Switching Operation", *IEEE Transactions on Power Electronics*, Vol. 29, No. 8, 2014, pp. 3919-3929.
- [26] S. S. Nag, S. K. Mishra, "A Multi-Input Single-Control (MISC) Battery Charger for Dc Nanogrids", *Proceedings of the IEEE ECCE Asia Downunder*, Melbourne, VIC, Australia, 3-6 June 2013, pp. 304-310.
- [27] F. Chen, R. Burgos, D. Boroyevich, D. Dong, "Control Loop Design of a Two-Stage Bidirectional Ac/Dc Converter for Renewable Energy Systems", *Proceedings of the IEEE Applied Power Electronics Conference and Exposition-APEC*, Fort Worth, TX, USA, 16-20 March 2014, pp. 2177-2183.
- [28] S. Poshtkouhi, M. Fard, H. Hussein, L. M. D. Santos, O. Trescases, M. Varlan, T. Lipan, "A Dual-Active-Bridge Based Bi-Directional Micro-Inverter with Integrated Short-Term Li-Ion Ultra-Capacitor Storage and Active Power Smoothing for Modular PV Systems", *Proceedings of the IEEE Applied Power Electronics Conference and Exposition-APEC*, Fort Worth, TX, USA, 16-20 March 2014, pp. 643-649.
- [29] D. Dong, F. Luo, X. Zhang, D. Boroyevich, P. Mattavelli, "Grid- Interface Bidirectional Converter For Residential DC Distribution Systems; Part 2: AC and Dc Interface Design with Passive Components Minimization", *IEEE Transactions on Power Electronics*, Vol. 28, No. 4, 2013, pp. 1667-1679.
- [30] D. Dong, I. Cvetkovic, D. Boroyevich, W. Zhang, R. Wang, and P. Mattavelli, "Grid-Interface Bidirectional Converter for Residential DC Distribution Systems; Part One: High-Density Two-Stage Topology", *IEEE Transactions on Power Electronics*, Vol. 28, No. 4, 2013, pp. 1655-1666.

An observer design for the flux of line start permanent magnet synchronous motors

Case Study

Hoang-Giang Vu

Electric Power University
Faculty of Electrical Engineering
235 Hoang Quoc Viet Street, Hanoi City, Vietnam

Abstract – The flux generated by permanent magnets is essential to the performance of the line start permanent magnet synchronous motor (LSPMSM), especially during the start-up operation. The permanent magnet is degraded with operating time due to the demagnetization phenomenon, which is principally caused by the armature magnetic field interaction and operating temperature. In the motor model, the permanent magnet flux is important since it directly affects the electromagnetic torque. This paper introduces an observer design that is aimed at estimating the permanent magnet flux of the LSPMSM from the measurement of stator currents. First, derived from the mathematical equations of the motor in the $dq0$ reference frame, a set of equations in state variables of stator currents, magnetic fluxes and rotor angular frequency is considered. Equations of the fluxes are analyzed with the introduction of a new flux variable that allows designing open loops to estimate the fluxes from the stator currents. Moreover, a system of equations only in the state variables of stator currents and permanent magnet flux is formulated in order to design a flux observer, which is with a constant gain. Simulation results confirm the efficiency and robustness of the designed observer.

Keywords: demagnetization, line start permanent magnet synchronous motor, nonlinear observer; parameter identification, permanent magnet flux

1. INTRODUCTION

Facing the challenges of future energy demand and environmental issues during the process of exploiting and using fossil energy, many countries in the world have stepped up the transition to efficient and renewable energies. Besides promoting the development of power generation technologies using renewable energy, improving efficiency is an appropriate option that has received much attention in recent times.

In fact, about 50% of electricity consumed by electrical loads comes from electric motors [1]. In each country, electric motors consume about two-thirds of the electricity absorbed in the industry [2], [3]. Among various types of electric motors, induction motors are extensively used as industrial drives due to the basic features of simple structure, reliable operation and low cost. However, the huge drawback of this type of machine is its limited efficiency and low power factor.

As a more recent structural improvement in last decades, the line start permanent magnet synchronous motor (LSPMSM) is an alternative choice for the squirrel cage induction motor. The LSPMSM has a similar structure of squirrel cage induction motor, but permanent magnets are embedded in the rotor.

The LSPMSM has many advantages of high starting torque, high power factor grade and efficiency range.

In addition, the power drive with this type of motor is cost-effective since no inverter is required to be installed for the connection to the power source [3], [4]. Therefore, it is increasingly used in various applications where the machine is required to be directly powered by the main grid. For instance, it is applied in the system of pumps and fans in the mining industry [4]. The start-up moment of the LSPMSM is improved in comparison with that of the squirrel cage induction motor thanks to the installation of the permanent magnet into the rotor. Unexpectedly, the permanent magnet is suffered by the magnetic field generated by the armature winding and temperature [5], [6], [7]. The demagnetization may occur during the start-up of the machine, abnormal operation, and heavy load conditions that degrades the magnets [8].

The investigation of demagnetization phenomenon has been widely carried out to analyze the process of partial demagnetization of permanent magnets (PMs) and its influence on the performance of the LSPMSM. Most of the studies apply the finite element method (FEM) to solve the equation which is established from the model of coupled electromagnetic and thermal phenomena [4], [5], [7], [8], [9]. The authors in [5] proposed a model of coupled electromagnetic and thermal phenomena in a LSPMSM to analyze the effect of temperature on the magnetic, electrical and thermal properties of the materials. Furthermore, the modeling of

the process of partial demagnetization was presented. It was suggested to be used for the analysis of the effect of magnet demagnetization on the operation of the LSPMSM. In [7], a study of the demagnetization of the Nd-Fe-B magnet by an inclined field was shown. A FEM-based model was built to calculate the demagnetization of the LSPMSM under heavily loaded and overheated conditions. Finite element analysis (FEA) was also used in [8] for the investigation of demagnetization process, in which the decaying of the magnets' properties due to the impact of the demagnetizing magnetic motive force was taken into account. Furthermore, a FEM simulation model was utilized to calculate the remaining magnetization of the permanent magnet that has been exposed to high demagnetizing fields and/or temperature [9]. It was recommended that the average model intrinsic coercivity and the magnet remanence must be calibrated in order to achieve good agreement between simulation and experiment results.

For the permanent magnet synchronous motor (PMSM) in general, many detection methods for the demagnetization of PMs have been proposed, for instance, the techniques based on the spectral analysis of output data [10], [11]; the method using high-frequency signal injection [12]. Other methods are based on flux observer [13], [14], [15] that allow carrying out on-line detection technologies.

In the construction, the LSPMSM is structured with a hybrid rotor that includes a rotor cage like induction motors for the high starting torque and permanent magnets installed in the rotor like permanent magnet synchronous motors for the high efficiency [3]. As a result, in the model-based studies, the motor mathematical model seems to be more complex with the appearance of the permanent magnet flux and, as a consequence, the common difference between d-axis and q-axis parameters in dq0 reference frame. The permanent magnet flux is a modeling parameter that is often identified at the initial stage of an application and will be used for various purposes such as the analysis of system operation during the start-up and steady state, condition monitoring and fault diagnosis of the motor. Furthermore, as mentioned before, the flux can be degraded due to the demagnetization phenomenon. Therefore, the value of permanent magnet flux is very useful in both normal operation and condition monitoring of the LSPMSM. In this investigation, an observer-based approach is proposed to estimate the flux of the permanent magnet. Based on the original model of the motor in the dq0 reference frame, the system and observer models are appropriately formulated with the input of the stator voltages and rotor angular frequency, and the output of the stator currents. The designed observer provides with information on the permanent magnet flux that is useful for condition monitoring during the operation of LSPMSM.

The rest of the article is organized as follows. Section 2 presents the model of the LSPMSM in the dq0 refer-

ence frame. Following this, the system and observer are formulated to observe the permanent magnet flux in section 3. Section 4 introduces the simulation results of the LSPMSM and its observer. Finally, the conclusion is given in Section 5.

2. MODEL OF LSPMSM

The model of the LSPMSM in the dq0 reference frame rotating with the rotor angular speed is given as [1], [16]:

$$v_{sd} = R_s i_{sd} + \frac{d\psi_{sd}}{dt} - \omega_r \psi_{sq} \quad (1)$$

$$v_{sq} = R_s i_{sq} + \frac{d\psi_{sq}}{dt} + \omega_r \psi_{sd} \quad (2)$$

$$v_{rd} = R_{rd} i_{rd} + \frac{d\psi_{rd}}{dt} = 0 \quad (3)$$

$$v_{rq} = R_{rq} i_{rq} + \frac{d\psi_{rq}}{dt} = 0 \quad (4)$$

$$\psi_{sd} = L_{sd} i_{sd} + L_{md} i_{rd} + \psi_m \quad (5)$$

$$\psi_{sq} = L_{sq} i_{sq} + L_{mq} i_{rq} \quad (6)$$

$$\psi_{rd} = L_{md} i_{sd} + L_{rd} i_{rd} + \psi_m \quad (7)$$

$$\psi_{rq} = L_{mq} i_{sq} + L_{rq} i_{rq} \quad (8)$$

where $L_{sd} = L_{ls} + L_{md}$, $L_{sq} = L_{ls} + L_{mq}$,

$L_{rd} = L_{lr} + L_{md}$ and $L_{rq} = L_{lr} + L_{mq}$.

In addition, the rotating equation of the LSPMSM is written by:

$$J \frac{d\omega}{dt} = T_e - T_m - T_f \quad (9)$$

where the electrical torque is computed by

$$T_e = \frac{3p}{2} (i_{sq} \psi_{sd} - i_{sd} \psi_{sq}). \quad (10)$$

In per unit system, equations from (1) to (9) become:

$$\frac{d\psi_{sd}}{dt} = \omega_b (v_{sd} - R_s i_{sd} + \omega_r \psi_{sq}) \quad (11)$$

$$\frac{d\psi_{sq}}{dt} = \omega_b (v_{sq} - R_s i_{sq} - \omega_r \psi_{sd}) \quad (12)$$

$$\frac{d\psi_{rd}}{dt} = -\omega_b R_{rd} i_{rd} \quad (13)$$

$$\frac{d\psi_{rq}}{dt} = -\omega_b R_{rq} i_{rq} \quad (14)$$

$$\psi_{sd} = L_{sd} i_{sd} + L_{md} i_{rd} + \psi_m \quad (15)$$

$$\psi_{sq} = L_{sq} i_{sq} + L_{mq} i_{rq} \quad (16)$$

$$\psi_{rd} = L_{md} i_{sd} + L_{rd} i_{rd} + \psi_m \quad (17)$$

$$\psi_{rq} = L_{mq} i_{sq} + L_{rq} i_{rq} \quad (18)$$

$$2H \frac{d\omega}{dt} = T_e - T_m - T_f \quad (19)$$

where all parameters are used in per unit system; motor inertia J becomes inertia constant H that is defined as $H = \frac{J\omega_{bm}^2}{2S_b}$ in which ω_{bm} is the base mechanical angular frequency; S_b is the base volt-ampere; and $T_e = i_{sq}\psi_{sd} - i_{sd}\psi_{sq}$.

$$\frac{d}{dt}i_{sd} = -a_{11}i_{sd} + a_{12}\omega i_{sq} + a_{13}\psi_{rdm} + a_{14}\omega\psi_{rq} + b_1v_{sd} \quad (20)$$

$$\frac{d}{dt}i_{sq} = -a_{21}\omega i_{sd} - a_{22}i_{sq} - a_{23}\omega\psi_{rdm} + a_{24}\psi_{rq} - (a_{23} + a_{25})\omega\psi_m + b_2v_{sq} \quad (21)$$

$$\frac{d\psi_{rdm}}{dt} = a_{31}i_{sd} - a_{33}\psi_{rdm} \quad (22)$$

$$\frac{d\psi_{rq}}{dt} = a_{42}i_{sq} - a_{44}\psi_{rq} \quad (23)$$

$$2H \frac{d\omega}{dt} = T_e - T_m - T_f \quad (24)$$

where new constants

$$a_{11}, a_{12}, a_{13}, a_{14}, a_{21}, a_{22}, a_{23}, a_{24}, a_{25}, a_{31}, a_{33}, a_{42}, a_{44}, b_1, b_2$$

are defined in Appendix B.

In equations from (20) to (22), a new definition is introduced that $\psi_{rdm} = \psi_{rd} - \psi_m$. It will be shown in the next section that the fluxes of ψ_{rdm} and ψ_{rq} can be estimated via open loops.

To estimate the permanent magnet flux, the following equation is added:

$$\frac{d\psi_m}{dt} = 0 \quad (25)$$

Using the equation from (20) to (25), the model of system and observer will be formulated in the next section.

3. SYSTEM MODEL FORMULATION AND OBSERVER DESIGN

In this section, the system and observer models are formulated to design an observer for the estimation of the permanent magnet flux, Fig. 1.

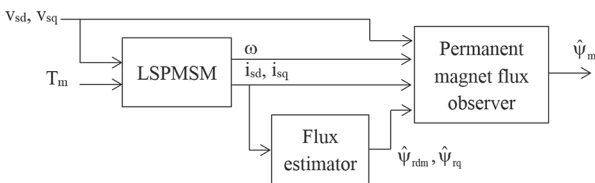


Fig. 1. Diagram of LSPMSM with the flux estimator and permanent magnet flux observer.

The LSPMSM is simulated with a detail diagram depicted in Fig.2. It is composed of the following main blocks:

- The top block is used to transform the grid voltage from a three-phase reference frame into the dq0 reference frame that rotates at the angular speed of the rotor;
- The three bottom blocks implement the model of the motor in the dq0 reference frame. First, the equations from (11) to (18) are used to calculate the components of stator currents and stator fluxes. They are then used for the computation of the electromagnetic torque (T_e). Finally, Equation (19) is utilized to calculate the speed and the angle of the rotor.

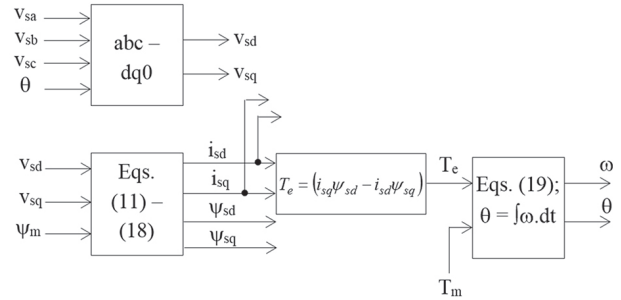


Fig. 2. Detailed diagram of LSPMSM simulation

Equivalently, the LSPMSM can be simulated by using equations from (20) to (24).

3.1. SYSTEM AND OBSERVER MODELS

The system model is established by using equations (20), (21), and (25):

$$\begin{cases} \dot{x} = A(u, x).x + B(u) = f(u, x) \\ y = x_l = C.x \end{cases} \quad (26)$$

where x is the state, $x = [x_1 \ x_2]^T$ with $x_1 = [i_{sd} \ i_{sq}]^T$ and $x_2 = \psi_m$;

$f(u, x) = [f_1(u, x) \ f_2(u, x)]^T$; y is the output; u is the input, $u = [v_{sd} \ v_{sq} \ \omega]^T$; and the matrices in the equation are given as

$$A(u, x) = \begin{bmatrix} -a_{11} & a_{12}\omega & 0 \\ -a_{21}\omega & -a_{22} & -(a_{23} + a_{25})\omega \\ 0 & 0 & 0 \end{bmatrix},$$

$$B(u) = \begin{bmatrix} a_{13}\psi_{rdm} + a_{14}\omega\psi_{rq} + b_1v_{sd} \\ -a_{23}\omega\psi_{rdm} + a_{24}\psi_{rq} + b_2v_{sq} \\ 0 \end{bmatrix}$$

$$\text{and } C = \begin{bmatrix} 1 & 0 & 0 \\ 0 & 1 & 0 \end{bmatrix}.$$

The fluxes of ψ_{rdm} and ψ_{rq} are estimated from the stator currents via open loops. In the next subsection, a simple proof will be described for the observation of these fluxes.

3.2. ESTIMATION OF FLUXES

Indeed, equations (22) and (23) are of the following form:

$$\frac{dz}{dt} = -a.z + b.y_z \quad (27)$$

where z is the state, y_z is the output.

Note that if $y_z=0$ then equation (27) becomes:

$$\frac{dz}{dt} = -a.z \quad (28)$$

It is clearly that if $a>0$ then z decay exponentially to 0 with any initial condition $z(0)$. With $y_z \neq 0$, defining the estimation error of z as $\tilde{z}=z-\hat{z}$, the resulting estimation dynamic can be expressed by:

$$\begin{aligned} \frac{d\tilde{z}}{dt} &= \frac{d(z-\hat{z})}{dt} = (-a.z + b.y_z) - (-a.\hat{z} + b.y_z) \\ &= -a(z-\hat{z}) = -a\tilde{z} \end{aligned}$$

or

$$\frac{d\tilde{z}}{dt} = -a.\tilde{z} \quad (29)$$

Now, we can repeat for (29) from the analysis for (28). In conclusion, two separate open- loop flux estimators can be built:

$$\frac{d\hat{\psi}_{rdm}}{dt} = a_{31}i_{sd} - a_{33}\hat{\psi}_{rdm} \quad (30)$$

$$\frac{d\hat{\psi}_{rq}}{dt} = a_{42}i_{sq} - a_{44}\hat{\psi}_{rq} \quad (31)$$

3.3. OBSERVER FORM

From (26), differentiating $f_1(u, x)$ with respect to x_2 , we obtain $\frac{\partial f_1}{\partial x_2} = \begin{bmatrix} 0 \\ -(a_{23} + a_{25})\omega \end{bmatrix}$.

It is obviously seen that $\frac{\partial f_1}{\partial x_2}$ is located in a half plane when the rotor speed varies. Therefore, $A(u, x)$ is convex by $(A_1$ and $A_2)$ where

$$A_1 = \begin{bmatrix} -a_{11} & a_{12}\omega_{min} & 0 \\ -a_{21}\omega_{min} - a_{22} & -(a_{23} + a_{25})\omega_{min} & 0 \\ 0 & 0 & 0 \end{bmatrix} \quad \text{and}$$

$$A_2 = \begin{bmatrix} -a_{11} & a_{12}\omega_{max} & 0 \\ -a_{21}\omega_{max} - a_{22} & -(a_{23} + a_{25})\omega_{max} & 0 \\ 0 & 0 & 0 \end{bmatrix}$$

in which the minimum and maximum values of ω can be respectively selected as $\omega_{min}=0$, $\omega_{max}=\omega_e/p$ where ω_e is the angular frequency of the main grid.

Therefore, a candidate of observer is of the following form [17], [18]:

$$\dot{\hat{x}} = A(u, \hat{x}).\hat{x} + B(u) + \Delta_\lambda K (Cx - y) \quad (32)$$

where

$$\Delta_\lambda = \begin{bmatrix} \lambda & 0 & 0 \\ 0 & \lambda & 0 \\ 0 & 0 & \lambda^2 \end{bmatrix}$$

and $K=Q^{-1} C^T$ with Q is the solution of the following inequality for A_1 and A_2 :

$$QA + A^T Q - \rho C^T C \leq -\eta I \quad (33)$$

In addition, the following inequalities are added to restrict gain matrix K :

$$\begin{aligned} I &\leq Q \leq \zeta I \\ -\xi I &\leq C'(QK) + (QK)C \leq \xi I \end{aligned} \quad (34)$$

where $\zeta>1$ and $\xi>0$.

Select $\eta=1$, $\rho=1$ then K is obtained by:

$$K = \begin{bmatrix} -4328 & -73 \\ -73 & -888 \\ 536 & 12 \end{bmatrix} \quad (35)$$

Finally, by tuning, we obtain $\lambda=1$.

4. SIMULATION RESULTS AND DISCUSSION

In this section, the performance of the proposed observer is validated via simulation. The block diagram of the LSPMSM system with observer is given in Fig.1. The complete simulation block model developed in the Scilab/Xcos environment is given in Appendix C. The flux estimator uses only stator currents and provides estimated values of ψ_{rdm} and ψ_{rq} for the permanent magnet flux observer.

The simulation is developed in the following conditions:

- The LSPMSM is simulated using equations from (11) to (19);
- The motor parameters are given in Appendix A, which are adopted from [19];
- The initial condition to simulate LSPMSM is

$$\begin{bmatrix} \psi_{rd0} & \psi_{rq0} & i_{sd0} & i_{sq0} & \omega_{r0} & T_{m0} \end{bmatrix} = [0.86 \quad 0 \quad -0.92 \quad 0.86 \quad 0 \quad 0.1]$$

- The initial condition of estimator and observer respectively are:

$$\begin{bmatrix} \hat{\psi}_{rdm} & \hat{\psi}_{rq} \end{bmatrix}^T = [-0.26 \quad 0.2]^T$$

$$\text{and } \begin{bmatrix} \hat{i}_{sd} & \hat{i}_{sq} & \hat{\psi}_m \end{bmatrix}^T = [0 \quad 0 \quad 0.60]^T;$$

- The power source voltage has the amplitude that $V_m=1pu$, at the angular frequency that $\omega_e=1pu$.

The load fluctuation is generated by changing the load torque over a period of 5s, as shown in the top subfigure of Fig. 3. The motor starts working at load torque 0.1pu, then its load is increased to rated level ($T_m=1pu$) at $t=2.5s$. After a period of 1s operating at this level, the load torque is reduced to 0.5pu at $t=3.5s$ and back to the rated level at $t=4.5s$. In addition, the permanent magnet flux is assumed to be degraded and dropped by 30% at $t=4s$, as can be seen in the bottom subfigure of Fig. 3.

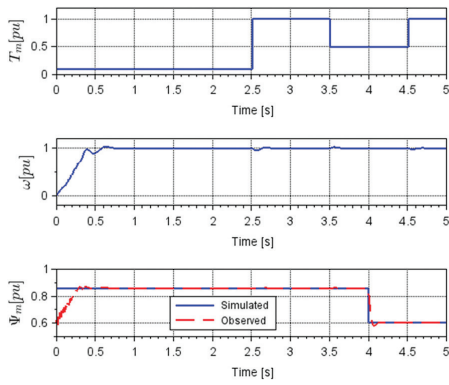


Fig. 3. Applied load torque (top); rotor speed (middle); and estimated permanent magnet flux (bottom)

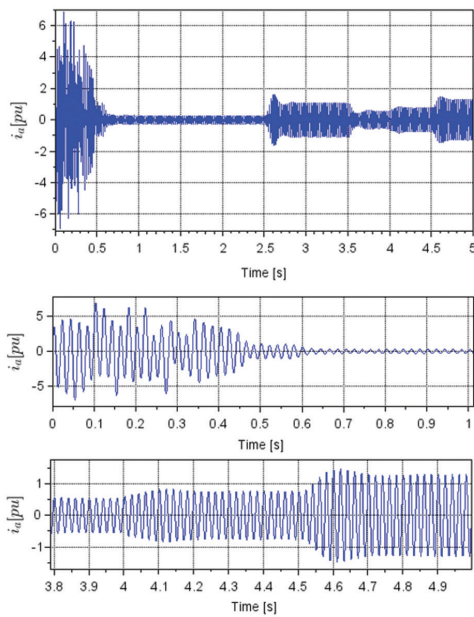


Fig. 4. The current of phase A (top); subfigure zoomed the start-up (middle); and subfigure zoomed the duration with sudden change of the permanent magnet flux (bottom)

The signal of phase stator current from the start-up to the synchronized operation with the main grid is shown in Fig. 4. It can be seen that the amplitude of the current varies due to the change of the load torque and the permanent magnet flux parameter.

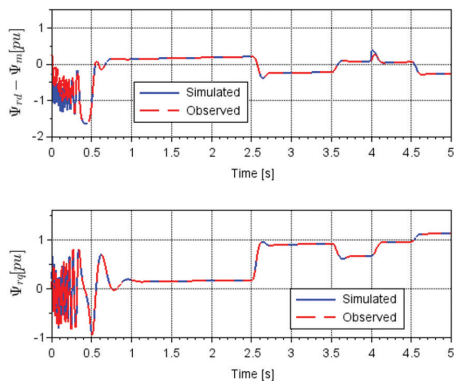


Fig. 5. Estimation results of ψ_{rdm} (upper) and ψ_{rq} (lower)

Fig. 5 shows the good estimation results for the fluxes ψ_{rdm} and ψ_{rq} , which are essential to the performance of the permanent magnet flux observer.

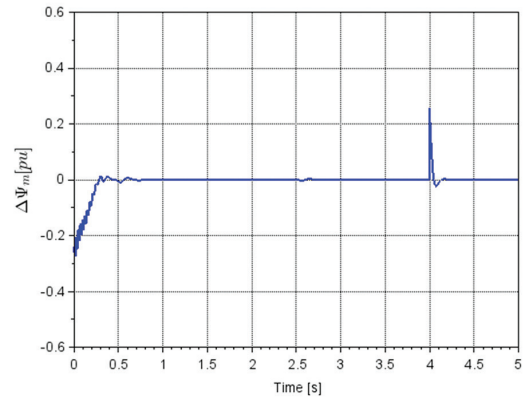


Fig. 6. Error between observed and simulated permanent magnet fluxes

Due to the load variation, the motor speed is slightly fluctuated around the events as can be viewed in the middle subfigure of Fig. 3. The speed is also influenced by the sudden change of the flux.

It can be seen in the bottom subfigure of Fig. 3 that the permanent magnet flux is well observed and the convergence is reached before the steady state of the system. The error between the estimated and simulated values is shown in Fig. 6. It robustly decays to zero after a sudden change of the permanent magnet flux. In addition, no error is recorded during the steady state, even with variations in load torque.

To evaluate the influence of parameters such as resistor uncertainty on the performance of the observer, the simulation is repeated under the condition that the resistor values used for the observer are set equal to 80% of the corresponding system parameters.

The estimated results and the error of permanent magnet flux are shown in the Figs 7 and 8, respectively.

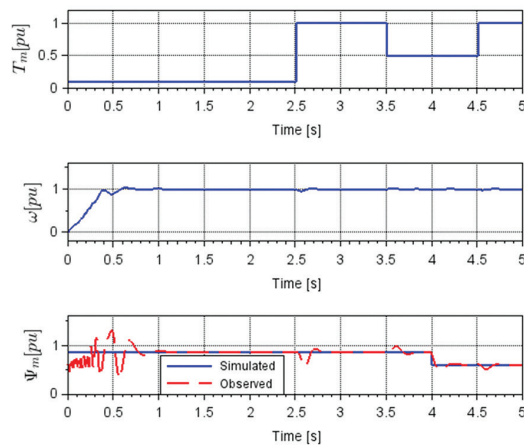


Fig. 7. Applied load torque (top); rotor speed (middle); and estimated permanent magnet flux (bottom) (resistance uncertainty)

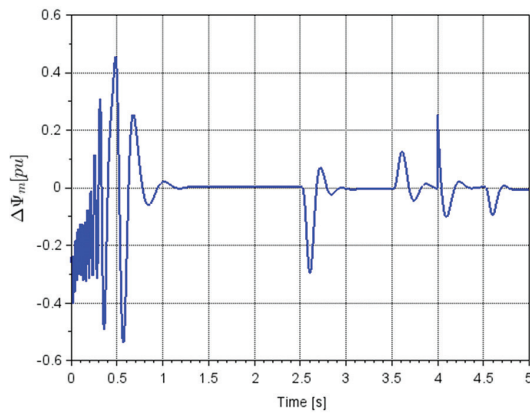


Fig. 8. Error between observed and simulated permanent magnet flux (resistance uncertainty)

It can be seen that the observer converges more slowly from the start with a larger estimation error. Furthermore, variations in load torque also cause the error; however, it is only significant around the time of the events. In steady state, the error is larger than that of the estimation with parameter certainty but insignificant.

The simulation results have illustrated the effective operation of the observer in the estimation of permanent magnet flux, even in the condition of parameter uncertainty. It must be reminded that the observer model in synchronous reference frame is characterized by robust computation with dc components of voltages, currents or fluxes.

In practice, a physical experiment platform can be implemented with a DSP driver board, a LSPMSM and power supply. Moreover, some sensors are needed for the information of stator currents, stator voltages, rotor position or rotor angular speed.

5. CONCLUSION

In this study, from the commonly mathematical model of LSPMSM, a model of the machine with the variables of stator currents, magnetic fluxes and rotor angular frequency was proposed. For the purpose of estimating the permanent magnet flux, a simple set of variables has allowed an open-loop estimation of the magnetic fluxes. In addition, an appropriate form of the observer with constant gain was obtained that provides robust performance in the estimation of the permanent magnet flux during different operation conditions of the motor. In order to obtain the flux information, three-phase voltage, three-phase current, rotor angular speed or rotor angular position information are needed. An on-line detection method can be introduced by applying the proposed flux observer that allows evaluating the demagnetization of the magnets for the condition monitoring of the LSPMSM.

6. ACKNOWLEDGEMENTS

The author would like to express gratitude to Dr. Nguyen Xuan Truong from the University of Science

and Technology of Hanoi for his help in performing calculations.

7. LIST OF SYMBOLS

f_n	Rated frequency,
H	Inertia constant (pu)
i_{rd} and i_{rq}	Rotor currents in d-axis and q-axis referred to stator side,
i_{sd} and i_{sq}	Stator currents in d-axis and q-axis,
J	Motor inertial,
L_{lr_d} and L_{lr_q}	Rotor leakage inductances in the d- and q-axis referred to the stator side,
L_{ls}	Leakage stator inductance,
L_{m_d} and L_{m_q}	Mutual inductances in the d- and q-axis,
L_{r_d} and L_{r_q}	Rotor total inductances in the d- and q-axis referred to the stator side,
L_{s_d} and L_{s_q}	Stator total inductances in the d- and q-axis,
ω	Rotor mechanical angular frequency,
ω_r	Rotor electrical angular frequency, $\omega_r = p \cdot \omega$,
p	Number of pole pairs,
P_n	Rated power,
ψ_m	Flux of the permanent magnet refer to stator side,
ψ_{rd} and ψ_{rq}	Rotor leakages fluxes in d-axis and q-axis referred to stator side,
ψ_{sd} and ψ_{sq}	Stator leakage fluxes in d-axis and q-axis,
R_s	Stator resistance per phase,
R_{rd} and R_{rq}	Rotor resistances per phase in d-axis and q-axis referred to stator side,
T_f	Frictional torque,
T_m	Load torque,
V_n	Rated voltage,
v_{rd} and v_{rq}	Rotor voltages in d-axis and q-axis referred to stator side,
v_{sd} and v_{sq}	Stator voltages d-axis and q-axis.

8. APPENDIX

A. Parameters of LSPMSM

Nominal Parameter	Value
f_n	50 Hz
P_n	750 W
V_n	230 V
Model parameter	Value
H	0.3 pu
L_{lrd}	0.132 pu
L_{lrq}	0.132 pu
L_{ls}	0.065 pu
L_{sd}	0.543 pu
L_{sq}	1.086 pu
ψ_m	0.86 pu
R_{rd}	0.054 pu
R_{rq}	0.108 pu
R_{rs}	0.017 pu

B. Definition of constants in equations from (20) to (23)

$$\sigma_d = L_{sd} - \frac{L_{md}^2}{L_{rd}}; \quad a_{11} = \omega_b \frac{R_s + R_{rd} \frac{L_{md}^2}{L_{rd}^2}}{\sigma_d};$$

$$a_{12} = \omega_b \frac{p \left(L_{sq} - \frac{L_{mq}^2}{L_{rq}} \right)}{\sigma_d}; \quad a_{13} = \omega_b \frac{R_{rd} \frac{L_{md}^2}{L_{rd}^2}}{\sigma_d};$$

$$a_{14} = \omega_b \frac{p \frac{L_{mq}}{L_{rq}}}{\sigma_d}; \quad b_1 = \omega_b \frac{1}{\sigma_d}; \quad \sigma_q = L_{sq} - \frac{L_{mq}^2}{L_{rq}};$$

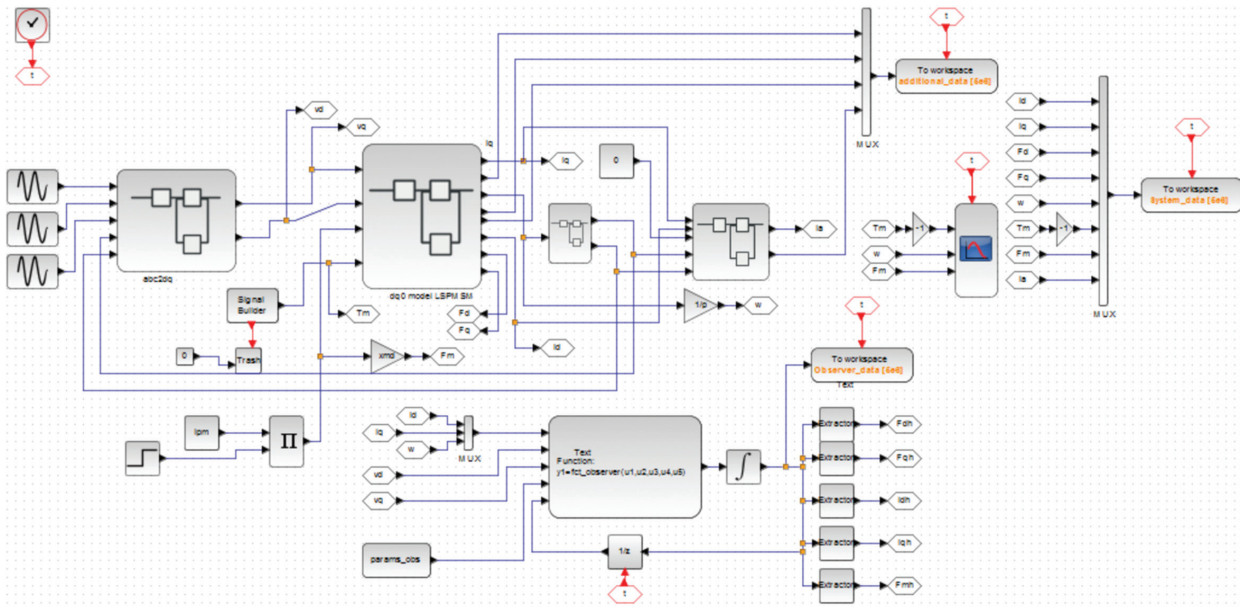
$$a_{21} = \omega_b \frac{p \left(L_{sd} - \frac{L_{md}^2}{L_{rd}} \right)}{\sigma_q}; \quad a_{22} = \omega_b \frac{R_s + R_{rq} \frac{L_{mq}^2}{L_{rq}^2}}{\sigma_q};$$

$$a_{23} = \omega_b \frac{p \frac{L_{md}}{L_{rd}}}{\sigma_q}; \quad a_{24} = \omega_b \frac{R_{rq} \frac{L_{mq}}{L_{rq}^2}}{\sigma_q}; \quad b_2 = \omega_b \frac{1}{\sigma_q};$$

$$a_{25} = \omega_b \frac{p \left(1 - \frac{L_{md}}{L_{rd}} \right)}{\sigma_q}; \quad a_{31} = \omega_b \frac{R_{rd} L_{md}}{L_{rd}}; \quad a_{33} = \omega_b \frac{R_{rd}}{L_{rd}};$$

$$a_{42} = \omega_b \frac{R_{rq} L_{mq}}{L_{rq}}; \quad a_{44} = \omega_b \frac{R_{rq}}{L_{rq}};$$

C. Simulation block model of LSPMSM and observer



9. REFERENCES

- [1] A. H. Sfahani, S. Vaez-Zadeh, "Line start permanent magnet synchronous motors: Challenges and opportunities", *Energy*, Vol. 24, No. 11, 2009, pp. 1755-1763.
- [2] R. Saidur, "A review on electrical motors energy use and energy savings", *Renewable and Sustainable Energy Reviews*, Vol. 14, No. 3, 2010, pp. 877-898.
- [3] M. R. Mehrjou, N. Mariun, N. Misron, M. A. M. Radzi, "Analysis of statistical features based on start-up

- current envelope for broken rotor bar fault detection in line start permanent magnet synchronous motor", *Electrical Engineering*, Vol. 99, No. 1, 2017, pp. 187-201.
- [4] M. Baranski, W. Szlag, W. Lyskawinski, "Analysis of the Partial Demagnetization Process of Magnets in a Line Start Permanent Magnet Synchronous Motor", *Energies*, Vol. 13, No. 21, 2020, p. 5562.
- [5] M. Baranski, W. Szlag, W. Lyskawinski, "Experimental and simulation studies of partial demagnetization process of permanent magnets in electric motors", *IEEE Transactions on Energy Conversion*, Vol. 36, No. 4, 2021, pp. 3137-3145.
- [6] S. Ruoho, J. Kolehmainen, J. Ikaheimo, A. Arkkio, "Interdependence of demagnetization, loading, and temperature rise in a permanent-magnet synchronous motor", *IEEE Transactions on Magnetics*, Vol. 46, No. 3, 2009, pp. 949-953.
- [7] S. Ruoho, A. Arkkio, "Partial demagnetization of permanent magnets in electrical machines caused by an inclined field", *IEEE Transactions on Magnetics*, Vol. 44, No. 7, 2008, pp. 1773-1778.
- [8] J. X. Shen, P. Li, M. J. Jin, G. Yang, "Investigation and countermeasures for demagnetization in line start permanent magnet synchronous motors", *IEEE Transactions on Magnetics*, Vol. 49, No. 7, 2013, pp. 4068-4071.
- [9] S. Sjökvist, S. Eriksson, "Experimental verification of a simulation model for partial demagnetization of permanent magnets", *IEEE Transactions on Magnetics*, Vol. 50, No. 12, 2014, pp. 1-5.
- [10] M. Krichen, E. Elbouchikhi, B. Naourez, M. Chaieb, R. Neji, "Motor current signature analysis-based permanent magnet synchronous motor demagnetization characterization and detection", *Machines*, Vol. 8, No. 35, 2020.
- [11] C. Candelo-Zuluaga, J. Riba, D. Thangamuthu, A. Garcia, "Detection of partial demagnetization faults in five-phase permanent magnet assisted synchronous reluctance machines", *Energies*, Vol. 13, No. 13, 2020, p. 3496.
- [12] J. Hong, "Detection and classification of rotor demagnetization and eccentricity faults for PM synchronous motors", *IEEE Transactions on Industry Applications*, Vol. 48, 2012, p. 923-932.
- [13] Y. Min, W. Huang, J. Yang, Y. Zhao, "On-line estimation of permanent-magnet flux and temperature rise in stator winding for PMSM", in *Proceedings of the 22nd International Conference on Electrical Machines and Systems*, Harbin, China, 11-14 August 2019.
- [14] X. Xiao, C. Chen, "Reduction of torque ripple due to demagnetization in PMSM using current compensation", *IEEE Transactions on Applied Superconductivity*, Vol. 20, 2010, pp. 1068-1071.
- [15] L. Cao, Z. Wu, "On-Line Detection of Demagnetization for Permanent Magnet Synchronous Motor via Flux Observer", *Machines*, Vol. 10, No. 5, 2022, p. 354.
- [16] L. Maraaba, Z. Al-Hamouz, A. Milhem, S. Twaha, "Comprehensive Parameters Identification and Dynamic Model Validation of Interior-Mount Line-Start Permanent Magnet Synchronous Motors", *Machines*, Vol. 7, No. 4, 2019.
- [17] H.-G. Vu, H. Yahoui, H. Hammouri, "Nonlinear Observer Design for Load Torque Estimation of Induction Motors", *Advances in Electrical and Electronic Engineering*, Vol. 18, No. 3, 2020.
- [18] H. Hammouri, M. Farza, "Nonlinear observers for locally uniformly observable systems", *ESAIM. COCV*, Vol. 9, pp. 353-370, 2003, pp. 153-159.
- [19] M. A. Rahman, T. A. Little, "Dynamic performance analysis of permanent magnet synchronous motors magnet synchronous motors", *IEEE Transactions on Power Apparatus and Systems*, Vol. 6, 1984, pp. 1277-1282.

INTERNATIONAL JOURNAL OF ELECTRICAL AND COMPUTER ENGINEERING SYSTEMS

Published by Faculty of Electrical Engineering, Computer Science and Information Technology Osijek,
Josip Juraj Strossmayer University of Osijek, Croatia.

About this Journal

The International Journal of Electrical and Computer Engineering Systems publishes original research in the form of full papers, case studies, reviews and surveys. It covers theory and application of electrical and computer engineering, synergy of computer systems and computational methods with electrical and electronic systems, as well as interdisciplinary research.

Topics of interest include, but are not limited to:

- Power systems
- Renewable electricity production
- Power electronics
- Electrical drives
- Industrial electronics
- Communication systems
- Advanced modulation techniques
- RFID devices and systems
- Signal and data processing
- Image processing
- Multimedia systems
- Microelectronics
- Instrumentation and measurement
- Control systems
- Robotics
- Modeling and simulation
- Modern computer architectures
- Computer networks
- Embedded systems
- High-performance computing
- Parallel and distributed computer systems
- Human-computer systems
- Intelligent systems
- Multi-agent and holonic systems
- Real-time systems
- Software engineering
- Internet and web applications and systems
- Applications of computer systems in engineering and related disciplines
- Mathematical models of engineering systems
- Engineering management
- Engineering education

Paper Submission

Authors are invited to submit original, unpublished research papers that are not being considered by another journal or any other publisher. Manuscripts must be submitted in doc, docx, rtf or pdf format, and limited to 30 one-column double-spaced pages. All figures and tables must be cited and placed in the body of the paper. Provide contact information of all authors and designate the corresponding author who should submit the manuscript to <https://ijeces.ferit.hr>. The corresponding author is responsible for ensuring that the article's publication has been approved by all coauthors and by the institutions of the authors if required. All enquiries concerning the publication of accepted papers should be sent to ijeces@ferit.hr.

The following information should be included in the submission:

- paper title;
- full name of each author;
- full institutional mailing addresses;
- e-mail addresses of each author;
- abstract (should be self-contained and not exceed 150 words). Introduction should have no subheadings;
- manuscript should contain one to five alphabetically ordered keywords;
- all abbreviations used in the manuscript should be explained by first appearance;
- all acknowledgments should be included at the end of the paper;
- authors are responsible for ensuring that the information in each reference is complete and accurate. All references must be numbered consecutively and citations of references in text should be identified using numbers in square brackets. All references should be cited within the text;
- each figure should be integrated in the text and cited in a consecutive order. Upon acceptance of the paper, each figure should be of high quality in one of the following formats: EPS, WMF, BMP and TIFF;
- corrected proofs must be returned to the publisher within 7 days of receipt.

Peer Review

All manuscripts are subject to peer review and must meet academic standards. Submissions will be first considered by an editor-

in-chief and if not rejected right away, then they will be reviewed by anonymous reviewers. The submitting author will be asked to provide the names of 5 proposed reviewers including their e-mail addresses. The proposed reviewers should be in the research field of the manuscript. They should not be affiliated to the same institution of the manuscript author(s) and should not have had any collaboration with any of the authors during the last 3 years.

Author Benefits

The corresponding author will be provided with a .pdf file of the article or alternatively one hardcopy of the journal free of charge.

Units of Measurement

Units of measurement should be presented simply and concisely using System International (SI) units.

Bibliographic Information

Commenced in 2010.
ISSN: 1847-6996
e-ISSN: 1847-7003

Published: semiannually

Copyright

Authors of the International Journal of Electrical and Computer Engineering Systems must transfer copyright to the publisher in written form.

Subscription Information

The annual subscription rate is 50€ for individuals, 25€ for students and 150€ for libraries.

Postal Address

Faculty of Electrical Engineering,
Computer Science and Information Technology Osijek,
Josip Juraj Strossmayer University of Osijek, Croatia
Kneza Trpimira 2b
31000 Osijek, Croatia

IJECES Copyright Transfer Form

(Please, read this carefully)

This form is intended for all accepted material submitted to the IJECES journal and must accompany any such material before publication.

TITLE OF ARTICLE (hereinafter referred to as “the Work”):

COMPLETE LIST OF AUTHORS:

The undersigned hereby assigns to the IJECES all rights under copyright that may exist in and to the above Work, and any revised or expanded works submitted to the IJECES by the undersigned based on the Work. The undersigned hereby warrants that the Work is original and that he/she is the author of the complete Work and all incorporated parts of the Work. Otherwise he/she warrants that necessary permissions have been obtained for those parts of works originating from other authors or publishers.

Authors retain all proprietary rights in any process or procedure described in the Work. Authors may reproduce or authorize others to reproduce the Work or derivative works for the author's personal use or for company use, provided that the source and the IJECES copyright notice are indicated, the copies are not used in any way that implies IJECES endorsement of a product or service of any author, and the copies themselves are not offered for sale. In the case of a Work performed under a special government contract or grant, the IJECES recognizes that the government has royalty-free permission to reproduce all or portions of the Work, and to authorize others to do so, for official government purposes only, if the contract/grant so requires. For all uses not covered previously, authors must ask for permission from the IJECES to reproduce or authorize the reproduction of the Work or material extracted from the Work. Although authors are permitted to re-use all or portions of the Work in other works, this excludes granting third-party requests for reprinting, republishing, or other types of re-use. The IJECES must handle all such third-party requests. The IJECES distributes its publication by various means and media. It also abstracts and may translate its publications, and articles contained therein, for inclusion in various collections, databases and other publications. The IJECES publisher requires that the consent of the first-named author be sought as a condition to granting reprint or republication rights to others or for permitting use of a Work for promotion or marketing purposes. If you are employed and prepared the Work on a subject within the scope of your employment, the copyright in the Work belongs to your employer as a work-for-hire. In that case, the IJECES publisher assumes that when you sign this Form, you are authorized to do so by your employer and that your employer has consented to the transfer of copyright, to the representation and warranty of publication rights, and to all other terms and conditions of this Form. If such authorization and consent has not been given to you, an authorized representative of your employer should sign this Form as the Author.

Authors of IJECES journal articles and other material must ensure that their Work meets originality, authorship, author responsibilities and author misconduct requirements. It is the responsibility of the authors, not the IJECES publisher, to determine whether disclosure of their material requires the prior consent of other parties and, if so, to obtain it.

- The undersigned represents that he/she has the authority to make and execute this assignment.
- For jointly authored Works, all joint authors should sign, or one of the authors should sign as authorized agent for the others.
- The undersigned agrees to indemnify and hold harmless the IJECES publisher from any damage or expense that may arise in the event of a breach of any of the warranties set forth above.

Author/Authorized Agent

Date

CONTACT

International Journal of Electrical and Computer Engineering Systems (IJECES)
Faculty of Electrical Engineering, Computer Science and Information Technology Osijek
Josip Juraj Strossmayer University of Osijek
Kneza Trpimira 2b
31000 Osijek, Croatia
Phone: +38531224600,
Fax: +38531224605,
e-mail: ijeces@ferit.hr